Synthesis and Properties of Light-Emitting Si-Based Nanostructures
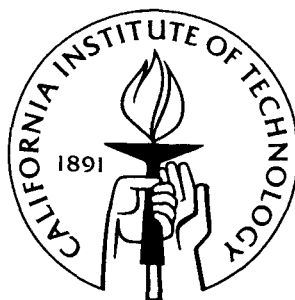
Thesis by

Kyu Sung Min

In Partial Fulfillment of the Requirements

for the Degree of

Doctor of Philosophy

California Institute of Technology

Pasadena, California

2000

(Submitted July 2, 1999)

In loving memory

of my extraordinary father,

Benjamin Min,

who wanted so dearly to see

the completion of this thesis.

Acknowledgements

It gives me great pleasure to acknowledge colleagues and faculty members at Caltech who have contributed directly or indirectly, through stimulating discussions or their expert technical expertise, in making this thesis possible. It also gives me great pleasure to acknowledge my friends and my family for their inexhaustible love and friendship in making this thesis possible. The great minds I've encountered at Caltech have always inspired me to explore the unexplored and to imagine the unimagined. I have gained far more through research than just knowledge. Research has taught me the values of creativity, objectivity, and most of all, perseverance. I have matured a great deal, both as a scientist and a person, through the time and effort I've spent at Caltech. And it should be aforementioned that words are not enough to fully express my gratitude to the people who have contributed to the completion of this thesis and to my maturity as a person.

First and foremost, I would like to thank Dr. Maggie Taylor, who has pulled me through all the difficult times and has doubled the pleasure of the happy times of my graduate career. Whether it was during the time of great joy in a scientific discovery or during the moments of deepest frustration and sorrow, she has always been there to provide expert scientific advice, to share the laughter and joy, and to provide the deepest sympathy and a shoulder to cry on. Maggie has been the best

colleague, my best friend, and much more, in and out of the lab. I want to thank my advisor, Prof. Harry A. Atwater, who has provided me with the best guidance in learning much of what I know about the contents of this thesis. He has always been my biggest source of enthusiasm and inspiration. He has shown me the proper winning attitude in facing and tackling unsolved and often times seemingly unsolvable problems. I want to thank Dr. Mark Brongersma, with whom I have shared countless hours in understanding the origin and mechanism of visible luminescence from ion beam synthesized nanocrystals in SiO_2. We have shared countless cups of late-night coffee, numerous scientific ideas (that were quite far-fetched in a few occasions), and great friendship. I want to thank Dr. K.V. Shcheglov and Dr. Chih Yang for sharing scientific thoughts on the ion beam synthesis and characterization of Si and Ge nanocrystals in SiO_2. I want to thank Dr. Gang He, who has taught me the ABC's of molecular beam epitaxy. I also want to thank other colleagues for their stimulating scientific opinions and much more: Dr. Hyun S. Joo, Dr. Sue Melnik, Dr. Renato P. Camata, Dr. John Hartman, Joseph Christopherson, Claudine Chen, Maribeth Swaitek, Elizabeth Boer, Dr. David Boyd, Regina Ragan, Torsten Bistritchan, Rosaria Puglisi, Rhett Brewer, and Nicholas Choly. I am greatly indebted to the following Caltech faculty members for contributing to my intellectual maturity at various stages: Prof. Harry A. Atwater, Prof. Brent T. Fultz, Prof. Thomas C. McGill, Prof. William L. Johnson, and Prof. David G. Goodwin for serving on my candidacy examination committee; Prof. Harry A. Atwater, Prof. Brent Fultz, Prof. Thomas C. McGill, Prof. William L. Johnson, Prof. Noel R. Corngold, Dr. Channing C. Ahn, Dr. Earl Freise, Prof. Marc-A. Nicolet, and Prof. Theodore Y. Wu for the

Abstract

The concept of silicon-based optoelectronics has attracted much scientific and technological interests over the past decade. The vision of Si-based optoelectronics is based on integration of Si-based photonic components, in which light can be generated, waveguided, modulated, amplified, and detected, with the advanced Si electronics onto the same Si substrate to make monolithically integrated Si-based optoelectronic circuits. The main driving force for development of Si-based optical components comes from unsurpassed qualities of Si as the substrate material on which the electronic components rest: superior native oxide as well as excellent thermal, mechanical, and economic properties. Despite superior substrate properties, the field still remains a frontier at large. The main technological limitation comes from the lack of materials for efficient Si-based light sources such as Si-based lasers and light-emitting devices.

Two novel Si-based nanostructures are studied for potential application as visible and infrared light sources: ion-beam synthesized Ge and Si nanocrystals in SiO_2 and coherently strained quantum well and quantum dots based on the Si-Sn system grown by molecular beam epitaxy.

The study of Ge and Si nanocrystals is motivated by the prediction that quantum confinement of carriers leads to efficient luminescence despite the indirect nature of the energy gaps. Ge and Si nanocrystals in thermal SiO_2 films are synthesized via precipitation from a supersaturated solid solution of Ge and Si in SiO_2 made by Ge^+ and Si^+ ion implantation. The precipitation of nanocrystals occurs upon thermal annealing in vacuum. It is demonstrated that the SiO_2 films containing Ge nanocrystals only exhibit defect-related luminescence and that the Ge nanocrystals do not exhibit luminescence from quantum-confined excitons due to the poor nanocrystal/SiO_2 interface. The visible luminescence from SiO_2 films containing Si nanocrystals, on the other hand, is unambiguously demonstrated to be originating from quantum-confined excitons in Si nanocrystals, based on systematic photoluminescence and photoluminescence decay rate measurements. In agreement with the predictions of the theory of quantum confinement, the peak energy of visible photoluminescence from Si nanocrystals can be continuously tuned throughout most of the visible spectrum by controlling the size distribution of the nanocrystals.

The growth of nanostructures based on the Si-Sn system by molecular beam epitaxy is motivated by the fact that diamond cubic α-Sn is a zero band gap semiconductor and that band structure calculations predict a direct and tunable energy gap for Sn-rich Sn_xSi_{1-x} alloy system. However, the large lattice mismatch (19%) and severe segregation of Sn to the surface during growth prevent growth of Sn-rich Sn_xSi_{1-x} films by ordinary thermal molecular beam epitaxy. The growth of pseudomorphic Sn/Si and Sn_xSi_{1-x}/Si heterostructures is demonstrated via a modified molecular beam epitaxy technique employing temperature and growth rate

modulations. The growth of pseudomorphic single quantum well structures as well as superlatttice structures is demonstrated. In addition, a novel route for synthesis of coherent Sn-rich Sn_xSi_{1-x} quantum dots in Si matrix is presented. Due to chemical instability of the Si-Sn mixture, Stranski-Krastonow growth of coherently strained Sn-rich Sn_xSi_{1-x} quantum dot structures using conventional molecular beam epitaxy techniques is very difficult. The novel technique involves phase separation of Sn-rich Sn_xSi_{1-x} quantum dots at elevated temperatures from an epitaxially stabilized homogeneous Sn_xSi_{1-x}/Si metastable solid solution grown by low temperature molecular beam epitaxy. The dots have been verified to be completely coherent with the surrounding Si matrix by high-resolution transmission electron microscopy.

List of Publications

Parts of this thesis have been, or are to be, published under the following titles:

1. "Coherently Strained Sn_xSi_{1-x} Quantum Dot Formation in Si via Thermodynamically Driven Phase Separation," Kyu Sung Min, Nicholas J. Choly, and Harry A. Atwater, to be submitted for publication.

2. "Growth and Characterization of Epitaxially Stabilized Pseudomorphic α-Sn/Si Heterostructures," Kyu Sung Min and Harry A. Atwater, *Mat. Res. Symp. Proc. Vol.* **533**, 355 (1998).

3. "Ultrathin Pseudomorphic Sn/Si and Sn_xSi_{1-x}/Si Heterostructures," Kyu Sung Min and H.A. Atwater, *Appl. Phys. Lett.* **72**, 1884 (1998).

4. "Size Dependent Electron-Hole Exchange Interaction in Si Nanocrystals," M.L. Brongersma, P.G. Kik, A. Polman, K.S. Min, and H.A. Atwater, submitted to *Appl. Phys. Lett*, 1/99.

5. "Depth Distribution of Luminescent Si Nanocrystals in Si$^+$-implanted SiO$_2$ Films on Si," M.L. Brongersma, A. Polman, K.S. Min, and H.A. Atwater, to be published in *J. Appl. Phys.*, 9/99.

6. "Tuning the Emission Wavelength of Si Nanocrystals in SiO$_2$ by Oxidation," M.L. Brongersma, K.S. Min, E. Boer, T. Tambo, Harry A. Atwater, and A. Polman," *Appl. Phys. Lett.* **72**, 2577 (1998).

7. "Photoluminescence Characterization of GaAs Nanocrystals in SiO$_2$ Films Formed by Sequential Ion Implantation," Y. Kanemitsu, H. Tanake, T. Kushida, K.S. Min, and H.A. Atwater, to be published in *J. Appl. Phys.*, 8/1/99.

8. "Photoluminescence from GaAs Nanocrystals Fabricated by Ga$^+$ and As$^+$ co-implantation into SiO$_2$ Matrices," S. Okamoto, Y. Kanemitsu, K.S. Min, and H.A. Atwater, *Appl. Phys. Lett.* **73**, 1829 (1998).

9. "Tailoring the Optical Properties of Si Nanocrystals in SiO$_2$: Materials Issues and Nanocrystal Laser Perspectives," M.L. Brongersma, K.S. Min, E. Boer, T. Tambo, A. Polman, and H.A. Atwater, *Mater. Res. Soc. Symp. Proc.* **486** (1998).

10. "Defect-related versus Excitonic Light Emission from Ion Beam Synthesized Si Nanocrystals in SiO$_2$," K.S. Min, K.V. Shcheglov, C.M. Yang, H.A. Atwater, M.L. Brongersma, and A. Polman, *Appl. Phys. Lett.* **69**, 2033 (1996).

11. "The Role of Quantum-Confined Excitons vs. Defects in the Visible Luminescence of SiO_2 Films Containing Ge Nanocrystals," K.S. Min, K.V. Shcheglov, C.M. Yang, H.A. Atwater, M.L. Brongersma, and A. Polman, *Appl. Phys. Lett.* **68**, 2511 (1996).

12. "On the Origin of Visible Luminescence from SiO_2 Films Containing Ge Nanocrystals," K.S. Min, K.V. Shcheglov, C.M. Yang, R.P. Camata, H.A. Atwater, M.L. Brongersma, and A. Polman, *Mater. Res. Soc. Symp. Proc* **405** (1996).

Contents

3. The Origin and Mechanism of Visible Luminescence from Ion Beam Synthesized Ge and Si Nanocrystals in SiO_2 45

4. Engineering the Depth Distribution of Ion Beam Synthesized Si Nanocrystals and Tuning the Emission Energy of Visible Luminescence   94

5. Growth and Characterization of Epitaxially Stabilized Sn_xSi_{1-x}/Si and α-Sn/Si Heterostructures   134

List of Figures

-

Chapter 1

Introduction: Si-based Nanostructures

1.1 Introduction

Important breakthroughs in technology have rendered mankind more independent from the forces of nature and have arguably lead to more convenient lives. At the least, key technological advances have always lead to giant leaps in the economic progress of all hitherto existing societies. And as the most important technological developments have often involved breakthroughs in the discovery and the development of novel materials, the eras in the history of mankind have been

properly categorized according to the materials that shaped the technology of the times. In this light, the 20th century might historically be categorized as the Age of Semiconductors. And few would argue that silicon is the most important semiconductor material for the microelectronics industry that revolutionized the technology and the world economy of the 20th century.

The full impact of solid-state electronics came with the invention of the bipolar transistor by Bardeen, Brattain, and Shockley in 1949 [1]. The initial material of choice had been Ge but was soon replaced by Si because of its natural superiority in key aspects. First, the 1.12 eV band gap of Si makes it an ideal material for device operation at room temperature, whereas the 0.67 eV band gap of Ge results in high junction leakage currents. Second, Si forms a thermal silicon oxide (SiO_2) that is inherently superior to the thermal oxide of Ge both in its properties and processibility. Silicon dioxide is the material that provides the processing flexibility enabling integration of 10^8 devices on a single chip. Third, the intrinsic resistivity of Si (230 kΩ-cm) is much higher than that of Ge (47 Ω-cm) and therefore allows for fabrication of rectifying devices with high breakdown voltages. Finally, pure Si can be more readily produced for much lower cost than Ge. The superiority of Si as the material for integrated circuits is also obvious when compared to other compound semiconductors. Not surprisingly, Si devices constitute over 95% of all semiconductor devices sold worldwide. Even the integrated circuit technologies of compound semiconductors like GaAs have derived their process technologies from processes developed for advanced Si microelectronics.

The success of Si-based devices has resulted in an unprecedented level of integration that has in turn enabled an unprecedented level of high-speed device performance. Device performance in integrated circuits has come to the point where the largest bottleneck is posed by the high density of interconnect wires. The increasing density of interconnects pose limitations in the performance, reliability, and cost [2]. An increasing density of interconnects will limit the clock frequency at which the devices can operate, which is expected to exceed 1 GHz on-chip by the year 2010, due to excessive power dissipation and cross talk [3]. In addition, an increase in the density with a simultaneous decrease in the feature size of the interconnects increase the chances of device failures resulting from interconnect failures. Perhaps the biggest problem of increasing density of interconnects is an economic one. Remarkably, there is an exponential relationship between the cost per interconnect and the length of interconnect [4]. The technological and economic pressure caused by an increasing density of interconnects has created a driving force to replace some hard-wired interconnects with wireless interconnects. This driving force has motivated the field of Si-based optolelectronics.

The vision of Si-based optoelectronics is based on integration of Si-based photonic components, in which light can be generated, waveguided, modulated, amplified, and detected, with the advanced Si electronics onto the same Si substrate to make monolithically integrated Si-based optoelectronic circuits [5,6]. A monolithically integrated circuit refers to integrated circuits having every component made from group IV materials. At the present, a hybrid approach of integrating optical components based on compound semiconductors with Si microelectronics is

providing limited integration but not monolithic integration. While there are obstacles to be overcome, monolithic integration indeed promises to be a cost-effective way of creating optoelectronic integrated circuits, most of all since the advanced Si processing technology can be fully utilized.

The past decade has seen a steady progress in various scientific and technological aspects of Si-based optoelectronics. Recent works have demonstrated that infrared light can be waveguided, detected, emitted, modulated, and switched in Si [5,6]. The progress towards the development of Si-based optoelectronic integrated circuits has been steady but not precipitous, mainly due to a lack of efficient light sources, i.e., Si-based lasers and light emitting devices. This "bottle-neck" is related to the indirect band gap of Si; i.e., the electron and hole states are located at band extrema located at different wave vector positions in k-space. Despite its success as a material of choice in the microelectronics industry, the indirect band gap of Si poses a serious obstacle for the realization of photonic devices. There has been significant advancement in the past decade, however, in overcoming the obstacles posed by the intrinsic optical properties of bulk crystalline Si. Efficient light emission has been demonstrated to be possible both theoretically and experimentally, by clever engineering of the electronic and physical structure of Si and Si-based alloys. The purpose of this thesis is to explore some fundamental materials issues involved in the synthesis and properties of Si-based nanostructures for potential applications as Si-based light emitting materials.

1.2 Light Emission from Si-based Materials

Semiconductor materials can be categorized according to the way in which the band extrema are positioned in k-space. In the case of diamond cubic and zinc blende structures, the band extrema are almost always positioned along the zone center (k=0) or lie along the high symmetry directions like <111> and <100>. When the conduction band minimum and the valence band maximum occur at the same position in k-space, the material is said to possess a direct band gap. Conversely, the material is said to possess an indirect band gap when the band extrema occur at different positions in k-space. The positioning of the band extrema has a profound effect on the optical properties of semiconductors. The difference between the two types of semiconductors is illustrated best using representations of allowed energy values as a function of the wavevector k called E-k diagrams. The E-k diagrams characterizing the energy band structures of Ge, Si, and GaAs are shown in Fig. 1.1(a), Fig 1.1(b), and Fig 1.1(c), respectively [7]. An analysis of the three E-k diagrams reveals that there are some features that are common to all three diagrams. For example, in all cases the valence band is composed of three subbands and the valence band maxima occur at the zone center (k=0). The conduction band in each case is also composed of a number of subbands that exhibit localized and absolute minima at the zone center or along one of the high symmetry directions <111> or <100>. However, the positioning of the absolute minimum of the conduction band, which is where all the

excited electrons congregate, varies for the three materials. This is the single factor that has the most profound effect on the optical properties of semiconductors. For Ge (Fig. 1.1(a)) the conduction band minimum occurs at the zone boundary along the <111> direction and for Si (Fig. 1.1(b)) it occurs at $k \approx 0.8(2\pi/a)$ from the zone center along the <100> direction. For Si and Ge, therefore, the conduction band minimum and the valence band maximum lie at different values in k-space and are therefore said to be indirect gap semiconductors. On the other hand, for GaAs (Fig 1.1(c)) the band extrema coincide at the zone center and is said to be a direct gap semiconductor.

The relative positioning of the band extrema is crucial in determining the optical properties of semiconductors. Because the conduction band minimum and the valence band maximum overlap at the zone center, electronic transitions between the band extrema in a direct gap semiconductor take place with little or no change in crystal momentum. As a result, the intrinsic recombination process in a direct gap semiconductor is a fast, two-particle process. On the other hand, the electronic transitions between the band extrema situated at different values in k-space in an indirect gap semiconductor take place only with momentum transfer involving creation or annihilation of phonons. The intrinsic recombination process in an indirect gap semiconductor is therefore a slow, three-particle phenomenon involving phonons, whose probability of occurrence is much lower than a two-particle process. The radiative efficiency η depends on the competition between radiative processes with characteristic transition time τ_r and nonradiative processes with characteristic transition time τ_{nr} and is given by

$$\eta = \frac{\tau_{nr}}{\tau_r + \tau_{nr}} \quad .$$
(1.1)

The radiative recombination rate $1/\tau_r$ of intrinsic direct transition in GaAs is about 2×10^7 sec.$^{-1}$ compared to that of indirect transition in Si which is about 10^2 sec.$^{-1}$ The poor light emission efficiency in Si and Ge results directly from the low recombination rate of phonon-involving three-particle events because there are faster, competing nonradiative processes. From Eq. (1.1) it is evident that the radiative efficiency is high when the radiative processes are very fast or when the nonradiative processes are very slow.

In light of Eq. (1.1) several approaches are conceivable for increasing the radiative efficiency in an indirect gap semiconductor like Ge and Si [8,9]. First approach is band structure engineering via alloying to make a direct gap semiconductor. Direct energy gaps can be realized in group IV alloy systems if the difficulties associated with growth, which are severe in many cases, can be overcome. Of the crystalline binary group IV alloys, band structure engineering of the alloy systems of GeSn, SiSn and SnC is expected, in theory, to produce direct energy gaps [10-13]. Experimental evidence of a direct gap group IV material has recently been demonstrated from Sn_xGe_{1-x} alloys grown by molecular beam epitaxy [14]. Second approach is bandgap engineering of a Si-based material by quantum confinement of carriers to achieve radiative transition rate that is much faster than that of the bulk Si [15-20]. Luminescence through quantum confinement effect can be exploited when the crystal dimensions decrease down to sizes comparable to the exciton Bohr radii. The small crystal dimensions "force" the electron and hole wavefunctions to overlap

in both real and reciprocal space, enabling efficient visible light emission. The first example of efficient (>1%) room temperature visible light emission arising from quantum-confinement effect was reported by Canham [21] in electrochemically etched Si (porous Si). Many reports of similar luminescence from Si nanostructures followed [22,23]. The third general approach of achieving light emission from Si is through impurity-mediated transitions. A prime example of impurity-mediated luminescence is that which involves rare-earth impurities such as Er [24]. The luminescence of Er in Er-doped Si involves the generation of an electron-hole pair across the intrinsic Si band gap followed by a nonradiative energy transfer of the recombination energy to the Er inner 4f shell. The result is a sharp luminescence at the important fiber optic communication wavelength of $\lambda=1.54$ μm that arises from the $I_{13/2} \rightarrow I_{15/2}$ transition from the excited inner $4f^{11}$ shell of the Er^{3+} configuration.

In short, luminescence from radiative transitions is a result of an appreciable overlap in the electron and the hole wavefunctions. The efficiency of luminescence depends on the strength of this overlap, which could be increased in real space, reciprocal space, or both. The theme of this thesis involves the application of the first two concepts, i.e., band structure engineering by alloying and by quantum carrier confinement, to synthesize light emitting Si-based nanostructures. The two concepts are described in more detail in the following sections.
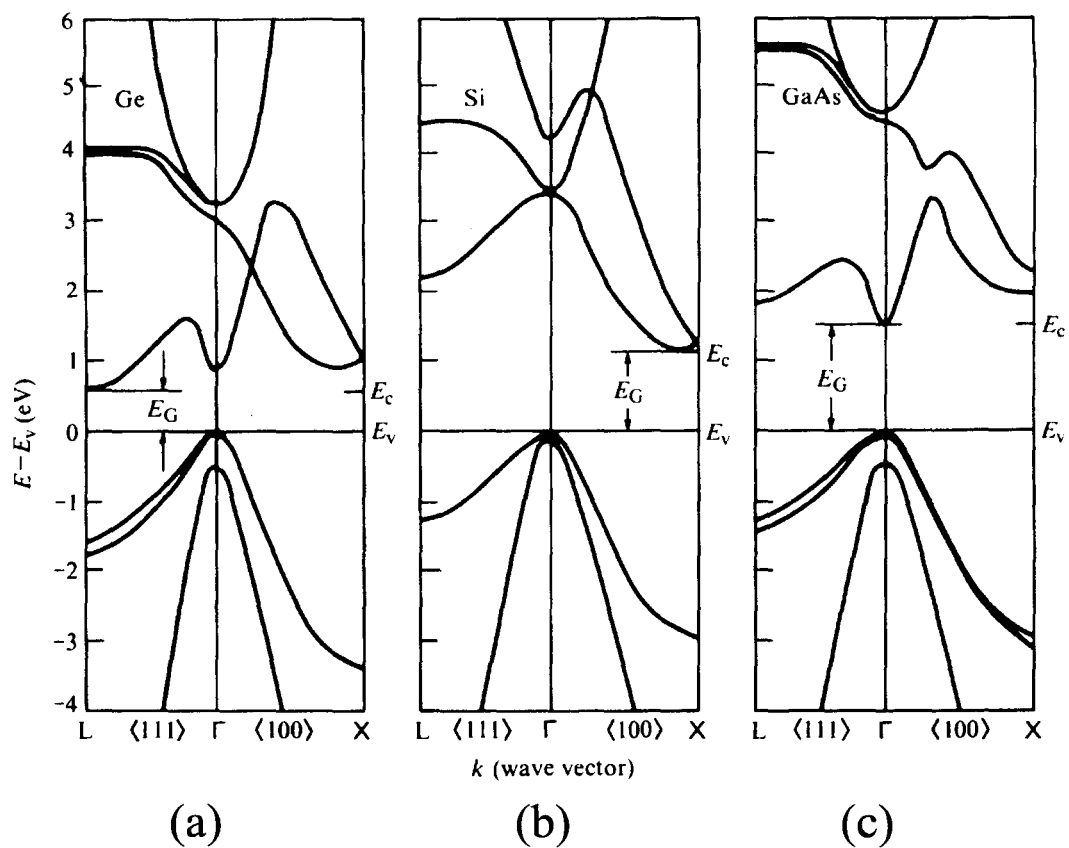
Figure 1.1. *E-k* diagrams characterizing the band structures of Ge, Si, and GaAs
[from Ref. 7].

1.3 Engineering Luminescent Transitions in Si and Ge via Quantum Confinement

Quantum confinement of carriers within a nanometer-scale volume results in an appreciable overlap of the electron and the hole wavefunctions in both real space and reciprocal space, which in turn results in an enhancement of the efficiency of luminescence. Quantum confinement effect is expected when the system dimension reduces down to a size comparable to the exciton Bohr radius for the given material. For Si, Ge, and GaAs, the exciton Bohr radii are 4.3 nm, 11.5 nm, and 12.4 nm, respectively [25].

The carriers can be confined in two, one, and zero dimensions corresponding to structures referred to as quantum wells, quantum wires, and quantum dots. Regardless of the dimensionality, one important effect of quantum confinement is that the energy of the fundamental electronic transition increases in the direction of confinement, in analogy with the quantum mechanical prediction of increasing kinetic energy levels for a particle in a box. In addition, the Coulombic attraction increases due to spatial confinement. An analytical expression for the case of zero-dimensional confinement in a spherically symmetric direct gap system with a radius R for the lowest excited $1s$ state has been given by Brus [26] as

$$E = E_g + \frac{\hbar^2 \pi^2}{2R^2}\left[\frac{1}{m_e} + \frac{1}{m_h}\right] - \frac{1.8e^2}{\varepsilon R} + \text{smaller terms} \qquad (1.2)$$

where m_e and m_h are the effective masses of electrons and holes, respectively, and E_g is the bulk band gap. The second term in Eq. (1.2) represents the quantum localization energy and the third term represents the Coulomb attraction screened by the dielectric constant ε of the system. It is clear that the quantum localization energy term with a R^{-2} dependence dominates over the Coulomb attraction term with a R^{-1} dependence as R decreases and the lowest excited state shifts to higher energy with respect to E_g.

Quantum confinement of carriers is expected to have very similar effects on the energy gap of indirect gap semiconductors like Si and Ge. The expected energy gap of Si and Ge as a function of crystal size is given in Fig. 1.2(a) and Fig. 1.2(b), respectively, from different theoretical approaches [16-19]. The general trend of size-dependent energy gap is perhaps one of the most versatile features of quantum-confined systems from an engineering point of view, for it allows for Si-based light sources with tunable emission energy. The most important effect of quantum confinement from the point of view of developing materials for Si-based light emitters is that it potentially allows for efficient light emission even from indirect gap semiconductors like Si that exhibit negligible luminescence efficiency in the bulk state. The improvement in emission efficiency is a result of the disruption of crystal symmetry and the resulting relaxation of momentum selection rules. A calculation based on the density functional theory in Fig. 1.3 shows that the oscillator strength increases by nearly six orders of magnitude as the number of Si atoms is decreased by three orders of magnitude from about 1000 to 10 [20]. A more subtle effect of quantum confinement is that the excitonic binding energy is expected to exceed the

room temperature value of kT (0.026 eV). For Si and Ge, this leads to luminescence of excitonic origin even at room temperature [19]. For example, Si nanocrystals with diameter of 5-6.5 nm correspond to exciton binding energy of about 75-95 meV, which is well above kT at room temperature. The large exciton binding energy allows for a Si-based light source that is operational at room temperatures. In sum, the physics of quantum confinement allows for the possibility of efficient room temperature light emission with tunable energy from Ge and Si despite their indirect gap.
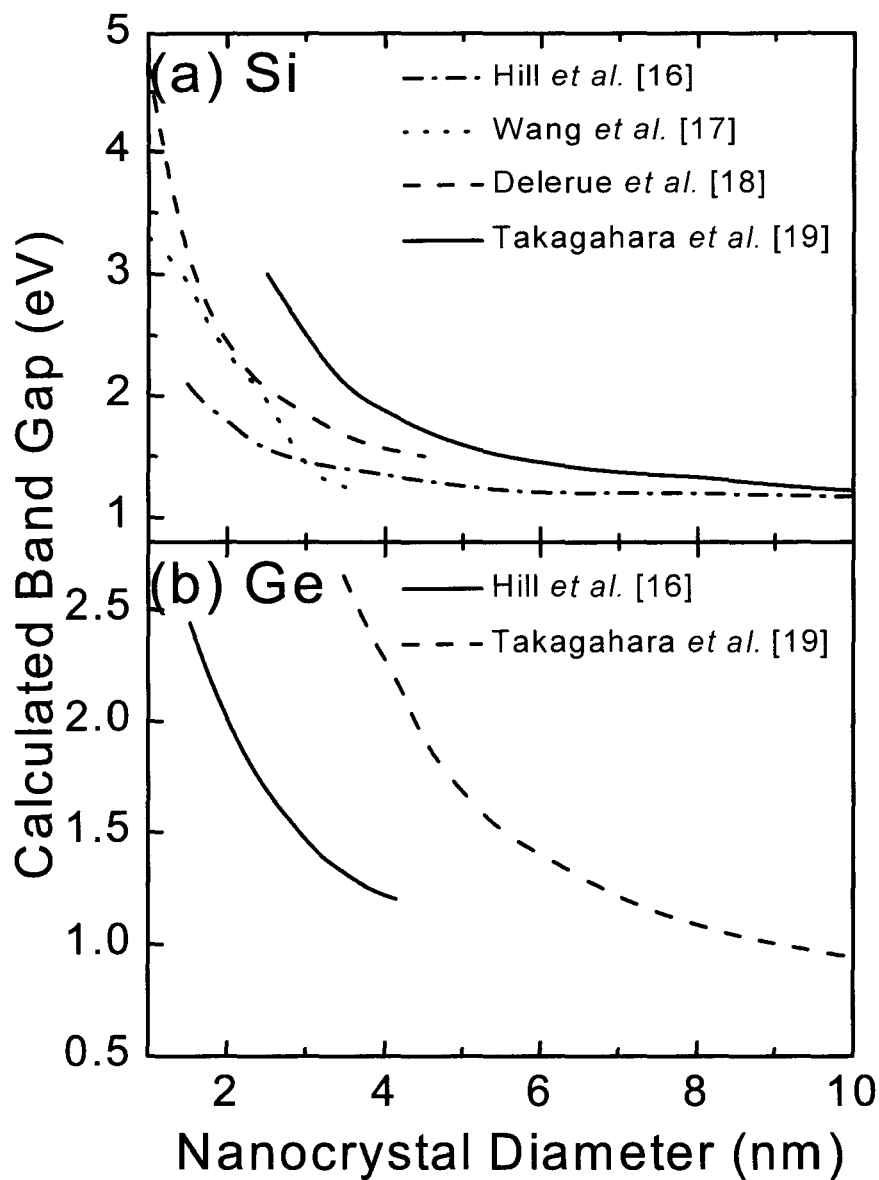
Figure 1.2. Theoretical predictions of the band gap of (a) Si nanocrystals and (b) Ge

nanocrystals as a function of nanocrystal diameter [16-19].
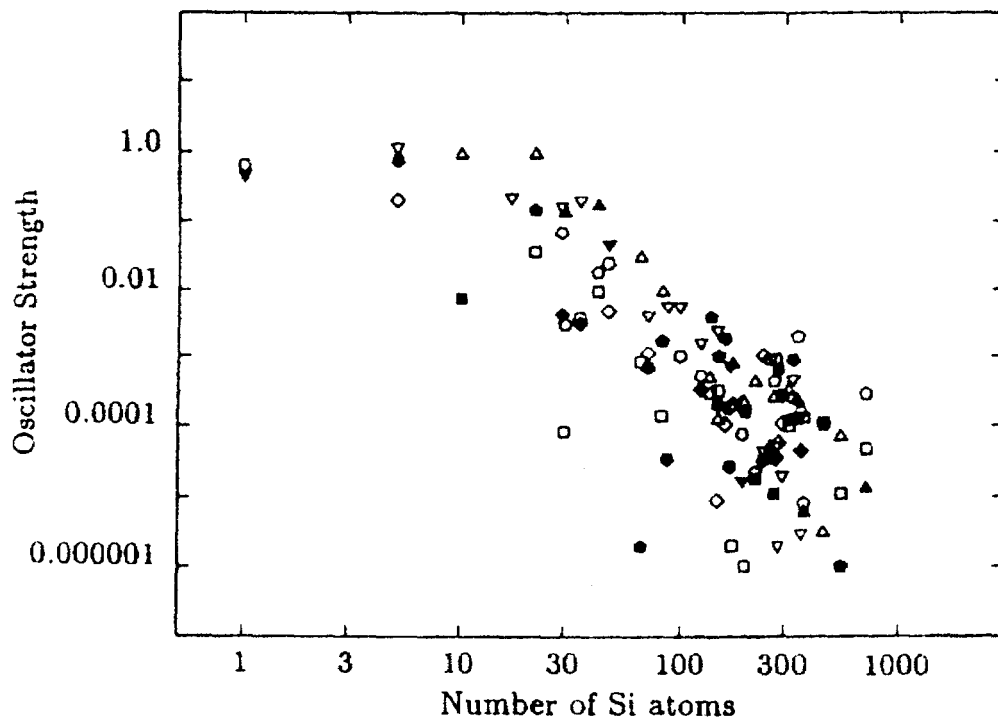
Figure 1.3. Oscillator strength of Si as a function of crystal size, calculated by a density functional technique [from Ref. 20].

1.4 Band Structure Engineering Through Alloying

Advanced growth techniques such as molecular beam epitaxy have allowed

for heteroepitaxial growth of alloys of Si and its diamond cubic group IV neighbors –

Ge, C, and α-Sn [27]. The most amount of research effort has been invested in

heteroepitaxial growth of SiGe on Si for heterojuction technology aimed at producing

enhanced versions of Si microelectronic devices by band structure engineering and

through superior material properties of SiGe [28]. Although remarkable results have

been achieved in engineering of the electronic properties of Si by alloying with Ge,

efficient light emission cannot be achieved by direct alloying because neither the end

components nor the resulting alloy is expected to possess a direct energy gap. The

same is true for the case of Si-C alloys and Ge-C alloys in that the alloy combinations

are not expected to increase the direct interband transition probability. Alloys of Si-

Sn and Ge-Sn, however, are expected to possess direct energy gaps for limited

composition ranges [10-13]. This is because α-Sn, which is the diamond cubic phase

of Sn, possesses degenerate conduction and valence bands at the Γ point, making it a

direct gap semiconductor with zero gap energy [29]. Furthermore, the energy gaps of

the Si-Sn and the Ge-Sn alloy systems are predicted to be tunable by tuning the

composition within a window. Figure 1.4 illustrates one such construction of energy

band diagram of $Sn_{1-x}Ge_x$, $Ge_{1-y}Si_y$, and $Si_{1-z}Sn_z$ as a function of composition x, y,

and z, based on theoretical calculations [11]. The critical point energies in Fig. 1.4

are results of the Slater-Koster parameter model [30] and the line segments are simply

predictions of linear dependence of energy on the composition known as the virtual

crystal approximation. According to Fig. 1.4, where bandgap bowing effects are

neglected, the energy gaps of $Si_{1-z}Sn_z$ and $Sn_{1-x}Ge_x$ are expected to be direct for Sn

composition exceeding about 0.82 and 0.45, respectively. Calculations by Jenkins *et

al.* [12] and Oguz *et al.* [13] predict the indirect-to-direct transition for $Sn_{1-x}Ge_x$ to

occur at much lower concentrations of 0.2 and 0.23, respectively. And recent

experimental evidence suggests that it might even occur at concentrations as low as

11%-15% [14]. This has positive implications from the growth point of view,

because both the Ge-Sn and Si-Sn systems suffer from huge lattice mismatch and

extremely limited solid solubility and phase instability [31].
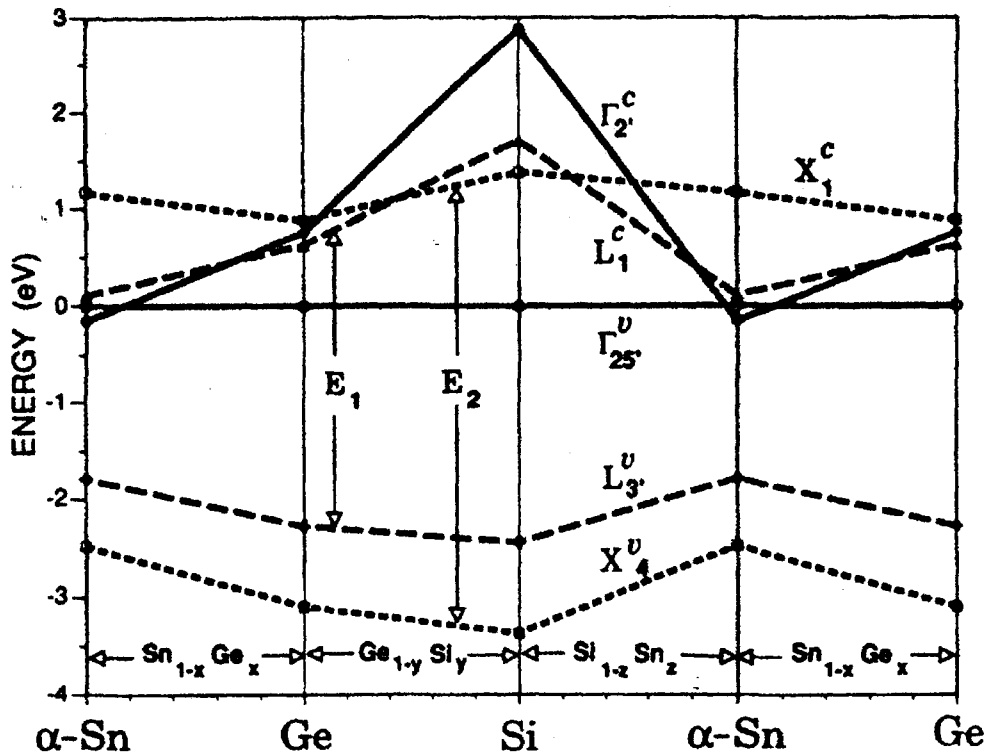
Figure 1.4. A diagram of projected energy vs. composition for the binary alloy systems Sn-Ge, Si-Ge, and Si-Sn based on the assumption of virtual crystal approximation (linear dependence of energy on composition) and critical point eigenvalues of three elemental semiconductors Si, Ge, and α-Sn obtained from Slater-Koster parameter model (from Ref. 30).

1.5 Summary and Outline of the Thesis

The invariable trend in microelectronics technology has been towards ever-increasing level of functional integration and a simultaneous reduction of cost. With device and interconnect densities quickly reaching inherent saturation points defined by the lithographic resolution, there is technological and economic pressure for development of new Si-based light emitting materials that would enable integration of optical components onto a Si-based chip.

Of the various avenues available for engineering luminescent transitions in Si-based materials, this thesis addresses two approaches. The goal of this thesis is to understand the materials issues associated with the lithography-free synthesis and characterization of Si-based nanostructures for potential application as Si-based optoelectronic materials.

Chapters 2, 3, and 4 address the first approach of enhancing the strength of luminescence through zero-dimensional carrier confinement in Si and Ge nanocrystals. Chapter 2 reports on the synthesis of light emitting nanocrystals in thermal SiO_2 films carried out via precipitation from supersaturated solid solutions of the relevant species in SiO_2 made by ion implantation. The visible luminescence from SiO_2 films containing Si nanocrystals is unambiguously demonstrated to be originating from quantum-confined excitons in Si nanocrystals in Chapter 3, based on observations of systematic shifts in photoluminescence peak energy and the corresponding photoluminescence decay time measurements. It is demonstrated in

Chapter 4 that the peak energy of visible photoluminescence can be continuously tuned throughout most of the visible spectrum by engineering the depth and size distribution of the Si nanocrystals.

Chapters 5 and 6 address an approach that combines the concept of band structure engineering via alloying and the concept of quantum confinement to synthesize quantum-confined direct-gap nanostructures based on the Si-Sn binary system. The study is on the growth of epitaxially stabilized quantum well and quantum dot structures based on Sn/Si and $Si_{1-x}Sn_x$/Si heterostructures grown by molecular beam epitaxy. Growth of such materials is motivated by the fact that diamond cubic α-Sn is a semimetal with a zero energy direct gap and band structure calculations have suggested that when alloyed with Si, Sn-rich $Si_{1-x}Sn_x$ alloy system is predicted to have direct and tunable energy gap for Sn composition exceeding some critical concentration. Chapter 5 reports successful growth and characterization of ultrathin 2-D quantum well heterostructures based on coherently strained Sn/Si and $Si_{1-x}Sn_x$/Si structures. Difficulties associated with the growth due to the extremely low solubility of Sn in Si is achieved by an unconventional molecular beam epitaxy technique employing large modulations in substrate temperature and growth rate. Chapter 6 reports a novel approach in making lithography-free, nanometer-scale Sn-rich Sn_xSi_{1-x} quantum dots in Si. Coherently strained Sn quantum dots are formed within a Si (001) crystal by phase separation of an epitaxially stabilized ultrathin Sn_xSi_{1-x} metastable solid solution embedded in Si (001). Phase separation of the ultrathin alloy film is demonstrated to initially proceed by spinodal decomposition, and subsequent evolution proceeds via growth and then coarsening of regularly

shaped nanometer-sized Sn-rich Sn_xSi_{1-x} quantum dots with facets oriented along the

elastically soft <100> directions.

Bibliography

[1]   W. Shockley, Bell Syst. Tech. J. **28**, 435 (1949).

[2]   E.A. Fitzgerald and L.C. Kimerling, Mater. Res. Soc. Bull. **23**, 39 (1998).

[3]   Proc. Semiconductor Industry Assoc. Workshop, Semiconductor Industry Assoc. (1993).

[4]   C.A. Warwick, R.-H. Yan, Y.O. Kim, and A. Ourmazd, AT&T Tech. J. **72**, 50 (1993).

[5]   R.A. Soref, Proc. IEEE **81**, 1687 (1993).

[6]   R. Soref, Mater. Res. Soc. Bull. **23**, 20 (1988).

[7]   S.M. Sze, *Physics of Semiconductor Devices*, 2nd edition, John Wiley & Sons, Inc., New York, 1981.

[8]   Mater. Res. Soc. Bull. **23**, 39 (1998).

[9]   S. S. Iyer and Y.-H Xie, Science **260**, 40 (1993).

[10] K.A. Johnson and N.W. Ashcroft, Phys. Rev. **B 20**, 14480 (1996).

[11] R.A. Soref and C.H. Perry, J. Appl. Phys. **69**, 539 (1991).

[12] D.W. Jenkins and J.D. Dow, Phys. Rev. **B 36**, 7994 (1987).

[13] S. Oguz, W. Paul, T.F. Deutsch, B.Y. Tsaur, and D.V. Murphy, Appl. Phys. Lett. **43**, 848 (1983).

[14] G. He and H.A. Atwater, Phys. Rev. Lett. **79**, 1937 (1997).

[15] M. Hybertson, Phys. Rev. Lett. **72**, 1514 (1994).

[16] N.A. Hill and K.B. Whaley, Phys Rev. Lett. **75**, 1130 (1995); N.A. Hill and K.B. Whaley, private communication, for Ge nanocrystals.

[17] L.W. Wang and A. Zunger, J. Phys. Chem. **98**, 2158 (1994).

[18] C. Delerue, G. Allan, and M. Lannoo, Phys. Rev. **B 48**, 11024 (1993).

[19] T. Takagahara and K. Takeda, Phys. Rev. **B 46**, 15578 (1992).

[20] B. Delly and E.F. Steigmeier, Phys. Rev. B 47, 1397 (1993).

[21] L.T. Canham, Appl. Phys. Lett. **57**, 1046 (1990).

[22] Y. Kanemitsu, Physics Reports **263**, 1 (1995).

[23] L. Tsybeskov, Mater. Res. Soc. Bull. **23**, 33 (1998).

[24] See, for example, Mater. Res. Soc. Symp. Proc. **422**, Pittsburgh, 1996, and references contained therein.

[25] A.D. Yoffe, Adv. in Phys. **42**, 173 (1993).

[26] L. Brus, IEEE J. Quant. Elect. **QE-22**, 1909 (1986).

[27] See, for example, Mater. Res. Soc. Symp. Proc. **533**, Pittsburgh, 1998, and references contained therein.

[28] T.E. Whall, E.H.C. Parker, J. Mat. Sci.: Mat. in Elect. **6**, 249 (1995).

[29] S. Groves and W. Paul, Phys. Rev. Lett. **11**, 194 (1963).

[30] Y. Li and P.J. Lin-Chung, Phys. Rev. **B 27**, 3465 (1983).

[31] T.B. Massalski *et al., Binary Alloy Phase Diagrams*, 2nd edition, American Society of Metals, Materials Park, 1990.

Chapter 2

Ion Beam Synthesis and Structural Characterization of Ge, Si, and GaAs Nanocrystals in SiO_2

2.1 Introduction

Zero-dimensional semiconductors have steadily attracted much scientific and technological interest over the past years due to the effects of quantum confinement and their potential applications [1]. Until the discovery of visible room temperature photoluminescence (PL) in porous silicon [2], however, much of the interest centered on compound semiconductors due to their direct energy gaps. The discovery of room

temperature visible luminescence from porous Si, synthesized by anodic etching of Si, inspired intense interest in group IV nanocrystals because of its potential application in development of integrated optoelectronic devices directly on Si. Since then, many other techniques have been employed to synthesize group IV nanocrystals to investigate their optical properties and to develop useful devices [3-13].

Ion beam synthesis is among the more controlled methods for synthesizing various nanocrystals in different matrices. The synthesis involves two steps, namely ion implantation followed by thermal annealing. Ion implantation produces a metastable supersaturated solid solution of the implanted species and the target material, and subsequent annealing drives precipitation of the implanted species.

Group IV semiconductor nanocrystals embedded in an SiO_2 matrix offer an attractive model material system for investigating the quantum confinement effects for several reasons. First, SiO_2 has many desirable properties, including chemical and mechanical stability. Most important, SiO_2 forms one of the best interfaces with Si, with a very low density of dangling bonds [14]. In fact, it is the passivating nature of SiO_2 that has gained Si its success as a material of choice in the Si microelectronics industry. Because of its technological importance, Si/SiO_2 interface has been the subject of intense investigation, and the amount of information available on the interface characteristics far exceeds that of any other semiconductor surface and interface. Not surprisingly, the passivating nature of SiO_2 turns out to be a crucial factor in determining the luminescence efficiency in Si and Ge nanocrystals, as will be discussed in Chapter 3.

2.2   Ion Beam Synthesis of Ge, Si, and GaAs Nanocrystals in SiO_2

In the current work, ion beam synthesis has successfully been employed to synthesize Si, Ge, and GaAs nanocrystals in SiO_2. For all samples, 100 nm-thick SiO_2 films grown by wet thermal oxidation on a lightly p-doped (100) Si wafers were used as matrices into which relevant species were implanted at room temperature. The implanted samples were subsequently annealed in high vacuum, holding either time or temperature as a constant and varying the other as the processing variable. The following experimental conditions were used for the synthesis of Ge, Si, and GaAs nanocrystals in SiO_2.

For Ge nanocrystals, 70 keV $^{74}Ge^+$ was implanted at doses of $1\times10^{16}/cm^2$, $2\times10^{16}/cm^2$, and $5\times10^{16}/cm^2$. The energy was chosen such that the implanted Ge concentration profile is completely within the oxide film, with the peak concentration lying 30-40 nm from the surface. For the three implantation doses, the peak concentrations are 3, 6, and 13 at. % Ge, respectively, as determined by Rutherford backscattering spectrometry. After implantation, the samples were annealed in high vacuum at 600°C, 800°C, and 1000°C for 40 min.

For Si nanocrystals the SiO_2 films were either implanted with 50 keV $^{28}Si^+$ at doses of $1\times10^{16}/cm^2$, $2\times10^{16}/cm^2$, and $5\times10^{16}/cm^2$, corresponding to peak excess Si concentrations of 2, 4, and 10 at. % Si, respectively, or with 35 keV $^{28}Si^+$ at doses of $2\times10^{16}/cm^2$, $4\times10^{16}/cm^2$, and $6\times10^{16}/cm^2$, corresponding to peak excess Si

concentrations of 5, 10, and 15 at. %, respectively, as calculated from an estimated

projected range and straggle using the TRIM code [15]. The samples were either

annealed at temperatures ranging between 800°C and 1200°C for a fixed time of 10

min. or for times ranging between 10 min. and 320 min. at a fixed temperature of

1000°C.

GaAs nanocrystals were synthesized by sequential implantation of 75 keV

Ga^+ at a dose of $3\times10^{16}/cm^2$ followed by 75 keV As^+ at a dose of $2\times10^{16}/cm^2$ into

SiO_2 films. The implanted SiO_2 films were then annealed in vacuum between 800°C

and 1100°C for 10 min. to 300 minutes.

2.3 Structural Characterization of Nanocrystals in SiO$_2$

Transmission electron microscopy (TEM) was performed on the SiO_2 films

containing Ge, Si, and GaAs nanocrystals using Philips EM 430 using 300 keV

electrons. For Si nanocrystals, X-ray photoelectron spectroscopy (XPS) was

performed using the model M-Probe manufactured by Surface Science Instruments,

Inc., equipped with a hemispherical electron analyzer. A monochromated Al Kα

radiation at 1487 eV was used for all X-ray photoelectron spectroscopy

measurements.

2.3.1 Ge Nanocrystals in SiO$_2$

Transmission electron microscopy characterization was performed on the samples synthesized by the above method to verify the presence of Ge nanocrystals and to determine the average nanocrystal sizes for various processing conditions.

Figures 2.1(a)-(d) show planar-view bright field TEM images of 100 nm SiO$_2$ films implanted with 2×10^{16}/cm^2 Ge$^+$ and subsequently annealed at 600°C, 800°C, 1000°C, and 1200°C, respectively. One clearly sees that the nearly-spherical Ge nanocrystals are clearly present, and that increasing the annealing temperature leads to an increase in the average nanocrystal size. The electron diffraction patterns shown as insets indicate diamond cubic Ge. The widths of the diffraction rings decrease with increasing annealing temperature, indicating that higher temperature yields larger average nanocrystal size.

Figures 2.2(a) and 2.2(b) show planar-view high resolution TEM images of the 100 nm SiO$_2$ films implanted with 2×10^{16}/cm^2 Ge$^+$ and subsequently annealed at 600°C and 1200°C, respectively, for 40 min. All particles are clearly single crystalline, and some exhibit twinning.

Figures 2.3(a) and 2.3(b) show planar-view bright field TEM images of 100 nm SiO$_2$ films implanted with 2×10^{16}/cm^2 Ge$^+$ and 5×10^{16}/cm^2 Ge$^+$, respectively, and subsequently annealed at 1000°C for 40 min. It is clearly seen that higher dose results in higher density of particles.

Figures 2.4(a)-(d) show planar-view bright field TEM images of the 100 nm SiO$_2$ films implanted with 2×10^{16}/cm^2 Ge$^+$ and subsequently annealed isothermally at 1000°C for 2.5 min., 10 min., 40 min., and 80 min., respectively. Somewhat surprisingly, no significant time dependence of particle size evolution has been observed within the experimental uncertainty.

Several general trends are noteworthy about the evolution of Ge nanocrystal size distribution as a function of different processing parameters. First, there is a strong dependence of size distribution on the annealing temperature, as determined from Gaussian fits to the size distributions obtained from Fig. 2.1. For the 6 at. % (2×10^{16}/cm^2) Ge$^+$-implanted sample, the average sizes are 1.9 nm, 3.2 nm, and 7.2 nm, with full-widths at half-maximum of 1.5 nm, 3.4 nm, and 4.0 nm, for the samples annealed at 600°C, 800°C, and 1000°C, respectively. Second, higher implantation doses yield samples with higher nanocrystal density, but with similar average sizes and size distributions after annealing. An analysis of the size distribution obtained from Fig. 2.2 indicates that the average size is the same within experimental uncertainly, for the two different implantation doses. Apparently, the initial Ge concentration strongly affects particle density but not particle size. Finally, isothermal annealing experiments shown in Fig. 2.4 indicates that the size distribution does not change significantly with annealing time. This is contrary to what one might expect for a system undergoing coarsening. In general, a system undergoing coarsening exhibits a power law time dependence. For example, the classical mean-field treatments [16, 17] predict time dependencies of the average particle size given

by $\langle r \rangle \propto t^{1/3}$ and $\langle r \rangle \propto t^{1/2}$, where $\langle r \rangle$ is the average particle radius, for diffusion-controlled coarsening and interface-controlled coarsening, respectively. The apparent non-dependence of particle size on annealing time and a strong dependence on annealing temperature suggests that the diffusion occurs rapidly for those temperature regimes and that coarsening is limited by a thermally activated process.
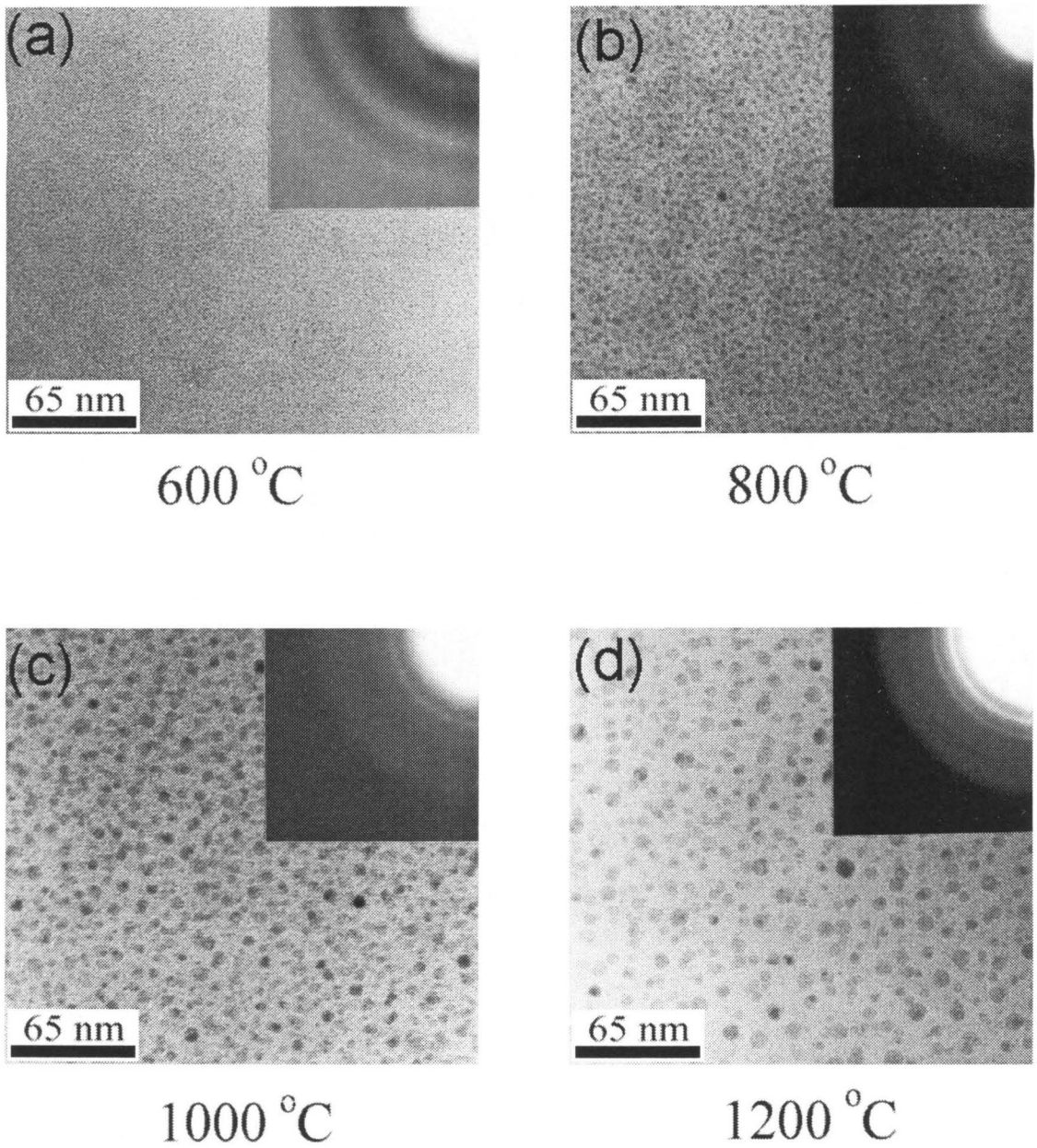
Figure 2.1. Planar-view bright field transmission electron micrographs of 100 nm SiO$_2$ films implanted with 2×10^{16}/cm^2 Ge$^+$ and subsequently annealed at (a) 600°C, (b) 800°C, (c) 1000°C, and (d) 1200°C.
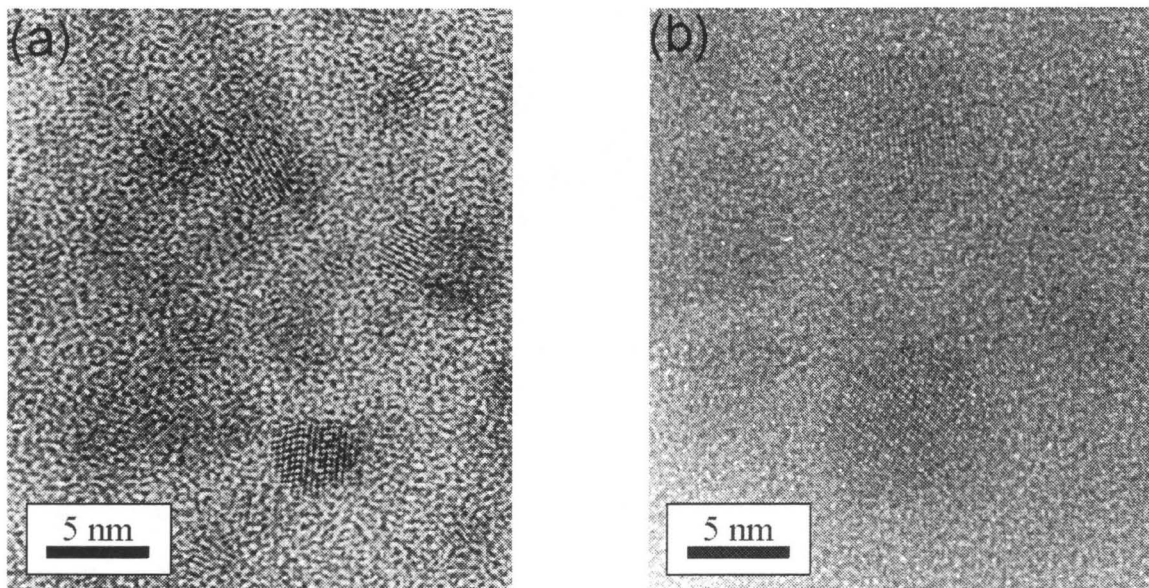
Figure 2.2. Planar-view high-resolution transmission micrographs of the 100 nm SiO$_2$ films implanted with 2×10^{16}/cm^2 Ge$^+$ and subsequently annealed at (a) 600°C and (b) 1200°C for 40 min. All particles are clearly single crystalline, and some exhibit twinning.
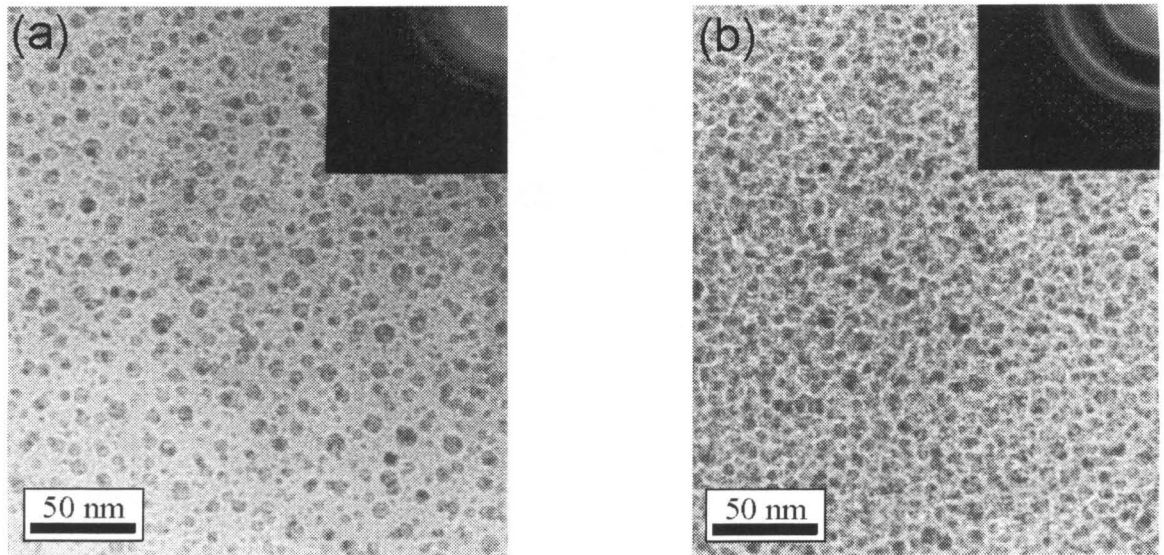
Figure 2.3. Planar-view bright field transmission electron micrographs of 100 nm SiO$_2$ films implanted with (a) 2×10^{16}/cm^2 Ge$^+$ and (b) 5×10^{16}/cm^2 Ge$^+$ and subsequently annealed at 1000°C for 40 min. It is clearly seen that higher dose results in higher density of particles.

2.5 min.
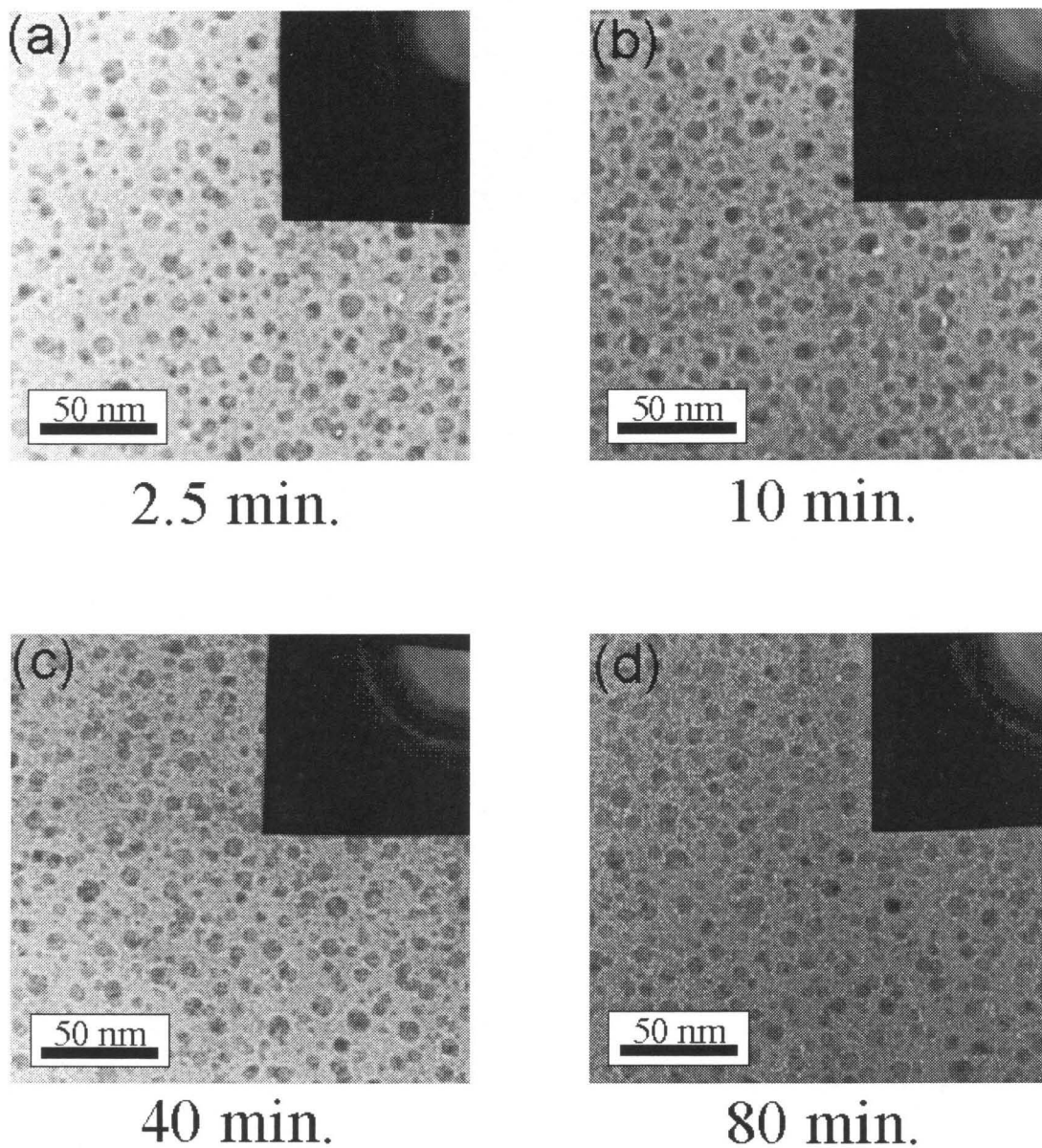
10 min.

40 min.

80 min.

Figure 2.4. Planar-view bright field transmission electron micrographs of the 100 nm SiO$_2$ films implanted with 2×10^{16}/cm^2 Ge$^+$ and subsequently annealed isothermally at 1000°C for 2.5 min., 10 min., 40 min., and 80 min., respectively. No significant time dependence of particle size evolution has been observed within the experimental uncertainty.

2.3.2   Si Nanocrystals in SiO_2

Transmission electron microscopy (TEM) was performed on the samples synthesized by the above method to verify the presence of Si nanocrystals and X-ray photoelectron spectroscopy was performed to study the precipitation kinetics and the structural evolution of the SiO_2 matrix.

Figure 2.5 shows a planar view high resolution TEM image of a sample implanted with $5 \times 10^{16}/cm^2$ Si^+ and annealed at 1000°C for 40 min. Despite a weak contrast, a dense array of Si nanocrystals is visible, with sizes ranging from 1 nm to 3 nm in diameter. It should be noted that due to low contrast between small Si nanocrystals and the amorphous SiO_2 background, quantitative information on size distribution of particles obtainable from these images is limited. One could easily underestimate the particle density of small nanocrystals less than about 1.5 nm. Information about particle density should therefore be supplemented with additional techniques.

In order to gain insights about the density of very small nanocrystals and the evolution of chemical environment of the implanted Si atoms and the damaged matrix, we have performed Si 2p core level studies using X-ray photoelectron spectroscopy (XPS). X-ray photoelectron spectroscopy can yield valuable information about the nanocrystal formation as well as the annealing kinetics of the damaged matrix. This is important since suboxides leading to imperfect

nanocrystal/SiO_2 interfaces can serve as a channel for indirect recombination of quantum confined excitons.

All samples were pre-etched using hydrofluoric acid so that the analyzed cross-section lies at the peak of the implantation distribution. Figure 2.6 shows the Si 2p core level spectra of samples implanted with 5×10^{16}/cm^2 Si annealed in vacuum at temperatures between 400°C and 1100°C for 10 min. For comparison, spectra of hydrogen terminated (100) Si and the unimplanted substrate (100 nm wet oxide on (100) Si) are also shown. A pure Gaussian deconvolution of (100) Si 2p$_{3/2}$ revealed a full with at half-maximum of 0.72 eV. The binding energy was calibrated by fixing the adventitious C (1s) binding energy at a value of 285 eV for all spectra. Several trends are noteworthy in Fig. 2.6. First of all, the Si 2p core level of the as-implanted oxide film is shifted and inhomogeneously broadened towards lower binding energy relative to unimplanted oxide, characteristic of a suboxide with contributions from all Si^{x+} oxidation states [18]. The phase separation of the suboxide into Si and SiO_2 occurs gradually with increasing annealing temperature, as can be deduced from the gradual shifting of the suboxide peak towards stoichiometric SiO_2 binding energy and a distinct bulk Si peak appearing for samples annealed at temperatures higher than 600°C. It should be noted that the Si 2p core level of the damaged matrix returns to the stoichiometric value only upon annealing at 1100°C, which is also the temperature at which a significant amount of nanocrystal formation occurs, as can be seen in Fig. 2.6. Also, the presence of small nanocrystals for samples annealed at 800°C and 600°C can be inferred from the XPS spectra, although we could not observe them by transmission electron microscopy.
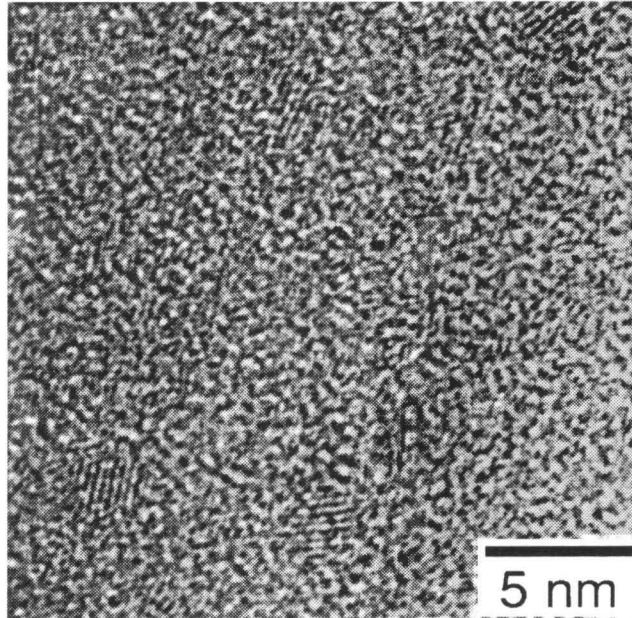
Figure 2.5. Planar-view high-resolution transmission electron micrograph of 100 nm SiO$_2$ implanted with 5×10^{16}/cm^2 Si$^+$ and annealed at 1000°C for 40 min. Despite weak contrast, a dense array of Si nanocrystals is visible, with sizes ranging from 1 nm to 3 nm in diameter.
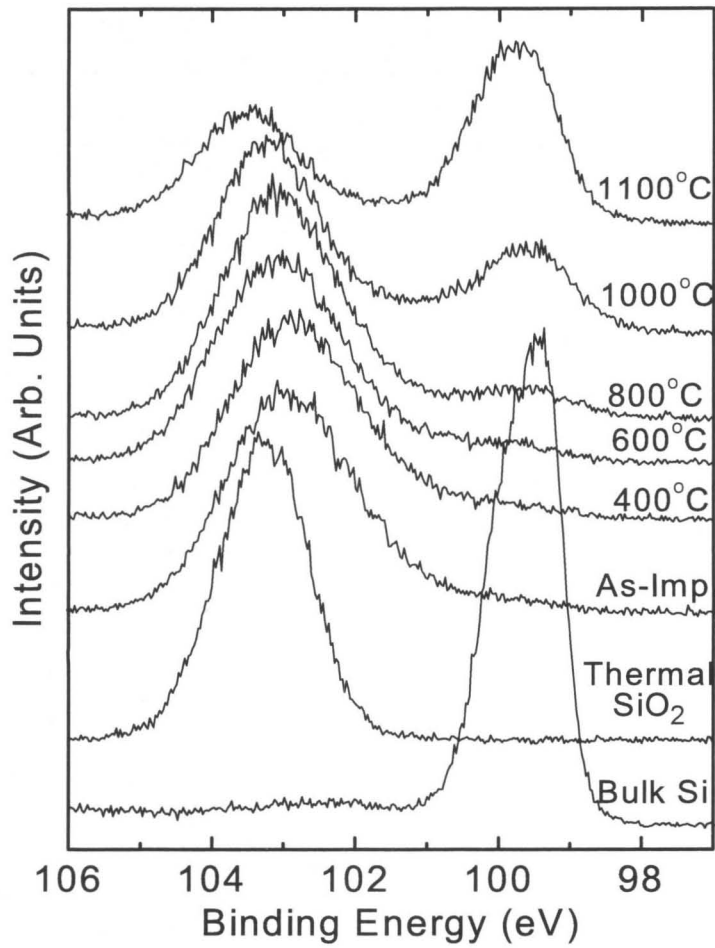
Figure 2.6 Si 2p X-ray photoelectron core level spectra of 100 nm SiO$_2$ implanted with 5×10^{16}/cm^2 Si$^+$ and subsequently annealed in vacuum at temperatures between 400°C and 1100°C for 10 min.

2.3.3 GaAs Nanocrystals in SiO_2

Transmission electron microscopy (TEM) characterization was performed on the samples synthesized by sequential implantation of Ga^+ and As^+ as described in Section 2.2 to verify the presence of stoichiometric GaAs nanocrystals.

Figures 2.7(a) and 2.7(b) are bright field and high-resolution TEM images, respectively, of GaAs nanocrystals in SiO_2 synthesized by sequential implantation of 75 keV Ga^+ at a dose of $3 \times 10^{16}/cm^2$, followed by 75 keV As^+ at a dose of $2 \times 10^{16}/cm^2$ into the 100 nm SiO_2. The implanted SiO_2 film in Fig. 2.7 was annealed in vacuum at 900°C for 10 minutes. From the high-resolution micrograph in Fig. 2.7 (b), the average diameter was determined to be 2.5 ± 1.3 nm.

Figure 2.8 (a) and (b) are the diffraction pattern and a dark field TEM image taken using the (113) reflection, respectively, of the same sample as in Fig. 2.7. The diffraction rings in Fig. 2.8 (a) are indexable only to bulk stoichiometric GaAs. No precipitation of Ga or As was observable in the diffraction pattern in Fig. 2.8(a), indicating that virtually all of the implanted Ga and As atoms go into forming GaAs nanocrystals.
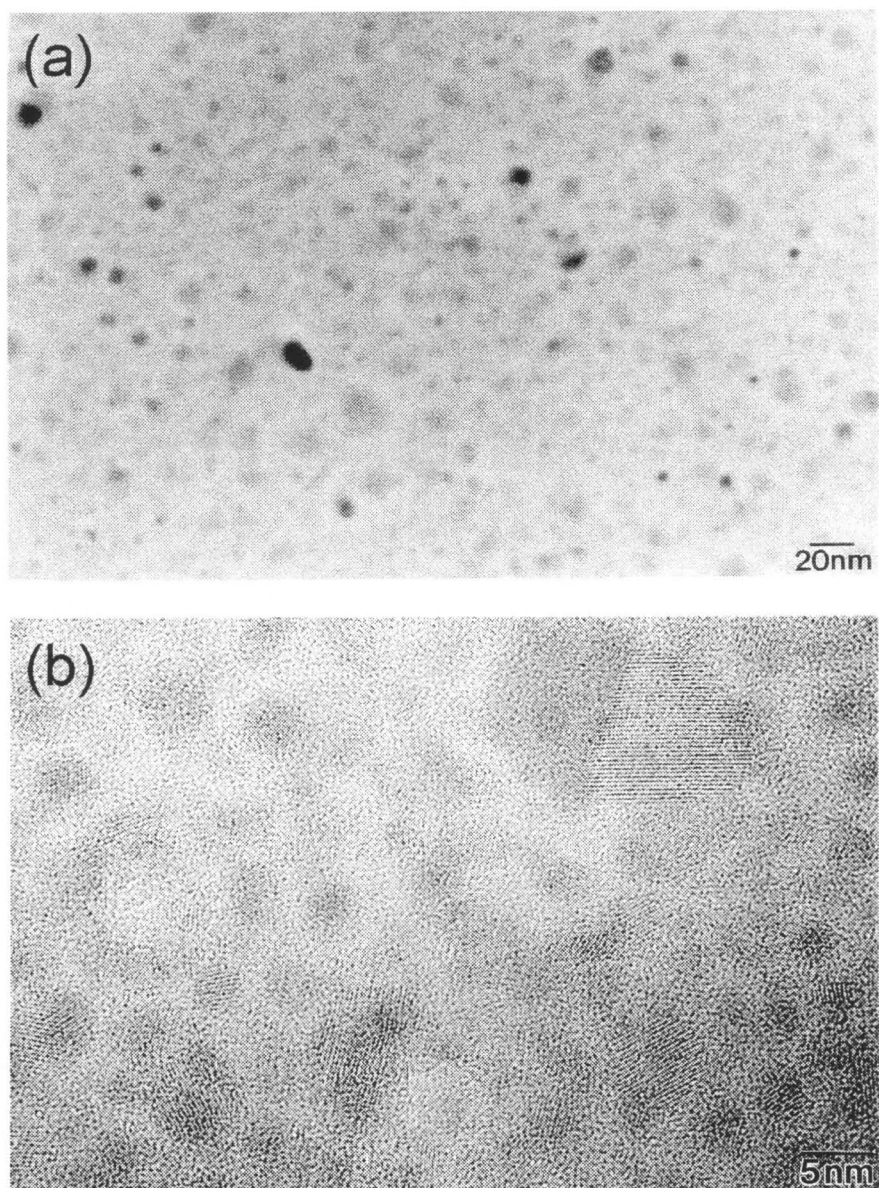
Figure 2.7. (a) Bright field and (b) high-resolution transmission electron micrographs of GaAs nanocrystals in SiO_2 synthesized by sequential implantation of 75 keV Ga^+ at a dose of $3 \times 10^{16}/cm^2$, followed by 75 keV As^+ at a dose of $2 \times 10^{16}/cm^2$ into SiO_2. The implanted SiO_2 film was annealed in vacuum at 900°C for 10 min.
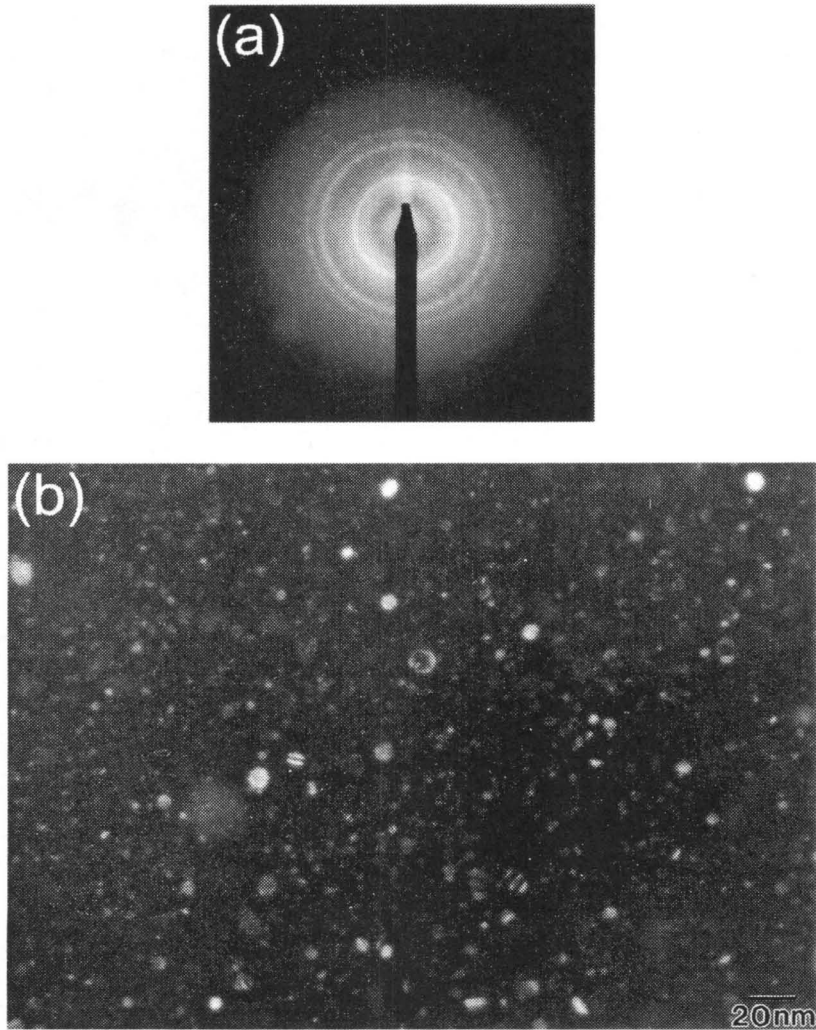
Figure 2.8 (a) Diffraction pattern and (b) dark field transmission electron micrograph taken using the (113) reflection of GaAs nanocrystals in SiO_2 synthesized by sequential implantation of 75 keV Ga^+ at a dose of 3×10^{16}/cm^2, followed by 75 keV As^+ at a dose of 2×10^{16}/cm^2 into the 100 nm SiO_2. The implanted SiO_2 film was annealed in vacuum at 900°C for 10 min. (same sample as in Fig. 2.7).

2.4 Conclusions

Ion beam synthesis is a powerful technique for synthesizing nanocrystals in matrices by precipitation. The only requirement is that the precipitation of the implanted species is thermodynamically favored. As demonstrated in this chapter, ion beam synthesis can be employed not only to synthesize elemental semiconductor nanocrystals, but also to synthesize compound semiconductor nanocrystals by sequential implantation.

Ion beam synthesis offers several important advantages. First of all, the initial film concentration profile can be controlled spatially and compositionally by controlling the implantation energy and the dose, somewhat independent of each other, within the Gaussian distribution width. The control over the initial film concentration profile enables significant control over the final size distribution. Flat concentration profiles can also be realized by sequential implantation to enable more uniform nanocrystal distributions. Second, the implanted material is chemically pure due to the mass selectivity of the ion implantation process. Third, ion beam synthesis produces nanocrystals with superior surfaces compared to other non-ultra-high-vacuum techniques because the nanocrystals never "see" the ambiance. Fourth, since the number of metastable solid solutions that can be made is limited only by the availability of the target and the source material, it is possible to synthesize a large variety of materials. In addition to Ge, Si, and GaAs nanocrystals synthesized in this work, many other compound semiconductor nanocrystals have been successfully

synthesized in SiO_2 and other matrices by the ion beam synthesis technique [19].

Finally, since all of the processes involved in the synthesis, namely thermal oxidation,

ion implantation, and thermal annealing, are standard processes used in ULSI

semiconductor processing, the technique can, in principle, be directly integrated with

the existing semiconductor processes.

Bibliography

[1] See, for example, A.D. Yoffe, Adv. Phys. **42**, 173 (1993), and the references therein.

[2] L.T. Canham, Appl. Phys. Lett. **57**, 1046 (1990).

[3] Y. Kanemitsu, H. Uto, Y. Matsumoto, and Y. Maeda, Appl. Phys. Lett. **61**, 2187 (1992).

[4] Y. Maeda, Phys. Rev. **B 51**, 1658 (1994).

[5] D.C. Paine, C. Caragianis, T.Y. Kim, Y. Shigesato, and T. Ishahara, Appl. Phys. Lett. **62**, 2842 (1993).

[6] H.A. Atwater, K.V. Shcheglov, S.S. Wong, K.J. Vahala, R.C. Flagan, M.L. Brongersma, and A. Polman, Mat. Res. Soc. Symp. Proc. **316**, 409 (1994).

[7] M. H. Ludwig, R.E. Hummel, and S, -S Chang, J. Vac. Sci. Technol. **B 12**, 3023 (1994).

[8] Q. Zhang, S.C. Bayliss, and D.A. Hutt, Appl. Phys. Lett. **66**, 1977 (1995).

[9] L. E. Brus, P.F. Szajowski, W.L. Wilson, T.D. Harris, S. Schuppler, and P. H. Citrin, J. Am. Chem. Soc. **117**, 2915 (1995).

[10] T. S-Iwayama, S. Nakao, and K. Saitoh, Appl. Phys. Lett. **65**, 1814 (1994).

[11] P. Mutti, G. Ghislotti, S. Bertoni, L. Bonnoldi, G.F. Cerofolini, L. Meda, E. Grilli, and M. Guzzi, Appl. Phys. Lett. **66**, 851 (1995).

[12] H.M. Cheong, W. Paul, S.P. Withrow, J.G. Zhu, J.D. Budai, C.W. White, and D.M. Hembree, Jr., Appl. Phys. Lett. **68**, 87 (1996).

[13] J. G. Zhu, C.W. White, J. D. Budai, S.P. Withrow, and Y. Chen, J. Appl. Phys. **78**, 4386 (1995).

[14] See, for example, R.R. Razouk and B.E. Deal, J. Eletrochem. Soc., **126**, 1573 (1979).

[15] J.F. Ziegler, J.P. Biersack, and U. Littmark, *The Stopping and Range of Ions in Solids*, Pergamon, New York, 1985.

[16] C. Wagner, Z. Elektrochem.**65**, 581 (1961).

[17] I.M. Lifshitz and V.V. Slyzov, J. Phys. Chem. Solids **19**, 35 (1961).

[18] See, for example, Z. H. Lu, M. J. Graham, D.T. Jiang, and K. H. Tan, Appl. Phys. Lett. **63**, 2941 (1993).

[19] A. Meldrum, C.W. White, L.A. Boatner, et al., Nuc. Inst. Meth. **B 148**, 957 (1999); C.W. White, A. Meldrum, J.D. Budai, et al. Nuc. Inst. Meth. **B 148**, 991 (1999); J.D. Budai, C.W. White, S.P. Withrow, et al., Nature **390**, 384 (1997).

Chapter 3

The Origin and Mechanism of Visible Luminescence from Ion Beam Synthesized Ge and Si Nanocrystals in SiO_2

3.1 Introduction

Visible light emission from low-dimensional group IV semiconductors due to quantum confinement effects has received worldwide attention over the past few years, due to scientific and technological interest in development of silicon-based light-emitters that could be monolithically integrated with advanced silicon microelectronics [1-3]. The discovery of porous Si [4] inspired intense scientific

investigation, both theoretical [5-10] and experimental [11-22], on the origin and the mechanism of visible luminescence in group IV semiconductor quantum dots.

Quantum confinement is expected to take noticeable effect when the crystal dimensions approach that of the exciton Bohr radii, which are 11.5 nm and 4.3 nm for Ge and Si, respectively. Quantum confinement of carriers is expected to have several important effects on the optical properties of Si and Ge. First, the excitonic binding energy is expected to exceed kT at room temperature (0.026 eV), leading to luminescence of excitonic origin even at room temperature [9]. For example, Si nanocrystals with diameter of 5-6.5 nm correspond to exciton binding energy of about 75-95 meV, which is well above kT at room temperature. Second, the exciton energy or the band gap energy is expected to increase rapidly with decreasing crystal size. A summary of representative theoretical predictions on the size dependence of the band gap of Ge and Si is given in Fig. 3.1(a) and Fig. 3.1(b), respectively. The agreement between different methods of calculations is rather poor but the general trend is clear. Third, small dimensions disrupt the crystal symmetry and lead to relaxation of momentum selection rules, which in turn is expected to lead to an improvement of emission efficiency. This is reflected in the estimated increase in the oscillator strength by nearly six orders of magnitude as the number of Si atoms is decreased from about 1000 to 10 [8].

Inspired by these theoretical predictions, many different techniques have been developed to synthesize light-emitting group IV nanocrystals [11-22]. As outlined in Chapter 2, ion beam synthesis of group IV nanocrystals in thermal SiO_2 offers several technologically important advantages, including integrated circuit process

compatibility and significant control over the nanocrystal size distribution, as well as chemical and mechanical stability. Although ion beam synthesis has been widely reported [19-21], the origin of visible luminescence from ion beam synthesized Ge and Si nanocrystals has so far been unclear, primarily due to a lack of distinction between luminescence originating from matrix defects and luminescence originating from quantum-confined excitons in nanocrystals. It is well known [23-26] that defects in SiO_2 display luminescence at various energies including the visible range, so any interpretation of luminescence spectra without an unambiguous distinction of the contribution from defects can be very misleading. A schematic diagram of possible radiative transitions in SiO_2 films containing Ge or Si nanocrystals are summarized in Fig. 3.2. Radiative transitions could involve any combination between quantum-confined excitonic states, interface states within the exciton energy gap, the conduction and valence band states of SiO_2, and defect states within the SiO_2 band gap. Among these, light emission by radiative recombination of quantum-confined excitons is the only process that is expected to display clear size dependence in emission energy and radiative transition rate.

In this chapter, we provide experimental results on Ge and Si nanocrystals in SiO_2 made by ion implantation that clearly distinguish visible photoluminescence originating from the nanocrystals from that which originates from matrix defects. For the case of SiO_2 films containing Ge nanocrystals, the observed visible luminescence is shown not to originate from quantum-confined excitons in Ge nanocrystals. Instead, observations of similar photoluminescence and photoluminescence decay rate measurements from Xe^+-implanted SiO_2, as well as reversible quenching

behavior of the luminescence by introduction hydrogen or deuterium suggest that radiative defect centers in the SiO_2 matrix are responsible for the observed luminescence. In the case of SiO_2 films containing Si nanocrystals, two sources of room temperature visible luminescence are identified. From a similar comparison of photoluminescence and photoluminescence decay rate measurements between Xe^+-implanted SiO_2 films and SiO_2 films containing Si nanocrystals, a luminescence feature attributable to defects in the SiO_2 matrix is unambiguously identified. After quenching the defect-related luminescence feature with deuterium, the size dependence of photoluminescence and the photoluminescence decay rate measurements on the remaining luminescence feature is unambiguously attributed to quantum-confined excitons in Si nanocrystals.

Further confirmation of the quantum confinement model for the Si nanocrystals comes from the temperature dependence of the photoluminescence intensity and the photoluminescence decay rate. The temperature dependence of the radiative decay rate is determined from the temperature dependence of the photoluminescence intensity and the photoluminescence decay rate, and is readily explained by a model [15] of highly quantum-confined excitons with large exchange splitting between the excitonic singlet and triplet levels in crystalline Si.
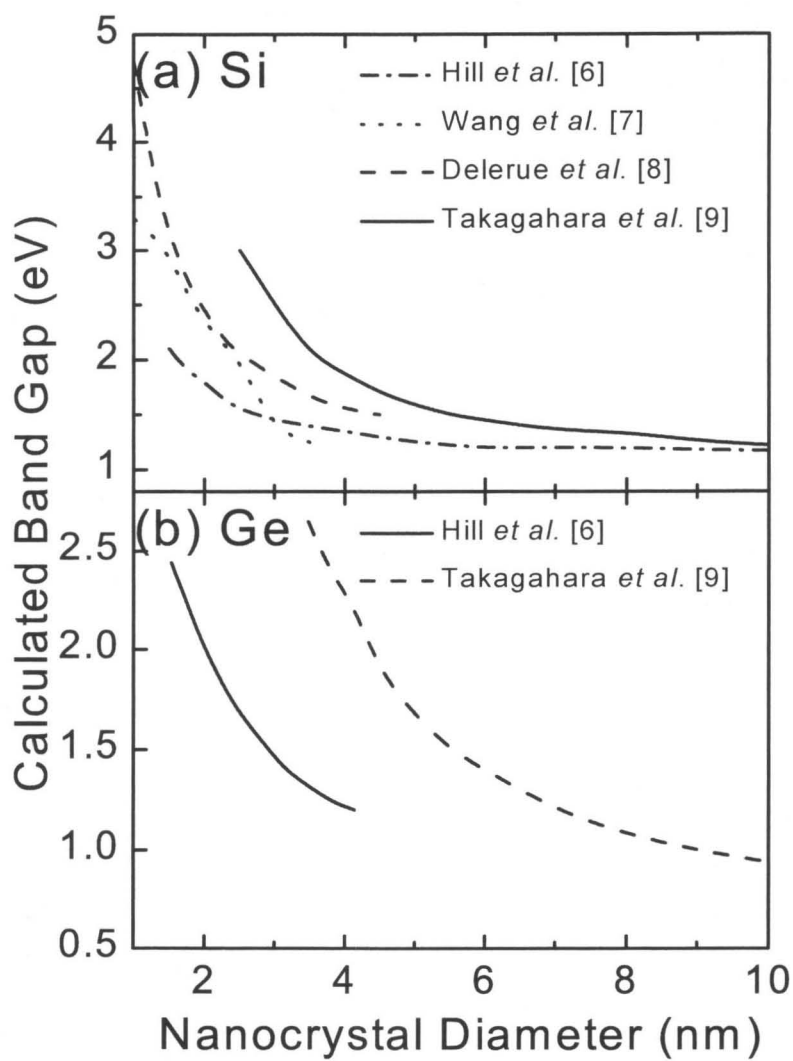
Figure 3.1. Theoretical predictions of the band gap of (a) Si nanocrystals and (b) Ge

nanocrystals as a function of nanocrystal diameter.
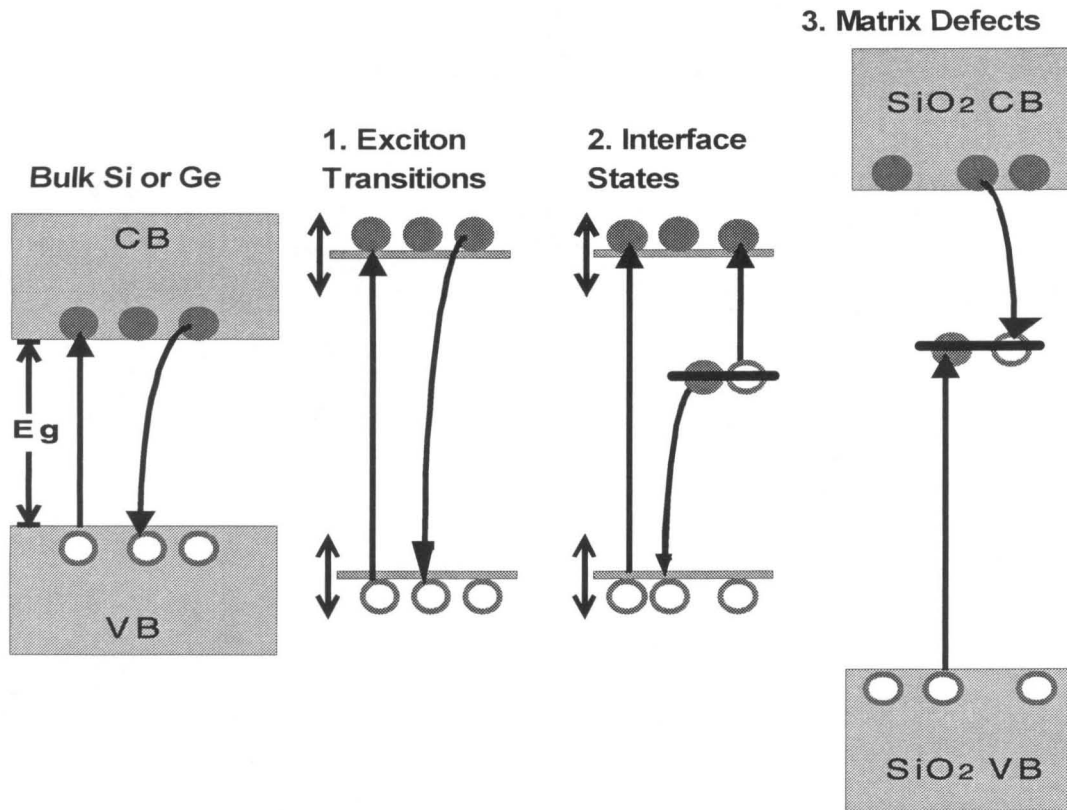
Figure 3.2. A schematic diagram of possible radiative transitions in SiO_2 films containing Ge or Si nanocrystals. Filled circles represent electrons and the open circles represent holes. Single-ended straight arrows indicate possible carrier excitations and single-ended curved arrows indicate corresponding possible radiative decay. Double-ended arrows indicate that the levels are size-dependent.

3.2 The Origin of Visible Luminescence from SiO$_2$ Containing Ge Nanocrystals

There have been several reports of visible photoluminescence (PL) from Ge nanocrystals embedded in SiO$_2$ [11-14]. Three principal methods have been employed to synthesize Ge nanocrystals in SiO$_2$: rf-cosputtering of Ge and SiO$_2$ [11,12], hydrothermal reduction of Si$_x$Ge$_{1-x}$O$_2$ [13], and Ge ion implantation [14]. For all methods of synthesis, similar visible PL spectra have been observed. Despite many suggestions, the origin of visible PL has not yet been made clear. The principal debate regarding the origin of luminescence centered around whether or not the luminescence mechanism can be attributed to the radiative recombination of quantum-confined electron/hole pairs (or excitons) in Ge quantum dots. [11-14]. In this section, we report results of experiments on Ge nanocrystals in SiO$_2$ made by ion implantation which indicate that the dominant process responsible for visible PL observed from SiO$_2$ containing Ge nanocrystals is *not* radiative recombination of quantum-confined excitons in Ge nanocrystals. Instead, evidence from PL and PL decay rate measurements as a function of nanocrystal size, temperature dependent PL measurements, studies on luminescence from Xe$^+$-implanted thermal SiO$_2$, and studies on the effect of hydrogen and deuterium on PL all strongly suggest that the visible PL is primarily due to luminescent defect centers in the matrix.

SiO_2 films, 100 nm thick, grown by wet thermal oxidation on a lightly p-doped (100) Si wafers were implanted at room temperature with 70 keV $^{74}Ge^+$ at doses of $1\times10^{16}/cm^2$, $2\times10^{16}/cm^2$, and $5\times10^{16}/cm^2$ resulting in peak Ge concentrations of 3, 6, and 13 at. %, respectively, as determined by Rutherford backscattering spectrometry. The energy was chosen such that the implanted Ge concentration profile is completely within the oxide film, with the peak concentration lying 30-40 nm from the surface. After implantation, the samples were annealed in high vacuum at 600°C, 800°C, and 1000°C for 40 min. The average nanocrystal sizes were determined from Gaussian fits to the size distributions obtained from bright field transmission electron micrographs in Chapter 2. The average sizes are 1.9 nm, 3.2 nm, and 7.2 nm, with full-widths at half-maximum of 1.5 nm, 3.4 nm, and 4.0 nm, for the samples annealed at the three temperatures, respectively. As discussed in Chapter 2, higher implantation doses yield samples with higher nanocrystal density, but with the same size distributions after annealing. All photoluminescence spectra were taken with 50 mW/mm^2 excitation using 457.9 nm Ar$^+$ laser radiation, detected using a grating spectrometer and a thermoelectrically cooled 256×1024 Si CCD array detector. All spectra have been corrected for detection efficiency. Samples for all PL decay rate measurements were cooled to 15K using a closed-cycle He cryostat and pumped to a steady state under 475 nm Ar$^+$ laser radiation (1 mW/mm) prior to measurements. The PL decay traces were taken using a GaAs photomultiplier tube in combination with a multichannel photon counter. The time resolution of the

experimental setup was 400 ns. A very weak PL was observed from annealed as-grown SiO_2 films.

Figure 3.3 shows the room temperature PL spectra of the $5 \times 10^{16}/cm^2$ Ge^+-implanted SiO_2 film (13 at. % Ge) annealed at different temperatures. Several notable characteristics of the PL spectra in Fig. 3.3 have also been reported previously for SiO_2 containing Ge nanocrystals synthesized by other methods [11-13]. First, the annealed samples show an intense PL signal, visible to the unaided eye, with characteristically broad spectra. Second, no appreciable shift in peak luminescence energy is observed with variation in the annealing temperature (i.e., nanocrystal size). Figure 3.4 shows a plot of the peak luminescence energy of the measured PL spectra as a function of nanocrystal diameter for the same set of samples as in Fig. 3.3. The horizontal and vertical error bars indicate the full widths at half maximum of the nanocrystal size distributions and PL spectra, respectively. For comparison, calculations of exciton energy as a function of quantum dot diameter are also shown [6,9]. For the nanocrystal size range in our samples (1.9 nm–7.2 nm), both calculations predict a systematic blue shift of the exciton energy by at least 1 eV. The experimental data shown in Fig. 3.4, however, exhibit no appreciable or systematic shift in the peak luminescence energy, similar to other reports on SiO_2 containing Ge nanocrystals [11-14]. To the best of author's knowledge, no experimental observation of large PL peak energy shifts, comparable to those predicted by calculations, has been reported for Ge nanocrystals. The reported values [11,12] of PL peak energy shift are an order of magnitude smaller than what has been predicted [9] for radiative recombination of quantum-confined excitons.

Ion implantation creates a defect density in the SiO_2 network that far exceeds the equilibrium value. As it is already known that some defects in SiO_2 and $Ge_xSi_{1-x}O_2$ exhibit visible luminescence [23-26], it is very important to characterize the luminescence due to these irradiation-induced defects. To address this issue, we have performed 120 keV $^{130}Xe^+$ implantation into 100 nm SiO_2 films at doses of $6.6 \times 10^{15}/cm^2$, $1.3 \times 10^{16}/cm^2$, and $3.3 \times 10^{16}/cm^2$. The energy and the three doses were carefully chosen using the TRIM Monte Carlo code [27], such that the projected range, the straggle, and the peak concentration of atomic displacements would closely resemble the atomic displacement profiles created by the three different Ge^+ implantation doses. We compare room temperature PL spectra of the as-annealed $3.3 \times 10^{16}/cm^2$ Xe^+-implanted SiO_2 and the as-annealed $5 \times 10^{16}/cm^2$ Ge^+-implanted SiO_2 in Fig. 3.5(a) and Fig. 3.5(b), respectively. Figure 3.5(a) shows the room temperature PL spectra of the Xe^+-implanted sample annealed at 1000°C for 40 min. and Fig. 3.5(b) shows the room temperature PL spectra of the Ge^+-implanted sample annealed at 1000°C for 40 min. Although not shown, it has been observed that a change in the implantation dose only affects the intensity of the PL spectra and not the peak energy nor the shape. The observed similarities in spectral features and trends between Ge^+-implanted SiO_2 and Xe^+-implanted SiO_2 are strikingly clear. Strong visible room temperature PL of comparable intensities was observed in both samples only after annealing. Although not shown, the PL intensity decreases with increasing implantation dose for the annealed samples. It was also observed that the PL peak energy and the spectrum shape do not depend on the annealing temperature.

As one would not expect visible PL from the implanted Xe atoms themselves, these similarities in the PL spectra are very likely a result of the similarities in defect profiles created by ion irradiation in the Ge^+-implanted and Xe^+-implanted samples.

Hydrogen is known to passivate electronic defects in semiconductors. Even the performance of an oxide-passivated Si p-n diode can be further improved upon hydrogen passivation, because oxygen, being a large atom, cannot passivate every dangling bond at the oxide/semiconductor interface [28]. By analogy, if there are dangling bonds at the nanocrystal/matrix interface that act as non-radiative recombination centers for quantum-confined electron-hole pairs (or excitons) in nanocrystals, hydrogen passivation would lead to an enhancement of the luminescence efficiency, hence higher PL intensity. On the other hand, if the luminescence is arising from radiative transitions involving point defects in the SiO_2 matrix, hydrogen passivation of these point defects might lead to a dramatic alteration of the luminescence properties of these defects. A schematic view of a nanocrystal in the SiO_2 network and possible structural point defects that can be passivated with hydrogen is illustrated in Fig. 3.6. Defects in the matrix include E' centers [29] and non-bridging oxygen hole centers [30]. Hydrogen can also passivate dangling bonds at the nanocrystal/SiO_2 interface. Investigation of the effect of hydrogen on the luminescence properties, therefore, can be a powerful tool in understanding the origin of the luminescence.

In order to investigate whether or not the luminescence is originating from quantum-confined excitons, therefore, we have performed passivation experiments

using deuterium. Deuterium was used instead of hydrogen in order to facilitate concentration determination by ion scattering measurements. Deuterium implantation was performed on annealed Ge^+-implanted samples using a Kauffman ion beam source at a beam energy of 600 eV. An estimate of the projected range of 600 eV D^+ in SiO_2 using the TRIM code [27] yields a value of about 25 nm. Although this range does not coincide with the projected ranges of Ge^+ implantations, previously reported values on the diffusivities of hydrogen atoms and molecules suggest that hydrogen and deuterium will easily diffuse through an oxide film of 100 nm in laboratory time frame at room temperature [31]. Figures 3.5(a) and 3.5(b) show the effect of deuterium passivation on the annealed $3.3 \times 10^{16}/cm^2$ Xe^+-implanted SiO_2 and annealed $5 \times 10^{16}/cm^2$ Ge^+-implanted SiO_2, respectively. As can be seen, the intensity of the PL drops with increasing dose of deuterium, without any change in the spectral shape. Fig. 3.7 shows the integrated PL intensity variation with deuterium concentration for the $2 \times 10^{16}/cm^2$ Ge^+-implanted SiO_2 sample (6 at. % Ge), annealed at 1000°C for 40 min. The implanted deuterium doses range from $2 \times 10^{15}/cm^2$ to $4 \times 10^{15}/cm^2$, as determined by elastic recoil spectrometry using a 2 MeV $^4He^{++}$ beam. The introduction of atomic deuterium drastically reduces the luminescence intensity, with nearly zero intensity for a deuterium dose of $4.0 \times 10^{15}/cm^2$. Deuterium can be removed from the SiO_2 film by thermal annealing in vacuum. Elastic recoil spectrometry measurements indicate that approximately 70% of the original deuterium atoms have diffused out of the film after a 30 min. anneal at 500°C. As

shown in Fig. 3.7, up to approximately 60% of the original intensity is recovered after such an anneal. The spectral features remain unchanged.

To verify that these observations are due to the chemical effect of deuterium rather than a physical effect such as deuterium ion irradiation damage, we have also performed rapid thermal annealing on the 1000°C-annealed 6 at. % Ge sample in dilute forming gas (3:97 H_2:N_2) at 800°C under atmospheric pressure. As in the D^+-implanted samples, a significant reduction in PL intensity was observed. A recovery of PL intensity upon out-diffusion of hydrogen was also observed. These results, showing that hydrogen or deuterium can reversibly deactivate radiative defect centers, suggest that the observed luminescence is indeed defect-related; it is known that many defect states in semiconductors can be reversibly deactivated by hydrogen [32].

A weak dependence of the PL decay rate on the nanocrystal size further supports the idea that the origin of PL in our samples is not related to the radiative recombination of quantum-confined excitons in Ge nanocrystals. Photoluminescence decay measurements were performed at various energies in the PL spectra in the temperature range of 12K to 300K using a photomultiplier tube in a multichannel photon counting arrangement. The time resolution of our experimental setup was 400 ns. The calculated radiative lifetime [9] ranges from microseconds to milliseconds for Ge quantum dot diameters ranging from 1 nm to 3 nm. However, for our samples ranging from 1.9 nm to 7.2 nm in diameter, all measured 1/e PL decay times were at or below the experimental resolution, thus putting an upper bound of the lifetime at

400 ns. This is too short compared to the expected characteristic decay time for radiative recombination of quantum-confined excitons in Ge nanocrystals.

The temperature dependence of PL spectra provides further evidence against the quantum-confinement model. Temperature dependent PL measurements were performed on 6 at. % Ge samples annealed at two different temperatures, 600°C and 1000°C, corresponding to nanocrystal diameters of 1.9 nm and 7.2 nm. For both samples, the PL intensity showed a weak dependence on the measurement temperature, varying by about a factor of 2 in the temperature range of 12K–300K. It will be seen from the case of excitonic luminescence from Si nanocrystals in Section 3.4 that the luminescence originating from quantum-confined excitons displays a systematic dependence of the PL intensity and the PL decay rate on the temperature due to a large exchange splitting between the singlet and triplet exciton levels [15]. For SiO_2 containing Ge nanocrystals, however, no meaningful information could be deduced from the PL intensity variation as a function of temperature. Furthermore, the spectral shape shows no dependence on temperature. This is contrary to what one would expect for crystalline Ge, which is a semiconductor material whose band gap is expected to increase with decreasing temperature due to thermal contraction of the crystal lattice [33]. It will be shown in Section 3.4 that for the case of excitonic luminescence from Si nanocrystals in SiO_2, the PL peak energy does decrease monotonically as the temperature is increased from 12K to 300K, by an amount comparable to the band gap variation with temperature in the bulk Si.

There are some observations that require further investigations. First, the PL intensity does not simply scale with the implantation dose and hence the number of

atomic displacements, contrary to what one might expect if irradiation-induced defects were indeed responsible for visible PL. This suggests that there exists some competitive processes between radiative and non-radiative defect centers. Second, strong luminescence is only observed after annealing. This suggests that the radiative defect centers are more stable at higher temperatures than the non-radiative defect centers. Third, for the Ge^+-implanted samples the PL intensity increases with increasing annealing temperature up to 1000°C, whereas for Xe^+-implanted samples the PL intensity increases with increasing annealing temperature only up to 800°C. Apparently, the luminescent defect centers in the Ge^+-implanted samples are more stable against thermal annealing than those in the Xe^+-implanted samples.
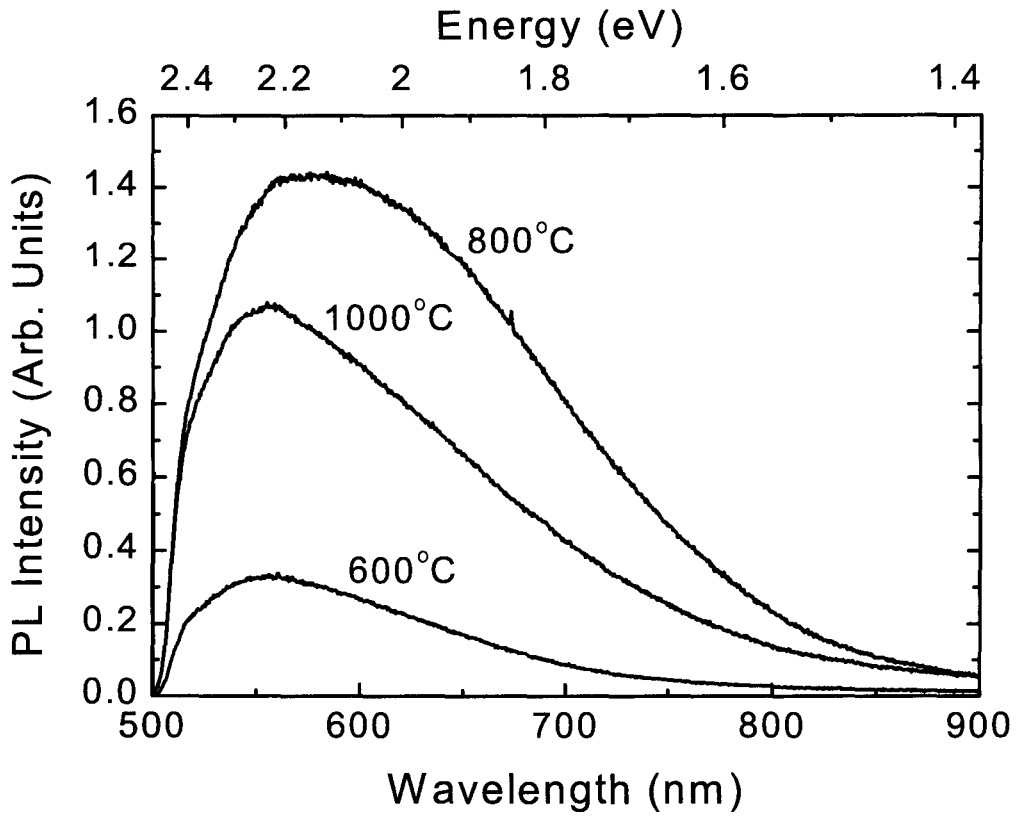
Figure 3.3. Room temperature photoluminescence spectra of $5 \times 10^{16}/cm^2$ Ge^+-implanted SiO_2 film (13 at. % Ge) annealed in vacuum at 600°C, 800°C, and 1000°C, for 40 minutes.
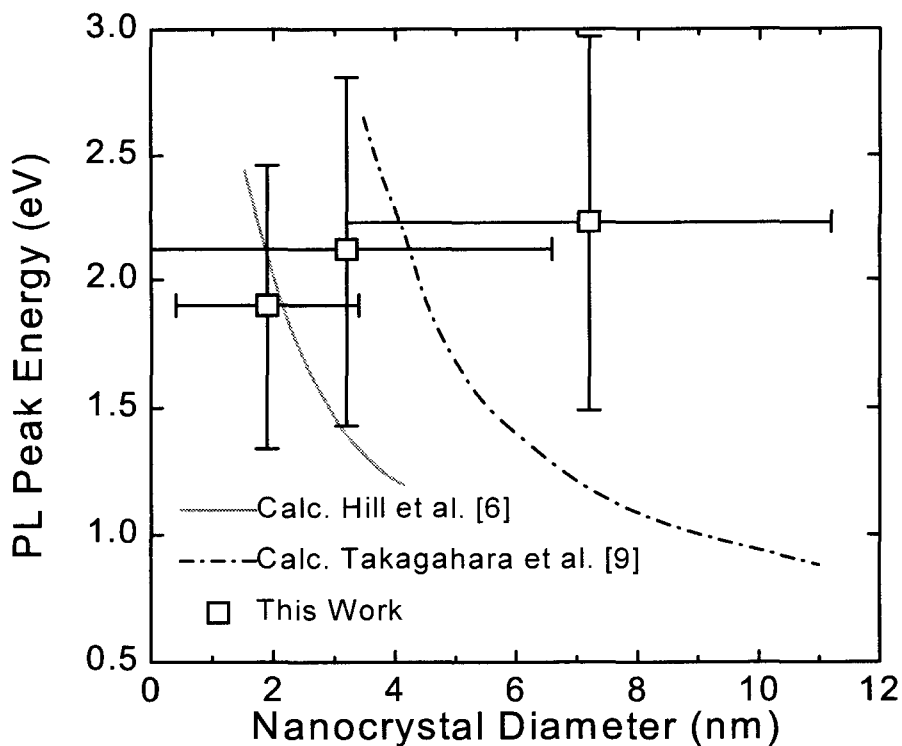
Figure 3.4. A comparison between measured peak photoluminescence energy (from

Fig. 3.3) and calculated exciton energy (from Ref. 9) as a function of nanocrystal

diameter for Ge nanocrystals in SiO_2. Horizontal and vertical error bars indicate full

widths at half maximum of the nanocrystal size distributions and photoluminescence

spectra, respectively.
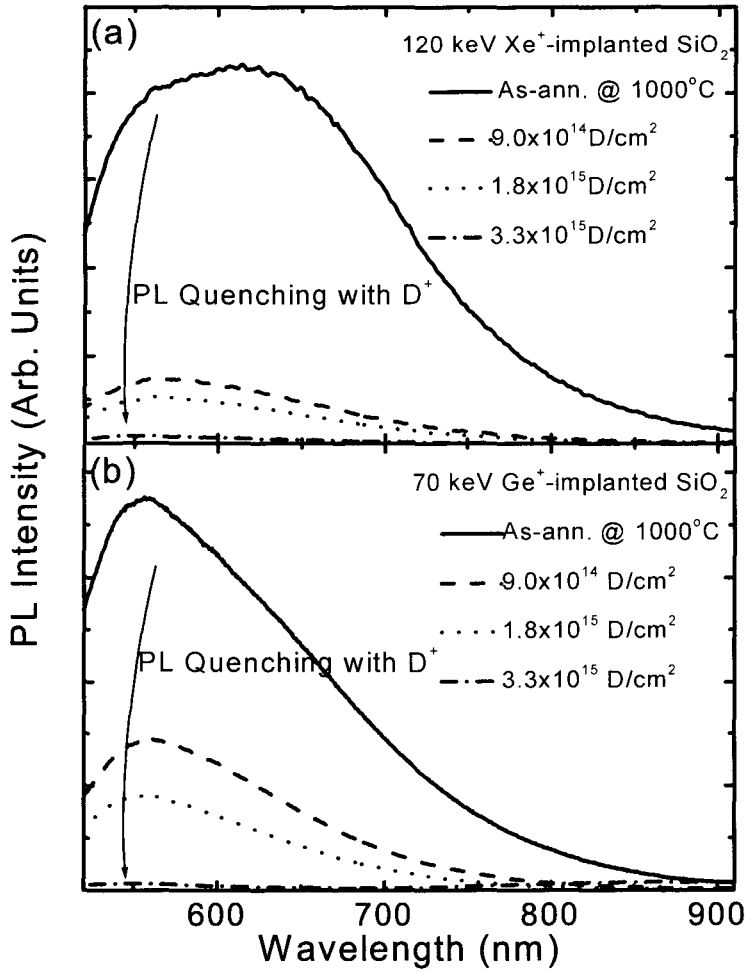
Figure 3.5. Room temperature visible photoluminescence spectra of (a) $3.3 \times 10^{16}/cm^2$ of 120 keV Xe^+-implanted 100 nm SiO_2 and (b) $5 \times 10^{16}/cm^2$ of 70 keV Ge^+-implanted 100 nm thick SiO_2 on Si. The films were annealed in vacuum at 1000°C for 40 min. The films were subsequently passivated with $9.0 \times 10^{14}/cm^2$, $1.8 \times 10^{15}/cm^2$, and $3.3 \times 10^{15}/cm^2$ of 600 eV D^+. The arrows indicate the intensity decrease as a result of deuterium passivation.
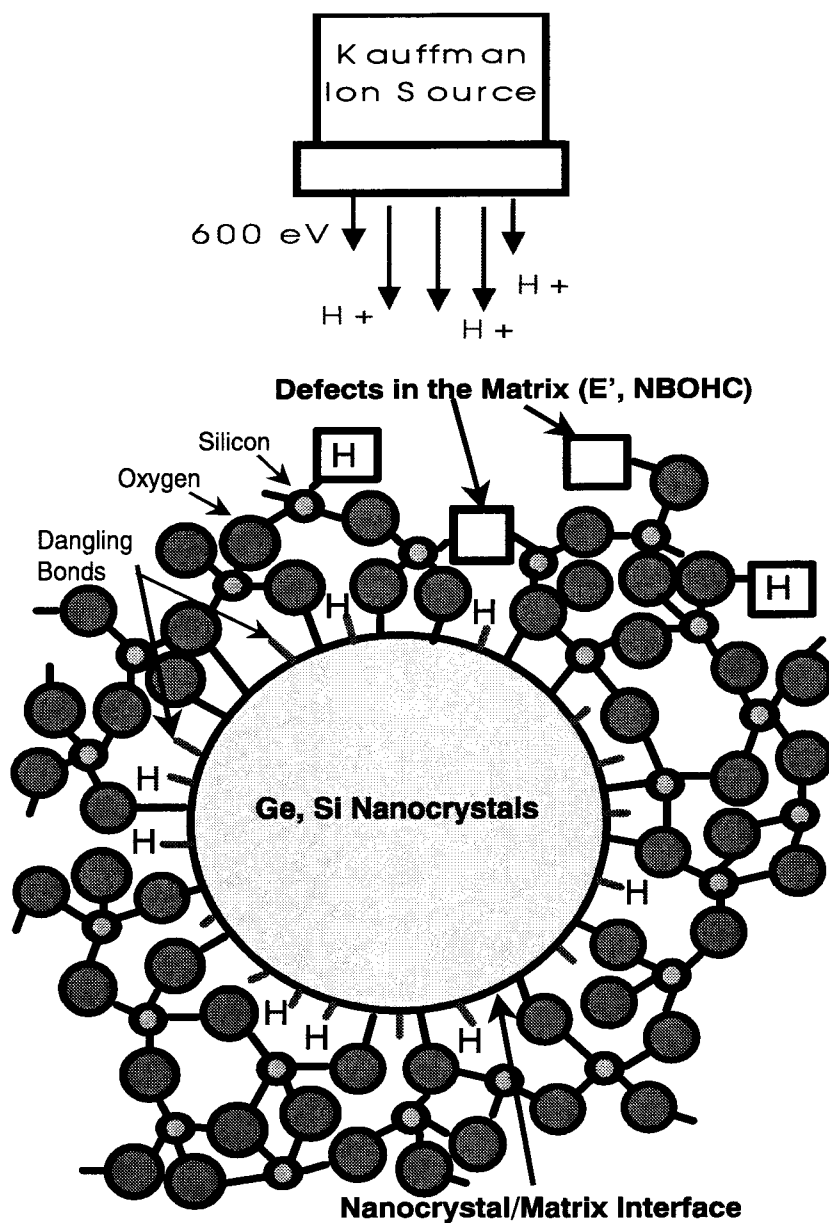
Figure 3.6. A schematic view of a nanocrystal in SiO_2 network and possible structural point defects that can be passivated with hydrogen. Defects in the matrix include E' centers and non-bridging oxygen hole centers. Defects at the nanocrystal/SiO_2 interface include dangling bonds.
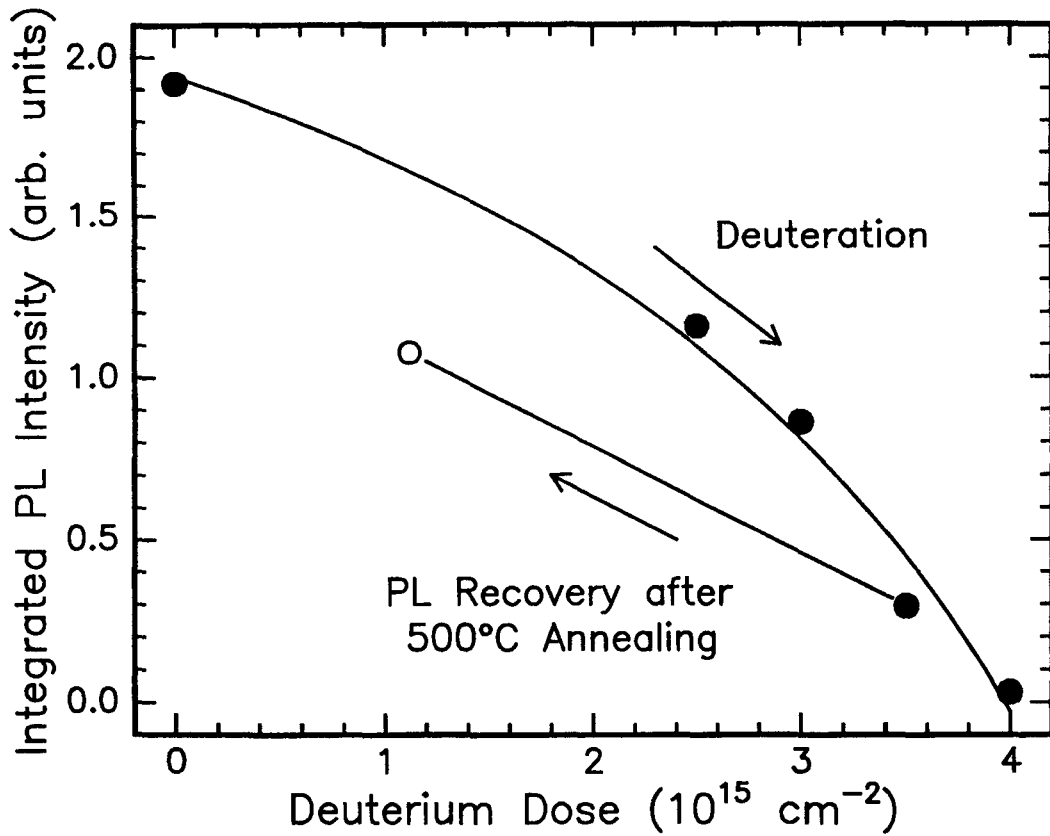
Figure 3.7. Integrated photoluminescence intensity as a function of implanted deuterium dose for 6 at. % Ge sample annealed at 1000°C for 40 min. (closed circles). The open circle indicate the deuterium concentration and the recovered PL intensity, after deuterium out-diffusion, of the sample with an original deuterium dose of 3.5×10^{15}/cm^2. Solid lines are guides to the eye.

3.3 The Origin of Visible Luminescence from SiO$_2$ Containing Si Nanocrystals

Although ion beam synthesis of Si nanocrystals in SiO$_2$ has been widely reported [19-21], the origin of visible luminescence from ion beam synthesized Si nanocrystals has been unclear, primarily due to a lack of distinction between luminescence originating from defects in the matrix and luminescence originating from nanocrystals. As it has been demonstrated in the previous section, defects in SiO$_2$ display visible luminescence and any interpretation of luminescence spectra without distinction of the contribution from defects can be very misleading.

Using similar analyses used to determine the origin of visible luminescence in SiO$_2$ containing Ge nanocrystals in the previous section, we provide experimental results that clearly distinguish visible photoluminescence (PL) originating from the nanocrystals from that which originates from matrix defects in SiO$_2$ films containing Si nanocrystals. Unlike SiO$_2$ films containing Ge nanocrystals, SiO$_2$ films containing Si nanocrystals do display a luminescence feature that is clearly attributable to quantum confined excitons in Si nanocrystals. From a comparison of PL spectra and PL decay rate measurements between Xe$^+$-implanted SiO$_2$ and SiO$_2$ films containing Si nanocrystals, a luminescence feature is clearly identified as arising from irradiation-damaged SiO$_2$. As in the previous section for the case of SiO$_2$ films containing Ge nanocrystals, we demonstrate that deuterium passivation of the films containing nanocrystals completely quenches the defect-related luminescence. The

peak energy of the remaining PL band attributable to Si nanocrystals unambiguously "red shifts" as a function of processing parameters that lead to an increase in nanocrystal size. In addition, the measured 1/e PL decay times are on the order of tens of microseconds, in qualitative agreement with theoretical predictions of radiative decay in Si nanocrystals [9]. Upon further annealing deuterium passivated samples at low temperatures, the intensity of the PL band originating from Si nanocrystals increases by more than an order of magnitude. These results indicate that the luminescence feature remaining after deuterium passivation can clearly be attributed to radiative recombination of quantum-confined excitons.

Wet thermal SiO_2 films, 100 nm thick, grown on lightly p-doped (100) Si wafers were either implanted with 50 keV $^{28}Si^+$ at doses of $1\times10^{16}/cm^2$, $2\times10^{16}/cm^2$, and $5\times10^{16}/cm^2$, corresponding to peak excess Si concentrations of 2, 4, and 10 at. % Si, respectively, or with 35 keV $^{28}Si^+$ at doses of $2\times10^{16}/cm^2$, $4\times10^{16}/cm^2$, and $6\times10^{16}/cm^2$, corresponding to peak excess Si concentrations of 5, 10, and 15 at. % Si, respectively, as calculated using the TRIM code [27]. The samples were subsequently annealed in high vacuum at temperatures ranging between 400°C and 1200°C for a fixed time of 10 min. Deuterium passivation experiments were performed by means of low energy (600 eV) deuterium implantation using a Kauffman ion source and the dose was determined by elastic recoil spectrometry using a 2.0 MeV $^4He^{++}$ beam. Deuterium was chosen instead of hydrogen in order to facilitate concentration determination. All PL spectra were taken with 50 mW/mm^2 excitation using 457.9 nm Ar$^+$ laser radiation, detected using a grating spectrometer

and a thermoelectrically cooled 256×1024 Si CCD array detector. All spectra have been corrected for detection efficiency. Samples for all PL lifetime measurements were cooled to 15K using a closed-cycle He cryostat and pumped to a steady state under 475 nm Ar^+ laser radiation (1 mW/mm) prior to measurements. Lifetime traces were taken using a GaAs photomultiplier tube in combination with a multichannel photon counter. The time resolution of the experimental setup was 400 ns.

As discussed in Chapter 2, planar-view high resolution TEM image (Fig. 2.5) of 100 nm SiO_2 implanted with $5×10^{16}/cm^2$ of 50 keV Si^+ and annealed at 1000°C show a dense array of Si nanocrystals, with sizes ranging from 1 nm to 3 nm in diameter. It has also been shown from X-ray photoelectron spectra (Fig. 2.6) that annealing results in phase separation of the suboxide into Si nanocrystals and SiO_2, and that the presence of small nanocrystals can be inferred from the implanted films annealed at temperatures as low as 600°C. This is important since the nanocrystals are too small to be observed by transmission electron microscopy after annealing at such a low annealing temperature.

From the results of X-ray photoelectron spectroscopy in Chapter 2 (Fig. 2.6), we can also obtain valuable information about the annealing kinetics of SiO_2, whose properties are known to be significantly altered during the process of ion implantation [34]. Information about structural defects in SiO_2 is valuable for two reasons. First, suboxides leading to imperfect nanocrystal/SiO_2 interfaces can give rise to channels for non-radiative recombination of quantum confined excitons. Second, it was clearly demonstrated [26] in Chapter 2 from Xe^+-irradiated SiO_2 that defects created during the implantation process display visible luminescence upon annealing at temperatures

greater than 800°C. An analysis of X-ray photoelectron spectra in Fig. 2.6 reveals that the peak of Si 2p core level of the damaged matrix approaches the value for stoichiometric SiO_2 only upon annealing at temperatures as high as 1100°C. The full width at half maximum, however, remains approximately 0.3 eV larger than the unimplanted film even after annealing at 1100°C. We can therefore expect the presence of optically active defects in the damaged matrix even after high temperature annealing.

Figure 3.8(a) shows the PL spectra of an SiO_2 film implanted with 120 keV Xe^+ to a dose of 3.3×10^{16}/cm^2 and annealed at 1000°C for 10 min. Upon annealing, the defect-related visible PL becomes intense, marked by a broad peak around 600 nm (2.07 eV) and 1/e PL decay time less than 400 ns at 550 nm (i.e., shorter than the experimental resolution of 400 ns). Fig. 3.8(a) also illustrates that this defect-related visible PL can be completely quenched with 3.3×10^{15}/cm^2 of deuterium. Fig 3.8(b) illustrates the same set of experiments on SiO_2 films implanted with 5×10^{16}/cm^2 of 50 keV Si^+. In addition to the defect-related PL band with 1/e PL decay time less than 400 ns at 550 nm as observed in the case of Xe^+-implanted SiO_2, the PL spectra of the Si^+-implanted SiO_2 is characterized by the emergence of another PL band around 790 nm (1.57 eV) upon annealing at 1100°C in vacuum for 10 min. And while deuterium passivation leads to a complete suppression of the defect-related PL band around 600 nm, the intensity of the "red" PL band around 790 nm does not decrease further upon increasing the deuterium dose beyond 3.3×10^{16}/cm^2.

Several trends suggest that the origin of the "red" luminescence can be attributed to radiative recombination of quantum-confined excitons. First, the value of PL decay rate measured at various energies is in qualitative agreement with theoretical predictions [5,9] for nanometer-sized Si nanocrystals. In addition to a faster component limited by the experimental resolution, a slower component attributable to Si nanocrystals was observed with a room temperature 1/e PL decay time of 45 μs, 24 μs, and 11 μs at photoluminescence energies of 1.46 eV (850 nm), 1.63 eV (750 nm), and 1.90 eV (650 nm), respectively. It will be seen in Section 3.4 that the temperature dependence of the photoluminescence intensity and photoluminescence decay rate at different energies yields the temperature dependence of radiative decay rate that further confirms the quantum confinement model.

Second, the peak energy of the "red" luminescence in deuterium passivated films containing Si nanocrystals "red shifts" as a function of annealing temperature. This is illustrated in the normalized PL spectra of Fig. 3.9 for SiO_2 implanted with $5 \times 10^{16}/cm^2$ of 50 keV Si^+ and annealed at different temperatures. All samples were deuterium passivated with an equal dose of deuterium of $3.3 \times 10^{15}/cm^2$. A clear shift in PL peak energy from 710 nm (1.75 eV) to 840 nm (1.48 eV) is observed between samples annealed at 800°C and 1200°C.

Third, the peak energy of the "red" luminescence after deuterium passivation "red shifts" also as a function of the initial excess Si concentration, i.e., the implantation dose. This is illustrated in the normalized PL spectra of Fig. 3.10 for SiO_2 films implanted with 35 keV Si^+ for three different doses, namely $2 \times 10^{16}/cm^2$,

4×10^{16}/cm^2, and 6×10^{16}/cm^2, and subsequently annealed at a fixed temperature of

1100°C. All samples were deuterium passivated with an equal dose of deuterium of

3.3×10^{15}/cm^2. A clear shift in PL peak energy from 760 nm (1.63 eV) to 810 nm

(1.53 eV) was observed between samples implanted with 2×10^{16}/cm^2 and 6×10^{16}/cm^2

Si$^+$, respectively, after annealing at 1100°C and passivated with 3.3×10^{15}/cm^2 of

deuterium.

Fourth, deuterium passivated samples display a dramatic increase in PL

intensity upon low temperature (<500°C) annealing. A schematic view of a

nanocrystal in the SiO$_2$ network and possible structural point defects that can be

passivated with hydrogen is illustrated in Fig. 3.6. As discussed in Section 3.2,

hydrogen or deuterium can passivate defects in the matrix as well as dangling bonds

at the nanocrystal/SiO$_2$ interface. It has been demonstrated in this section and in

Section 3.2 that passivation of defects in the matrix leads to quenching of the defect-

related luminescence. It has also been discussed in Section 3.2 that passivation of

dangling bonds at the nanocrystal/SiO$_2$ interface would lead to reduction of channels

for nonradiative recombination which would in turn lead to enhancement of the

luminescence. From Fig 3.8(b), it is clear that the as-implanted deuterium atoms have

enough mobility at room temperature to passivate defects in the matrix. This is

evident from quenching of the defect-related luminescence upon incorporation of

deuterium. The incorporation of deuterium at room temperature, however, does not

result in an increase of the remaining "red" luminescence attributable to Si

nanocrystals, as one might expect if the dangling bonds were being passivated at the

nanocrystal/SiO$_2$ interface. The intensity of the "red" luminescence does, however, increase dramatically upon post-deuterium passivation annealing. It appears that the deuterium atoms require an extra mobility to jump into and passivate defect sites, possibly dangling bonds at the interface, which can act as pathways for non-radiative recombination. The enhancement of the luminescence intensity illustrates that the extra mobility needed for passivation of dangling bonds can be provided by thermal annealing. The sequence of events in this two-stage defect passivation is illustrated in Fig. 3.11. The dramatic enhancement of the luminescence intensity is illustrated in Fig. 3.12 for the deuterium passivated sample of Fig. 3.8(b). Upon annealing the deuterium-implanted film at 400°C for 10 min., the intensity of the "red" luminescence increases dramatically, by more than an order of magnitude. This is consistent with the notion that passivation of dangling bonds at the nanocrystal/SiO$_2$ interface leads to enhanced radiative efficiency. The inset shows that the PL intensity increases to a maximum at post-deuterium passivation annealing temperature of 400°C and starts to decrease at higher temperatures, presumably due to the release of deuterium from defects at the nanocrystal/SiO$_2$ interface and subsequent out-diffusion from the film.
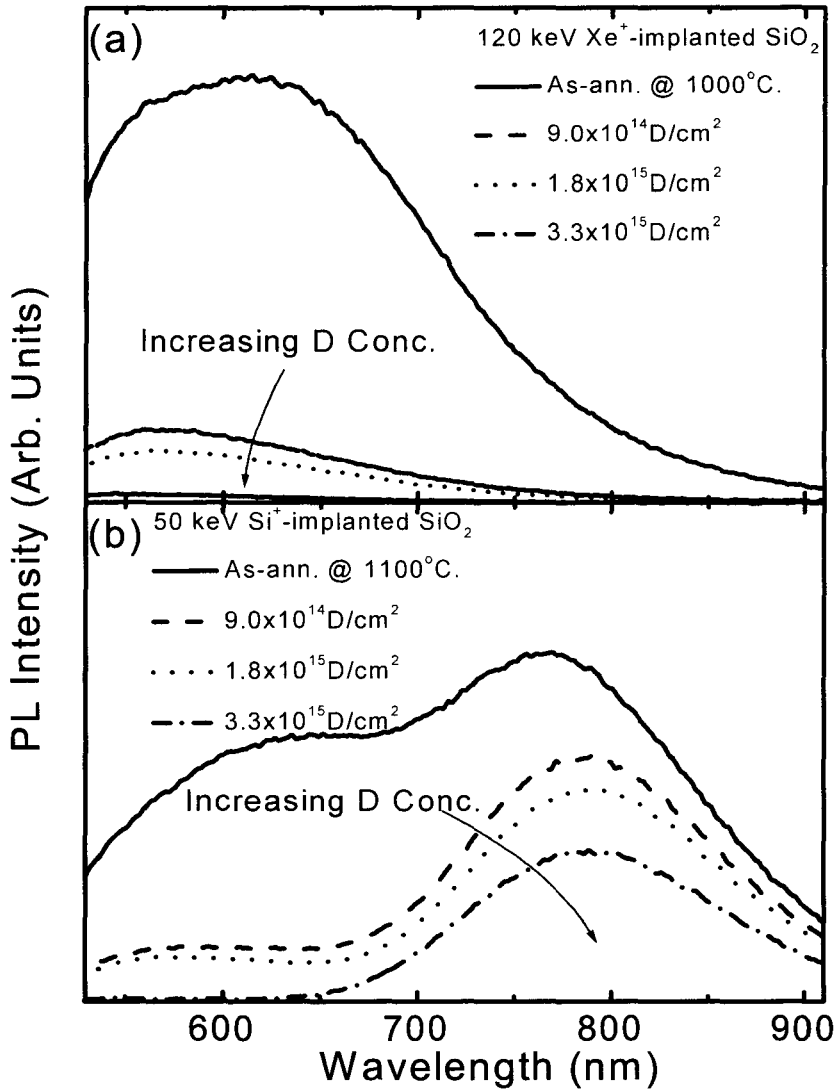
Figure 3.8. Room temperature visible photoluminescence spectra of 100 nm SiO_2 films implanted with (a) 120 keV Xe^+ to a dose of $3.3 \times 10^{16}/cm^2$ and annealed at 1000°C for 10 min., and (b) 50 keV Si^+ to a dose of $5 \times 10^{16}/cm^2$ and annealed at 1100°C for 10 min. The arrows indicate the effect of subsequent passivation with increasing doses of 600 eV deuterium.
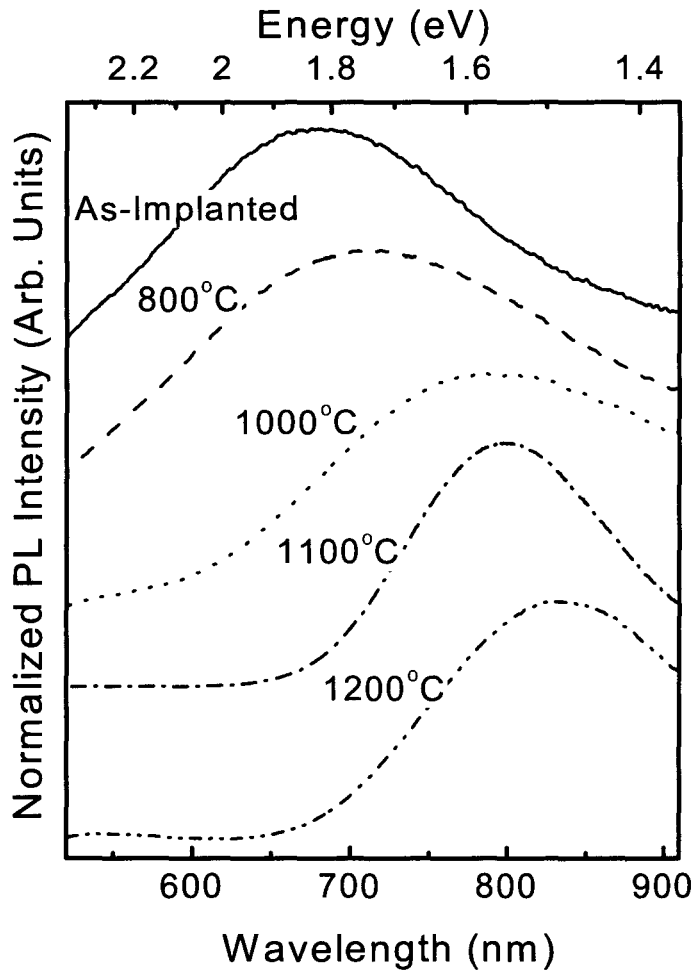
Figure 3.9. Room temperature visible photoluminescence peak energy shift as a function of annealing temperature of 50 keV Si^+-implanted 100 nm SiO_2. All samples were implanted to a dose of $5\times10^{16}/cm^2$, annealed in vacuum, and subsequently passivated with $3.3\times10^{15}/cm^2$ of deuterium to quench the defect-related photoluminescence band. All spectra are normalized.
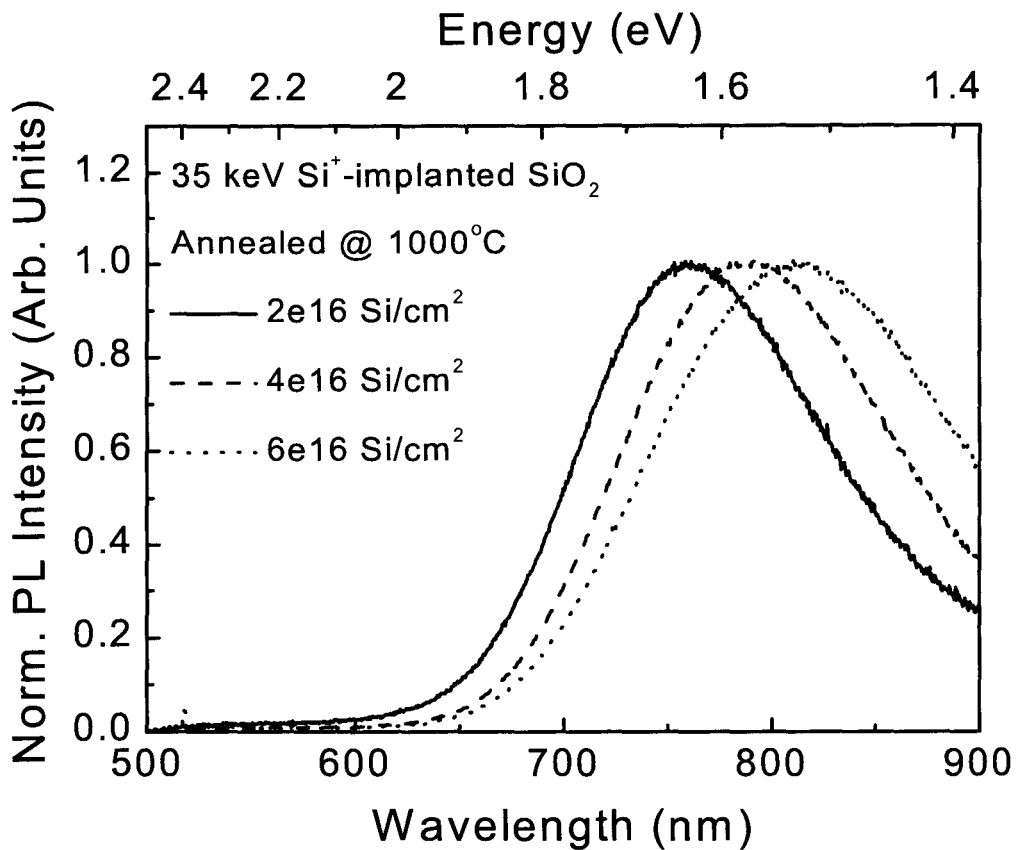
Figure 3.10. A systematic dependence of the luminescence feature attributable to Si

nanocrystals on the initial excess Si concentration, i.e., the implantation dose. The

normalized photoluminescence spectra are those of SiO_2 films implanted with 35 keV

Si^+ for three different doses, namely $2 \times 10^{16}/cm^2$, $4 \times 10^{16}/cm^2$, and $6 \times 10^{16}/cm^2$,

annealed at 1100°C, and passivated with $3.3 \times 10^{15}/cm^2$ of deuterium.
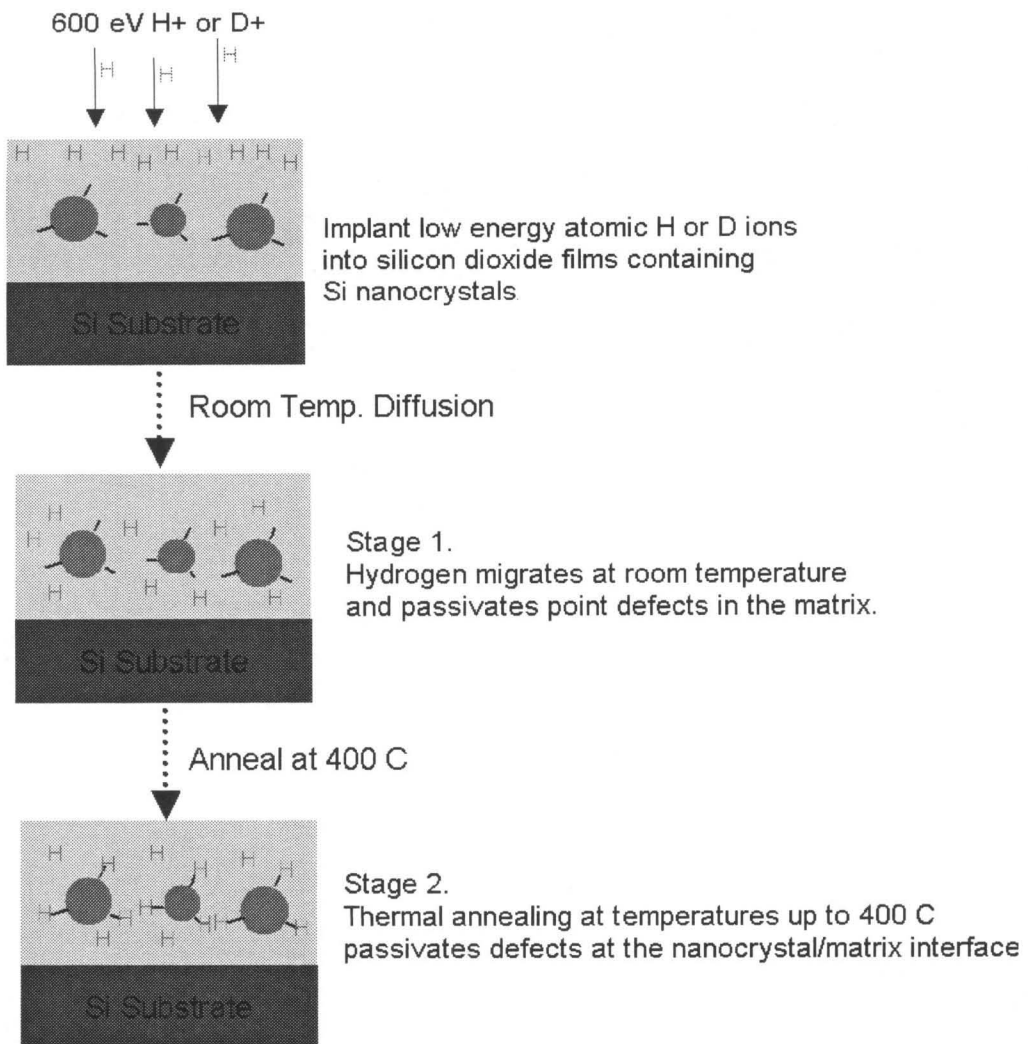
Figure 3.11. A schematic illustration of the two stages of passivation of defects in SiO$_2$ films containing Si nanocrystals. The circles represent nanocrystals and the sticks represent dangling bonds at the nanocrystal/SiO$_2$ interface. In the first stage, hydrogen migrates and passivates point defects in the matrix at room temperature. In the second stage, the extra mobility provided by thermal annealing enable passivation of dangling bonds at the interface.
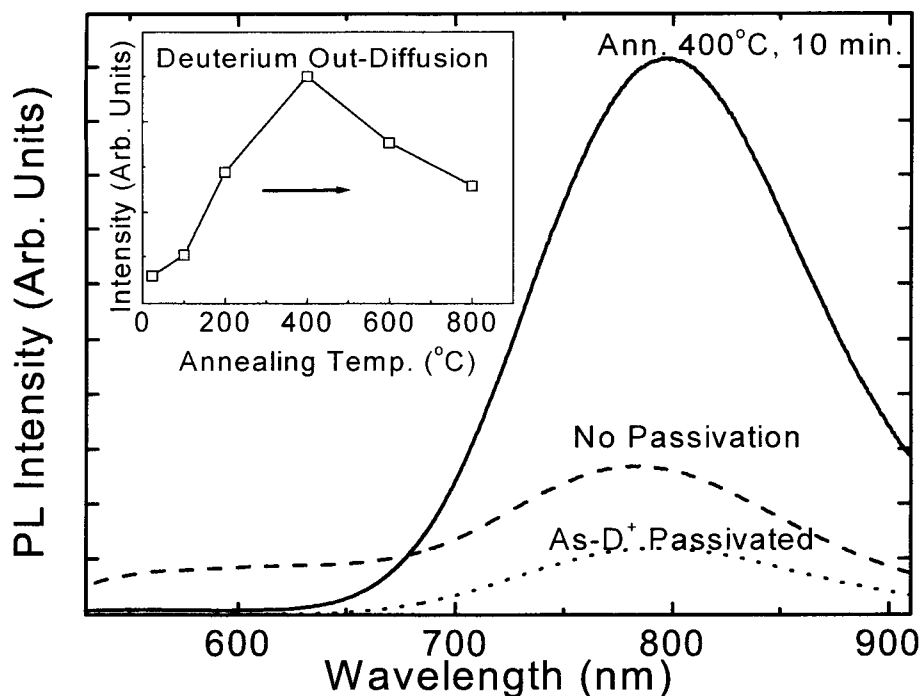
Figure 3.12. An increase in intensity of the room temperature visible luminescence feature attributable to Si nanocrystals upon post-deuteration annealing at 400°C for 10 min. The spectra are of the 100 nm SiO_2 implanted with 50 keV Si^+ to a dose of $5 \times 10^{16}/cm^2$, annealed in vacuum at 1100°C for 10 min. (dashed curve), passivated with $3.3 \times 10^{15}/cm^2$ of deuterium (dotted curve), and subsequently annealed at 400°C for 10 min. (solid curve). The initial deuterium incorporation reduces the overall intensity due to quenching of the luminescence feature around 600 nm that originates from defects in SiO_2. Subsequent post-deuteration annealing enhances the intensity by more than an order of magnitude. The intensity increases with increasing post-deuteration annealing temperature up to 400°C, after which the intensity starts decreasing due to the out-diffusion of deuterium from the film (inset).

3.4 The Spectroscopic Identification of the Luminescence Mechanism in Si Nanocrystals

Ion beam synthesized Si nanocrystals in SiO_2 provide an ideal system for the study of their size-dependent optical properties since the nanocrystals 1) generally have a wide size distribution, 2) are all close to spherical in shape, and 3) are well passivated by the SiO_2 matrix. This is in contrast to the case of porous Si, which has an irregular nanostructure and complex surface topology that makes it more difficult to study the size dependence of the optical properties [17]. Moreover, the luminescence from hydrogen terminated Si nanostructures, such as as-prepared porous Si, in general is not stable under ambient conditions at room temperature [35]. It has clearly been demonstrated in Section 3.3 that ion beam synthesized SiO_2 films containing Si nanocrystals show visible photoluminescence that can be attributed to two distinct sources [22]. It was demonstrated that the luminescence feature attributable to defects in SiO_2 can be fully quenched by introducing hydrogen or deuterium into the film, while the luminescence feature attributable to quantum-confined excitons shows a strong dependence of the emission energy on the nanocrystal size.

In this section, we present temperature dependent measurements of the photoluminescence (PL) intensity and photoluminescence decay rate of ion beam synthesized Si nanocrystals. The temperature dependence of the radiative decay rate

is determined and is well described by a model that takes into account the exchange interaction splitting of the singlet and triplet exciton energy levels [15,18]. The exchange splitting energy and the ratio of the singlet and triplet decay rates are determined as a function of emission energy.

All samples analyzed were 100 nm thick SiO_2 films implanted with 50 keV Si^+ to a dose of 5×10^{16} Si/cm^2. The films were subsequently annealed at 1100°C for 10 minutes in vacuum to induce nucleation and growth of Si nanocrystals. The presence of nearly spherical Si nanocrystals was confirmed by transmission electron microscopy in Chapter 2 (Fig. 2.5). Finally, the SiO_2 films were implanted with 3.3×10^{15} D/cm^2 at an energy of 600 eV to quench the defect luminescence, as demonstrated in the previous section [22]. PL spectra were taken using excitation with the 457 nm line of an Ar-ion laser at a power density of ~ 1 mW/mm^2. Phase sensitive detection was performed using a lock-in amplifier and acousto-optical modulation of the excitation beam at a frequency of 16 Hz. The luminescence was detected with an InGaAs photomultiplier and a grating spectrometer. The sample temperature was controlled between 12 K and 300 K in a closed-cycle He cryostat. All spectra were corrected for the system response. PL decay measurements were made after pumping to steady state with a power density of ~ 0.2 mW/mm^2, and using an InGaAs photomultiplier in combination with a multichannel photon counting system. The time resolution of the system was 400 ns.

Figure 3.13 shows PL spectra taken at 12 K, 100 K and 300 K. The spectrum at 12 K is broad (full width at half-maximum 0.28 eV) and peaks around 1.6 eV. When the temperature is raised, the peak intensity first increases with temperature up

to 100 K and then decreases again for higher temperatures. Furthermore, a clear shift of the peak position to lower energies is observed when the temperature is increased to 300 K. It is interesting to note that the overall shape of the spectrum hardly changes over this temperature range.

The spectrum is broad due to the wide distribution of nanocrystal sizes, each emitting at their characteristic, size dependent, energy. Using different model calculations of the band gap as a function of size, which are summarized in Ref. 10, the luminescence at 1.6 eV can be attributed to nanocrystals with a diameter of 3 nm–4 nm. The full spectral range from 1.4 eV–2.0 eV corresponds to a size range of about 5.5 nm–2 nm. The inset in Fig. 3.13 shows the dependence of the peak position on temperature as obtained from the PL spectra in Fig. 3.13 and other spectra taken at various temperatures in the range from 12 K–300 K (not shown in Fig. 3.13). The location of the peak positions was determined with an uncertainty of 0.01 eV by making parabolic fits to the spectra in the region of highest intensity. The peak energy decreases monotonically from 1.60±0.01 eV to 1.54±0.01 eV as the temperature is increased from 12 K to 300 K. The decrease can mainly be attributed to the decrease in the band gap energy with temperature [33]. For comparison: the band gap variation with temperature for bulk Si is 50 meV over the temperature range from 10–300 K [36].

Figure 3.14(a) shows the dependence of the integrated PL intensity on temperature. It first increases by a factor of 2 from 12 K to 100 K and then decreases by a similar amount when the temperature is increased to 300 K. The fact that the PL spectrum does not change shape, but just shifts with increasing temperature, suggests

that the temperature dependence of the emission intensity is the same for all nanocrystal sizes that contribute to the spectrum and is same as the temperature dependence of the integrated PL intensity plotted in Fig. 3.14(a).

PL decay traces at emission energies of 1.46 eV, 1.55 eV, 1.65 eV, 1.77 eV, and 1.90 eV have been measured at several temperatures in the range from 12 K to 300 K. The decay traces are not single exponential but are well described by a stretched exponential function

$$I_{PL}(t) = I_0 \exp\left[-\left(R_{PL}t\right)^{\beta}\right] \tag{3.1}$$

where I_0 is the PL intensity at t = 0, R_{PL} an effective decay rate, and β a constant between 0 and 1. A typical decay trace taken at 1.65 eV and 15 K is shown on a logarithmic scale in the inset of Fig. 3.14(b). For this trace $R_{PL} = 6.2 \times 10^2$ s^{-1} (1/R_{PL} = 1.6 ms) and β = 0.65. Figure 3.14(b) shows the temperature dependence of R_{PL} on a logarithmic scale, as obtained by fitting the decay traces taken at 1.46 eV (dots), 1.65 eV (squares) and 1.90 eV (triangles) with Eq. (3.1). The drawn lines serve to guide the eye. At each energy, R_{PL} increases by more than an order of magnitude between 12 K to 90 K. At higher temperatures R_{PL} continues to increase up to 300 K, but less rapidly.

The temperature dependence of the I_{PL} and R_{PL} (Fig. 3.14(a,b)) can be described by a model [15] that ascribes the luminescence to the recombination of strongly localized excitons in crystalline Si (see inset in Fig. 3.15). In this model the excitonic levels are split by an energy, Δ, due to the exchange interaction between the electron and hole. The lower level corresponds to a triplet state which is threefold

degenerate and has a radiative decay rate R_T. The upper level corresponds to a singlet

state and has a radiative decay rate R_S. The temperature dependence of the total

radiative decay rate, R_R, can be calculated by assuming thermal equilibrium between

the two levels:

$$R_R = \frac{3R_T + R_S \exp(-\Delta/kT)}{3 + \exp(-\Delta/kT)} \quad . \tag{3.2}$$

In general, the radiative decay competes with non-radiative decay channels (at a rate

R_{NR}) that can, for example, be provided by defects in the nanocrystal itself or at the

Si/SiO$_2$ interface. Also interaction with neighboring nanocrystals by tunneling or

dipole-dipole interaction can effectively cause non-radiative de-excitation of an

initially excited nanocrystal [37]. At the low pump power densities used, the decay of

excited electron hole pairs is unimolecular and $R_{PL} = R_R + R_{NR}$. In low-power steady

state conditions, I_{PL} is proportional to the quantum yield, $\eta = R_R/(R_R + R_{NR})$. Therefore,

by calculating the product of the measured I_{PL} and R_{PL} at each temperature, a relative

measure can be derived of the temperature dependence of R_R.

Figure 3.14(c) shows the calculated temperature dependence of R_R for

emission energies of 1.46 eV, 1.65 eV, and 1.90 eV, obtained from a multiplication of

I_{PL} (Fig. 3.14(a)) and R_{PL} (Fig. 3.14(b)). Note that, since these data are derived from

the unnormalized I_{PL}, each data set is expressed in arbitrary units and could be

multiplied by a different constant factor to facilitate easy comparison. The data in

Fig. 3.14(c) can now be fitted with Eq. (3.2) and the drawn lines show the resulting

fits. As can be seen, the temperature dependence of R_R is in excellent agreement with

this model. At low temperatures ($T\approx12$ K and kT≈1.0 meV), only the triplet state is occupied and the radiative decay rate is small. Note that the radiative decay rate of a pure triplet state would be zero as the transition is parity forbidden. However, the spin-orbit interaction slightly mixes the singlet and triplet states, making the transition weakly allowed. At higher temperatures the singlet state becomes populated and the radiative rate increases by more than an order of magnitude between 12 K and 100 K. When the temperature is increased even further, the population in the singlet state converges to its high temperature value which is equal to 1/3 of the total triplet population, and R_R is dominated by R_S. Indeed, R_R shows only a small variation with temperature for T>100 K. Note that the data for 1.46 eV, 1.65 eV and 1.90 eV show a slightly different behavior which can be explained by differences in the values of R_T, R_S, and Δ, as will be shown below.

Figure 3.15(a) shows the ratio of R_S to R_T as a function of emission energy obtained by fitting Eq. (3.2) to the temperature dependent data of R_R shown in Fig. 3.14(c) and to data taken at other energies (not shown). At all energies, R_S is 300–800 times larger than R_T. The triangles in Fig. 3.15(b) show the dependence of the exchange splitting energy, Δ, on the emission energy, E. The value of Δ increases monotonically from 8.4 meV to 16.5 meV between E=1.46 eV and E=1.90 eV, corresponding to a nanocrystal size range of about 5.5 nm–2 nm. For reference, we also plot values obtained for porous Si for E=1.7 eV to 2.0 eV [15,18]. These seem to follow a trend that is similar to our data. This is an interesting observation since both the shapes of the Si nanostructures and the dielectric constant of the host material are different for porous Si and our nanocrystals. Apparently, the magnitude of Δ is

basically determined by the value of the emission energy. It should be noted that for

bulk Si (E=1.1 eV), the exchange splitting is estimated to be smaller than 0.15 meV

[38]. For a spherical crystallite with a diameter of 3 nm (emission energy $\approx$1.8 eV)

effective mass theory predicts Δ=13.9 meV [15], in good agreement with the data in

Fig. 3.15(b). The values of Δ found in this work are much smaller than the 71 meV

that was reported earlier for oxidized Si nanocrystals [39]. In that case the

luminescence was thought to originate from states at the Si/SiO_2 surface. By

passivating our samples with deuterium, all luminescence features arising from

defects were quenched, so that all PL data thus obtained can be attributed purely to

quantum-confined excitons.
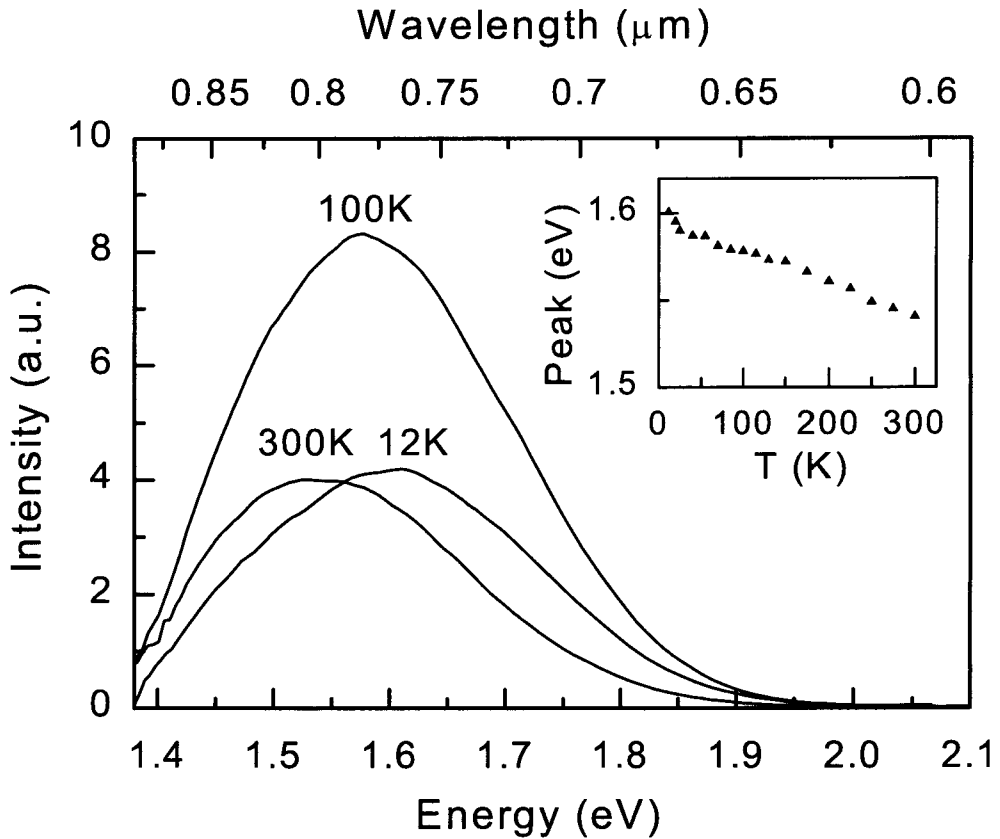
Figure 3.13. Photoluminescence spectra taken at 12 K, 100 K, and 300 K of 100 nm

SiO_2 film containing Si nanocrystals with a broad size distribution. The SiO_2 films

were implanted with 50 keV Si^+ to a dose of $5 \times 10^{16}/cm^2$, annealed at 1100°C for 10

min., and subsequently passivated with $3.3 \times 10^{15}/cm^2$ of deuterium. The inset shows

the peak energy of these spectra and other spectra (not shown) taken at various

temperatures in the range of 12 K–300 K.
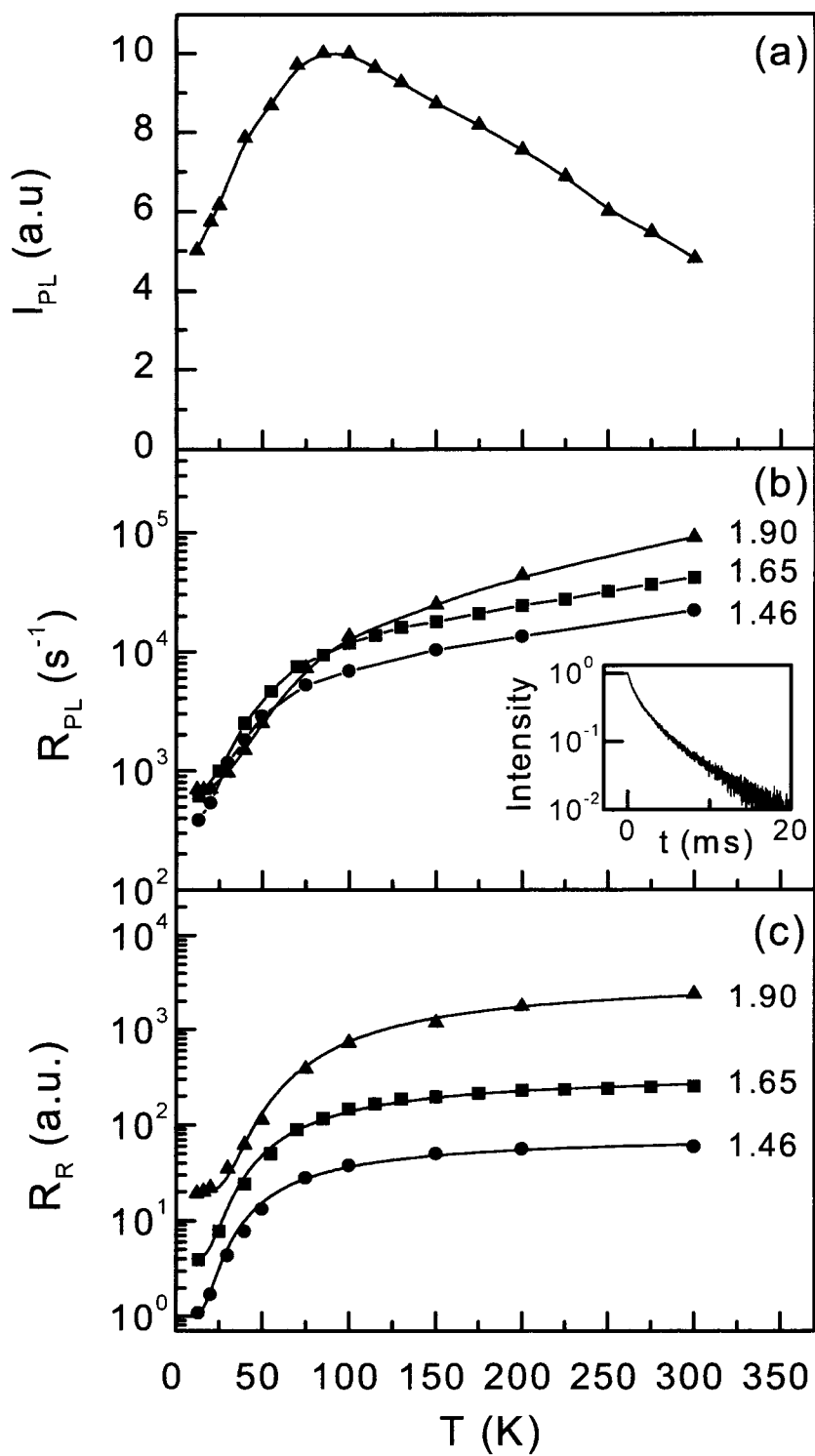
Figure 3.14. (a) Temperature dependence of the integrated photoluminescence intensity, I_{PL}, of Si nanocrystals in SiO_2. The solid line serves to guide the eye. (b) Temperature dependence of the photoluminescence decay rate, R_{PL}, on a logarithmic scale, measured at emission energies of 1.46 eV, 1.65 eV, and 1.90 eV. The solid lines through the data serve to guide the eye. The inset shows a typical decay trace taken at 1.65 eV and 15 K on a logarithmic intensity scale. (c) Calculated relative temperature dependence of the radiative rate at emission energies of 1.46 eV, 1.65 eV, and 1.90 eV, obtained from a multiplication of the temperature dependent I_{PL} data in (a) and R_{PL} data in (b). Each data set is expressed in arbitrary units and was multiplied by a different constant factor to facilitate easy comparison. The solid curves are best fits of a model that takes into account the exchange splitting of the energy levels of quantum-confined excitons in the Si nanocrystals.
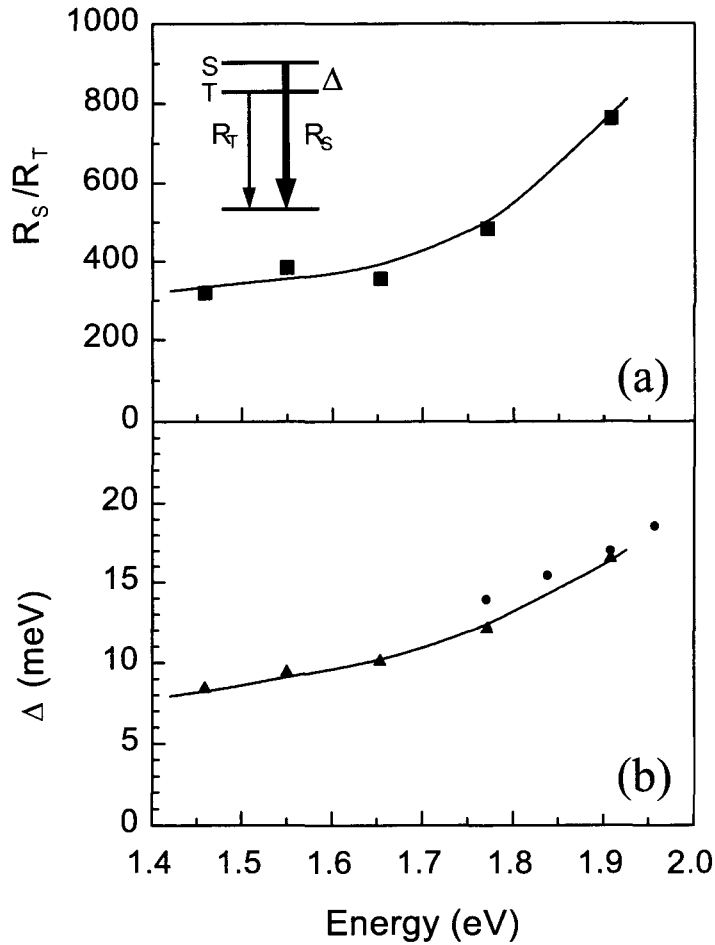
Figure 3.15. (a) Ratio of the singlet (R_S) and triplet (R_T) decay rates of quantum-

confined excitons in Si nanocrystals as a function of the emission energy. The inset

shows a schematic of the singlet and triplet energy levels, split by the electron-hole

exchange energy Δ. (b) Exchange energy as a function of the emission energy. The

triangles are obtained from the measurements described in this letter and, for

comparison, the dots represent values of Δ obtained for porous Si taken from Ref. 15.

The values of R_S/R_T and Δ were determined by fitting Eq. (3.2) to the temperature

dependence of the radiative rate shown in Fig. 3.14(c). The solid lines through the

data serve to guide the eye.

3.5 Conclusions

In summary, ion beam synthesized SiO_2 films containing Ge or Si nanocrystals exhibit strong room temperature visible photoluminescence. Due to the presence of irradiation-induced defects that display visible luminescence, the interpretation of luminescence spectra requires a clear distinction of the contribution from defects. A hydrogen passivation technique has been developed to selectively quench the defect-related luminescence and therefore allow for a clear distinction between different origins of the visible luminescence.

For the case of SiO_2 films containing Ge nanocrystals, the measured photoluminescence peak energy and photoluminescence decay rates show poor correlation with nanocrystal size compared to theoretical predictions for radiative recombination of quantum-confined excitons in Ge quantum dots. These observations strongly suggest that the observed visible luminescence in the films cannot be attributed to radiative recombination of quantum-confined excitons in Ge nanocrystals. Instead, observations of similar luminescence in Xe^+-implanted SiO_2 and reversible photoluminescence quenching by hydrogen or deuterium suggests that radiative defect centers in the SiO_2 matrix are responsible for the observed luminescence.

For the case of SiO_2 films containing Si nanocrystals, two sources of room temperature visible luminescence are identified. From a similar comparison of photoluminescence spectra and photoluminescence decay rate measurements between

Xe^+-implanted SiO_2 films and SiO_2 films containing Si nanocrystals, a luminescence feature attributable to defects in the SiO_2 matrix is unambiguously identified. Deuterium passivation of the films allows for selective quenching of the luminescence originating from defects in the matrix, after which the presence of a luminescence feature attributable to Si nanocrystals is evident, with $1/e$ photoluminescence decay times on the order of tens of microseconds. The peak energy of the remaining luminescence feature attributable to Si nanocrystals "red shifts" as a function of different processing parameters that lead to an increase in the average nanocrystal size. An additional mobility provided to deuterium atoms by means of low temperature ($<500°C$) annealing enables passivation of defects at the nanocrystal/SiO_2 interface, which leads to an enhancement of the photoluminescence intensity that originates from Si nanocrystals. In sum, by selective quenching of the defect-related luminescence using a hydrogen passivation technique, a systematic study of the "red" luminescence has been performed to conclusively determine whether or not the origin of visible photoluminescence can be attributed to radiative recombination of quantum-confined excitons in Si nanocrystals.

Further confirmation of the quantum confinement model for the Si nanocrystals comes from the temperature dependence of the photoluminescence intensity and the photoluminescence decay rate. Ion beam synthesized Si nanocrystals offer an ideal system for studying quantum size effects on the photoluminescence spectrum due to the presence of a distribution of particle size. The measured temperature dependence of the photoluminescence intensity and decay

rate for the analyzed size range is in agreement with a model that takes into account the size-dependent exciton exchange splitting between the singlet and triplet states.

The fact that visible photoluminescence attributable to quantum confined excitons has been observed from Si nanocrystals but not Ge nanocrystals is not surprising when one considers the superiority of the Si/SiO_2 interface over the Ge/GeO_2 or Ge/SiO_2 interfaces. The fact that SiO_2 forms one of the best interfaces with Si with a very low density of dangling bonds is the key reason behind the success of Si as material of choice in the microelectronics industry.

Bibliography

[1]   R.A. Soref, Proceedings of the IEEE, **81**, 1687 (1993).

[2]   K.D. Hirschman, L.Tsybeskov, S.D. Duttagupta, and P.M. Fauchet, Nature **384**, 338 (1996).

[3]   Y. Kanemitsu, Physics Reports **263**, 1 (1995).

[4]   L.T. Canham, Appl. Phys. Lett. **57**, 1046 (1990).

[5]   M. Hybertson, Phys. Rev. Lett. **72**, 1514 (1994).

[6]   N.A. Hill and K.B. Whaley, Phys Rev. Lett. **75**, 1130 (1995); N.A. Hill and K.B. Whaley, private communication, for Ge nanocrystals.

[7]   L.W. Wang and A. Zunger, J. Phys. Chem. **98**, 2158 (1994).

[8]   C. Delerue, G. Allan, and M. Lannoo, Phys. Rev. **B 48**, 11024 (1993).

[9]   T. Takagahara and K. Takeda, Phys. Rev. **B 46**, 15578 (1992).

[10] R.T. Collins, P.M. Fauchet, and M. Tischler, Physics Today, January 1997, p. 24.

[11] Y. Kanemitsu, H. Uto, Y. Matsumoto, and Y. Maeda, Appl. Phys. Lett. **61**, 2187 (1992).

[12] Y. Maeda, Phys. Rev. **B 51**, 1658 (1994).

[13] D.C. Paine, C. Caragianis, T.Y. Kim, Y. Shigesato, and T. Ishahara, Appl. Phys. Lett. **62**, 2842 (1993).

[14] H.A. Atwater, K.V. Shcheglov, S.S. Wong, K.J. Vahala, R.C. Flagan, M.L. Brongersma, and A. Polman, Mat. Res. Soc. Symp. Proc. **316**, 409 (1994).

[15] P.D.J. Calcott, K.J. Nash, L.T. Canham, M.J. Kane, and D. Brumhead, J. Phys. Condens. Matter **5**, L91 (1993).

[16] L.E. Brus, P.F. Szajowki, W.L. Wilson, T.D. Harris, S. Schuppler, and P.H. Citrin, J. Am. Chem. Soc. **117**, 2915 (1995).

[17] S. Schuppler, S.L. Friedman, M.A. Marcus, D.L. Adler, Y.H, Xie, F. M. Ross, T.D. Harris, W.L. Brown, Y.L. Chabal, L.E. Brus, and P.H. Citrin, Phys. Rev. Lett. **72**, 2648 (1994).

[18] P.D.J. Calcott, K.J. Nash, L.T. Canham, M.J. Kane, and D. Brumhead, Journ. of Lumin. **57**, 257 (1993).

[19] T. S-Iwayama and S. Nakao and K. Saitoh, Appl. Phys. Lett. **65**, 1814 (1994).

[20] P. Mutti, G. Ghislotti, S. Bertoni, L. Bonnoldi, G.F. Cerofolini, L. Meda, E. Grilli, and M. Guzzi, Appl. Phys. Lett. **66**, 851 (1995).

[21] H.M. Cheong, W. Paul, S.P. Withrow, J.G. Zhu, J.D. Budai, C.W. White, and D.M. Hembree, Jr., Appl. Phys. Lett. **68**, 87 (1996).

[22] K.S. Min, K.V. Shcheglov, C.M. Yang, H.A. Atwater, M.L. Brongersma, and A. Polman, Appl. Phys. Lett. **69**, 2033 (1996).

[23] L. Skuja, J. Non-Cryst. Solids **179**, 51 (1994).

[24] K. Awazu, K.Muta, and H. Kawazoe, J. Appl. Phys. **74**, 2237 (1993).

[25] K.S. Seol, A. Ieki, Y. Ohki, H. Nishikawa, and M. Tachimori, J. Appl. Phys. **79**, 412 (1996).

[26] K.S. Min, K.V. Shcheglov, C.M. Yang, H. A. Atwater, M.L. Brongersma, and A. Polman, Appl. Phys. Lett. **68**, 2511 (1996).

[27] J.F. Ziegler, J.P. Biersack, and U. Littmark, *The Stopping and Range of Ions in*

Solids, Pergamon, New York, 1985.

[28]   J.I. Pankove and M.L. Tarng, Appl. Phys. Lett. **34**, 156 (1979).

[29]   J.H. Stathis and M.A. Kastner, Phys. Rev. **B 29**, 7079 (1984).

[30]   S.M. Prokes, W.E. Carols, and O.J. Glembocki, Phys. Rev. **B 50**, 17 093 (1994).

[31]   D.L. Griscom, J. Appl. Phys. **58**, 2524 (1985).

[32]   See, for example, J. I. Pankove and N.M. Johnson, ed., *Semiconductors and Semimetals* **34**, Academic Press, Inc., San Diego, 1991, Chapters 3-7.

[33]   J. Pankove, Optical Processes in Semiconcductors, Dover Publications, Inc., New York, 1971, pp. 27-28.

[34]   G.W. Arnold, J. of Non-Cryst. Solids **179**, 288 (1994).

[35]   M.A. Tischler, R.T. Collins, J.H. Stathis, and J.C. Tsang, Appl. Phys. Lett. **60**, 639 (1992).

[36]   S.M. Sze, *Physics of semiconductor devices* (John Wiley & Sons, New York, 1981).

[37]   M.J.A. De Dood, M.L. Brongersma, P.G. Kik, A. Polman, and H.A. Atwater to be published.

[38]   J.-C. Merle, M. Capizzi, P. Fiorini, and A. Frova, Phys. Rev. B **17**, 4821 (1978).

[39]   Y. Kanemitsu, Phys. Rev. B **53**, 13515 (1996).

Chapter 4

Engineering the Depth Distribution of Ion Beam Synthesised Si Nanocrystals and Tuning the Emission Energy of Visible Luminescence

4.1 Introduction

The discovery of visible light emission from group IV nanocrystals has stimulated considerable experimental effort to understand the origin and mechanism

of luminescence and to develop Si-based opto-electronic devices [1-5]. Among different experimental synthesis techniques, ion beam synthesis [6-11] of Si nanocrystals in thermal SiO_2 films has an important advantage: the processes involved in the synthesis are fully compatible with the standard integrated circuit technology. In addition, the SiO_2 matrix is mechanically robust and provides a superior nanocrystal/SiO_2 interface that leads to high quantum efficiency.

It has been demonstrated in Chapter 3 that ion beam synthesized Si nanocrystals in SiO_2 display photoluminescence in the visible and near-infrared that can be attributed to two distinct sources [9]. One luminescence feature is related to ion irradiation-induced defects in the SiO_2 matrix and can be quenched by passivating with hydrogen or deuterium. The other has been attributed to radiative recombination of quantum-confined excitons in Si nanocrystals. The luminescence from quantum-confined excitons has been shown to continuously red-shift as a function of increasing average nanocrystal size. It has also been shown that the nanocrystal luminescence intensity can be increased by more than an order of magnitude by post-hydrogen passivation annealing at 400°C, which leads to passivation of dangling bonds at the nanocrystal/SiO_2 interface.

The photoluminescence (PL) spectra are broad due to the presence of a wide distribution of nanocrystal sizes, in agreement with quantum confinement theories that predict a size-dependent band gap [12,13]. If the Si ion implantation is performed with single ion energy, it will yield a Gaussian concentration depth profile of excess Si. As the nucleation and growth rates of Si nanocrystals from a

supersaturated solid solution are strongly dependent on the local degree of supersaturation, the nanocrystal size is depth-dependent.

In order to engineer the optical properties of the SiO_2 films containing Si nanocrystals, it is very important to understand the size distribution of nanocrystals as a function of film depth. In the first part of this chapter, depth-resolved measurements of the photoluminescence of SiO_2 films containing Si nanocrystals have been performed to determine the depth distribution of optically active Si nanocrystals. By chemical etching through the SiO_2 film in steps and analyzing the changes in the PL spectrum after each etch step, the depth from which each of the two luminescence features originate is determined. In the second part of this chapter, a method is presented by which the luminescence energy can be continuously tuned throughout the visible spectrum by thermal oxidation of the films so as to induce a reduction of the average size. Thermal annealing the SiO_2 films containing Si nanocrystals in flowing O_2 at 1000°C for up to 30 min. results in oxidation of the Si nanocrystals, first close to the SiO_2 film surface and later at greater depths. Upon oxidation for 30 min., the photoluminescence peak wavelength blue-shifts by more than 200 nm. This blue-shift is unambiguously identified with the quantum size effect in which a reduction of the average nanocrystal size leads to emission at shorter wavelengths [12,13].

4.2 Depth Distribution of Optically Active Si Nanocrystals in SiO_2

For application of Si nanocrystals dispersed spatially in SiO_2 with a distribution of sizes as light-emitting structures [2-5], single-electron memories [14], or optical storage devices, it is essential to have information on the nanocrystal size distribution as a function of depth. High-resolution transmission electron microscopy (TEM) has been used in Chapter 2 (Fig. 2.5) to verify the presence and crystallinity of Si nanocrystals. Due to low contrast between small Si nanocrystals and the amorphous SiO_2, however, quantitative information on the size distribution of particles is limited and can lead to underestimation of the particle density of small particles less than about 1.5 nm. This is especially true since the presence of small nanocrystals has been inferred from X-ray photoelectron spectra (Fig. 2.6) of samples annealed at temperatures as low as 600°C and 800°C, where transmission electron microscopy yields very little information. Furthermore, transmission electron microscopy and X-ray photoelectron spectroscopy only provide structural information and do not reveal information about the distribution of optically active nanocrystals.

In this section, the depth distribution of luminescent nanoparticles is determined by analyzing changes in the PL spectra as the SiO_2 film is etched in a layer-by-layer fashion. It is found that the luminescence at the long wavelength side of the spectrum (emitted by the largest nanocrystals) mainly originates from the center region of the SiO_2 film, in agreement with the results from TEM. Surprisingly, a

large contribution to the luminescence from small nanocrystals not detectable by TEM is found near the surface and near the SiO_2/Si interface. It was also found that the defect luminescence that is often found in Si implanted SiO_2 films originates from the near-surface region.

A 100 nm thick SiO_2 film grown by wet thermal oxidation of a lightly B-doped (100) Si wafer was implanted at room temperature with 35 keV Si^+ to a dose of 6×10^{16} Si/cm^2. The films were subsequently annealed at 1100°C for 10 minutes in high vacuum at a base pressure of 1×10^{-7} torr to induce nucleation and growth of Si nanocrystals [9]. Cross-sectional transmission electron microscopy was performed using a 300 keV electron microscope under slightly defocused conditions to enhance the contrast between the Si nanocrystals and the SiO_2 matrix. The SiO_2 films containing Si nanocrystals were subsequently etched off in a series of etch steps of 10 seconds each, using buffered hydrofluoric acid at room temperature. Rutherford backscattering spectrometry was used to determine the Si concentration depth profiles after each etch step. A 2 MeV He^+ beam was used at an angle of 4° off the sample normal and a scattering angle of 92°. The depth resolution was 10 nm. Room temperature PL spectra were taken using excitation with the 514 nm line of an Ar^+ ion laser at a power density of ~10 mW/mm^2. The angle between the randomly polarized laser beam and the sample normal was 30°. The luminescence was detected by a grating spectrometer in combination with a thermoelectrically cooled Si CCD detector array. All spectra were corrected for the system response. PL decay measurements were made at 15 K after pumping to steady state with a power density of ~ 0.2

mW/mm^2. The pump light was chopped with an acousto-optic modulator and the lifetime traces were taken with a GaAs photomultiplier in combination with a multichannel photon counting system. The time resolution of the system was 400 ns.

4.2.1   Si Concentration Depth Profile and Etch Rate

The successive layer-by-layer film removal by chemical etching is schematically illustrated in Fig. 4.1. It has been shown from photoluminescence measurements in Chapter 3 (Fig. 3.10) that the average nanocrystal size is dependent on the implantation dose, i.e., on the initial excess Si concentration. Since the single-energy ion implantation produces a Gaussian distribution of excess Si concentration, the resulting particle size distribution is expected to be somewhat similar; i.e., the center of the film with highest excess Si concentration is expected to contain the largest nanocrystals. Therefore, initial removal of the top layers will result in an overall increase in the average particle size because smaller particles are removed. As the etch front passes the depth of peak Si concentration, the average particle size starts decreasing.

Figure 4.2 shows Si concentration depth profiles of the Si$^+$-implanted and annealed SiO$_2$ film on Si after several etch times ranging from 0 sec. to 120 sec., as indicated in the figure.   The depth profiles were derived from Rutherford backscattering spectra taking into account the depth dependent electronic energy loss calculated from the relative Si/SiO$_2$ concentrations using Braggs-rule and assuming a

volume averaged density of Si (ρ=5.0x10^{22} Si/cm^3) and SiO$_2$ (ρ=2.27x10^{23} SiO$_2$/cm^3). The depth scales for the concentration profiles are each shifted so that the SiO$_2$/Si interface is located at the same depth for all samples. The concentration profile of the as-implanted (unannealed) film (not shown) is nearly identical to that of the annealed film. The spectrum before etching, indicated by '0', shows the Si concentration profile with a peak Si concentration of 49 atomic percent at a depth of ≈45 nm below the sample surface. Near the surface the Si concentration is 33 atomic percent, corresponding to that of stoichiometric SiO$_2$. The SiO$_2$/Si interface is located at a depth of ≈112 nm. Note that the Si concentration depth profile in the SiO$_2$ film is not Gaussian, as predicted by a Monte Carlo calculation (TRIM '97) [15], and shows a relatively high Si concentration (≈42 atomic percent) near the SiO$_2$/Si interface. The asymmetric shape of the profile could be the result of sputtering during the Si implantation, which progressively reduces the thickness of the film. The total sputtered layer thickness was estimated to be ≈10 nm [15]. The concentration profiles obtained after etching for 10 sec., 20 sec., 40 sec., 60 sec., 80 sec., 100 sec., and 120 sec. clearly demonstrate that etching for progressively longer times reduces the SiO$_2$ film thickness further and further until the Si substrate is reached after 120 sec.

Figure 4.3 shows the etch depth as a function of time as obtained from the Si concentration profiles shown in Fig. 4.2. The drawn curve is a guide for the eye. The etch rate, as determined from the slope of this curve, varies from 1.3 nm/sec. in the regions with small excess Si to 0.6 nm/sec. at the peak of the Si concentration profile.

An etch rate retardation has been observed before for Si-rich oxides with much higher

Si supersaturation than in the present experiments [16].
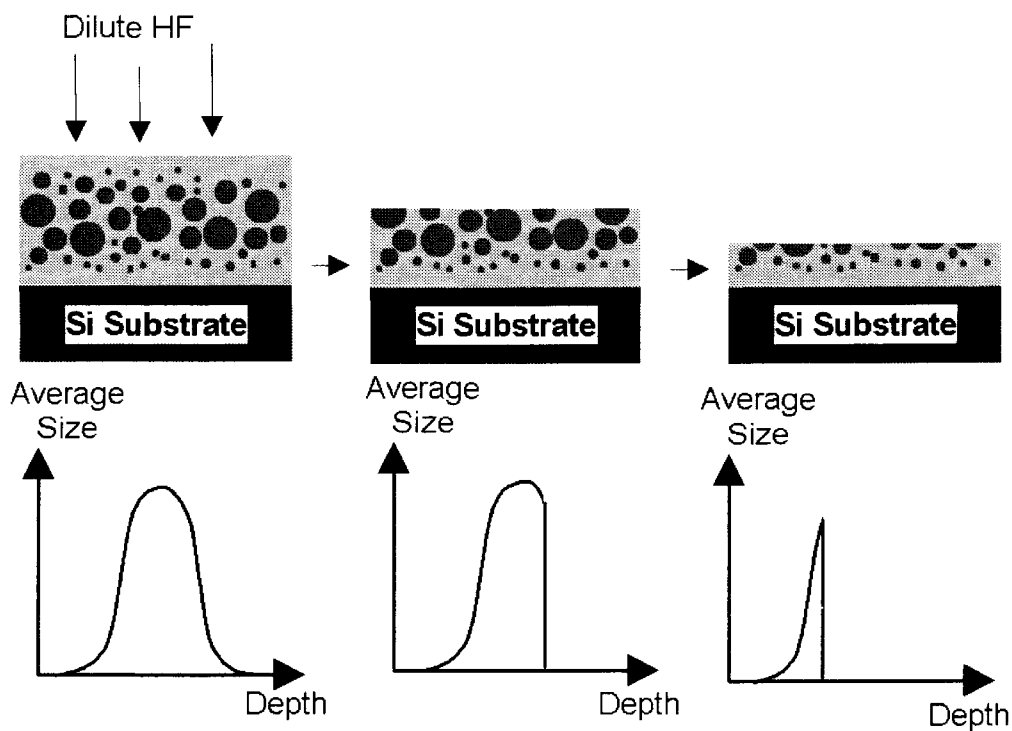
Figure 4.1. A schematic illustration of successive film removal by etching (top) and the resulting change in the size distribution (bottom). The average particle size is larger near the center of the film and as a result, as the film starts to be removed from the top, the average size first increases and then decreases.
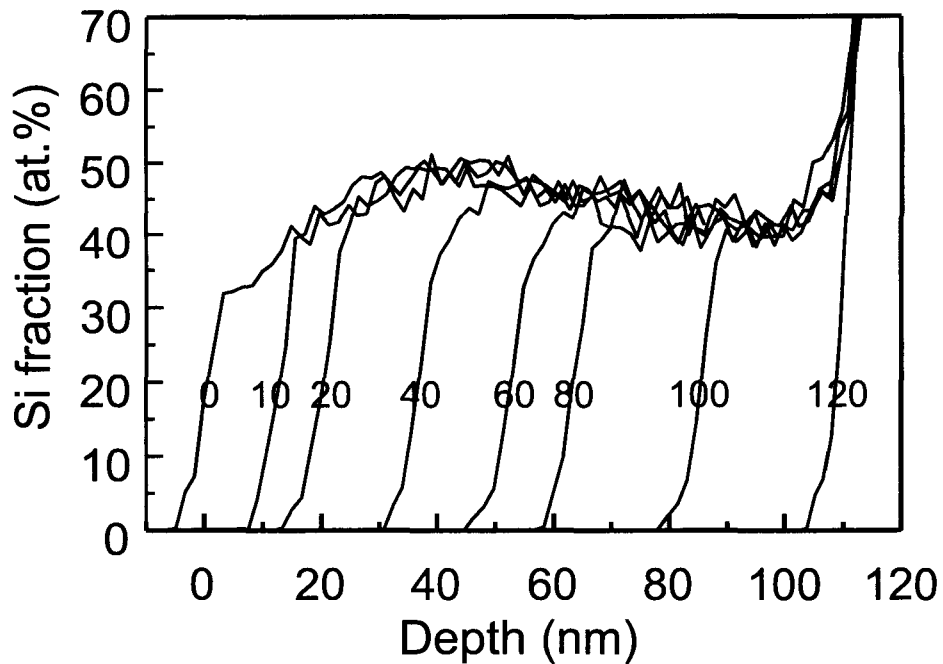
Figure 4.2.   Si concentration as a function of depth in SiO$_2$ films containing Si

nanocrystals after successive film removal in buffered hydrofluoric acid for times

ranging from 0 to 120 sec. The Si nanocrystals in SiO$_2$ are made by implantation of

35 keV Si$^+$ to a dose of 6×10^{16} Si/cm^2, and annealing at 1100°C for 10 minutes.

The depth scales are all shifted such that the SiO$_2$/Si interface is located at a depth

of 112 nm.   The profiles were calculated from Rutherford backscattering spectra

taken with a 2 MeV He$^+$ beam at an angle of 4° off the sample normal and a

scattering angle of 92°.
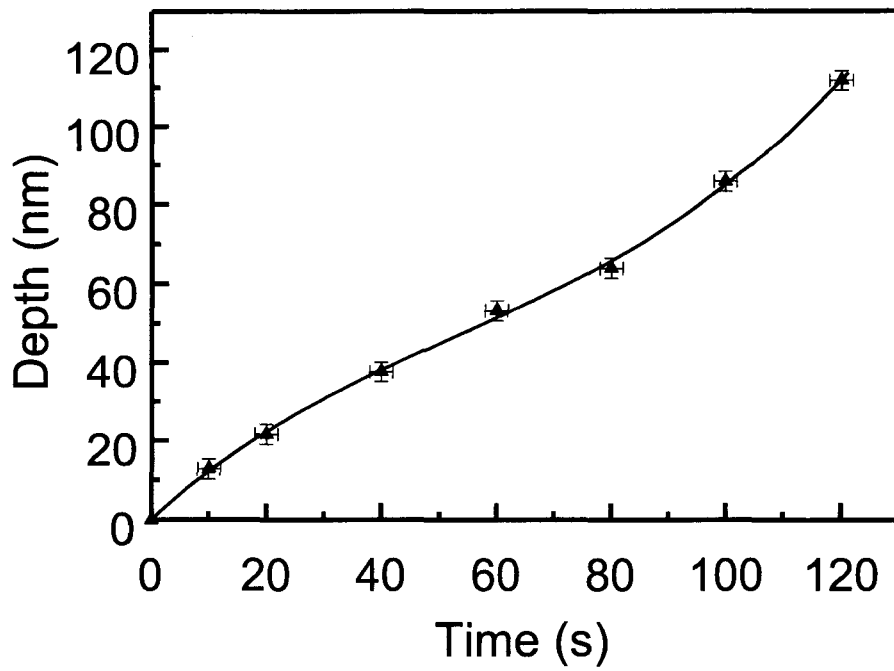
Figure 4.3. Etch depth as a function of time as obtained from the Si concentration

profiles shown in Fig. 4.2. The drawn curve serves as a guide to the eye.

4.2.2 Depth Distribution of Luminescent Si Nanocrystals

Figure 4.4(a) shows room temperature PL spectra obtained from the annealed Si^+- implanted SiO_2 film before and after etching for several times up to 120 sec. Before etching, the spectrum ranges from 500 nm to well beyond 900 nm. This corresponds to emission from nanocrystals with diameters of ≈ 1.5 nm and larger [17]. The spectrum peaks at 790 nm, corresponding to a nanocrystal diameter of ≈ 3 nm–4 nm [17]. For increasing etch time, the overall PL intensity decreases continuously. Furthermore, the spectral shape and the peak position also change after each etch step. For example, after etching for 10 sec.–40 sec., mostly components of the 500 nm–800 nm part of the spectrum disappear, causing an apparent red-shift of the peak position. For longer etch times, the spectral region from 800 nm–900 nm shows a decrease as well. The fact that a small luminescence signal remains after 120 sec. must mean that there are still some luminescent nanocrystals left on the substrate after the whole oxide layer is etched off.

Figure 4.5 shows two normalized luminescence decay traces at 650 nm, measured at 15 K before and after etching for 10 sec., and plotted on a logarithmic intensity scale. The trace taken before etching clearly shows two components with substantially different lifetimes. This is in agreement with previously obtained results, where two luminescence sources were identified in SiO_2 films containing Si nanocrystals made by ion implantation [9]. One broad luminescence feature peaking

at 600 nm was shown to be related to ion irradiation induced defects and has a 1/e PL decay time shorter than 400 nanoseconds. The other was attributed to radiative recombination of quantum-confined excitons in the Si nanocrystals with a 1/e PL decay time on the order of 1.0 milliseconds at 15 K. After etching for 10 sec., the short PL decay time component disappears. It is therefore concluded that the defect luminescence originates from the first etched layer, an approximately 15 nm-thick region near the surface. This is corroborated by the data in Fig. 4.4(a), which shows that the PL intensity around 600 nm, attributed to defect luminescence, completely disappears after etching for 10 sec. The fact that these luminescent defects are located in the near surface region indicates that they are either preferentially formed near or at the SiO_2 surface or in regions with a low Si supersaturation. PL decay time measurements (not shown) indicate that the defect luminescence is negligible at wavelengths longer than 700 nm.

After etching off the top part of the film that contained most of the luminescent defects, the decrease in PL intensity that was observed for longer etch times must be due to the removal of luminescent nanocrystals. Since the luminescence wavelength depends on the size of the nanocrystals, removal of nanocrystals of a particular size will result in a decrease in the PL intensity at the wavelength corresponding to that size. For example, a decrease in intensity at short and long wavelength side of the spectrum corresponds to the removal of a layer containing small and large nanocrystals, respectively. At each wavelength the concentration of luminescent nanocrystals as a function of depth, $n_\lambda(x)$, can then be

calculated from the decrease in PL intensity observed after each etch step. In the calculation of $n_\lambda(x)$ from the difference PL spectra, two correction factors should be taken into account. First, from the Si depth profiles in Fig. 4.2 it is clear that each etch step did not remove the same amount of material and this should be taken into account. Second, it should be realized that due to internal reflections of the pump light at the SiO_2/air and the SiO_2/Si interface, a standing light wave builds up in the SiO_2 film. This implies that nanocrystals located at different depths are not excited with the same intensity. A calculation of the pump intensity as a function of depth in the SiO_2 film before etching is shown as an inset in Fig. 4.4(b). Input parameters for this calculation are the SiO_2 film thickness of 112 nm and an average effective refractive index of the nanocrystal containing SiO_2 film of 1.65, as calculated by Maxwell Garnett theory [18]. The peak intensity is normalized to 1 and, as can be seen in the inset, the intensity varies by a factor 6.6 over the SiO_2 film thickness. For the determination of $n_\lambda(x)$, both the calculated shape of the pump intensity profile in the SiO_2 film and the changes that occur in this profile as the film gets thinner after each etch step were taken into account.

Figure 4.4(b) shows the corrected difference spectra of Fig. 4.4(a), numbered according to the layer that was etched off. For each etch step one can now clearly see in which part of the spectrum the luminescence decreases and thus whether small or large nanocrystals were removed. For example, the largest decrease in the PL intensity at wavelengths shorter than 700 nm occurs during the first (1) and last (6)

etch step. This means that almost all the small luminescent nanoparticles are located near the SiO$_2$ film surface or close to the SiO$_2$/Si interface.

Figure 4.6(a) shows a histogram of the depth dependence of the concentration of nanocrystals exhibiting luminescence at 700 nm, n_{700}, as obtained from the six difference spectra in Fig. 4.4(b). The distribution of relatively large nanocrystals emitting at 900 nm is shown in Fig. 4.6(b). The highest concentration of these nanocrystals is found in the center of the film, where the excess Si concentration is highest. For comparison, Fig. 4.6(c) shows the excess Si concentration as a function of depth before etching, as obtained from Fig. 4.2. Figure 4.6(d) shows a bright-field cross-sectional TEM image of the film. Despite the weak mass-thickness contrast between the Si and SiO$_2$, it shows Si particles in the size range of 2-5 nm. As can clearly be seen, the largest nanocrystals are mainly located near the center of the film, in agreement with the results obtained for n_{900} in Fig. 4.6(b). Because of the small size, it is very difficult to observe individual nanocrystals near the surface or near the Si/SiO$_2$ interface under TEM; nevertheless, the data in Fig. 4.6(a) indicate that the number density of nanocrystals emitting at 700 nm is indeed high. Also, it is noteworthy that the relative scales of $n_{700}(x)$ and $n_{900}(x)$ may not be compared directly, as nanocrystals of different sizes have different optical excitation cross sections and luminescence efficiencies.

The observation that the luminescence from small nanocrystals originates mainly from the near surface region and the region near the Si/SiO$_2$ interface is very intriguing. It has important consequences for engineering Si nanocrystal size

distributions in general. The origin of this peculiar distribution may be related to the nanocrystal size distribution itself, or to variations in the luminescence efficiency across the film, as will be discussed below.

From recent experiments [19,20] it is known that the local average nanocrystal size increases with Si supersaturation, in agreement with classical particle coarsening theory. This would explain that small nanocrystals are only found in the region with low supersaturation, i.e., near the surface. However, this argument does not explain the high density of small nanocrystals near the SiO_2/Si interface as the excess Si concentration in that region is high (8 atomic percent) compared to the surface region (see Fig. 4.6(c)). It may be that near the SiO_2/Si interface the nanocrystals are within the Si diffusion length from the Si substrate that acts as a sink due to the Gibbs-Thompson effect [21], which could result in the alteration of the local nanocrystal nucleation and growth kinetics such that relatively large amounts of small nanocrystals are formed. The Gibbs-Thompson effect [21] predicts a much higher equilibrium solubility of solute atoms in a spherical precipitate with a small radius of curvature compared to that with a large radius of curvature, and therefore higher local solute concentration near the small precipitate. So provided that the Si substrate, with an infinite radius of curvature, and the Si nanocrystal, with a small radius of curvature, are within the diffusion length, the higher local Si concentration near the nanocrystal compared to the interface region will result in a mass transfer from the nanocrystal to the Si substrate due to a concentration gradient. The diffusion length of Si in SiO_2 at 1100°C is a few nanometers for diffusion time of 10 min. [19].

Therefore, Si atoms are expected to migrate from the nanocrystals to the Si substrate, preventing the growth of the nanocrystals despite the high local concentration due to the net flux. Indeed, such an effect due to the Gibbs-Thompson effect has been observed for the case of Ge^+-implanted SiO_2 films where Ge atoms from the initial implantation profile diffuse towards the Si substrate, resulting in a relatively high concentration of Ge near (≈ 10 nm) the SiO_2/Si interface without significant growth of the naoncrystals [22,23]. The observation of Gibbs-Thompson effect is expected in the Si-Ge system because the two elements form an isomorphous binary solid solution. As one expects similar kinetics for the implanted Si atoms, surfaces and interfaces may be used in the future to tailor size distributions of Si nanocrystals in SiO_2.

An alternative explanation for the observed lack of luminescence from small nanocrystals near the center of the film could be the result of optical interactions between the nanocrystals. The high nanocrystal density at the center of the film might induce excitation migration due to dipole-dipole interaction or charge exchange [24-27]. In this process, migration only takes place from small nanocrystals (large bandgap) to large nanocrystals (small bandgap). As a result, luminescence from small nanocrystals would be quenched in the center of the film. Time-resolved PL experiments, published elsewhere [20], are consistent with this excitation migration model.
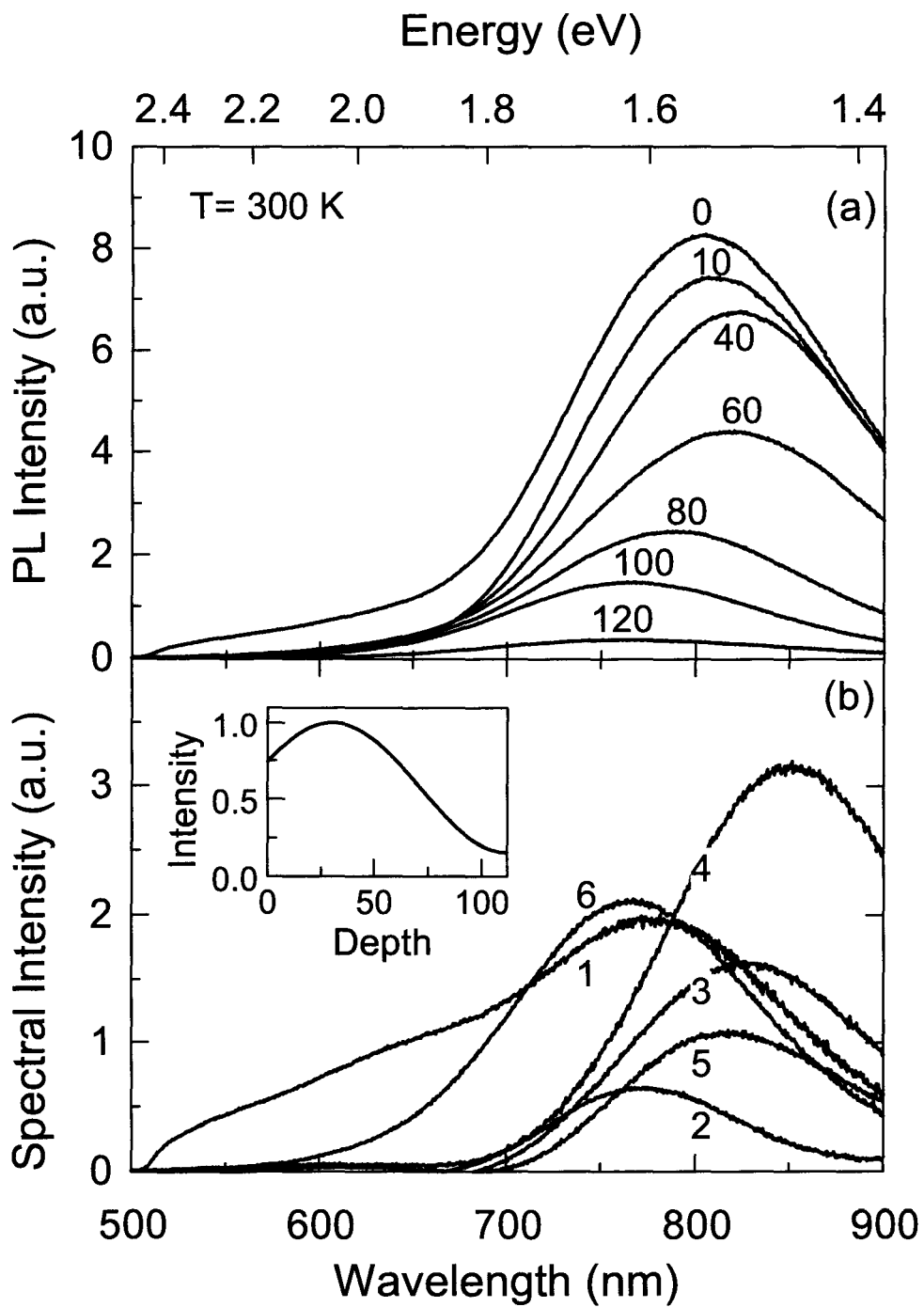
Figure 4.4.   (a) Room temperature PL spectra (λ_{pump} = 514 nm) obtained from

SiO_2 films containing Si nanocrystals, after etching in buffered HF for times ranging

from 0 to 120 sec. (b) The difference spectra obtained by subtracting the PL spectra

for subsequent etch steps in (a), and corrected in such a way that the spectral intensity

at a fixed wavelength is proportional to the average concentration of nanocrystals

emitting at that wavelength. The inset shows the pump intensity profile as a function

of depth in the SiO_2 film, resulting from internal reflections of the pump light at the

SiO_2/Si interface and SiO_2/air interface.
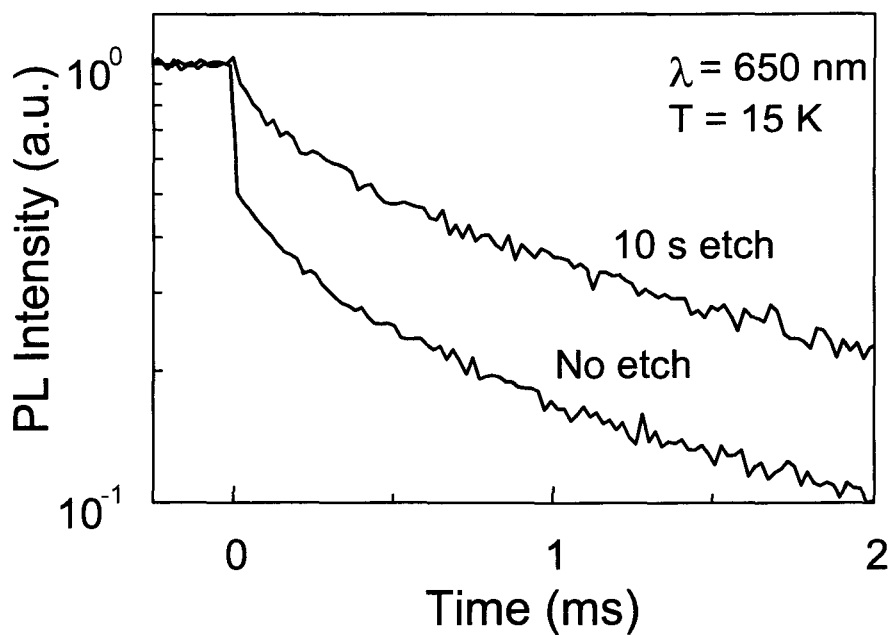
Figure 4.5.   Two luminescence decay traces taken at 15 K and 650 nm from the

nanocrystal containing SiO_2 films before and after etching for 10 sec. in buffered

HF, and plotted on a logarithmic scale. The pump beam at 514 nm was switched off

at time = 0 sec.
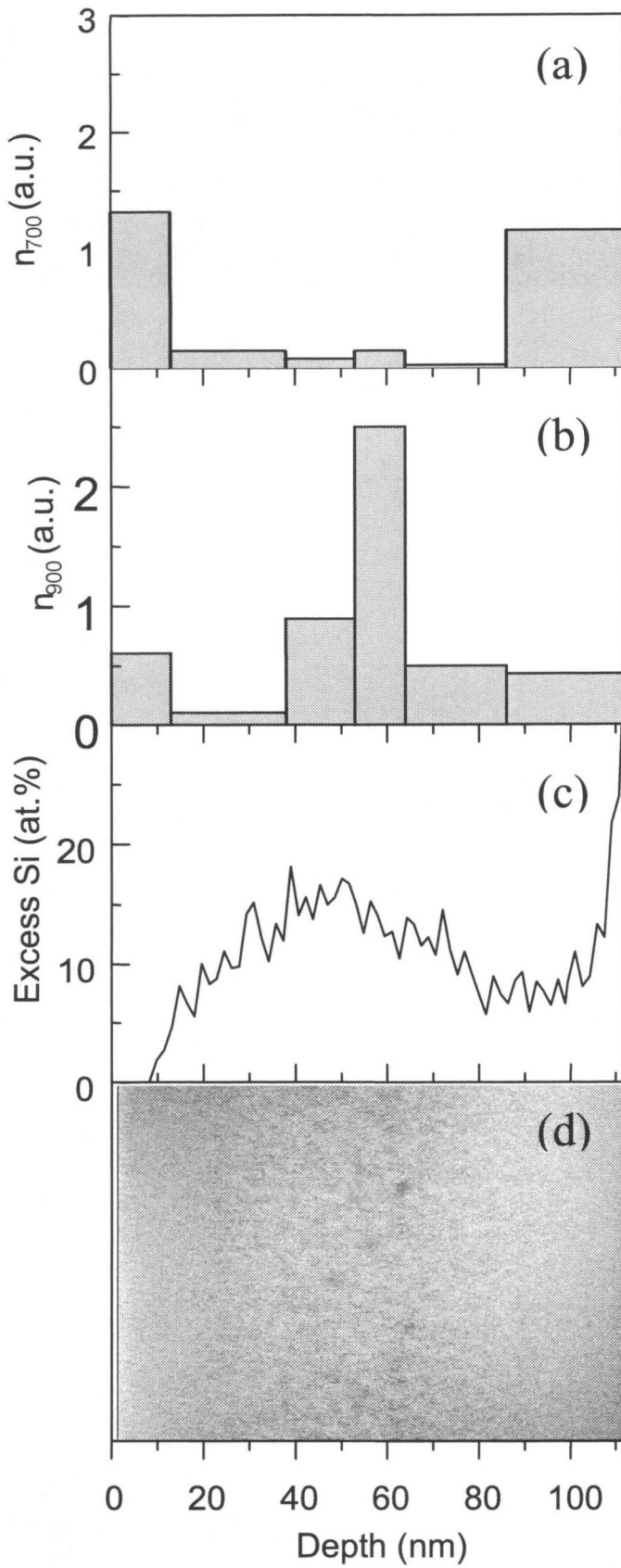
Figure 4.6   Histogram of the depth-dependent number density of optically active

Si nanocrystals emitting (a) at $\lambda = 700$ nm and (b) at $\lambda = 900$ nm, obtained from the

data in Fig. 4.4(b). (c) The concentration of excess Si in the SiO_2 film as calculated

from Fig. 4.2. (d) Bright-field cross-sectional TEM image of the SiO_2 film containing

Si nanocrystals.

4.3. Tuning the Emission Energy of Si Nanocrystals by Oxidation

In order to take advantage of quantum confinement effects to tune the emission energy of the Si nanocrystals, the size distribution must be tailored. In this section, a method is presented by which the luminescence energy can be continuously tuned throughout the visible spectrum by thermal oxidation, which induces a reduction of the average Si nanocrystal size in SiO_2 films. By inducing a reduction in average Si nanocrystal size by thermal oxidation at 1000°C, the photoluminescence (PL) peak wavelength from Si nanocrystals embedded in SiO_2 films can be blue-shifted by more than 200 nm. Transmission electron microscopy and Rutherford backscattering spectrometry measurements show the oxidation of Si particles starts near the surface of the SiO_2 film and as time progresses, an oxidation front moves deeper into the film. The blue-shift in PL peak energy is attributed to a decrease in the average nanocrystal size as the oxidation progresses, in agreement with quantum confinement theory.

SiO_2 films (100 nm thick) grown by wet thermal oxidation of lightly p-doped (100) Si wafers were implanted at room temperature with 35 keV Si^+ to a dose of $6 \times 10^{16}/cm^2$, resulting in a Si concentration at the peak of the implantation profile of 44 atomic percent, as determined by Rutherford backscattering spectrometry. These samples were subsequently annealed at 1100°C for 10 minutes in vacuum at a base pressure of 1×10^{-7} torr to induce nucleation and growth of Si nanocrystals [9].

Oxidation was performed in flowing O_2 (flow rate = 47 sccm.) at 1000°C and at 1 atm. for times ranging from 0 to 30 minutes. Finally, 600 eV all samples were deuterium passivated to quench the defect-related luminescence by means of deuterium implantation using a Kauffman ion source [9], and the Si nanocrystal luminescence intensity was optimized by a subsequent anneal at 400°C for 10 minutes. Cross-sectional bright-field transmission electron microscopy was performed to determine the presence and the distribution of the nanocrystals in the oxide film. Rutherford backscattering spectrometry was performed to determine the Si depth profile using a 2 MeV He^+ beam at a scattering angle of 93° and an angle of 3° between the sample normal and the incident He^+ beam. The depth resolution was 10 nm. Room temperature photoluminescence (PL) spectra were taken using the 457.9 nm line of an Ar^+ ion laser at a pump power density of 10 mW/mm^2 and detected by a grating spectrometer in combination with a thermoelectrically cooled Si CCD detector array. All spectra were corrected for the system response. Photoluminescence decay time measurements were made after pumping to a steady state with a power density of 0.2 mW/mm^2. The pump light was chopped with an acousto-optic modulator and the lifetime traces were taken with a GaAs photomultiplier in combination with a multichannel photon counting system. The time resolution of the setup was 400 ns.

4.3.1   Oxidation of Si Nanocrystals in SiO$_2$

The effect of annealing the SiO$_2$ film containing Si nanocrystals in oxygen ambience is schematically presented in Figure 4.7. Oxygen diffuses into the film and induces oxidation of the Si nanocrystals in a layer-by-layer fashion, leaving stoichiometric SiO$_2$ behind as the oxidation front moves into the film.

Figure 4.8(a) shows a bright field cross-sectional transmission electron micrograph of the Si$^+$-implanted SiO$_2$ film after annealing in vacuum at 1100°C. Despite the weak mass-thickness contrast between Si and SiO$_2$, it shows a dense array of Si particles distributed throughout the whole thickness of the oxide film. The presence of larger particles near the center of the film is clearly evident, compared to regions near the surface and near the Si/SiO$_2$ interface. This is attributed to the fact that implantation produces a Gaussian shaped Si concentration depth profile with a peak excess concentration of Si in the center of the oxide film. It has been demonstrated in Chapter 2 (Fig. 2.5) that these Si nanocrystals are single-crystalline using high-resolution transmission electron microscopy [9].

Figure 4.8(b) shows a cross-sectional bright-field transmission electron micrograph of the identical sample after receiving an additional oxidation annealing treatment at 1000°C for 15 minutes. The image was taken in a slightly defocused condition to enhance the Fresnel contrast so as to highlight the oxidation front. The arrow indicates the oxidation front, or the depth to which oxidation of nanocrystals

has taken place. In the first ~60 nm region from the surface all nanocrystals have been oxidized into SiO_2, while the rest of the film (~40 nm) closer to the SiO_2/Si substrate interface clearly shows the presence of nanocrystals. It is clear that the oxidation occurs in a layer-by-layer as depicted in Fig. 4.7, as opposed to all nanocrystals throughout the film thickness being oxidized simultaneously.

Figure 4.9 shows the Rutherford backscattering spectra of the as-annealed SiO_2 film containing Si nanocrystals before oxidation (indicated by a "0") and after annealing in flowing oxygen at 1000°C for 3, 6, 10, 15, and 30 min. The surface channel for Si in SiO_2 is indicated by an arrow. The Si depth profile of the as-annealed film before oxidation shows a peak concentration of 44 atomic percent at roughly 40 nm below the surface. It can be clearly seen that the oxidation of Si nanocrystals starts at the surface and as time progresses, the oxidation front moves deeper into the film. After three minutes, the oxidation front has reached a depth of 50 nm and the Si concentration near the surface is approximately 33 atomic percent, i.e., the Si concentration is that of stoichiometric SiO_2. Upon further oxidation the oxidation front moves more slowly but steadily deeper into the film and after 30 minutes the whole film is reconverted into stoichiometric SiO_2. It should be noted that the width of the oxidation front is much wider than the RBS depth resolution ($\approx$10 nm), indicating that a relatively wide nanocrystal-containing region is being oxidized at the same time.
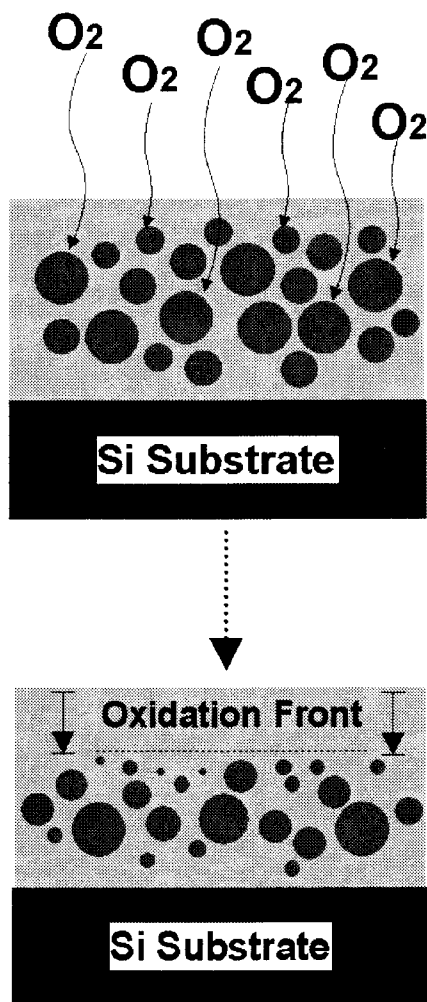
Figure 4.7. A schematic illustration of oxidation of SiO_2 films containing Si nanocrystals. The oxidation proceeds in a layer-by-layer fashion, leaving behind stoichiometric SiO_2 the oxidation front.
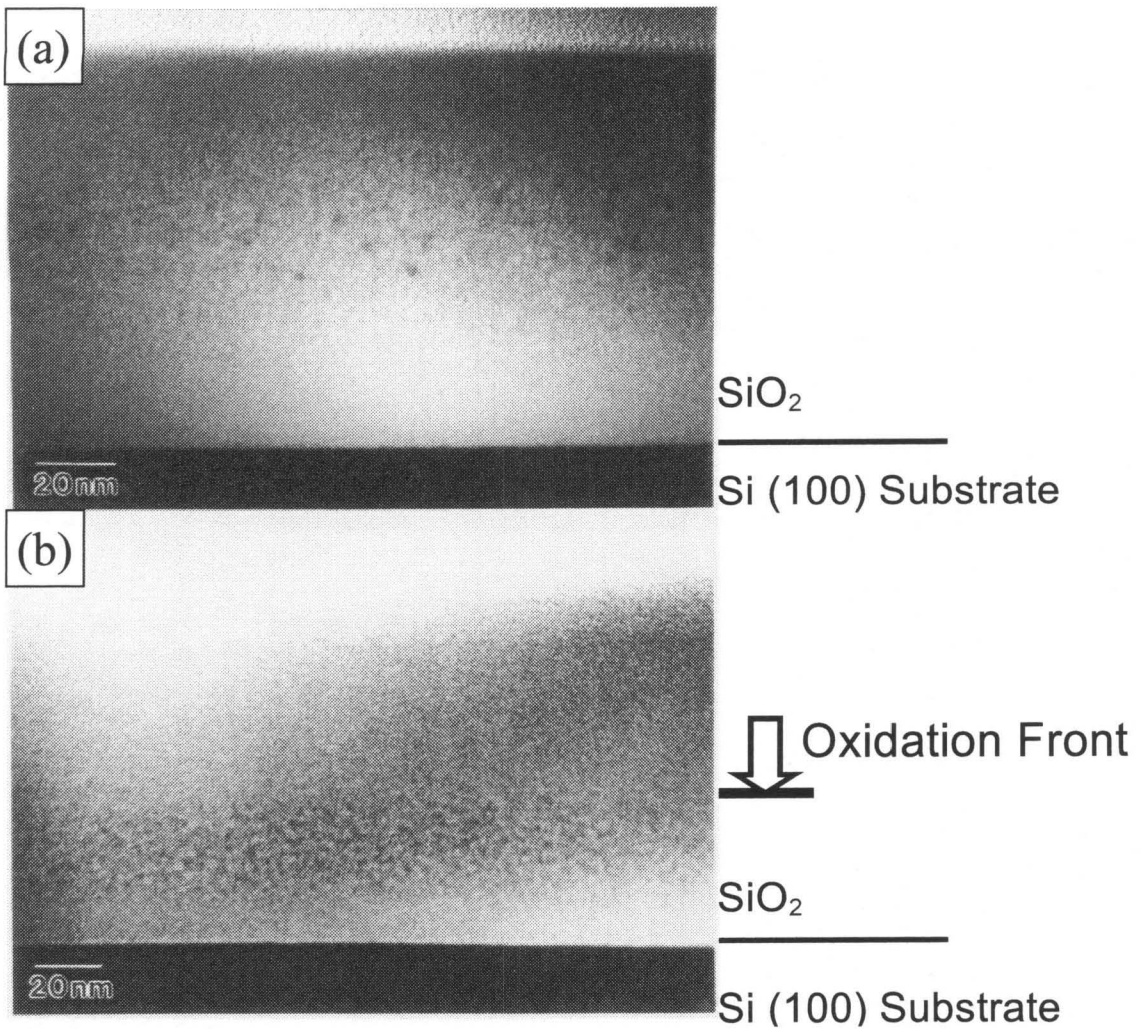
Figure 4.8. (a) Cross-sectional bright field transmission electron micrograph of 100 nm SiO_2 film containing Si nanocrystals made by implantation of 35 keV Si^+ to a dose of 6×10^{16} Si/cm^2 and subsequent annealing at 1100°C for 10 min. The center of the film clearly shows bigger particles; (b) The same sample after annealing in O_2 at 1000°C for 15 min. An oxidation front is clearly shown, where indicated by the arrow.
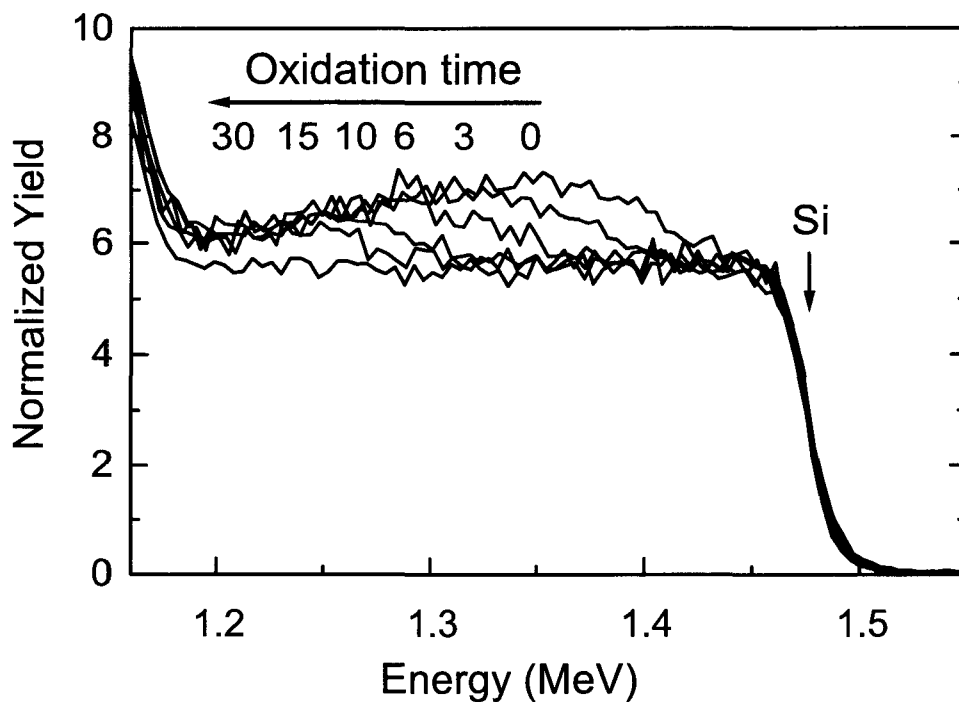
Figure 4.9. Rutherford backscattering spectra of 100 nm thick SiO_2 films implanted with 6×10^{16} Si/cm^2, annealed at 1100°C for 10 min., and subsequently oxidized at 1000°C for 0, 3, 6, 10, 15, and 30 minutes. The oxidation times are indicated at the peak of the Si depth profile of the corresponding spectrum. The horizontal arrow indicates the direction in which the oxidation front moves. The Si surface channel is also indicated by an arrow.

4.3.2   Continuous Tuning of the Emission Energy of Si Nanocrystals by Oxidation

Figure 4.10 shows the room temperature PL spectra of the films taken before and after oxidation for 3, 10, 15, 20, 25 and 29 min., plotted on a logarithmic intensity scale. The PL spectrum of the unoxidized sample ("0") shows a broad peak centered around 880 nm, in agreement with the estimated recombination energy for quantum-confined excitons in a ≈ 3 nm diameter Si nanocrystal [12] corresponding to about 700 atoms per crystal. The width of the emission band is attributed to a wide distribution in nanocrystal sizes [4,12]. It can be seen in Fig. 4.10 that the intensity increases over the whole wavelength region by a factor of ≈ 1.5 after 3 min. oxidation, and then decreases for longer oxidation times. Furthermore, oxidation leads to a continuous blue-shift of the spectrum. After oxidation for 29 min., the emission peaks at 680 nm. Taking into account the tails of the spectra, this oxidation technique can be used to tune the luminescence from 500 nm (green) all the way to the bandgap of bulk Si at 1.11 μm. An emission wavelength of 500 nm corresponds to a crystal diameter of ≈ 1 nm (≈ 26 atoms) [12].

In the case of a system of non-interacting Si nanocrystals, the luminescence intensity at each wavelength is determined by the number density of Si nanocrystals, the absorption cross-section, and the radiative efficiency. Nanocrystals exhibiting luminescence at different wavelengths will have different absorption cross-sections as the absorption cross-section depends on the size. However, at a fixed wavelength,

changes in the PL intensity can directly be translated into a change in the number density of optically active nanocrystals of a particular size. Since the total number of nanocrystals decreases upon oxidation, the initial intensity increase observed after 3 min. oxidation must be attributed to an increase in the luminescence efficiency. It is known that Si nanocrystals made by thermal annealing of a Si-rich oxide have a suboxide layer between the nanocrystal and the SiO_2 matrix [28] that could give rise to nonradiative decay channels for quantum confined excitons. The oxidation treatment might remove these nonradiative decay channels (and thus increase the luminescence efficiency) by making the nanocrystal surroundings more stoichiometric. The Rutherford backscattering spectra in Fig. 4.9 show that after 3 min. oxidation, half of the Si profile is affected by the oxidation, resulting in possible changes in the luminescence efficiency for all nanocrystal sizes, as observed. The overall decrease in the intensity observed for longer oxidation times is attributed to three effects: 1) a decrease in the number density of Si nanocrystals; 2) a decrease in the absorption cross-section for optical excitation with decreasing nanocrystal size [12]; 3) the oxidation process that may yield nanocrystals that do not exhibit luminescence.

According to quantum confinement theories, the bandgap of Si nanocrystals increases with decreasing nanocrystal size [12,13]. Comparing the luminescence spectra for 3, 10, and 15 min., it can be seen that the intensity <u>decreases</u> at wavelengths longer than 740 nm, while it <u>increases</u> for shorter wavelengths. This behavior can be explained in terms of a shift of the nanocrystal size distribution to

smaller sizes due to the oxidation process, as indicated schematically in the inset of Fig. 4.10. The number density of nanocrystals emitting at shorter wavelengths than 0.74 μm increases due to oxidation of larger nanocrystals emitting at longer wavelengths. After oxidation for 15 min., when nearly all the large nanocrystals in the center of the oxide film have been oxidized (as indicated by the transmission electron micrograph in Fig. 4.8 and Rutherford backscattering spectra in Fig. 4.9), the intensity at the long wavelength side of the PL spectrum (> 950 nm) has decreased by more than an order of magnitude. For longer oxidation times (20 min., 25 min., and 29 min.) the PL spectra continue to shift towards the blue, indicating a further decrease in the average size of the nanocrystals exhibiting luminescence. Eventually, after oxidation for 30 min., all nanocrystals have been oxidized and no PL can be observed.

Figure 4.11 shows normalized room temperature PL decay traces taken at 700 nm from some of the samples that were shown in Fig. 4.10. A stretched exponential function: $I(t) = exp(-t/\tau)^\beta$, was fitted to the data, in which τ is an effective 1/e PL decay time, and β is a constant between 0 and 1. For the unoxidized sample we find $\tau=12$ μs and $\beta=0.63$. Upon oxidation τ and β monotonously increase up to values of $\tau=43$ μs and $\beta=0.79$ for 29 min. oxidation.

A 1/e PL decay time on the order of tens of μs is indicative of the fact that the Si nanocrystals behave as an indirect bandgap semiconductor, as is expected for nanocrystals exhibiting luminescence at this wavelength [4,12]. Stretched exponential decay of the luminescence is commonly observed for Si nanocrystals in

an oxide matrix, porous Si, and other materials that are disordered or inhomogeneous on the microscopic scale [3,4]. In the ideal case of non-interacting nanocrystals that can only decay radiatively, a single exponential decay is expected, i.e., $\beta=1$. The experimental fact that $\beta<1$ demonstrates that interaction between neighboring nanocrystals, or between nanocrystals and defect-states may play an important role in the PL behavior. The increase in both τ and β then shows that upon oxidation the nanocrystals emitting at 700 nm more and more approach the ideal case of a collection of non-interacting radiatively decaying nanocrystals.
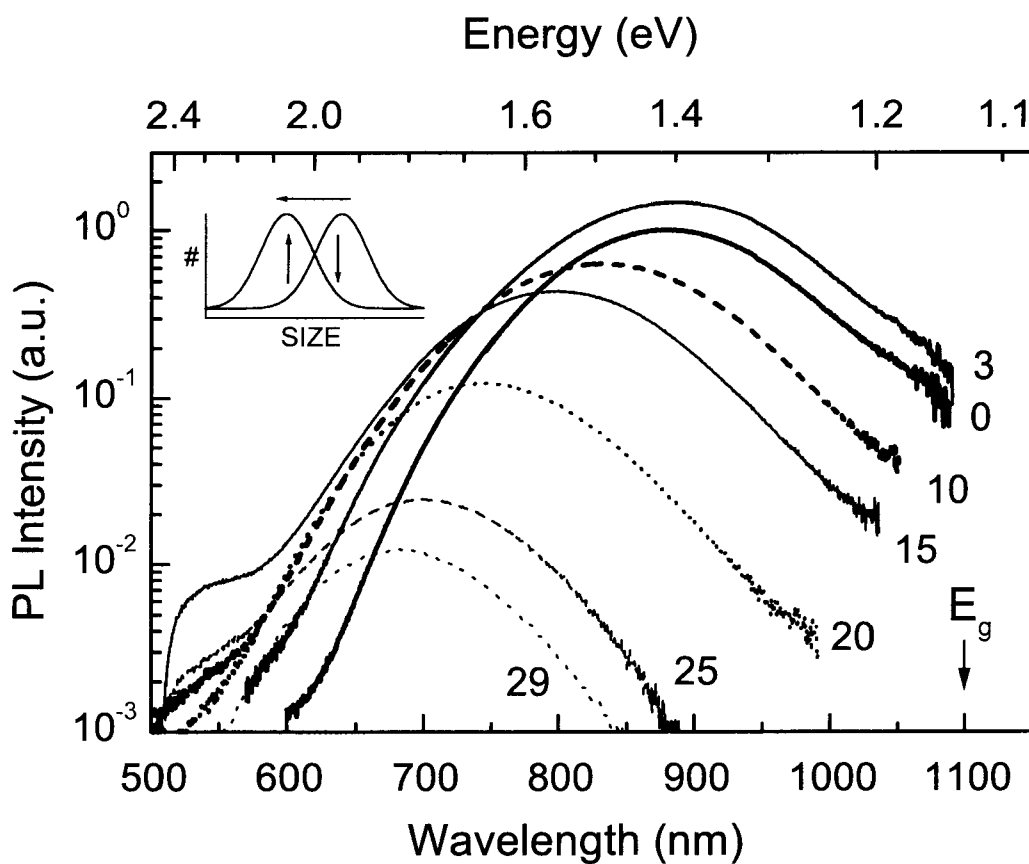
Figure 4.10. Room temperature photoluminescence spectra of 100 nm thick SiO_2 films containing Si nanocrystals, plotted on a logarithmic intensity scale, after oxidation for 0, 3, 10, 15, 20, 25, and 29 min. at 1000°C. For each spectrum, the corresponding oxidation time is indicated. The bandgap wavelength of bulk Si is indicated by an arrow. The inset schematically shows the change in the nanocrystal size distribution upon oxidation.
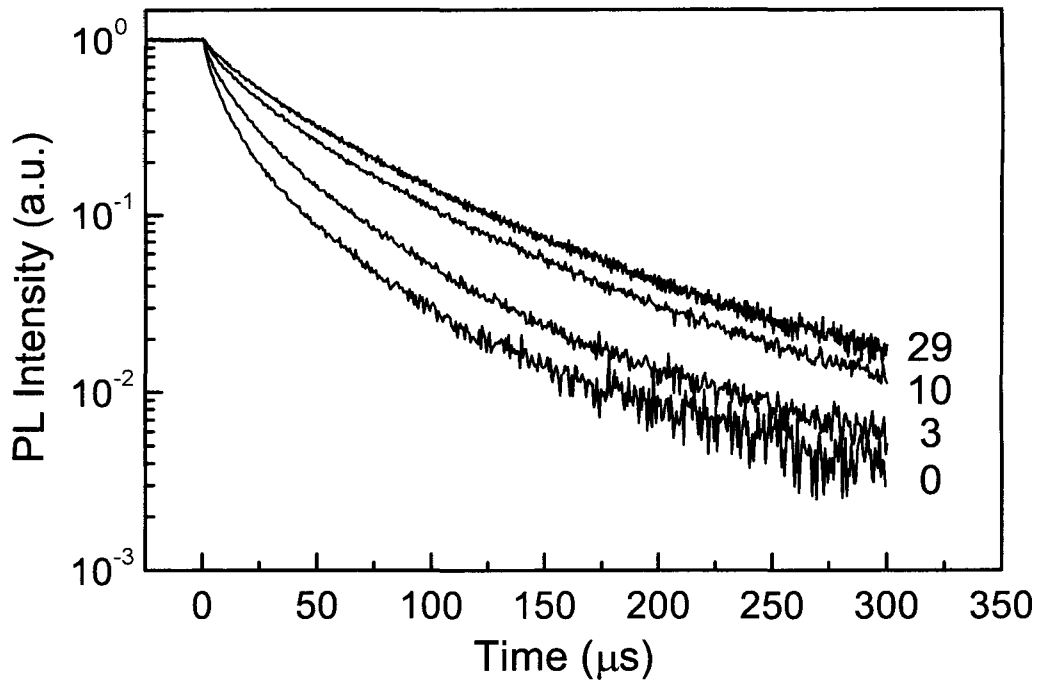
Figure 4.11. Normalized room-temperature photoluminescence decay traces of SiO_2

films containing Si nanocrystals taken at 700 nm after oxidation for 0, 3, 10, and 29

min. at 1000°C. For each decay trace the corresponding oxidation time is indicated.

4.4 Conclusions

In this chapter, the size distribution of Si nanocrystals as a function of film depth has been investigated in order to understand and engineer the optical properties of the SiO_2 films containing Si nanocrystals. In the first part of this chapter, depth-resolved measurements of the photoluminescence have been performed by chemical etching through the SiO_2 film in steps to determine the depth distribution of optically active Si nanocrystals. By analyzing the changes in the PL spectra after each etch step, depth-resolved information is obtained on the location of all luminescence sources present in the film. It is found that the defect-related luminescence centered around ≈600 nm mainly originates from the ≈15 nm-thick region near the surface. Large Si nanocrystals emitting at 900 nm are mainly located in the center of the oxide, where the initial Si concentration is the highest. This is in agreement with transmission electron micrographs that show the largest nanocrystals located in the center of the film. The luminescence from small nanocrystals, emitting at 700 nm and shorter wavelengths, mainly originates from regions close to the SiO_2 film surface and the SiO_2/Si interface. The high concentration of small nanocrystals near the surface and SiO_2/Si interface can be attributed to low initial Si excess concentration and Gibbs Thompson effect between the nanocrystals and the Si substrate, respectively. Alternatively, it may be that the luminescence of small nanocrystals is quenched in

the center of the film, due to excitation migration from small nanocrystals to large nanocrystals.

In the second part of this chapter, a method by which the luminescence energy can be continuously tuned throughout the visible spectrum has been presented. Transmission electron micrographs and Rutherford backscattering spectra show that thermal annealing the SiO_2 films containing Si nanocrystals in flowing O_2 at 1000°C for up to 30 min. results in oxidation of the Si nanocrystals, first close to the SiO_2 film surface and later at greater depths. The average size of the nanocrystals continuously decreases, and upon oxidation for 30 min., the photoluminescence peak wavelength blue-shifts by more than 200 nm. This blue-shift is unambiguously identified with the quantum size effect in which a reduction of the average nanocrystal size leads to emission at shorter wavelengths. The room temperature luminescence lifetime measured at 700 nm was on the order of 10 μs, indicative of the fact that the Si nanocrystals continue to behave as an indirect bandgap material. The decay traces become more single exponential upon oxidation, which is attributed to a decrease in the interaction of the nanocrystals with their surroundings.

Bibliography

[1]   L.T. Canham, Appl. Phys. Lett. **57**, 1046 (1990).

[2]   K.D. Hirschman, L.Tsybeskov, S.D. Duttagupta, and P.M. Fauchet, Nature **384**, 338 (1996).

[3]   J.C. Vial and J. Derrien, *Porous Si Science and Technology*, Springer-Verlag, Berlin (1995).

[4]   Y. Kanemitsu, Phys. Rep. **263**, 1 (1995).

[5]   M.L. Brongersma, K.S. Min, E. Boer, T. Tambo, A. Polman, and H.A. Atwater, Mater. Res. Soc. Symp. Proc. **486,** 213 (1998).

[6]   T. Shimizu-Iwayama, M. Oshima, T. Niimi, S. Nakao, K. Saitoh, T. Fujita, and N. Itoh, J. Phys. Condens. Matter **5**, L375 (1993).

[7]   J.G. Zhu, C.W. White, J.D. Budai, S.P. Withrow, and Y.Chen, Mater. Res. Soc. Symp. Proc. **358**, 175 (1995).

[8]   G. Ghislotti, B. Nielsen, P. Asoka-Kumar, K.G. Lynn, A. Gambhir, L.F. Di Mauro, and C.E. Bottani, J. Appl. Phys. **79**, 8660 (1996).

[9]   K.S. Min, K.V. Shcheglov, C.M. Yang, H.A. Atwater, M.L. Brongersma, and A. Polman, Appl. Phys. Lett. **69**, 2033 (1996).

[10]   J. Linnros, A. Galeckas, N. Lalic, and V. Grivickas, Thin Solid Films **297**, 167 (1997).

[11] L. Rebohle, J. Borany, R.A. Yankov, W. Skorupa, I.E. Tyschenko, H. Fröb, and K. Leo, Mater. Res. Soc. Proc. **486**, 175 (1998).

[12] M.S. Hybertsen, Phys. Rev. Lett. **72**, 1514 (1994).

[13] C. Delerue, G. Allan, and M. Lannoo, Phys. Rev. B **48**, 11024 (1993).

[14] S. Tiwari, F. Rana, H. Hanafi, A. Hartstein, E. Crabbe, and K. Chan, Appl. Phys. Lett. **68**, 1377 (1996).

[15] J.P. Biersack and L.J. Haggmark, Nucl. Instr. Meth. **174**, 257 (1980).

[16] W.E. Beadle, J.C.C. Tsai, and R.D. Plummer, eds., *Quick Reference Manual for Si Integrated Circuit Technology*, John Wiley & Sons, New York (1985).

[17] R.T. Collins, P.M. Fauchet, and M.A. Tischler, Physics Today 1 (1997).

[18] J.C. Maxwell Garnett, Phil. Trans. R. Soc. London **203**, 385 (1904).

[19] L.A. Nesbit, Appl. Phys. Lett. **46**, 38 (1985).

[20] M.L. Brongersma, Ph.D. Thesis, Utrecht University, Netherlands, 1998, Chapter 8, pp. 75-87.

[21] See, for example, R.W. Cahn and P. Haasen, eds., *Physical Metallurgy, 3rd, Revised and Enlarged Edition*, North-Holland Physics Publishing, Amsterdam, 1983, Chapter 14, pp. 933-1030.

[22] C.M. Yang, Ph.D. Thesis, California Institute of Technology, 1997, Chapter 3, pp. 56-83.

[23] M. Strobel, K. H. Heinig, and B. Schmidt, Mater. Res. Soc. Symp. Proc. (1997).

[24] Th. Förster, in *Comparative Effects of Radiation*, edited by M. Burton, J.S. Kirby-Smith, and J.L. Magee, Wiley, New York, 1960, p. 301.

[25] D.L. Dexter, J. Chem. Phys. **21**, 836 (1953).

[26] C.R. Kagan, C.B. Murray, M. Nirmal, and M.G. Bawendi, Phys. Rev. Lett. **76**, 1517 (1996).

[27] J.C. Vial, A. Bsiesy, F. Gaspard, R. Herino, M. Ligeon, F. Muller, R. Romestain, and R.M. Macfarlane, Phys. Rev. **B 45**, 14171 (1992).

[28] P. Brüesch, Th. Stockmeier, F. Stucki, and P.A. Buffat, J. Appl. Phys. **73**, 7666 (1993).

Chapter 5

Growth and Characterization of Epitaxially Stabilized Sn_xSi_{1-x}/Si and α-Sn/Si Heterostructures

5.1 Introduction

There has been a steady progress towards monolithic integration of optics and electronics on the same Si substrate to make monolithically integrated Si-based optoelectronic integrated circuits [1,2]. An optoelectronic integrated circuit refers to optical components and advanced microelectronic components integrated into the same integrated circuit on the same substrate. And a monolithically integrated circuit

refers to integrated circuits having every component made from group IV materials. Monolithic integration promises a cost-effective way of creating optoelectronic integrated circuits since the already-advanced Si processing technology can be readily implemented. The progress towards the development of Si-based optoelectronic integrated circuits has been steady, yet not precipitous, mainly due to a lack of efficient light emitters based on Si. The indirect band gap and a low carrier mobility of Si pose as formidable obstacles for realization of Si-based photonic devices. And while Ge is the only other group IV element known to form a stable solid solution with Si, the resulting alloy is still expected to be fundamentally an indirect gap semiconductor throughout the whole composition range. The various efforts to circumvent the limitations arising from the indirectness of the Si band gap have been outlined in Chapter 1.

One approach for realization of a direct energy gap group IV alloy semiconductor involves alloying Sn with Si or Ge to form epitaxially stabilized diamond cubic Sn_xGe_{1-x}/Ge and Sn_xSi_{1-x}/Si heterostructures [3-6]. Diamond cubic α-Sn is a zero band gap semiconductor with degenerate conduction and valence bands at the Γ point [7], and band structure calculations have suggested that when Si or Ge is alloyed with Sn the resulting alloy systems Sn_xSi_{1-x} and Sn_xGe_{1-x} are predicted to have direct and tunable energy gaps for Sn compositions exceeding some critical concentration [3-6]. Recently the indirect-to-direct band gap transition was observed in Sn_xGe_{1-x} alloys grown by molecular beam epitaxy [8].

Two types of heterostructure growth are investigated in this chapter. First, the pseudomorphic growth of dilute (x<0.06) Sn_xSi_{1-x} alloys on Si, which have also been

reported by others [9,10], are investigated. Although not predicted to be a direct gap

semiconductor, the dilute Sn_xSi_{1-x} alloy films are interesting due to the potential for

strain and band gap engineering of Si-based heterostructures. Second, this chapter

also demonstrates the growth of coherently strained, epitaxially stabilized ultrathin α-

Sn/Si and high Sn concentration Sn_xSi_{1-x}/Si quantum well heterostructures and α-

Sn/Si quantum well superlattice structures by a modified molecular beam epitaxy

technique employing temperature and growth rate modulations. Growth of such

heterostuctures is motivated by the prediction that a Sn_xSi_{1-x} alloy has to be high in Sn

concentration for the realization of a semiconductor material with a direct band gap

that can be tuned in energy [3-6]; one might also potentially take advantage of the

quantum carrier confinement to further tune the energy gap in α-Sn/Si and high Sn

concentration Sn_xSi_{1-x}/Si quantum well heterostructures over a wide range in the

infrared frequency range [11].

Growth of such heterostructures is challenged by the large lattice mismatch

between α-Sn and Si (19.5%), very low solid solubility of Sn in crystalline Si

($\sim 5 \times 10^{19}$ cm^{-3}) [12], and pronounced Sn segregation to the surface during growth at

ordinary Si epitaxy temperatures (T>$\sim$400°C). To incorporate Sn at high

concentrations while maintaining high epitaxial film quality, we employ temperature

and growth rate modulations in molecular beam epitaxy, as has previously been

employed for growth of Sb delta-doped layers in Si [13] and Ge/α-Sn

heterostructures on Ge [14].

5.2 The Si-Sn Alloy System

5.2.1 Predicted Electronic Structure of the Novel Semiconductor Alloy Sn_xSi_{1-x}

Diamond cubic α-Sn, which is thermodynamically stable below 13.2°C [13], is a direct gap semimetal with the conduction band minimum overlapping into the valence band maximum by 0.15 eV at Γ point (k =<0,0,0>) [7]. This is illustrated in Fig. 5.1 from a semiempirically constructed band structure of α-Sn using the Slater-Koster parameter model [4]. Motivated by the possibility for developing a novel group IV semiconductor with a direct and tunable energy gap in the infrared, there have been several theoretical investigations on the predicted band gap as a function of composition for Sn-Si alloy system [3-6].

Interestingly, when the indirect gap semiconductor Si is alloyed with α-Sn, the conduction band at L point (k =<1,1,1>) decreases in energy with increasing Sn concentration at a slower rate compared to the conduction band at Γ point [3-6]. As a result the Sn_xSi_{1-x} alloy is predicted to have a direct and tunable optical energy gap for compositional range exceeding some critical Sn concentration [3-6]. The linear projections of the critical eigenvalues from results of the Slater-Koster parameter model is illustrated in Fig. 5.2 [4]. In the linear projection of critical point eigenvalues as a function of alloy composition known as Vegard's Law, the energy gap is predicted to be direct and semiconducting for the composition window 0.82 ≤ x

≤ 0.95, corresponding to an energy gap window of $0 \leq E_g$ (eV) ≤ 0.40. In order for

the Sn_xSi_{1-x} alloy system to have a direct gap, therefore, the composition must be in

the Sn-rich end. The requirement of high Sn content poses an obstacle since the

lattice mismatch is extremely large (19%) between α-Sn and Si. Then, this suggests

that the stabilization of Sn in a strained pseudomorphic Sn_xSi_{1-x} alloy with high Sn

content would require the strained layer to be very thin.
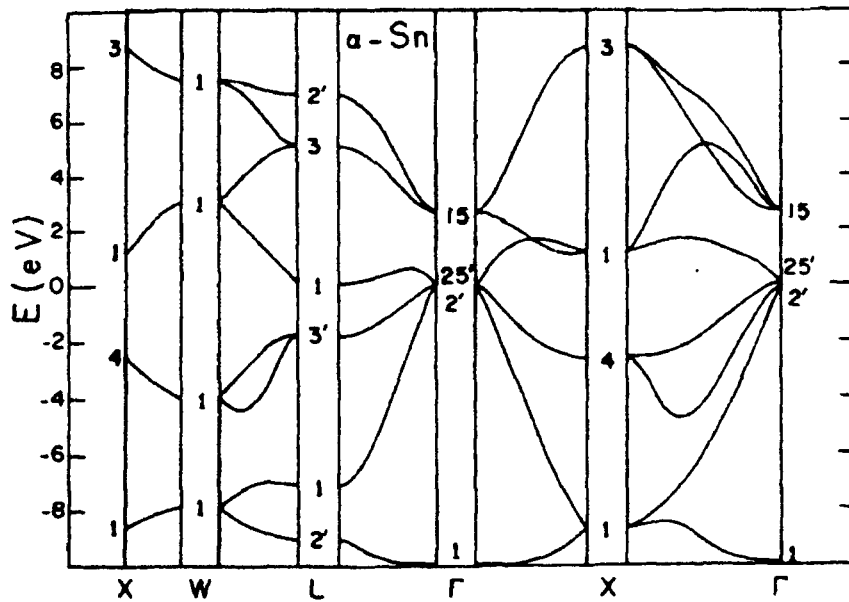
Figure 5.1. A semiempirically constructed electronic band structure of α-Sn using the Slater-Koster parameter model [4].
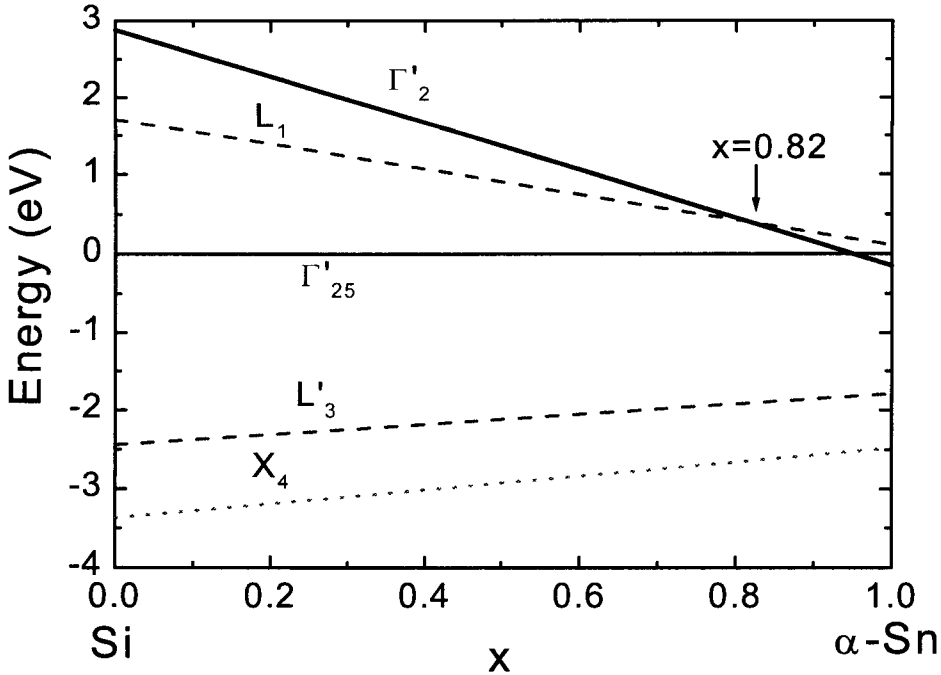
Figure 5.2. The predicted energy band diagram for the elemental semiconductors Si

and α-Sn, showing projections of critical-point eigenvalues from Ref. 4. The

eigenvalues for Si and α-Sn are connected by line segments to represent the energy

for the binary system Sn_xSi_{1-x}; i.e., the valence band and conduction band shapes are

assumed to change linearly with composition (Vegard's law). The energy gap is

predicted to be direct and semiconducting for the composition window $0.82 \leq x \leq$

0.95, corresponding to an energy gap window of $0 \leq E_g$ (eV) ≤ 0.40.

5.2.2 Thermodynamic Properties of the Si-Sn Alloy System

The equilibrium phase diagram [12] of the Si-Sn binary alloy system shown in Fig. 5.3 illustrates a simple eutectic system with a eutectic point with boundaries very close to the melting point of pure Sn at 232°C. From the inset in the phase diagram in Fig. 5.3, the solid solubility of Sn in Si is expected to be very low, with the maximum value being only 0.1% at 1066°C. This indicates that any alloy composition of interest for heterostructures would clearly have to be highly metastable chemically as well as elastically. For example, the equilibrium phases of a 50%-Sn Si-Sn mixture at a typical Si growth temperature of 500°C is composed of almost pure solid Si and liquid Sn. Even below the melting point of Sn at 232°C, the equilibrium phases are almost-pure Si and almost-pure body-centered tetragonal β-Sn, which is stable above 13.2°C [13]. So unless the system is prevented from phase-separating due to a kinetic barrier, the mixture would not form a thermodynamically stable compound. The phase separation can be prevented by epitaxial stabilization of Sn atoms in Si-Sn alloy grown at a low temperature on a single crystal Si substrate. Epitaxially stabilized pure α-Sn on a lattice-matched single crystal substrate has been demonstrated to be stable up to much higher temperature (130°C) [14-17]. Another deleterious effect of the low bulk solid solubility is the related low surface solid solubility, which results in severe surface segregation of Sn during epitaxial growth.

For this reason, Sn has actually been used as a surfactant in growth of Si-Ge alloys [18-20].
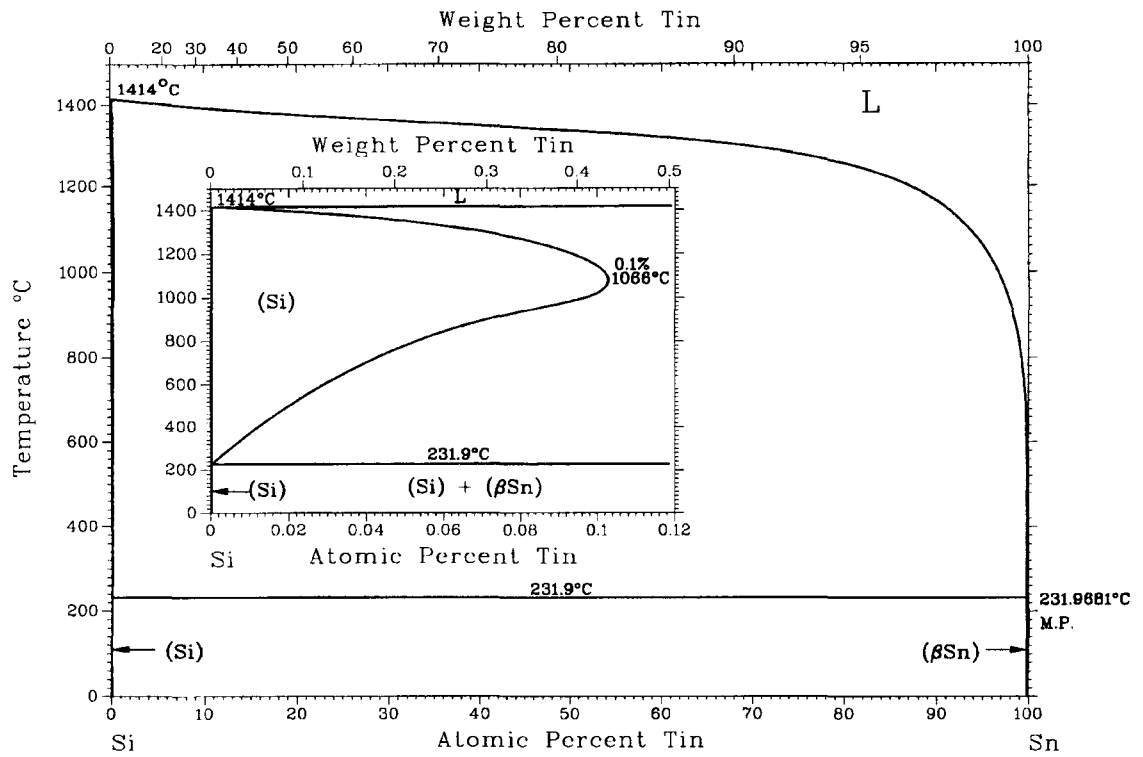
Figure 5.3. Equilibrium phase diagram of the Si-Sn alloy system [12].

5.2.3   Critical Thickness for Coherent Growth of Sn_xSi_{1-x}/Si

In addition to being chemically metastable, epitaxial Sn_xSi_{1-x}/Si is also metastable with respect to coherency strain due to the large lattice mismatch between Si and α-Sn (19%). It is well known that when lattice mismatched epitaxial layers are grown on a single crystal substrate, the first atomic layers will be strained to match the substrate to form a coherent interface. Coherent growth continues until the built-up strain energy in the epitaxial layer exceeds a critical value, whence it becomes energetically favorable for the epitaxial layer to lower its energy by introduction of misfit dislocations.

Numerous authors [21-23], followed by the initial prediction by Van der Merwe [24], have theoretically predicted the existence of a critical thickness corresponding to the critical strain energy. Figure 5.4 shows the predicted equilibrium critical thickness for introduction of misfit dislocations for the Sn_xSi_{1-x}/Si system, calculated using two representative approaches. The calculation by Van der Merwe [24] consists of an energy density balance between the density of elastic strain energy and the energy of non-interacting arrays of edge dislocations. The expression used for the curve of critical thickness h_{crit} in Fig. 5.4 is given by

$$h_{crit} = \frac{b}{8\pi f(1+\nu)}\left[\ln\frac{h_{crit}}{b}+1\right] \qquad (5.1)$$

where f is the misfit, ν is the Poisson's ratio, and b is the Burgers vector given by $(a/2)<110>$ for 60° misfit dislocations on $\{111\}$ glide planes. The calculation by

Mathews and Blakeslee [22] consists of a force balance between the force acted on the dislocation by misfit stress and the dislocation line tension and is given by the expression

$$h_{crit} = \frac{b}{8\pi f} \frac{(1 - \nu \cos^2 \alpha)}{(1 + \nu)\cos \lambda} \left[\ln \frac{4h_{crit}}{b} + 1 \right], \qquad (5.2)$$

where α is the angle between the dislocation line and the Burgers vector b, and λ is the angle between the slip direction and that direction in the film plane that is perpendicular to the line of intersection of the slip plane and the interface. For the epitaxial films grown on a (100) substrate, assuming the Burgers vector to be (a/2)<110> for 60° misfit dislocations on {111} glide planes, both cos α and cos λ have the value 0.5.

From examination of Fig. 5.4, it is clear that for the composition range where the Sn_xSi_{1-x} alloy is expected to be a direct gap semiconductor (x≥82%), the predicted equilibrium critical thickness does not exceed more than a monolayer. Thus, it is clearly expected that the epitaxial stabilization of a Sn-rich epitaxial Sn_xSi_{1-x}/Si would require the strained layer thickness to be severely limited, if the epitaxial film were to remain coherent at high temperatures.
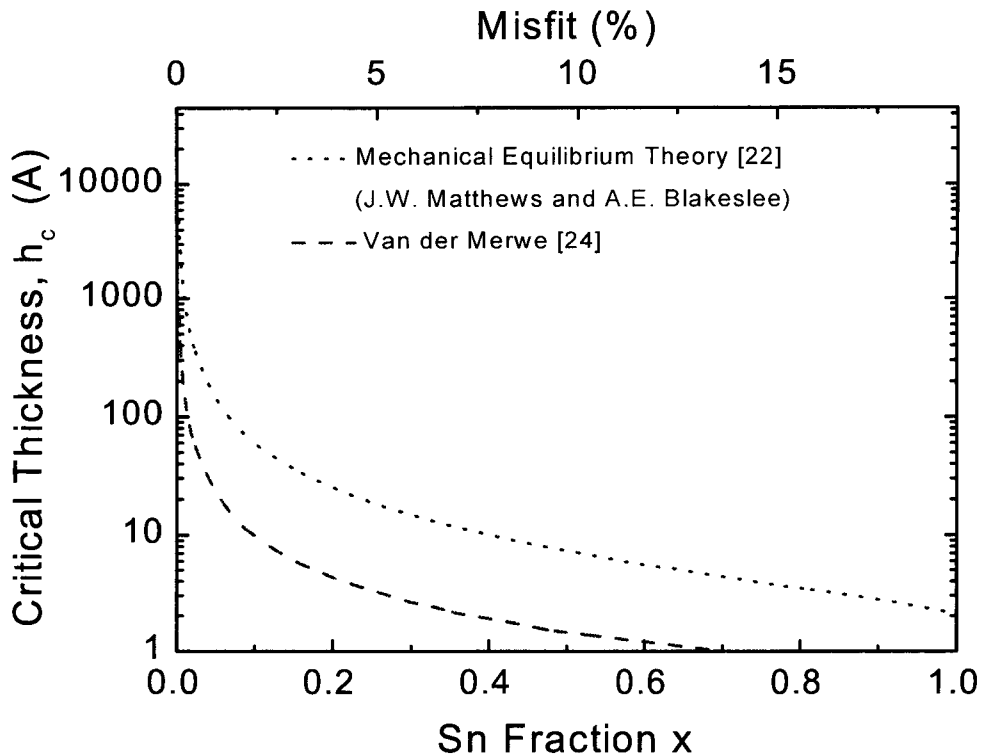
Figure 5.4. Calculated equilibrium critical layer thickness for the introduction of

misfit dislocations for the alloy Sn_xSi_{1-x} grown on Si as a function of Sn content x and

misfit. The misfit varies from 0 to 19% for x=0 to x=1.0. The upper dotted curve

represents the critical layer thickness as calculated using Eq. (5.1) from mechanical

equilibrium theory by Mathews and Blakeslee [22] and the lower dashed curve

represents the critical layer thickness calculated using Eq. (5.2) from the theory of

Van der Merwe [24].

5.3 Growth of Dilute Sn_xSi_{1-x}/Si by Conventional Molecular Beam Epitaxy

Although not expected to be direct band gap semiconductors from the foregoing discussion in Section 5.2.1, dilute Sn_xSi_{1-x} alloys still offer a strong potential for strain and band gap engineering. There have already been reports [9,10] of successful growth of dilute (x<4%) pseudomorphic Sn_xSi_{1-x}/Si and observation of low-temperature band-edge photoluminescence attributable to the strained alloy film. In this section, a study on the growth of dilute Sn_xSi_{1-x}/Si using conventional molecular beam epitaxy is presented.

All films were grown in a custom-built molecular beam epitaxy system with a base pressure of 3×10^{-10} torr. The system is equipped to perform 30 keV reflection high energy electron diffraction (RHEED) for *in situ* surface analysis. The (100) float zone Si substrates were prepared by first removal in HF of a 100 nm thermally-grown oxide and then by cleaning in 5:1:1 H_2O:H_2O_2:NH_4OH solution and subsequent complete removal of the chemically-grown oxide in a 10% HF-H_2O solution to obtain a hydrogen-terminated Si (100) surface. After transfer to ultrahigh vacuum, the substrates were baked *in situ* at 200°C for 2 hours to desorb hydrocarbon contaminants. Just prior to growth of the Si buffer layer, the substrates were heated to 550°C to desorb hydrogen and obtain a (2×1) surface reconstruction. Si and Sn were deposited by electron beam evaporation and thermal effusion, respectively. Si

deposition rates were controlled using a quartz crystal monitor and Sn deposition rate was controlled via effusion cell temperature. The Sn effusion cell temperature was varied between 675–755°C to yield deposition rates between 0.003–0.02 ML/sec (1 ML=6.79×10^{14}/cm^2).

For all films 50–80 nm-thick Si buffer layers were deposited prior to the deposition of the alloy layer. The buffer layers were first started to be deposited at 550°C and gradually lowered in temperature so that the substrate temperature reaches the alloy layer growth temperature by the end of the buffer layer growth.

The samples were analyzed by *in situ* reflection high-energy electron diffraction (RHEED), Rutherford backscattering spectrometry (RBS) with a 2 MeV He^{++} beam, and high-resolution X-ray rocking curve analysis using Cu K$_{\alpha 1}$ radiation.

5.3.1   High Temperature Growth of Dilute Sn_xSi_{1-x}/Si

The single greatest difficulty in the growth of Sn_xSi_{1-x}/Si by conventional molecular beam epitaxy at high temperatures (T>350°C) is the severe segregation of Sn to the surface. This section illustrates the problems associated with the growth of dilute Sn_xSi_{1-x}/Si films at ordinary epitaxial growth temperatures for Si. The samples analyzed consist of 120 nm-thick Sn_xSi_{1-x}/Si films grown at 450°C with beam flux composition between x=0.0025 to x=0.006.

All films exhibited severe Sn surface segregation during growth. The final composition variation as a function of depth is illustrated in the Rutherford backscattering spectrum of 120 nm-thick Sn_xSi_{1-x}/Si alloy grown at 450°C with nominal beam flux x=0.004 at a total atom flux of 5.0×10^{14}/cm^2/sec, shown in Fig. 5.5. The sharp peak on the high-energy side of the Sn spectrum corresponds to Sn atoms segregated to the surface. It can be seen that even with such a low Sn flux, a significant fraction of the deposited Sn has segregated to the surface.

The segregation of Sn has also been observed *in situ* during the initial stages of the alloy layer growth by reflection high-energy electron diffraction. As more and more Sn segregated to the surface, the surface reconstruction evolved in agreement with previous observations for various Sn coverage on Si (100) [25-27]: (6×2) for 0.375–0.5 ML, c(4×8) for 0.5–1.0 ML, and (5×1) for 1.0–1.5 ML. Accumulation of more than one monolayer of Sn on the surface lead to a spotty diffraction pattern, indicative of the growth mode changeover of Sn on Si from two-dimensional to three-dimensional.
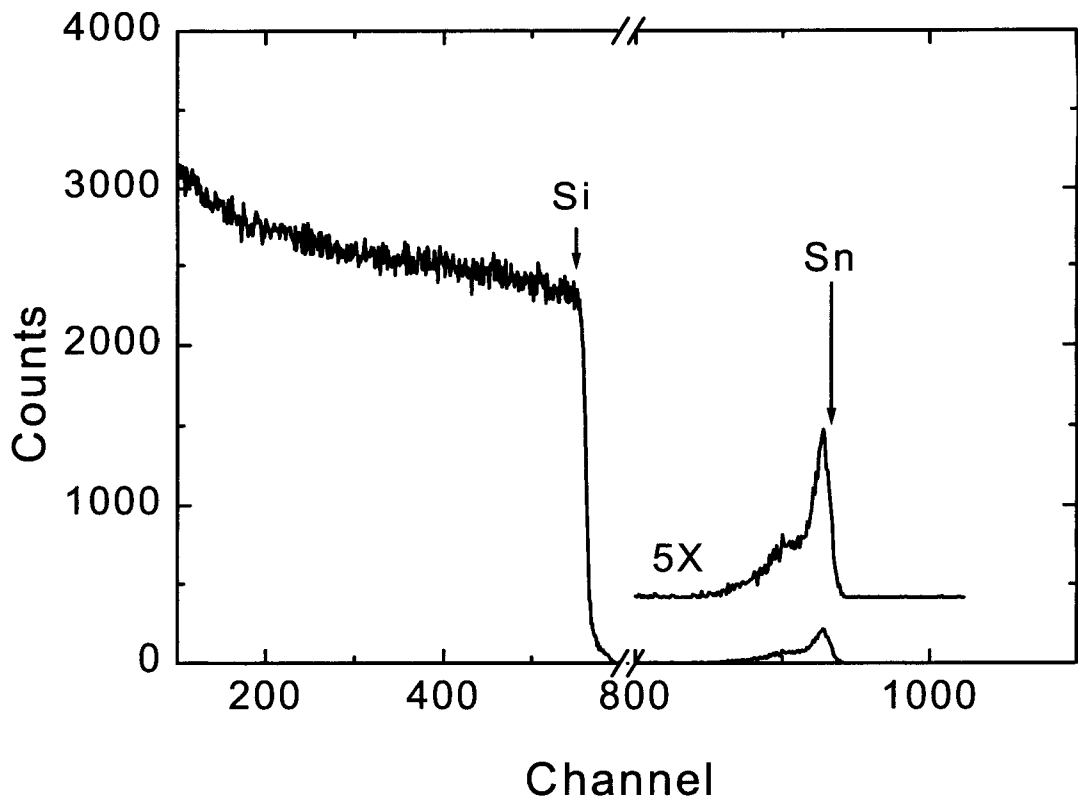
Figure 5.5. Rutherford backscattering spectrum of 120 nm-thick Sn_xSi_{1-x}/Si with nominal beam flux composition x=0.004 grown by conventional molecular beam epitaxy at 450°C. The sharp peak on the high energy edge of the Sn spectrum corresponds to the surface-segregated Sn.

5.3.2   Low Temperature Growth of Dilute Sn_xSi_{1-x}/Si

The results of Section 5.3.1 indicate that the substrate temperature has to be lowered significantly in order to incorporate appreciable amounts of Sn. In this section, the growth of Sn_xSi_{1-x}/Si films with the incorporated Sn concentration up to 6% is demonstrated by conventional molecular beam epitaxy at low temperatures.

Investigated samples consist of 100 nm-thick Sn_xSi_{1-x}/Si films of nominal beam flux compositions x=0.024 and x=0.06 grown at three temperatures: 250°C, 300°C, and 350°C. The total atom flux for the two compositions were $1.54\times10^{14}/cm^2/sec$ and $1.59\times10^{14}/cm^2/sec$, respectively.

Figures 5.6(a)-(c) illustrate the evolution of the surface during growth of $Sn_{0.024}Si_{0.976}$ at 300°C as observed by *in situ* reflection high-energy diffraction. The temperature is continuously dropped from 550°C to 300°C during the buffer layer growth so that the surface remains clean and Fig 5.6(a) shows the (2×1) reconstructed Si (100) surface of the buffer layer during the cool-down. Figure 5.6(b) shows the diffraction pattern after deposition of 4 nm of the alloy. The substrate temperature is 330°C. The diffraction pattern becomes spotty and diffuse, indicative of a three-dimensional growth mode. Figure 5.6(c) shows the diffraction pattern after deposition of 50 nm of the alloy at 300°C. In addition to diffraction spots corresponding to three-dimensional growth, streaks are also visible, indicative of a faceted three-dimensional growth.

Figures 5.7(a) and (b) show Rutherford backscattering spectra of $Sn_{0.06}Si_{0.94}$/Si alloys grown at 300°C and 350°C, respectively. It can be seen that segregation is very pronounced for the film grown at 350°C in Fig. 5.7(b). Similar spectra have been observed (not shown) for the $Sn_{0.024}Si_{0.976}$/Si alloys. At the given deposition rate and flux ratio, the surface segregation becomes pronounced at T>300°C.

Figures 5.8 (a)–(d) show symmetric (004) reflection high-resolution X-ray rocking curves of $Sn_{0.024}Si_{0.976}$/Si. Figure 5.8(a) is a dynamical simulation [28] for a 106 nm-thick $Sn_{0.024}Si_{0.976}$/Si alloy and Fig. 5.8(b) is the experimental rocking curve of the 100 nm-thick film grown at 250°C. It can be seen that the experimental curve in Fig. 5.8(b) compares well with the simulation in Fig. 5.8(a), indicating that the film grown at 250°C is fully strained and pseudomorphic. This is in agreement with previous results [9,10]. Figures 5.8(c) and (d) show the rocking curves of 100 nm-thick films of the same nominal composition grown at 300°C and at 350°C, respectively. Despite the fact that the deposition rate, the thickness, and the nominal beam flux composition are identical within experimental error, the spectra of the films grown at 300°C and 350°C show the peaks corresponding to the compressively strained Sn_xSi_{1-x} at much smaller angular distances from the Si substrate (004) peak compared to the film grown at 250°C, indicating that the films grown at 300°C and 350°C are not fully strained and therefore not pseudomorphic. Very little surface segregation was observed from the Rutherford backscattering spectrum (not shown) of the 100 nm-thick $Sn_{0.024}Si_{0.976}$/Si film grown at 300°C. This suggests that for the film grown at 300°C, the less-than-fully-strained peak in the rocking curve in Fig.

5.8(c) is due to a partial relaxation of the strain energy by the introduction of misfit dislocations. The Rutherford backscattering spectrum (not shown) of the 100 nm-thick $Sn_{0.024}Si_{0.976}$/Si film grown at 350°C does, however, indicate that the surface segregation of Sn is pronounced at 350°C. Thus at 350°C, the observation of less-than-fully-strained peak in the rocking curve in Fig. 5.8(d) is due to the surface segregation of Sn and/or strain relaxation by introduction of misfit dislocations.

A similar X-ray rocking curve analysis performed on $Sn_{0.06}Si_{0.94}$/Si films grown at 250°C, 300°C, and 350°C indicate that films grown at all temperatures are less than fully strained. From a comparison of the X-ray spectra and Rutherford backscattering spectra, it can be concluded that the $Sn_{0.06}Si_{0.94}$/Si films grown at 250°C and 300°C have undergone strain relaxation by introduction of misfit dislocations. Also, a comparison of the X-ray spectrum and the Rutherford backscattering spectrum in Fig. 5.7(b) of the $Sn_{0.06}Si_{0.94}$/Si film grown at 350°C indicates that the film has undergone surface segregation of Sn and/or strain relaxation by introduction of misfit dislocations.
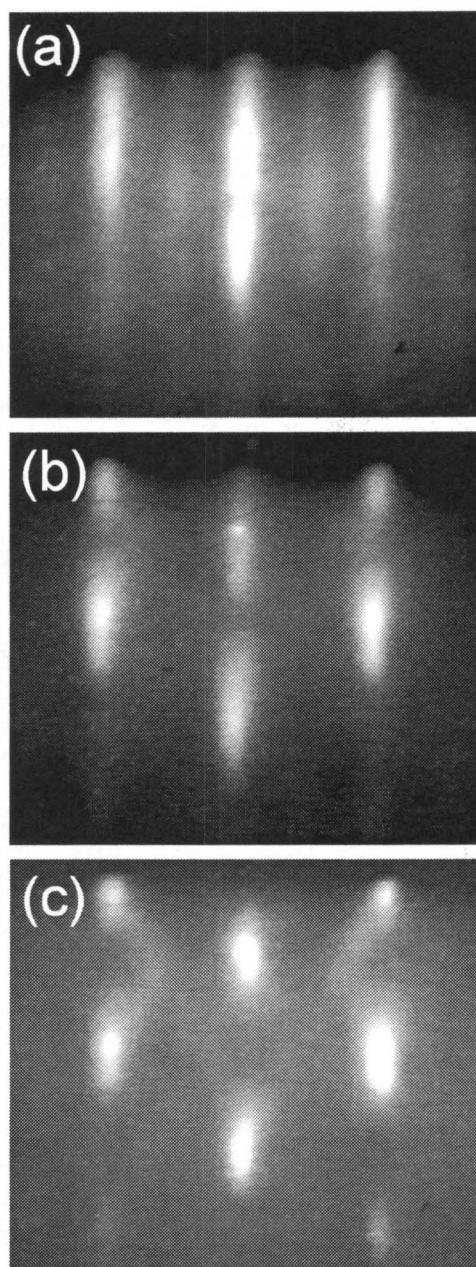
Figure 5.6. Evolution of the surface during growth of $Sn_{0.024}Si_{0.976}$ at 300°C as observed by *in situ* reflection high-energy electron diffraction: (a) the (2×1) reconstructed Si (100) surface of the buffer layer; (b) after deposition of 4 nm of the alloy at 330°C; (c) after deposition of 50 nm of the alloy at 300°C.
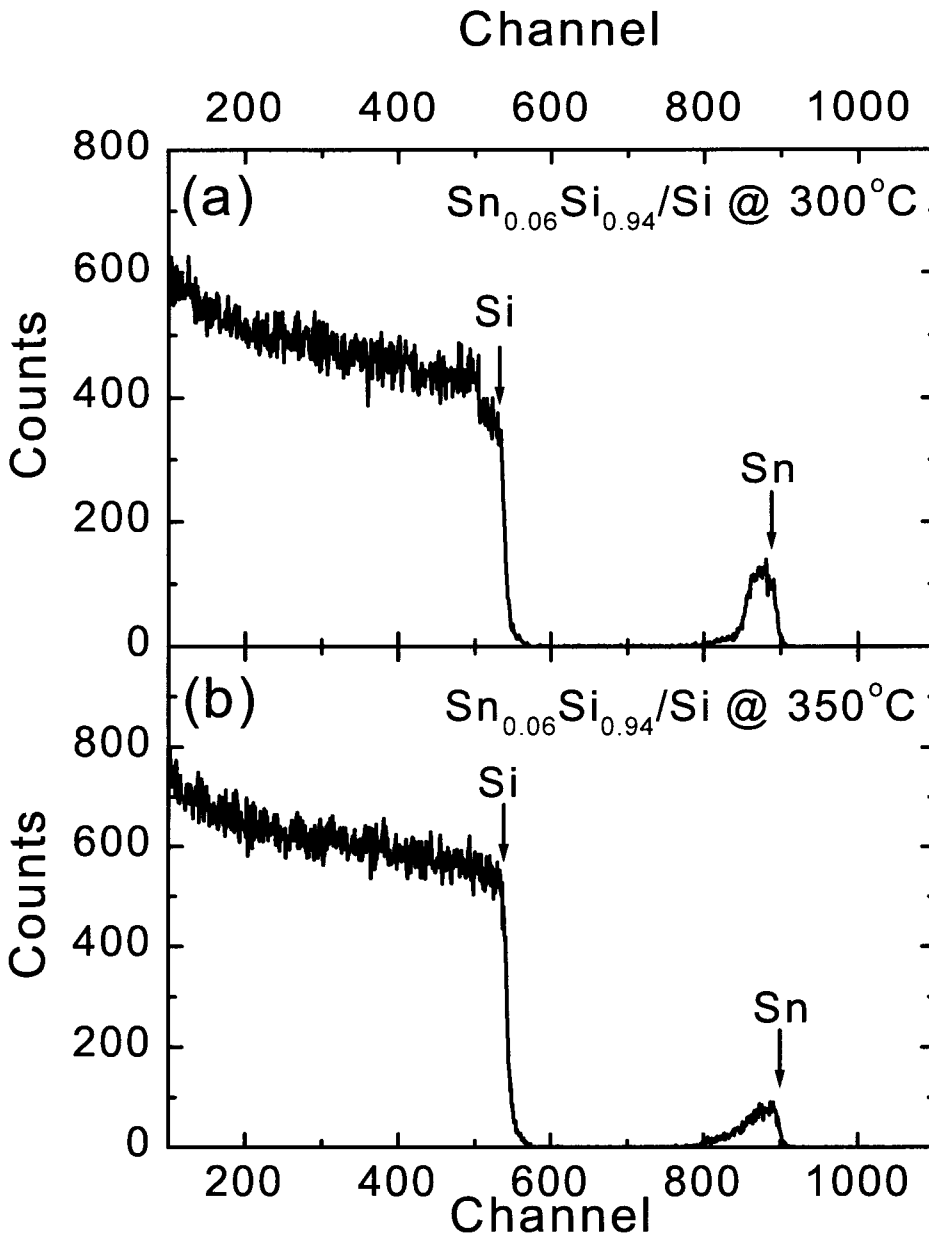
Figure 5.7. Rutherford backscattering spectra of 100 nm-thick $Sn_{0.06}Si_{0.94}$ /Si films grown by conventional molecular beam epitaxy at (a) 300°C and (b) 350°C. An increasing Sn concentration towards the surface on the high-energy edge of the Sn spectrum in (b) indicates pronounced surface segregation of Sn.
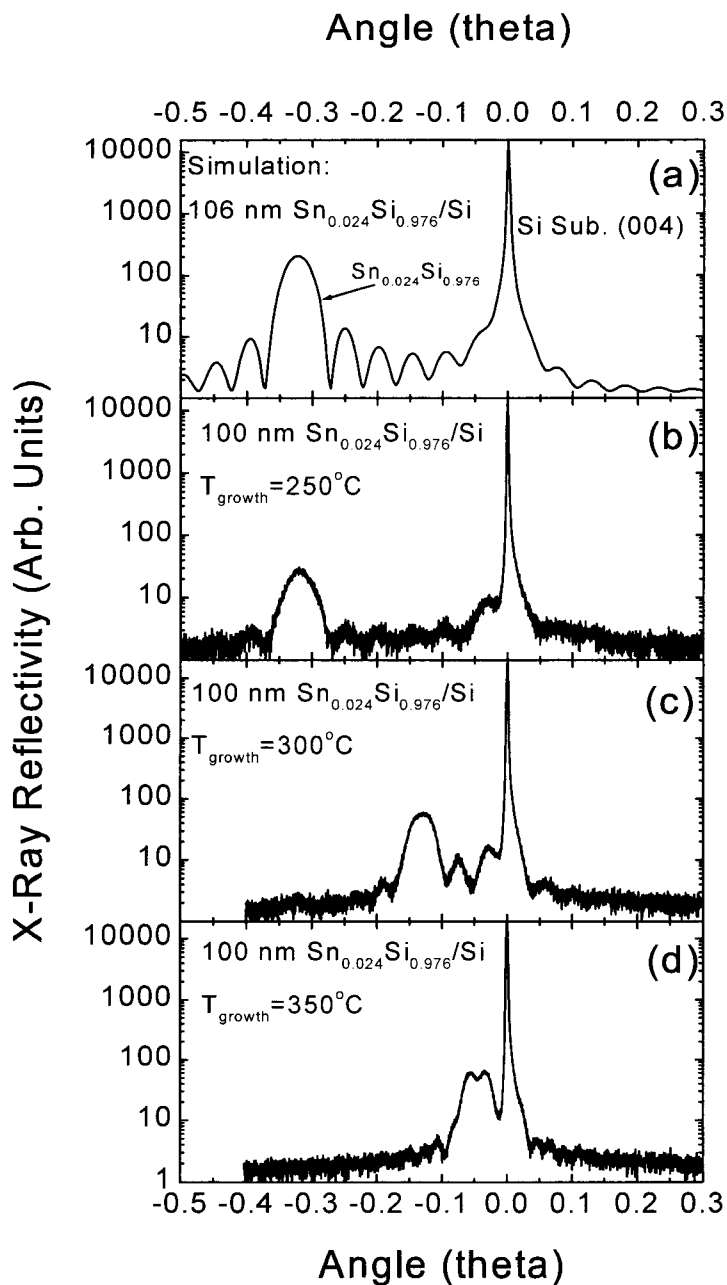
Figure 5.8. Symmetric (004) reflection high-resolution X-ray rocking curves of Sn_xSi_{1-x}/Si with nominal beam flux composition x=0.024: (a) a dynamical simulation [28] for a 106 nm film; (b) 100 nm film grown at 250°C; (c) 100 nm film grown at 300°C; (d) 100 nm film grown at 350°C.

5.4 Growth of Ultrathin Pseudomorphic α-Sn/Si and Sn_xSi_{1-x}/Si Heterostructures by Temperature-Modulated Molecular Beam Epitaxy

We report in this section the growth of coherently strained, epitaxially stabilized ultrathin quantum well heterostructures based on α-Sn/Si and Sn_xSi_{1-x}/Si with high x by employing temperature and growth rate modulations in molecular beam epitaxy. As discussed in Section 5.2.1 the growth of such heterostuctures is motivated by the prediction that a Sn_xSi_{1-x} alloy has to be high in Sn concentration for realization of a tunable direct band gap group IV semiconductor [3-6]. An additional potential advantage of growing ultrathin quantum well heterostructures based on α-Sn/Si and Sn_xSi_{1-x}/Si with high Sn content is the possibility of taking advantage of the quantum carrier confinement to further tune the energy gap over a wide range in the infrared frequency range [11]. This is of interest particularly since quantum confinement may be able to raise the optical transition energy to the fiber optics communication wavelength of 1.55 μm. In terms of coherency strain, epitaxial stabilization of pseudomorphic Sn_xSi_{1-x}/Si with high x can be realized as long as the strained layer thickness remains severely limited, as discussed in Section 5.2.3.

As discussed in Sections 5.2.2 and 5.2.3, the growth of such heterostructures is challenged by the large lattice mismatch between α-Sn and Si (19.5%), very low solid solubility of Sn in crystalline Si ($\sim 5 \times 10^{19}$ cm^{-3}) [12], and pronounced Sn

segregation to the surface during growth at ordinary Si epitaxy temperatures (T>~

400°C). In order to incorporate high concentration of Sn while maintaining a high

epitaxial quality, a modified molecular beam epitaxy technique is employed where

the temperature and growth rate are modulated. Similar technique has previously

been used for growing Sb delta-doped layers in Si [29] and Ge/α-Sn heterostructures

on Ge [30].

5.4.1 Temperature-Modulated Molecular Beam Epitaxy

All films were grown in a custom-built molecular beam epitaxy system with a

base pressure of 3×10^{-10} torr. The (100) float zone Si substrates were prepared by

first removal in HF of a 100 nm thermally-grown oxide and then by cleaning in 5:1:1

$H_2O:H_2O_2:NH_4OH$ solution and subsequent complete removal of the chemically-

grown oxide in a 10% HF-H_2O solution to obtain a hydrogen-terminated Si (100)

surface. After transfer to ultrahigh vacuum, the substrates were baked *in situ* at

200°C for 2 hours to desorb hydrocarbon contaminants. Just prior to growth of the Si

buffer layer, the substrates were heated to 550°C to desorb hydrogen and obtain a

(2×1) surface reconstruction. Si and Sn were deposited by electron beam evaporation

and thermal effusion, respectively. Si deposition rates were controlled using a quartz

crystal monitor and Sn deposition rate was controlled via effusion cell temperature.

The Sn effusion cell temperature was varied between 675°C–755°C to yield deposition rates between 0.003–0.02 ML/sec (1 ML = 6.79×10^{14}/cm^2).

Temperature-modulated molecular beam epitaxy is described as follows. A typical modulation of growth temperature during molecular beam epitaxy is schematically illustrated in Fig. 5.9. For all types of heterostructures, Si buffer layers were first grown at 550°C at 0.05 nm/sec. to obtain a smooth Si surface, as judged by reflection high energy electron diffraction (RHEED) prior to deposition of Sn or Sn_xSi_{1-x} layers. For growth of α-Sn/Si quantum well and quantum well superlattice structures, Sn deposition at 0.02 ML/sec (1.4×10^{13}/cm^2/sec) immediately followed the high-temperature Si buffer layer growth at 550°C. After Sn deposition, the growth was interrupted to cool the substrate to 110°C–170°C, which took approximately 25–35 min., for growth of a low temperature Si capping layer. The growth procedure for Sn_xSi_{1-x}/Si was similar except that the growth was interrupted after deposition of the Si buffer layer to cool the substrate to 110°C–170°C prior to deposition of the alloy layer. Since the substrate was cooled prior to deposition of Sn_xSi_{1-x} layers, Si overlayer growth followed immediately without further growth interruption. The substrate cool-down procedure for both types of heterostructures is critical in preventing the Sn atoms from segregating to the surface. After either Sn or Sn_xSi_{1-x} is deposited, a low-temperature (110°C–170°C) Si capping layer was deposited at a low growth rate of 0.01 nm/sec.–0.03 nm/sec. The low-temperature Si capping layer ensures that the Sn atoms from the Sn-containing epitaxial layer do not segregate to

the surface. In effect, the Sn atoms in the Sn-containing epitaxial layers are "frozen-in" so that they don't have enough atomic mobility to segregate to the surface.

As illustrated in Fig. 5.9, after 3-6 nm of Si overlayer deposition at 110°C-170°C, the substrate temperature is increased so as to return the substrate temperature to 550°C at a desired overlayer thickness. For quantum well superlattice structures, this thickness corresponds to the period thickness (8-27 nm). After the substrate temperature reaches 550°C, the growth rate is also increased back to 0.05 nm/sec. After growing the Si overlayer with a desired thickness, this process is repeated for multilayer and superlattice structures. A gradual raising-up of the substrate temperature ensures that each layer of Sn or Sn_xSi_{1-x} layer starts on a smooth Si surface. After growing the Si overlayer to a desired thickness, another Sn or Sn_xSi_{1-x} layer can be deposited and the whole process can be repeated for a desired number of times for multilayers and superlattice structures. It is noteworthy that after being capped with Si, the buried Sn layers are annealed during growth at temperatures considerably exceeding the bulk Sn melting temperature (232°C).

The deposition of a low-temperature Si capping layer must be carefully performed in order to avoid the crystal-to-amorphous transition. Two requirements must be met for the Si overlayer: the deposition temperature has to be low enough and the layer must be thick enough (at least greater than the diffusion length of Sn in Si at subsequent high temperature cycles) to be able to completely "bury" the Sn-containing layer to prevent the surface segregation of Sn. Low temperature growth of the capping layer at a low growth rate ensures good crystal quality of the capping layer without significant Sn segregation to the surface. The basic guidelines for the

growth of the capping layer are based on earlier works on limited thickness homoepitaxy of Si where crystalline growth over an epitaxial thickness h_{epi} is followed by a transition to amorphous deposition [31-33]. The universal parameter in the epitaxial breakdown is the critical epitaxial thickness h_{epi}, which is thermally activated in the substrate temperature. Several models have been proposed to describe the epitaxial breakdown at low temperature [32]. Among the proposed mechanisms responsible for epitaxial breakdown at low temperatures are [32]: continuous nucleation of the amorphous phase, a continuous buildup of lattice disorder, segregation of impurities, and kinetic roughening. Whatever the mechanism may be, the breakdown of epitaxy is clearly thermally activated, and therefore the critical thickness h_{epi} at which epitaxial Si films undergo a crystal-to-amorphous transition has been shown to be governed by an Arrhenius temperature dependence [31,32]. Furthermore, the critical thickness has also been shown to depend on the deposition rate [31,32]: h_{epi} is larger for lower growth rates. Therefore, by lowering the growth rate, a maximum thickness of the low temperature Si overlayer can be deposited at the low temperature to prevent Sn segregation without undergoing the crystal-to-amorphous transition. The epitaxial critical thickness h_{epi}, however, is expected to be lower for over-growth on Sn_xSi_{1-x} layers due to the presence of tensile strain.

Evolution of the surface morphology and reconstruction during temperature-modulated molecular beam epitaxy has been investigated using *in situ* reflection high-energy electron diffraction (RHEED). A typical cycle of surface evolution during growth of one period of the α-Sn/Si heterostructure is shown in Fig. 5.10. Figure

5.10(a) is the RHEED pattern of a smooth Si (100) surface at 550°C right before the

deposition of Sn, showing a (2×1) reconstruction characteristic of smooth and clean

Si (100). Figures 5.10(b)-5.10(d) show RHEED patterns for different amounts of Sn

coverage at 550°C: (6×2) for 0.375-0.5 ML, c(4×8) for 0.5-1.0 ML, and (5×1) for 1.0-

1.5 ML, respectively. The observed Sn-induced reconstructions are in agreement

with previous studies [25-27]. After Sn deposition, growth is interrupted and the

sample is cooled down to 160°C. Si overlayer growth commences at 160°C, with a

rough surface as indicated by the spotty RHEED pattern shown in Fig. 5.10(e). After

deposition of about 3-6 nm of Si at 160°C, the temperature is increased again.

Beyond about 350°C, the overlayer surface begins to smoothen and (2×1) Si (100)

surface reconstruction returns, as shown in Fig. 5.10(f). As the temperature is

increased higher, the surface morphology returns back to smooth Si (100) as shown in

Fig 5.10(a).

A typical cycle of surface evolution during growth of one period of the Sn_xSi_{1-x}/Si heterostructure is shown in Fig. 5.11. The patterns in Fig. 5.11 correspond to the

deposition cycle of a 1 nm-thick $Sn_{0.16}Si_{0.84}$/Si. Figure 5.11(a) is the RHEED pattern

of a smooth Si (100) surface at 550°C right before the deposition of Sn, showing a

(2×1) reconstruction characteristic of smooth and clean Si (100). Figure 5.11(b) is

the RHEED pattern after deposition of 0.5 nm of $Sn_{0.16}Si_{0.84}$ following a substrate

cool-down to 170°C. Due to the low growth temperature, only diffuse (1×1) Si

reconstruction lines were visible during the deposition of the alloy layer. Figures

5.11(c) and 5.11(d) are the RHEED patterns after deposition of 3 nm of Si overlayer

at 170°C and 4 nm of additional Si overlayer at 300°C, respectively. The return of

(2×1) Si (100) reconstruction is clearly evident in Fig. 5.11(d). As the temperature is

increased higher, the surface morphology returns back to smooth Si (100) as shown in

Fig 5.11(a).
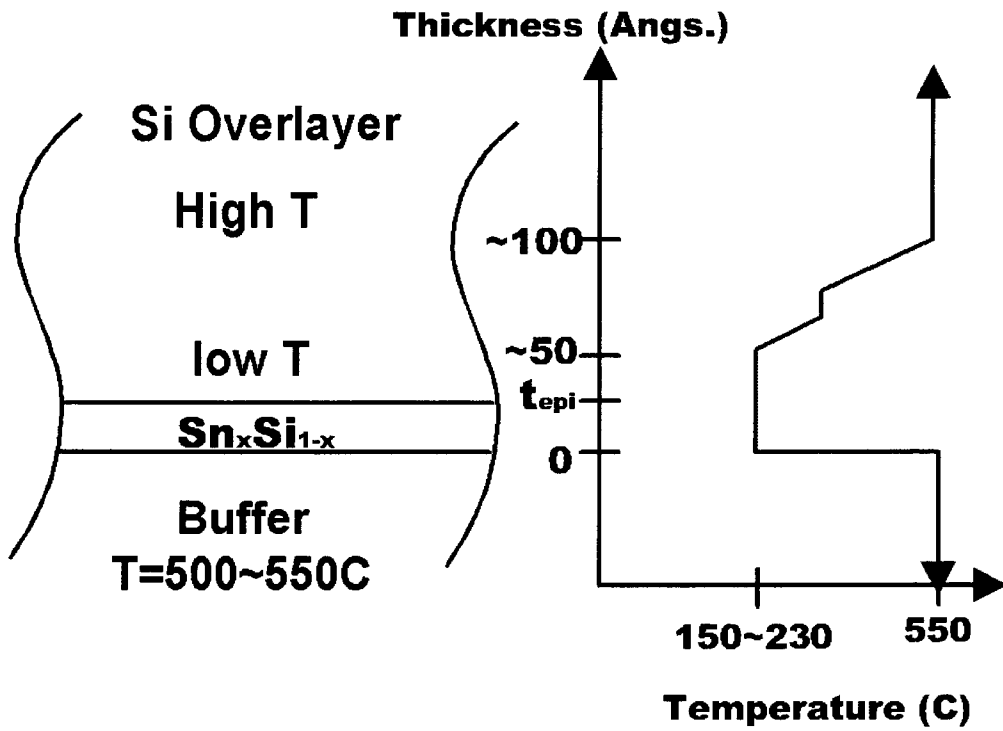
Figure 5.9. A schematic illustration of temperature modulation in the growth of ultrathin α-Sn/Si and Sn_xSi_{1-x}/Si heterostructures by molecular beam epitaxy.
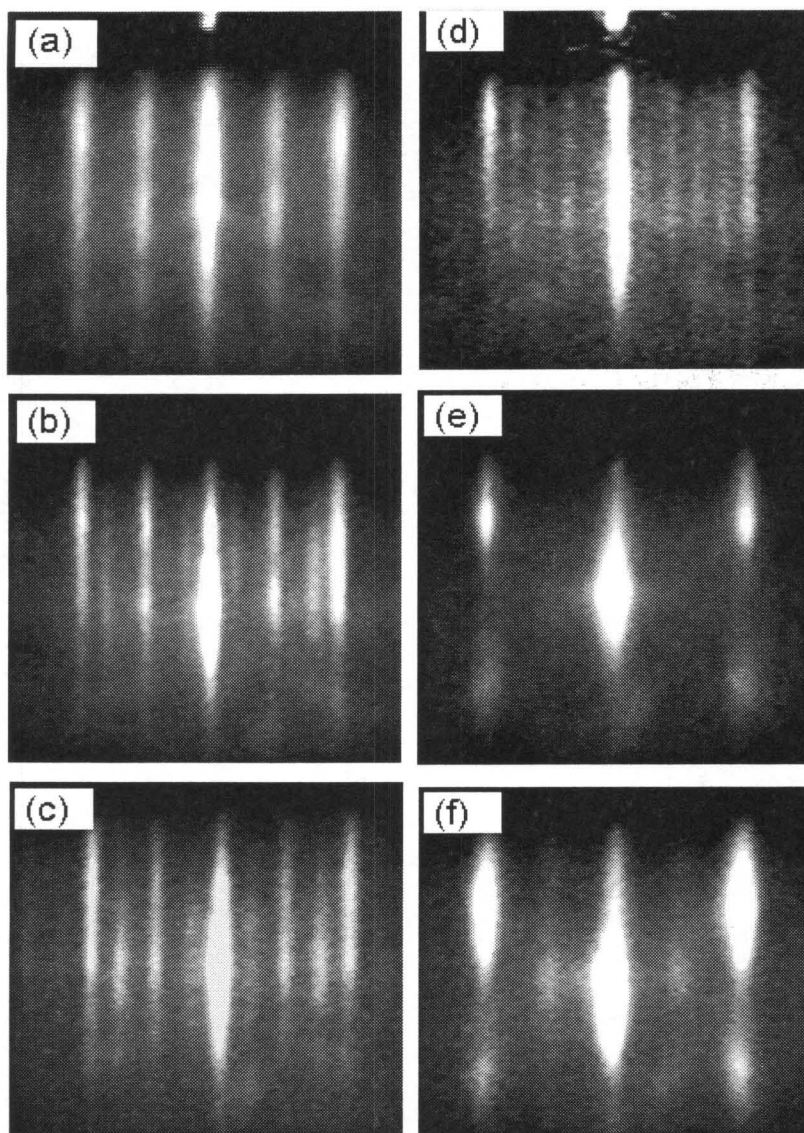
Figure 5.10. *In situ* reflection high-energy electron diffraction patterns along the [011] direction for a typical cycle of growth of α-Sn/Si (100) heterostructures: (a) a smooth (2×1) reconstructed Si (100) surface at 550°C right before the deposition of Sn; at various Sn coverage on Smooth Si (100): (b) (6×2) at converges of 0.375–0.5 ML, (c) c(4×8) at 0.5–1.0 ML, and (d) (5×1) at 1.0–1.5 ML; after deposition of (e) 1.5 nm of initial Si overlayer (160°C) and (f) 7.5 nm of Si overlayer (350°C).
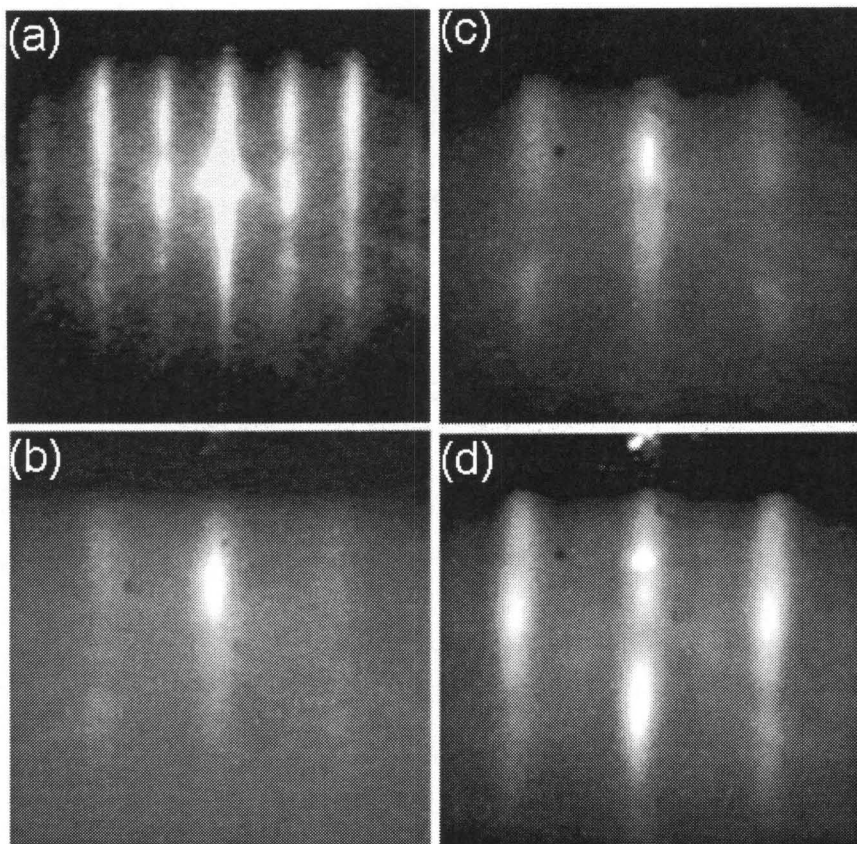
Figure 5.11. *In situ* reflection high-energy electron diffraction patterns for a cycle of growth of Sn_xSi_{1-x}/Si heterostructures: (a) a smooth (2×1) reconstructed Si (100) surface at 550°C right before the deposition of Sn; (b) after deposition of 0.5 nm of $Sn_{0.16}Si_{0.84}$ at 170°C; (c) after deposition of 3 nm of initial Si overlayer at 160°C; (d) after deposition of an additional 4 nm of Si overlayer at 300°C.

5.4.2   Ultrathin Pseudomorphic α-Sn/Si and Sn$_x$Si$_{1-x}$/Si Quantum Well Heterostructures

In this section the growth properties of ultrathin, coherently strained α-Sn/Si and Sn$_x$Si$_{1-x}$/Si alloy quantum well structures with substitutional Sn incorporation far in excess of the equilibrium solubility limit is presented. These heterostructures have been fabricated by a modified molecular beam epitaxy technique where the substrate temperature and growth flux are modulated as described in Section 5.4.1. α-Sn/Si single and multiple quantum wells with Sn coverage up to 1.3 ML (1 ML=6.79×10^{14}/cm^2), Sn$_{0.05}$Si$_{0.95}$/Si multiple quantum wells of up to 2.0 nm, and Sn$_{0.16}$Si$_{0.84}$/Si multiple quantum wells of up to 1.1 nm are determined to be pseudomorphic. The critical thickness for coherent growth and coverage dependent Sn segregation dynamics are investigated.

The films were grown by temperature-modulated molecular beam epitaxy described in Section 5.4.1. Samples were analyzed by cross-sectional transmission electron microscopy, Rutherford backscattering spectrometry, and high-resolution X-ray rocking curve analysis. Four types of sample configurations were investigated:

(i)   Single 0.49–1.4 ML Sn layers sandwiched between Si, with 140 nm–170 nm Si cap layers (single α-Sn/Si quantum well structures);

(ii)   Multiple 1.3 ML Sn layers sandwiched between Si, with 115 nm Si spacer and cap layers (multiple α-Sn/Si quantum well structures);

(iii)   Multiple 2 nm Sn_xSi_{1-x} (x=0.02, 0.05, and 0.10) layers sandwiched between Si with 78 nm Si spacer and cap layers (multiple Sn_xSi_{1-x}/Si quantum well structures);

(iv)   Multiple 1.1 nm Sn_xSi_{1-x} (x=0.10, 0.16, and 0.25) layers sandwiched between Si with 79 nm Si spacer and cap layers (multiple Sn_xSi_{1-x}/Si quantum well structures).

A summary of incorporated Sn versus Sn segregated to the surface per buried layer is given in Table 5.1, as determined from Rutherford backscattering spectroscopy. For α-Sn/Si structures, the temperature indicated is the temperature at which the initial Si overlayer was deposited after the Sn layer was deposited. For Sn_xSi_{1-x}/Si structures, the indicated temperature is the temperature at which the alloy layer and a subsequent thin Si overlayer was deposited. For all Sn_xSi_{1-x}/Si multiple quantum well structures, the fraction of Sn segregated to the surface was low (<2%) for temperatures between 110°C and 170°C. For α-Sn/Si structures, the segregated fraction increases sharply above a critical initial coverage of about 1.4 ML. This is illustrated in Fig. 5.12 which shows the fraction of Sn segregated to the surface as a function of initial coverage for single Sn layers capped with Si at 140°C and 170°C. For both temperatures, the segregated fraction increases sharply above about 1.4 ML. It is noteworthy that this coverage coincides with the predicted coverage for completion of the (5×1) surface reconstruction phase by Baski *et al.* [27], who viewed the (5×1) phase as a half-complete layer of Sn dimers over a complete c(4×8) phase of a monolayer of symmetrically dimerized Sn. The fact that islanding follows (5×1)

phase suggests that it may become more energetically favorable to relieve the surface strain by means of segregating Sn in excess of a complete (5×1) phase (~ 1.4 ML) to the surface even at such low temperatures.

Figure 5.13 shows a summary of the analyzed samples, plotted on a thickness versus Sn fraction/misfit plot. The filled upward triangles represent pseudomorphic films and the empty downward triangles represent films that have undergone partial strain-relaxation by introduction of dislocations and/or stacking faults, as observed in transmission electron microscopy. The solid line is a calculation of the critical thickness h_{crit} for introduction of misfit dislocations described in Section 5.2.3, using a model originally proposed by van der Merwe [24]. It should be noted that this type of model has only schematic value beyond about 4% mismatch, because the calculated critical thickness is sub-monolayer in this range. The Sn fraction in Fig. 5.13 represents the amount of incorporated Sn in the film, as determined by Rutherford backscattering spectroscopy, which is less than the total amount deposited because the amount of Sn beyond a critical coverage segregates to the surface.

Figure 5.14 shows the Rutherford backscattering spectrum of a multiple α-Sn/Si quantum well structure with 4 periods of 1.3 ML Sn layers sandwiched between 115 nm Si spacer layers. The large scattering cross section of Sn and the large relative mass ratio between Sn and Si, enable very accurate measurements of the absolute Sn coverage. The sample tilt angle was 60 degrees. The increased energy width in the spectrum at increased Sn layer depth in the film is primarily due to He^{++} ion energy straggling. Within the resolution of RBS, no significant interdiffusion has occurred, despite anneals at temperatures far exceeding the melting temperature of Sn.

Figure 5.15 shows cross-sectional transmission electron micrographs of the sample described in Fig. 5.14. Figure 5.15(a) is a bright field image taken under (400) 2-beam excitation showing the first 3 layers. The interfaces are sharp, with no dislocations or stacking faults. Figure 5.15(b) is a high-resolution image in the [110] projection of one of the layers shown in Fig. 5.15(a). No growth-related defects were visible within the analyzed region. The Sn layers in both images appear thicker due to strain contrast below and above each buried Sn; nonetheless, it is evident in Fig. 5.15(b) that the incorporated Sn is localized within a few atomic layers.

Figure 5.16(a) shows a bright field transmission electron micrograph showing 3 layers of 1.1 nm $Si_{0.84}Sn_{0.16}$ separated by 78 nm-thick Si spacer layers, taken under (400) two-beam excitation. The lowest dark band is the substrate/buffer interface. Fig. 5.16(b) shows the high-resolution transmission electron micrograph in the [110] projection of one of the layers in Fig. 5.16(a). Although no extended defects are observed, the interfaces of the individual layers are not sharply defined. What appears to be interface roughness in these micrographs may actually be spatial modulations in the composition resulting from phase separation of the initially homogeneous alloy layer into Sn-rich and Sn-deficient regions during the high-temperature spacer layer growth. This leads to formation of nanometer-sized Sn-rich Sn_xSi_{1-x} quantum dots, whose growth mechanism will be discussed extensively in Chapter 6.

Figure 5.17 shows a bright field transmission electron micrographs showing 3 layers of 1.1 nm $Si_{0.75}Sn_{0.25}$ separated by 79 nm-thick Si spacer layers, taken under (400) two-beam excitation. Strain relaxation by means of stacking faults are clearly

observed, as has been summarized in Fig. 5.13. Again, spatial modulations in the composition caused by phase separation of the initially homogeneous alloy layer are observed.

Single α-Sn/Si quantum well structures with Sn layers of 0.49±0.09 ML, 0.93±0.09 ML, and 1.3±0.1 ML sandwiched between Si with 140 nm−170 nm Si cap layers were analyzed using X-ray rocking curve analysis. Figures 5.18(a) and 5.18(b) show representative X-ray rocking curves of symmetric (400) and asymmetric (422) reflections, respectively. The dotted curves represent experimental data for the film with a single layer of 0.93±0.09 ML Sn capped with 162 nm of Si, as determined by RBS. The solid curves represent dynamical simulations [28] for a model film with 0.15 nm Sn capped with 163 nm Si. The intensity match between the simulation and the experimental curve for the (422) asymmetric reflection is not as good as the (400) symmetric case because a broad background due to surface and/or interface roughness is intensified in the glancing angle geometry. The simulations were performed under the assumption of a tetragonally distorted α-Sn unit cell with the bulk lattice constant of 0.64890 nm (in-plane lattice constant of 0.54310 nm and perpendicular lattice constant of 0.73875 nm) and bulk elastic constants. Several features about the interference fringes are noteworthy. The angular distance between Pendellösung fringes is independent of the physical properties of the sandwiched layer. However, the angular position and the intensity of the interference fringes near the (400) Si reflection depend strongly on the factors that cause dephasing of X-rays scattered from the Si cap layer and the Si substrate. Because of the large atomic size difference between Sn and Si, analysis of the angular position and the intensity of the

interference fringes offer a very sensitive technique for quantitatively characterizing

low coverage Sn incorporation, enabling thickness resolution within a fraction of a

monolayer. As can be seen in Figs. 5.18(a) and 5.18(b), the interference fringes of

the simulation curves match that of the experimental curves very well. The best

values of Sn thickness determined from the dynamical X-ray simulation for (400)

symmetric reflections of films with Sn coverage of 0.49±0.09 ML, 0.93±0.09 ML,

and 1.3±0.1 ML, as determined by Rutherford backscattering spectrometry, were 0.07

nm, 0.15 nm, and 0.17 nm, respectively. The thickness determined from the

dynamical X-ray simulation is, however, lower than the expected thickness from a

tetragonally distorted α-Sn on Si. The tetragonally distorted lattice parameter $a_\perp$

perpendicular to the growth direction is given by

$$a_\perp = a_f \left[1 - \frac{2C_{12}}{C_{11}} \left(\frac{a_s}{a_f} - 1 \right) \right] \tag{5.3}$$

where C_{11} and C_{12} are elastic constants and a_f and a_s are the relaxed lattice parameters

of the film substrate, respectively. For the Sn coverage of 0.49±0.09 ML, 0.93±0.09

ML, and 1.3±0.1 ML, the expected values of thickness for pseudomorphic and

tetragonally distorted α-Sn on (100) Si from Eq. (5.3) are 0.090±0.009 nm, 0.17±0.02

nm, and 0.24±0.02 nm, respectively. Figure 5.19 summarizes the comparison

between the values for thickness expected by Eq. (5.3) under the assumption that all

Sn atoms measured by RBS are in their tetragonally distorted regular diamond cubic

cell sites and the thickness obtained from dynamical X-ray simulation [23]. It can be

seen that the thickness values obtained from dynamical X-ray simulation are always

lower than that calculated from the coverage measured by RBS, and that the difference increases with increasing coverage. One possible source of discrepancy is the deviation of the Sn profile from an atomically sharp delta function profile. An exponentially decaying Sn profile in the growth direction can be expected when partial segregation of deposited Sn occurs in the initial overlayer (4-6 nm) deposited at low temperatures. The second possible explanation is that a fraction of the deposited Sn atoms is not in substitutional diamond cubic lattice sites but in an interstitial site. Third possibility is that a local strain relaxation in the Si-Sn bond length results in a significant departure of the actual Si-Sn bond lengths from the virtual crystal approximation. Finally, the sandwiched ultrathin layers may form an ordered structure with Si-Sn bond lengths departing from the predictions of the virtual crystal approximation.

Sample	Temp.($^{\circ}$C)	Initial Sn Coverage per Layer (ML)	Fraction Segregated
(i) Single Sn/Si	170°C	0.52[a], 1.0[a]	<0.05
		1.4	0.09
		1.7	0.23
		2.2	0.52
(ii) Multiple Sn/Si	130°C	1.3[a]	<0.02
	120°C	2.1[b]	0.32
(iii) Multiple 2.0 nm Si$_{1-x}$Sn$_x$/Si	140°C	0.30[a], 0.76[a], 1.5[b] (x=0.02[a], 0.05[a], 0.10[b])	<0.02
(iii) Multiple 1.1 nm Si$_{1-x}$Sn$_x$/Si	110°C	0.74[a], 1.5[a], 1.9[b] (x=0.10[a] 0.16[a], 0.25[b])	<0.02

[a]determined to be pseudomorphic by cross-sectional TEM.

[b]determined to be at least partially relaxed by cross-sectional TEM.

Table 5.1. A summary of incorporated Sn versus Sn segregated to the surface per buried layer.
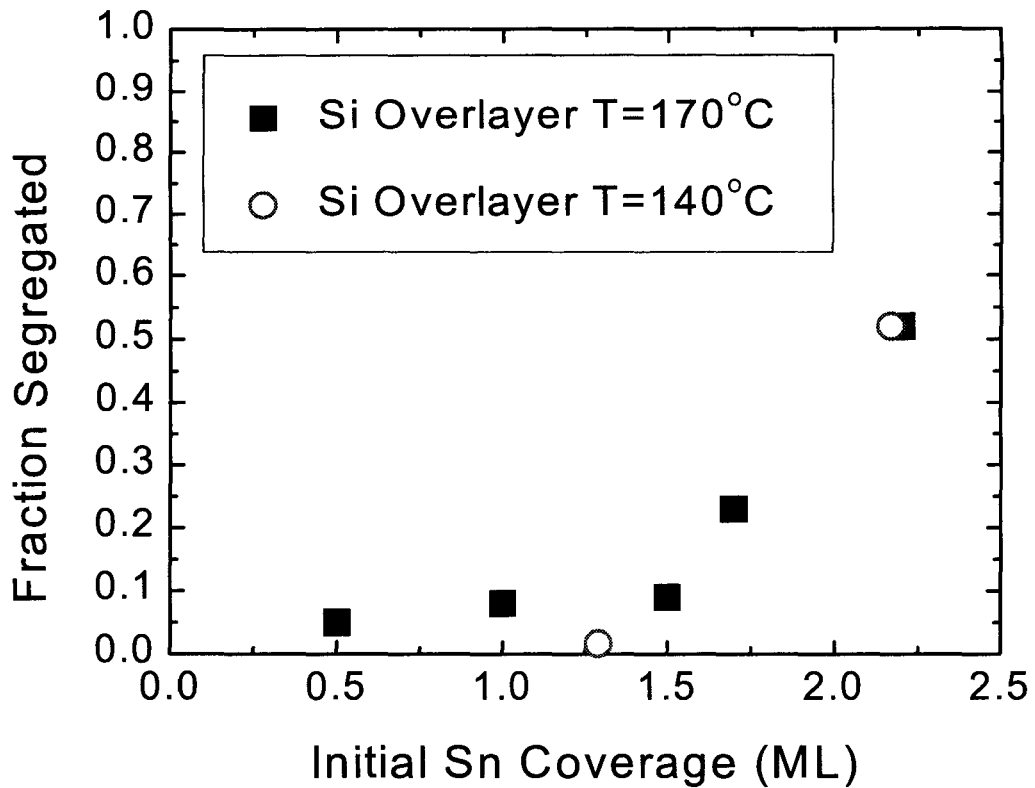
Figure 5.12. Fraction of Sn segregated to the surface for single Sn layers capped with 140 nm–170 nm of Si at 140°C and 170°C, as a function of initial Sn coverage. The segregated fraction increases sharply above the coverage of about 1.4 monolayers.
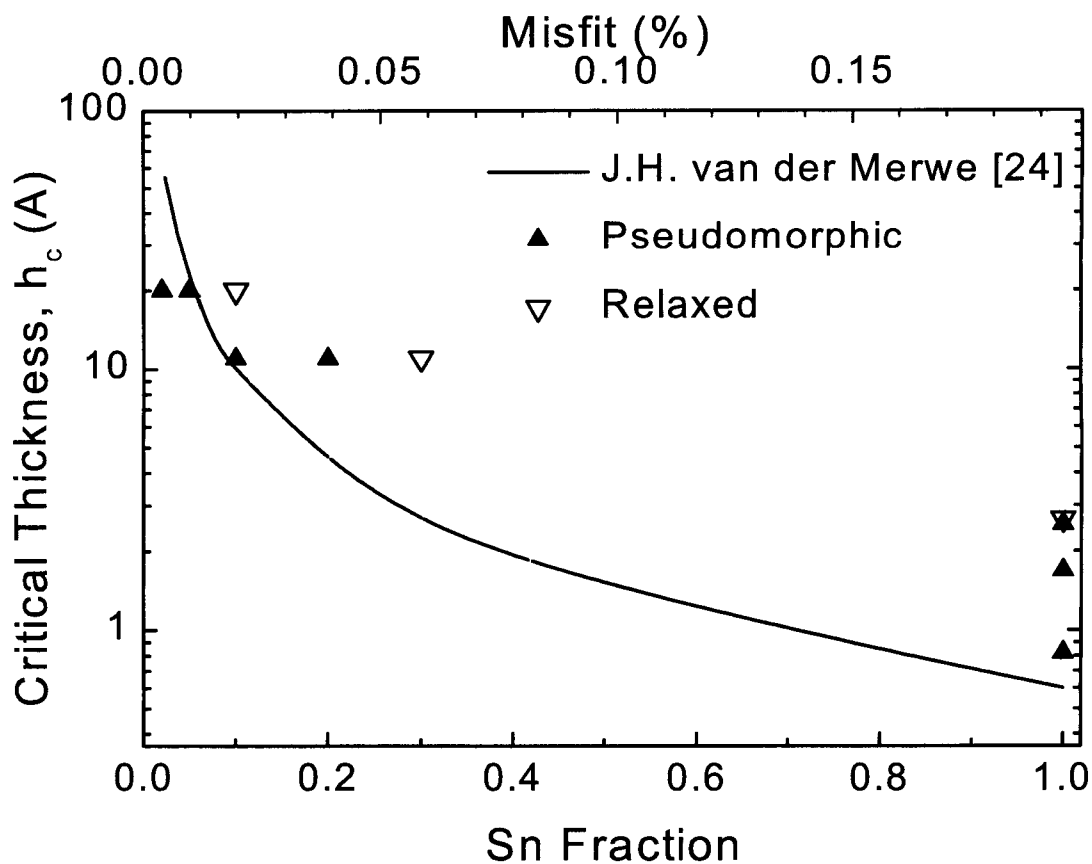
Figure 5.13. A summary of sample strain states. The filled upward and empty downward triangles are pseudomorphic and partially strain-relieved films, respectively, as determined by transmission electron microscopy. The solid line is a calculation of the critical thickness h_c for introduction of misfit dislocations, using the model of van der Merwe [24].
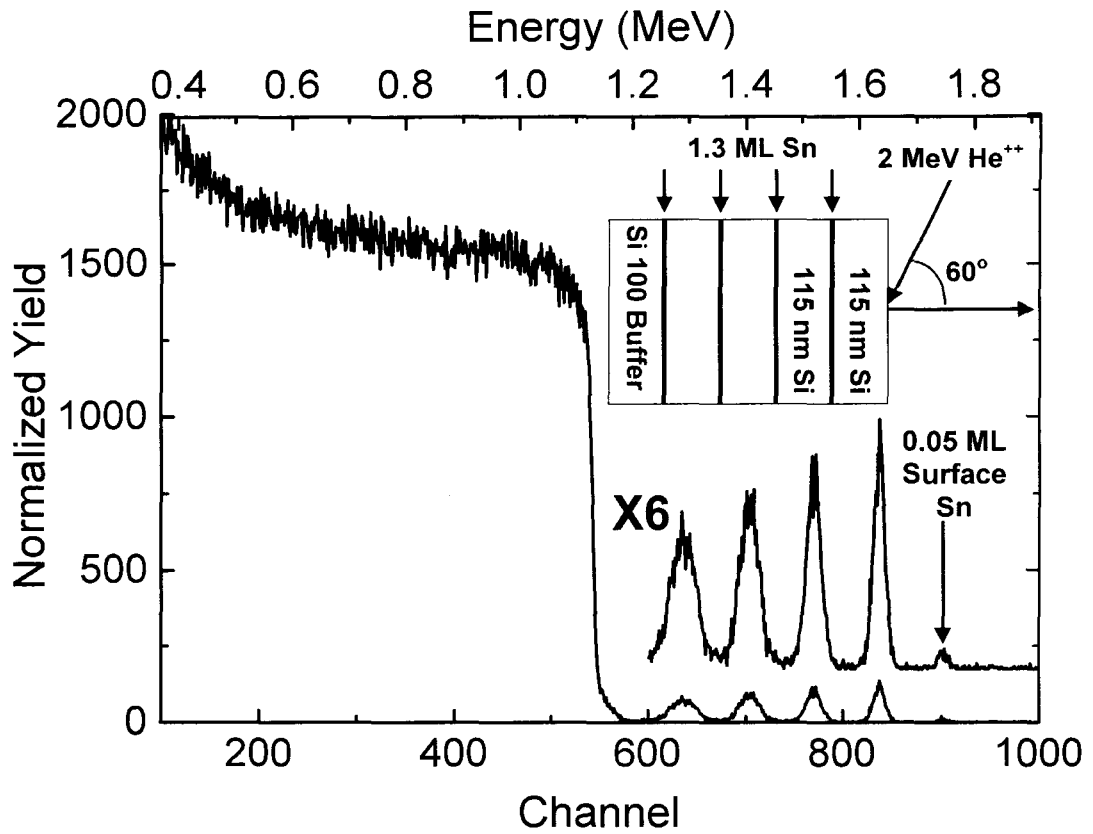
Figure 5.14. Rutherford backscattering spectrum of a multiple α-Sn/Si quantum well structure with 4 periods of 1.3 ML Sn layers sandwiched between 115 nm Si spacer layers.
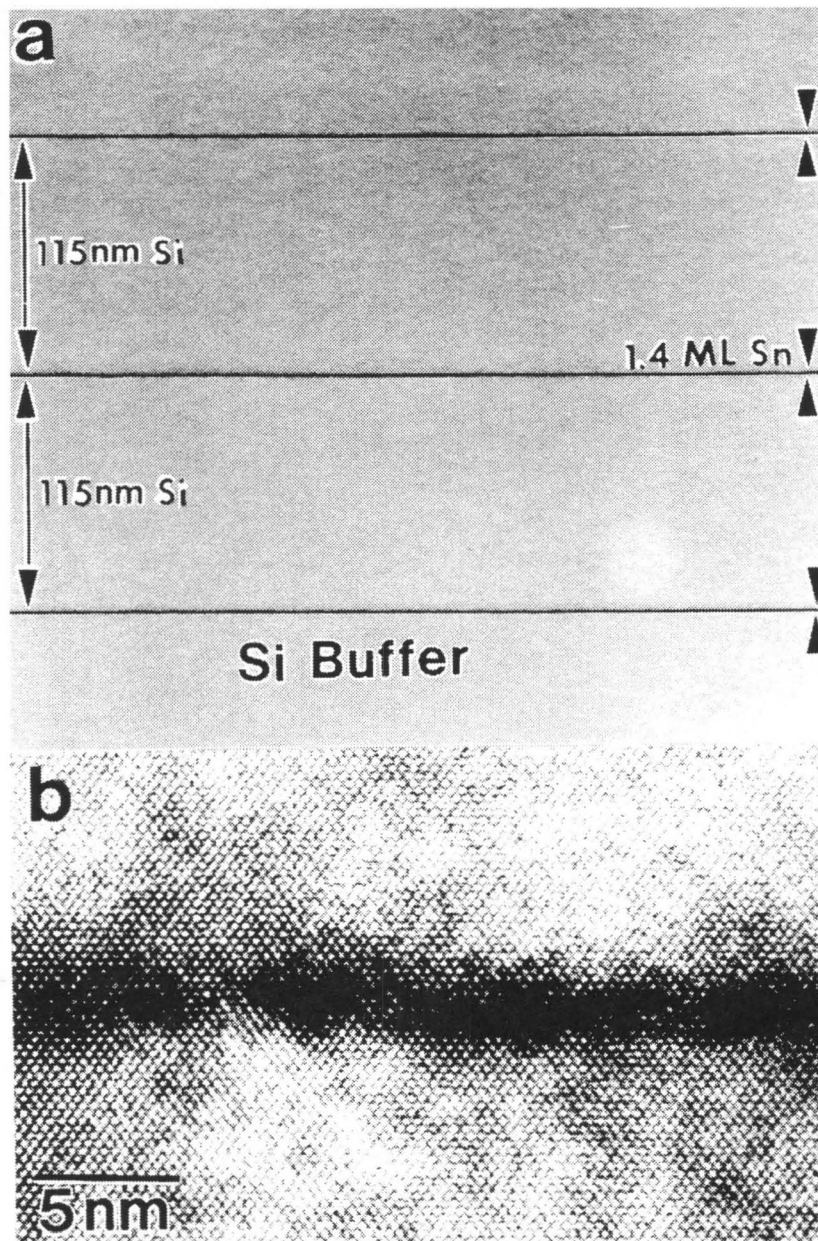
Figure 5.15. Cross-sectional transmission electron micrographs of sample in Fig. 5.14. In (a), bright field image taken under (400) 2-beam excitation showing the first 3 Sn layers; in (b), high-resolution image in the [110] projection of one of the Sn layers.
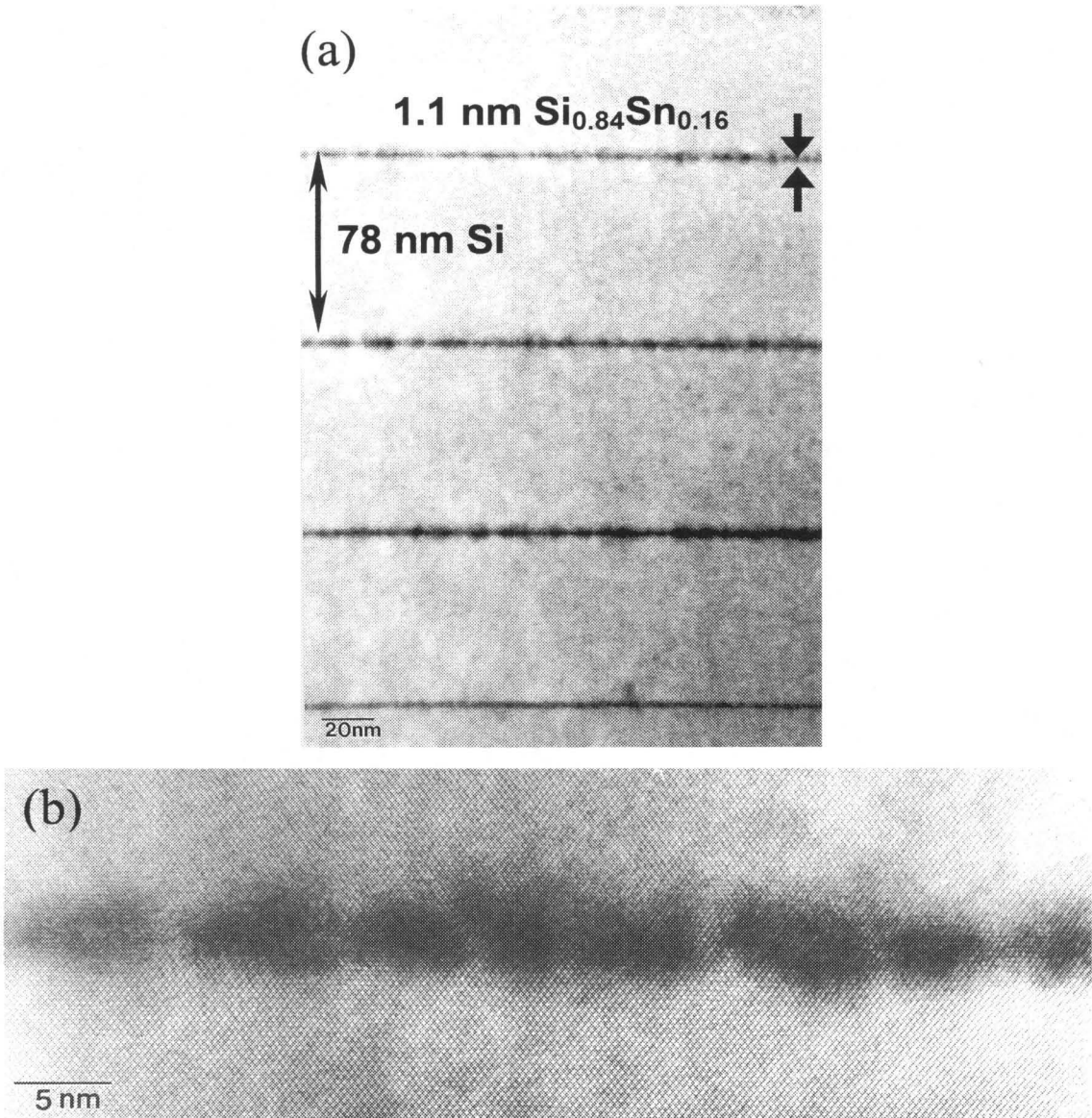
Figure 5.16. (a) Bright field transmission electron micrograph of 3 layers of 1.1 nm $Si_{0.84}Sn_{0.16}$ separated by 78 nm-thick Si spacer layers, taken under (400) two-beam excitation. The lowest dark band is the substrate/buffer interface. (b) High-resolution transmission electron micrograph of one of the layers in the [110] projection of one of the Sn layers. No extended defects are observed.
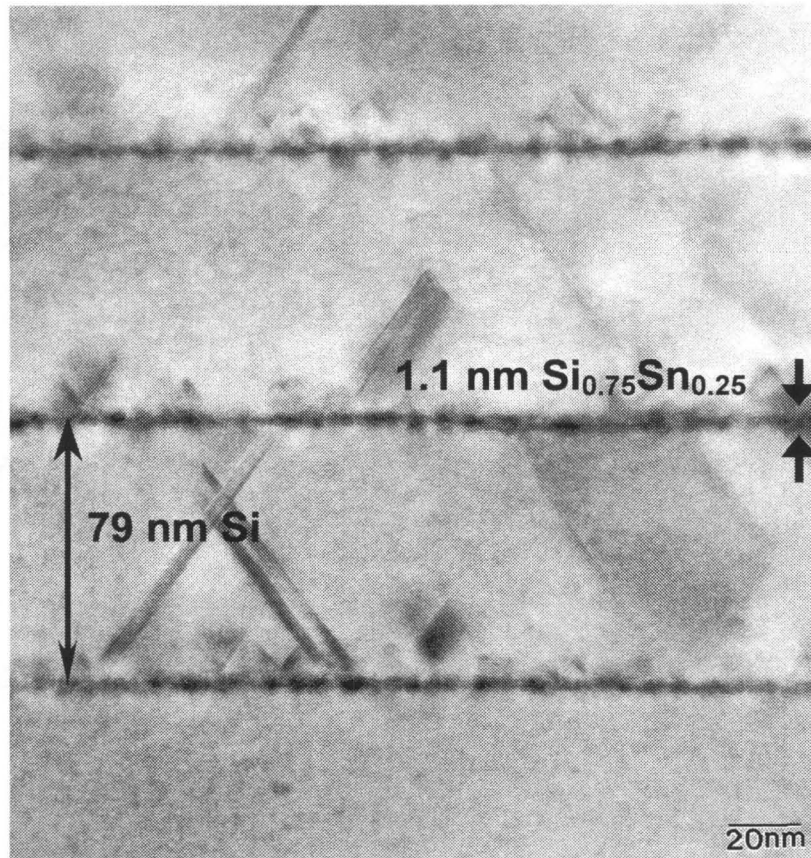
Figure 5.17. Bright field transmission electron micrograph of 3 layers of 1.1 nm $Si_{0.75}Sn_{0.25}$ separated by 79 nm-thick Si spacer layers, taken under (400) two-beam excitation. Strain relaxation by means of stacking fault generation is clearly observed at all interfaces.
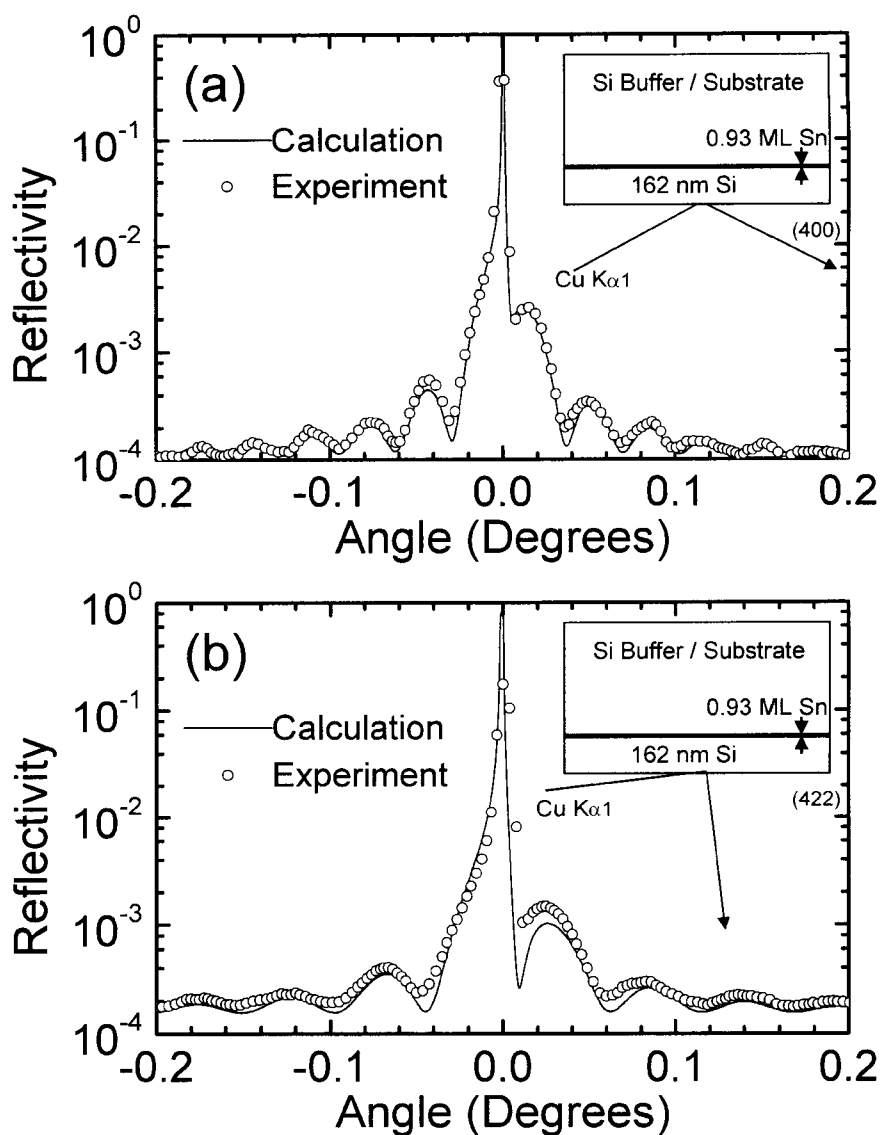
Figure 5.18. (a) Symmetric (400) reflection and (b) asymmetric (422) X-ray rocking curves of a single α-Sn/Si quantum well structure with 0.93 ML Sn sandwiched between Si with 162 nm Si cap layer, as determined by Rutherford backscattering spectrometry. The dotted curves represent the experimental data and the solid curves represent dynamical simulations [28] for 0.15 nm Sn capped with 163 nm.
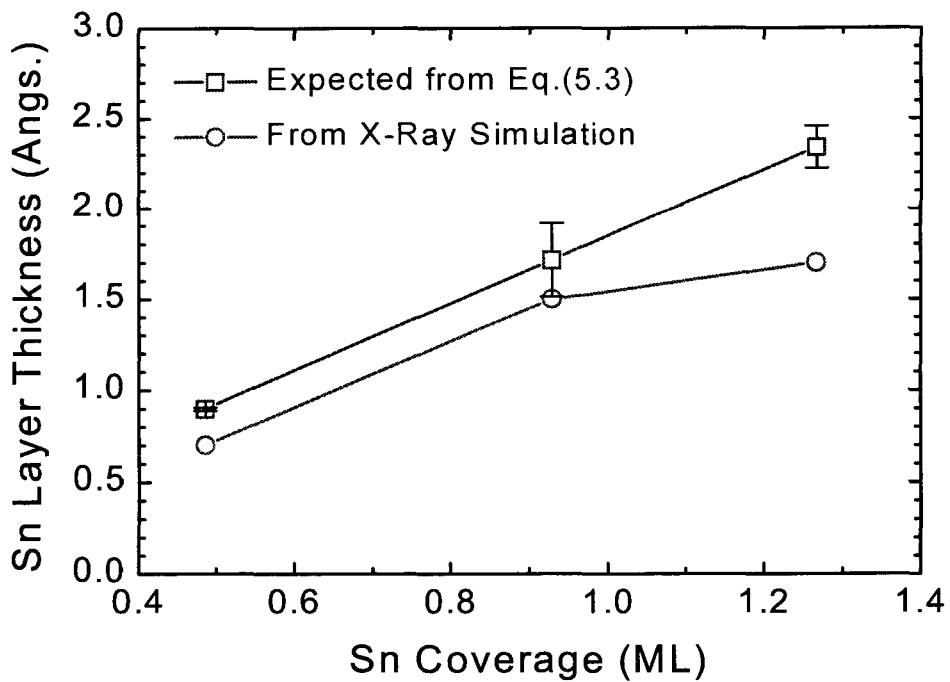
Figure 5.19. A comparison between the values of Sn layer thickness expected by Eq. (5.3) under the assumption that all Sn atoms measured by Rutherford backscattering spectra are in their tetragonally distorted regular diamond cubic cell sites versus the thickness obtained from dynamical X-ray simulation [28]. The vertical error bars indicate the uncertainty in the calculated thickness arising from the uncertainty in the measured Sn coverage from Rutherford backscattering spectra.

5.4.3   Pseudomorphic α-Sn/Si Quantum Well Superlattice Structures

It has been demonstrated from the study on samples consisting of single α-Sn/Si quantum well structures in Section 5.4.2 that initial Sn coverage in excess of about 1.4 monolayers (ML) segregates to the surface during the Si overlayer growth even at temperatures as low as 120°C [34]. It has also been demonstrated that the Si overlayer relaxes when the deposited Sn layer thickness exceeds about 1.4 ML. This suggests that 1.4 ML represent a kinetic critical thickness t_C for commensurate growth of the individual Sn layers. In strained-layer superlattice growth, however, there are two critical thicknesses [35]: the critical thickness t_C for the individual strained layers and the critical thickness t_{SL} for the overall superlattice. Even if the individual strained layers are below t_C, the superlattice could still relax if the strain energy integrated over the entire film exceeds the t_{SL}. This suggests that one should be able to grow commensurate α-Sn/Si quantum well superlattice structures up to t_{SL} for individual Sn layer thickness less than t_C=1.4 ML.

Motivated by the possibility of realization of a novel group IV semiconductor with a direct energy gap, superlattices of α-Sn/Ge [30,36], α-Sn/Ge/Si/Ge [37], and Sn_xGe_{1-x}/Ge [38] have been synthesized by means of low temperature and temperature-modulated molecular beam epitaxy. In this section, growth and structural characterization of coherently strained α-Sn/Si superlattice structures is presented. Severe Sn segregation to the surface during growth, which prevents

growth of these structures at ordinary Si epitaxy temperatures, has been minimized by substrate temperature and growth rate modulations during molecular beam epitaxy described in Section 5.4.1. The investigated superlattice structures consisted of 7–10 periods of 1.0 ML Sn sandwiched between 8–27 nm Si spacer layers. Pseudomorphic superlattices with up to 10 periods of 1 ML Sn/7.7 nm Si have been verified to be free of extended defects.

Surface morphology and reconstruction was analyzed using *in situ* reflection high energy electron diffraction for the growth of Sn and Si overlayers. A typical cycle of surface evolution during growth of the Sn layer on smooth Si followed by a Si overlayer growth has been shown in Fig. 5.10 in Section 5.4.1. The Sn-induced reconstructions observed by RHEED were in agreement with previous observations [25-27]: (6×2) for 0.375–0.5 ML, c(4×8) for 0.5–1.0 ML, and (5×1) for 1.0–1.5 ML. After Sn deposition, growth is interrupted and the sample is cooled down to 160°C. Si overlayer growth commences at 160°C, with a rough surface as indicated by the spotty RHEED pattern shown in Fig. 5.10(e). After deposition of about 3–6 nm of Si at 160°C, the temperature is increased again. Beyond about 350°C, the overlayer surface begins to smoothen and (2x1) Si (100) surface reconstruction returns, as shown in Fig. 5.10(f). As the temperature is increased higher, the surface morphology returns back to smooth Si (100) as shown in Fig 5.10(a).

Crystal quality of selected samples was analyzed by cross-sectional transmission electron microscopy. Figures 5.20(a) and 5.20(b) show bright field images taken under (400) 2-beam excitation of an 8-period superlattice of 1 ML

Sn/7.7 nm Si and a 10-period superlattice of 1 ML Sn/20.5 nm Si, respectively. No growth-related extended defects are visible within the imaged electron-transparent area (dislocation density $\sim<1 \times 10^6$ cm^{-2}). Figure 5.20(c) is a high-resolution image of one of the Sn layers of the sample in Fig. 5.20(b) taken in the [110] projection. The Sn layers appear thicker than a monolayer, most likely due to two reasons. First, the embedded Sn layer is highly strained, giving rise to high strain contrast in addition to mass-thickness contrast in the vicinity of the Sn layer. Second, as demonstrated previously [30] for the case of short period α-Sn/Ge superlattices, the Sn layer may not be atomically abrupt; the Sn atoms may be distributed over few atomic layer in an exponentially decaying profile. From the X-ray rocking curve analysis, however, it is evident that the distribution cannot be spread over more than a few ($\sim<5$) monolayers [34].

Figure 5.21 shows a representative high-resolution X-ray rocking curve of the superlattice structures analyzed. The dotted curve shows a high-resolution scan around Si (004) of the 10-period 1 ML Sn/20.5 nm Si superlattice shown in Figs. 5.20(b) and 5.20(c). Well-defined fundamental (SL$_0$) and higher order (SL$_{-1}$, SL$_{\pm2}$) superlattice peaks as well as interference fringes are clearly identified. From the position of the peaks, an accurate measurement of the average periodicity can be obtained. The periodicity of the superlattice can be accurately determined from the angular spacing $\Delta\theta$ between adjacent superlattice peaks through the relationship

$$\Delta\theta = \frac{\lambda|\gamma_h|}{t \sin 2\theta_B} \qquad (5.4)$$

where t is the thickness of one period, λ is the wavelength of the radiation, θ_B is the

Bragg angle, and γ_h is the direction cosine of the diffracted beam. The superlattice

periodicity can be determined to within ± 0.1 nm using Eq. (5.4). For the film in Fig.

5.21, the superlattice periodicity was determined to be 20.7 nm. In addition, the

number of Pendellösung oscillations of angular spacing $\Delta\omega$ within the superlattice

periodicity $\Delta\theta$ gives the number of periods. From the position of the "SL_0" peak, an

equivalent average concentration can be determined. For the film in Fig. 5.21, the

equivalent strain is that of 20.7 nm film of 0.6% average Sn concentration. From a

similar analysis of the 8-period superlattice of 1 ML Sn/7.7 nm Si shown in Fig.

5.20(a), the highest equivalent strain achieved was determined to be that of 61.6 nm

1.8% average Sn concentration (0.4% strain). A summary of pseudomorphic

superlattice structures, plotted on a thickness versus misfit scale, is plotted in Fig.

5.22. The filled upward triangles represent pseudomorphic films that have not

undergone any strain-relaxation, as verified by transmission electron microscopy.

The solid lines are calculations of the critical thickness h_{crit} for the introduction of

misfit dislocations described in Section 5.2.3, using the models by Mathews and

Blakeslee [22] and van der Merwe [24].

The angular distance between superlattice peaks and Pendellösung fringes is

independent of the physical properties of the sandwiched layer. However, the angular

position and the intensity of the interference fringes near the (004) Si reflection

depend strongly on the factors that cause dephasing of X-rays scattered between the

superlattice layers and the Si substrate. Because of the large atomic size difference

between Sn and Si, analysis of the angular position and the intensity of the

interference fringes offer a very sensitive technique for quantitatively characterizing low coverage Sn incorporation, enabling thickness resolution within a fraction of a monolayer. The amount of incorporated Sn can be measured from the best theoretical fit to the experimental curve. The solid curve in Fig. 5.21 is the best dynamical simulation curve of a model structure of 10 periods of 1 ML Sn/20.5 nm Si, capped with 59 nm Si [28]. The simulation was performed under the assumption of atomically abrupt interfaces and tetragonally distorted α-Sn unit cell with the bulk lattice constant of 0.64890 nm (in-plane lattice constant of 0.54310 nm and perpendicular lattice constant of 0.73875 nm) and bulk elastic constants. The peak positions as well as the shape and intensities of the satellite peaks are in very good agreement with the experimental curve. The fact that both the peak positions as well as the relative intensities match well suggests that the interfaces are sharp, with most Sn atoms localized within about one unit cell thickness.
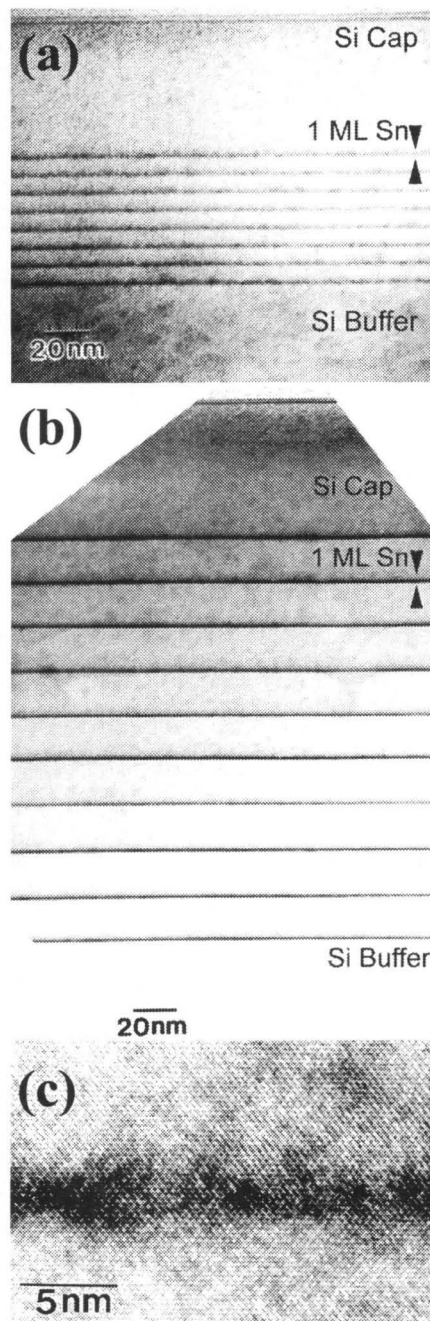
Figure 5.20. Bright field transmission electron micrographs taken under (400) 2-beam excitation of (a) an 8-period superlattice of 1 ML Sn/7.7 nm Si and (b) a 10-period superlattice of 1 ML Sn/20.5 nm Si. A high-resolution image of one of the Sn layers of the sample in (b) is shown in (c).
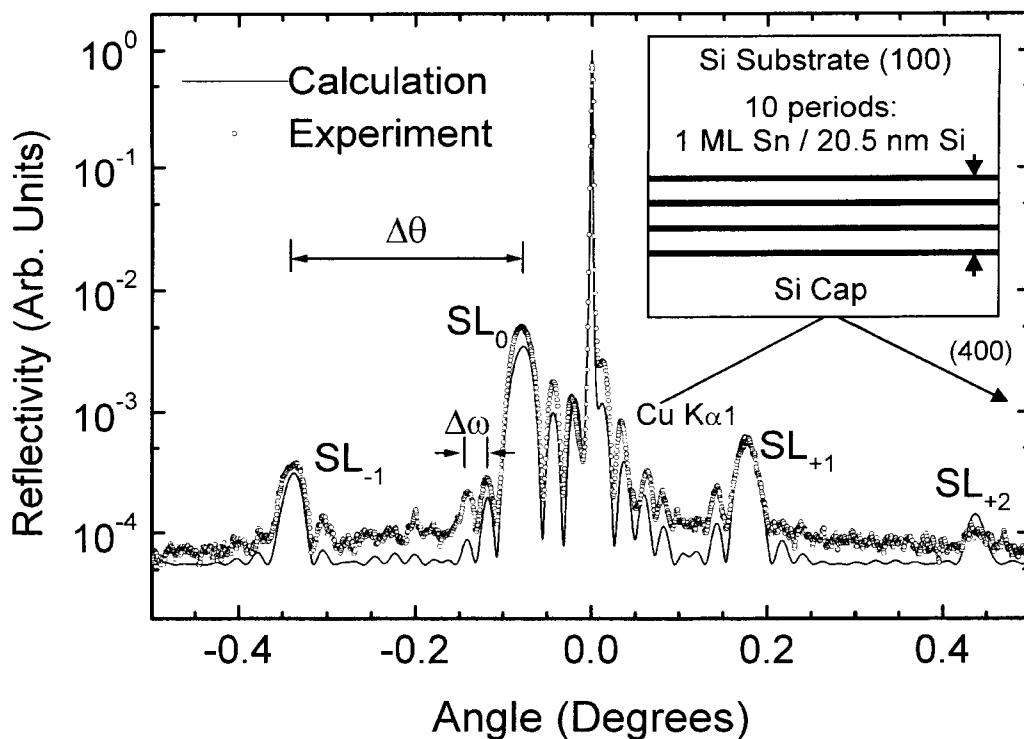
Figure 5.21. A representative symmetric (004) reflection high-resolution X-ray rocking curve of the superlattice structures. The dotted curve is a scan around Si (004) of the 10-period 1 ML Sn/20.5 nm Si superlattice shown in Figs. 5.20(b) and 5.20(c). The dotted curve and the solid curve represent the experimental scan and the dynamical simulation [28], respectively.
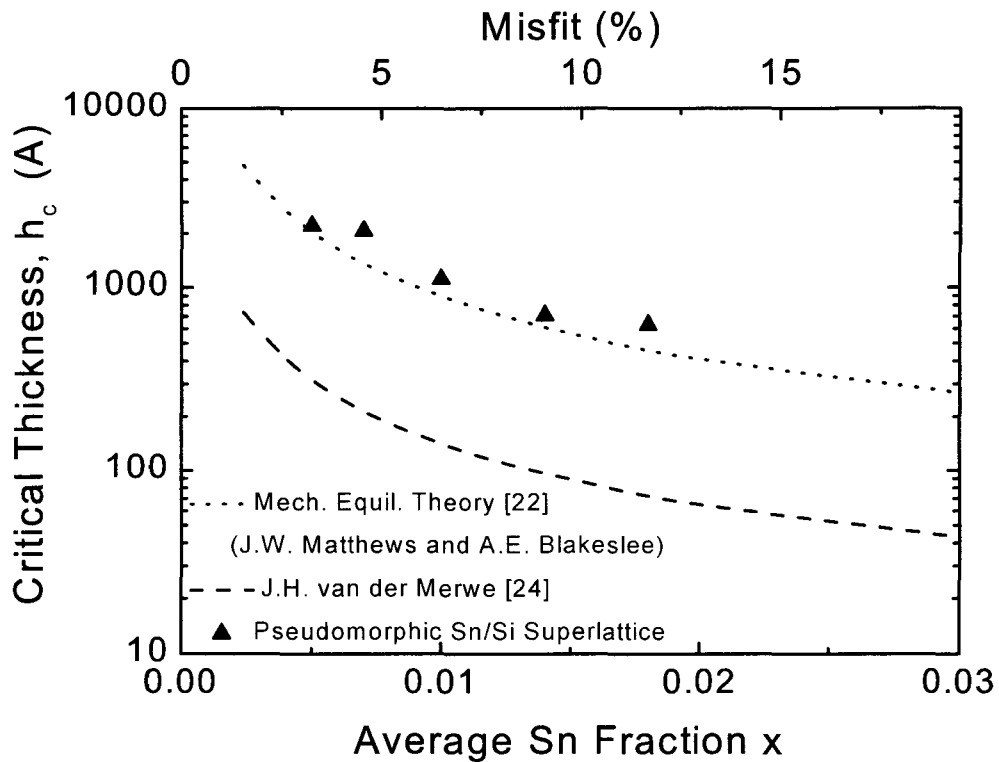
Figure 5.22. A summary of analyzed α-Sn/Si superlattice films, plotted on an

equivalent thickness versus average Sn fraction plot. The filled upward triangles

represent pseudomorphic films, as verified by transmission electron microscopy. The

solid lines are calculations of the critical thickness h_{crit} for introduction of misfit

dislocations described in Section 5.2.3 [22,24].

5.5 Conclusions

Novel heterostructures having the direct gap semimetal α-Sn as one of the constituents open up a whole new frontier in band gap engineering of group IV alloys.   Most important, the heterostructures offer an approach towards the realization of a direct gap group IV semiconductor.   In this chapter, novel heterostructures based on the Si-Sn system have been explored. Formidable barriers must be overcome for experimental realization of these heterostructures, however, due to the extremely large lattice mismatch (19%) and negligible solid solubility (<0.1%).   It has been demonstrated that due to the unfavorable thermodynamic properties of the Si-Sn system, conventional molecular beam epitaxy at ordinary temperatures for Si epitaxy (T>350°C) results in severe Sn surface segregation. In order to incorporate appreciable amounts of Sn, low temperature (T<350°C) molecular beam epitaxy has been investigated.   By means of low temperature molecular beam epitaxy, partially relaxed Sn_xSi_{1-x}/Si films with Sn concentration up to 6% and fully strained Sn_xSi_{1-x}/Si films with Sn concentration of 2.4% have been grown. Because of the large lattice mismatch, however, only dilute alloys can be grown if the thickness is to be greater than a few nanometers.

Band structure calculations suggest, however, that in order for the Sn_xSi_{1-x} alloy system to have a direct gap, the composition must be high in Sn content. The extremely large lattice mismatch between α-Sn and Si, then, requires the pure Sn or Sn_xSi_{1-x} strained alloy layer to be ultrathin for stabilization of high concentration of

Sn in a strained pseudomorphic alloy, if the epitaxial film is to remain coherent at high temperatures.

Therefore, by means of temperature-modulated molecular beam epitaxy, the growth of epitaxially stabilized ultrathin α-Sn/Si and high Sn concentration Sn_xSi_{1-x}/Si quantum well structures have been investigated. α-Sn/Si single and multiple quantum wells grown with Sn coverage up to 1.4 ML, $Si_{95}Sn_{05}$/Si multiple quantum wells of up to 2.0 nm, and $Si_{84}Sn_{16}$/Si multiple quantum wells of up to 1.1 nm are determined to be free of dislocations and stacking faults. For α-Sn/Si structures, the fraction of segregated Sn increases dramatically beyond a critical coverage of about 1.4 ML. Rutherford backscattering spectrometry, cross-sectional transmission elctron microscopy, and X-ray rocking curve analysis indicate that the Si/Sn interfaces are sharp to within a few atomic layers. Transmission electron microscopy reveals, however, interface roughness and spatial modulations in composition for the Sn_xSi_{1-x} layers arising from two-dimensional phase separation.

Also by temperature-modulated molecular beam epitaxy, α-Sn/Si superlattice structures with periods as short as 7.9 nm (Sn_1Si_{57} with average Sn concentration of ~2%) have been demonstrated to be pseudomorphic. The films analyzed have been verified to be free of extended defects by cross-sectional transmission electron microscopy and the interfaces have been verified to be sharp within the resolution of X-ray rocking curve analysis.

Bibliography

[1]   R. Soref, Mater. Res. Soc. Bull. **23**, 20 (1998).

[2]   R.A. Soref, Proc. IEEE **81**, 1687 (1993).

[3]   K. A. Johnson and N.W. Ashcroft, Phys. Rev. **B 20**, 14480 (1996).

[4]   Y. Li and P.J. Lin-Chung, Phys. Rev. **B 27**, 3465 (1983).

[5]   R.A. Soref and C. H. Perry, J. Appl. Phys. **69**, 539 (1991).

[6]   H. A. Atwater, G. He, and K. Saipetch, Mat. Res. Symp. Proc. **355**, 123 (1995).

[7]   S. Groves and W. Paul, Phys. Rev. Lett. **11**, 194 (1963).

[8]   G. He and H. A. Atwater, Phys. Rev. Lett. **79**, 1937 (1997).

[9]   S. Yu. Shiryaev, J. Lundsgaard Hansen, P. Kringhøj, and A. Nylandsted Larsen, Appl. Phys Lett. **67**, 2287 (1995).

[10]   Al-Sameen T. Khan, Paul R. Berger, Fernando J. Guarin, Subramanian S. Iyer, Appl. Phys. Lett. **68**, 3105 (1996).

[11]   B. I. Craig, Superlattices and Microstructures **12**, 1 (1992).

[12]   T.B. Massalski *et al.*, *Binary Alloy Phase Diagrams*, 2nd ed., Am. Soc. Metals, Materials Park, 1990.

[13]   W. Klemm and H. Stöhr, Z. Anorg. Chem. **241**, 305 (1939).

[14]   R.F.C. Farrow, D.S. Robertson, G.M. Williams, A.G. Cullis, G.R. Jones, I.M. Young, and P.N.J. Dennis, J. Cryst. Growth **54**, 507 (1981).

[15]   J.L. Reno and L.L. Stephenson, Appl. Phys. Lett. **54**, 2207 (1989).

[16] M.T. Asom, A.R. Kortan, L.C. Kimerling, and R.C. Farrow, Appl. Phys. Lett. **55**, 1439 (1989).

[17] T. Itoh, Jpn. J. Appl. Phys. **31**, L920 (1992).

[18] X.W. Lin, Z. Liliental-Weber, J. Washburn, E.R. Wever, A. Sasaki, A. Wakahara, and T. Hasegawa, J. Vac. Sci. Technol. **B 13**, 1805 (1995).

[19] H.J. Gossman and L.C. Feldman, Appl. Phys. Lett. **48**, 1141 (1986).

[20] S. Iwanari and K. Takayanagi, J. Cryst. Growth **119**, 229, 241 (1992).

[21] J.W. Mathews, S. Mader, and T.B. Light, J. Appl. Phys. **41**, 3800 (1970).

[22] J.W. Mathews and A.E. Blakeslee, J. Cryst. Growth **27**, 118 (1974).

[23] J.W. Mathews, J. Vac. Sci. Technol. **12**, 126 (1975).

[24] J.H. Van der Merwe, J. Appl. Phys. **34**, 123 (1962).

[25] K. Ueda, K. Kinoshita, and M. Mannami, Surf. Sci. **145**, 261 (1984).

[26] D.H. Rich, T. Miller, A. Samsavar, H.F. Lin, and T-C. Chiang, Phys. Rev. **B 37**, 10221 (1988).

[27] A. A. Baski and C. F. Quate, Phys. Rev. **B 44**, 11167 (1991).

[28] M. Wormington, *Rocking Curve Analysis by Dynamical Simulation (RADS)*, v3.10, Bede Scientific Instruments Ltd. (1997).

[29] H. P. Zeindl, T. Wegehaupt, I. Eisele, H. Oppolzer, H. Reisinger, G. Tempel, and F. Koch, Appl. Phys. Lett. **50**, 1164 (1987).

[30] W. Wegscheder, J. Olajos, U. Menczigar, W. Dondl, and G. Abstreiter, J. Cryst. Growth **123**, 75 (1992).

[31] D.J. Eaglesham, H.-J. Gossmann, and M. Cerullo, Phys. Rev. Lett. **65**, 1227 (1990).

[32] D.J. Eaglesham, Appl. Phys. Rev. **77**, 3594 (1995).

[33] M.V. Murty and H.A. Atwater, Phys. Rev. **B 49**, 8483 (1994).

[34] K.S. Min and H.A. Atwater, Appl. Phys. Lett. **72**, 1884 (1998).

[35] R. Hull, J.C. Bean, F. Cerdeira, A.T. Flory, and J.M. Gibson, Appl. Phys. Lett. **48**, 56 (1986).

[36] J. Olajos, P. Vogl, W. Wegscheider, and G. Abstreiter, Phys. Rev. Lett. **67**, 3164 (1991).

[37] W. Dondl, E. Silveira, and G. Abstreiter, J. Cryst. Growth **157**, 400 (1995).

[38] O. Gurdal, M.-A. Hasan, M.R. Sardela, Jr., J.E. Greene, H.H. Radamson, J.E. Sundgre, and G.V. Hansson, Appl. Phys. Lett. **67**, 956 (1995).

Chapter 6

Coherently Strained Sn-Rich Sn_xSi_{1-x} Quantum Dot Formation in Si via Phase Separation from Ultrathin Sn_xSi_{1-x}/Si

6.1 Introduction

Spontaneous or self-organized heteroepitaxial growth of Ge and SiGe quantum dots on Si has been extensively studied in the past several years due to their scientific and technological importance [1-12]. The most important advantage of

group IV semiconductor quantum dots is the potential for integration of novel optoelectronic or electronic devices that exploit quantum confinement effects with advanced Si microelectronics via monolithic integration.   Although quantum confinement effects are clearly observed [10-12], Ge and SiGe quantum dots behave as indirect band gap semiconductors. For applications in optoelectronic devices such as quantum dot lasers, however, direct band gap materials are required.

The synthesis of Sn-rich Sn_xSi_{1-x} quantum dots in Si demonstrated in this chapter is motivated by the potential for realization of Si-based direct bandgap semiconductor quantum dots.   As discussed in Section 5.2.1, one approach for realization of a direct energy gap group IV alloy semiconductor involves alloying Sn with Si or Ge to form epitaxially stabilized diamond cubic Sn_xGe_{1-x}/Ge and Sn_xSi_{1-x}/Si heterostructures [13-16].   Diamond cubic α-Sn is a direct band gap semimetal with degenerate conduction and valence bands at the Γ point [17].   Band structure calculations have predicted that when Si or Ge is alloyed with Sn, the resulting alloy systems Sn_xSi_{1-x} and Sn_xGe_{1-x} possess direct and tunable energy gaps for Sn compositions exceeding some critical concentration [13-16].   Experimental evidence for direct interband transitions has recently been demonstrated for the bulk Sn_xGe_{1-x} films grown by molecular beam epitaxy [18].   For the Sn_xSi_{1-x} system, the projections of the critical eigenvalues from results of the Slater-Koster parameter model [14] predicts the energy gap to be direct and semiconducting for the composition window $0.82 \leq x \leq 0.95$, corresponding to an energy gap window of $0 \leq E_g$ (eV) ≤ 0.40.   In addition to having a composition-dependent energy gap, Sn-rich Sn_xSi_{1-x} quantum dot structures also offer an added degree of freedom in tuning the energy gap by taking

advantage of the size-dependent quantum confinement effects [19]. Through the size-dependent increase in the band gap predicted by the quantum confinement theory [20], the direct zero band gap at the Γ point of the Brillouin zone in the bulk diamond cubic α-Sn is anticipated to increase when the crystal dimensions approach that of the exciton Bohr radius.

As outlined in Chapter 5, the requirement of high Sn content poses an obstacle for growing bulk alloy films due to the large lattice mismatch between α-Sn and Si (19.5%), extremely low solid solubility of Sn in crystalline Si ($\sim 5 \times 10^{19}$ cm^{-3}) [21], and severe Sn segregation to the surface during growth at ordinary Si epitaxy temperatures (T>$\sim$ 400°C). Although the growth of pseudomorphic Sn-rich Sn$_x$Si$_{1-x}$/Si is extremely difficult, coherently strained Sn-rich Sn$_x$Si$_{1-x}$ quantum dot structures can be synthesized as long as two requirements are met. The surface segregation must be circumvented and the critical particle size for the introduction of misfit-related interface defects must not be exceeded.

The growth of quantum dots have been realized in semiconductor heterostructures via exploitation of the interplay between epitaxial misfit strain and growth kinetics, yielding considerable control over the composition and spatial ordering of heterostructure architecture [1-12,22]. In most cases, each layer or region of the heterostructure consists of a chemically stable alloy (which might be metastable by virtue of coherency strains). When the end components of the alloy from which the quantum dots are formed from are chemically miscible, such as in the case of the Si-Ge system, the epitaxial quantum dots can usually be grown in the Stranski-Krastanow mode [1-12,22]. In the classic theory of Stranski-Krastanow

mode of growth, a uniformly strained wetting layer grows pseudomorphically up to a certain thickness (few monolayers) followed by an abrupt transition to the growth of three-dimensional islands on top of the uniform wetting layer [23]. The physical picture of the changeover from two-dimensional growth mode to three-dimensional growth mode in Stranski-Krastonow growth is schematically illustrated in Fig. 6.1(b). In Fig. 6.1(a) the chemical potential difference between the strained epitaxial layer and the unstrained bulk material is schematically plotted as a function of the adlayer thickness in monolayers. Provided that the bond strength between the adlayer atom and the substrate atom is higher relative to the bond strength between the adlayer atoms themselves, the deposition of an initial monolayer will result in a negative chemical potential difference. Due to the lattice strain energy, however, the chemical potential difference will increase linearly with the amount of material deposited. Each step represents the completion of deposition of one monolayer of the epitaxial material. When the chemical potential of the strained film exceeds that of the film material in the unstrained bulk state, the island formation is energetically favored. This occurs at the critical thickness for Stranski-Krastonow growth mode, t_{SK}, where island formation is energetically favored. And eventually when the thickness reaches t_{disl}, the system will relieve the strain and lower the chemical potential by the introduction of misfit dislocations. This classic view of Stranski-Krastonow growth has been successfully implemented to explain the growth of Ge dots on Si [1-12].

In order to take advantage of the Stranski-Krastanow growth mode as the method for synthesis of quantum dots, however, it must be ensured that the growth surface is not undergoing kinetic roughening; i.e., the atoms on the surface must have

enough mobility to diffuse on the surface to form islands. This means that for Stranski-Krastonow growth the substrate temperature must be relatively high; more correctly, the ratio of the atom flux to the surface diffusivity must be low. This requirement poses the main obstacle for Stranski-Krastonow growth of Sn_xSi_{1-x} quantum dots on Si. As discussed in Section 5.2.2, due to the low bulk and surface solubility of Sn in Si, any attempt to grow with a low ratio of the atom flux to the surface diffusivity will result in severe Sn segregation to the surface. And the lattice mismatch between Sn and Si is too large for the segregated Sn atoms to form coherent α-Sn islands on Si (100). An alternative pathway has to be taken, therefore, for synthesis of coherently strained α-Sn or Sn-rich Sn_xSi_{1-x} quantum dots.

In this chapter, we describe a novel approach to synthesis of quantum dots, via post-growth phase separation of initially chemically metastable semiconductor alloys. The phase separation process is schematically illustrated in Fig. 6.2. The quantum dots are formed via phase separation at a high (T>400°C) temperature from an embedded ultrathin Sn_xSi_{1-x} alloy layer grown and capped at a temperature low enough (T=170°C) to prevent Sn surface segregation during growth. Unlike the chemically stable system such as the Si-Ge system, each layer or region of the heterostructure in the case of the Si-Sn alloy system consists of a chemically metastable alloy. In addition, the layers are also metastable by virtue of coherency strain. Because of the alloy from which the quantum dots form is chemically metastable, the quantum dots cannot be grown by the Stranski-Krastanow growth process. In the case of Si-Sn, because both chemical and strain driving forces favor the decomposition of the homogeneous semiconductor alloy, the final structures that

result are quite different in shape and size from those formed by, e.g., strain-driven Stranski-Krastonow growth. The typical (e.g., SiGe and InGaAs) quantum dot structures that result from Stranski-Krastonow growth are more disks than dots, being oblate shaped structures with base diameter usually greater than 10 nm and aspect ratios approximately 10:1 [1-12,22]. By contrast, quantum dots formed by phase separation can yield structures with 1:1 aspect ratios and diameters in the 4-6 nm range, and shape is determined not by epitaxial growth kinetics, but approaches the thermodynamically preferred shape.

It will also be demonstrated that the alloy decomposition during post-growth thermal annealing of the ultrathin epitaxial metastable Sn_xSi_{1-x} alloys sandwiched in Si (001) initially proceeds via spinodal decomposition. Spinodal decomposition theory was originally developed by Cahn [24] more than three decades ago, and has been observed in a number of metallic alloy systems [25]. However, this is the first example of coherent semiconductor quantum dot formation via spinodal decomposition of a metastable single crystal solid solution. This is noteworthy, since spinodal decomposition has the potential to yield epitaxial structures with very different morphologies than those formed via strain-driven surface island nucleation and growth, since spinodal decomposition does not involve a thermodynamic barrier, and the spatial scale for morphological evolution is set by the strain and composition. Subsequent isothermal annealing experiments reveal that dots grow by a coarsening mechanism with particle growth kinetics that exhibits a sub-linear power law dependence on the annealing time.
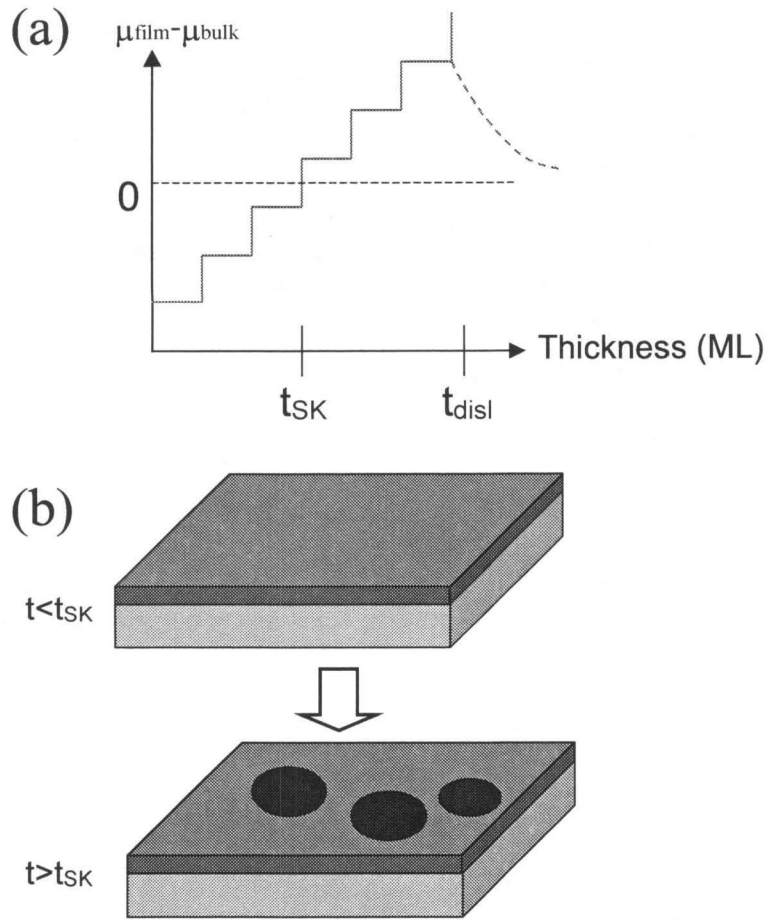
Figure 6.1. A schematic illustration of the changeover from two-dimensional to three-dimensional growth mode in the Stranski-Krastonow growth process. In (a) the chemical potential difference between the strained epitaxial layer and the unstrained bulk material (solid line) is plotted as a function of the adlayer thickness in monolayers. t_{SK} is the critical thickness for Stranski-Krastonow growth mode, at which the island formation is energetically favored, and t_{disl} is the critical thickness at which the system relieves the strain and lowers the chemical potential by the introduction of misfit dislocations (dashed line). In (b) is a schematic microstructural transformation from two-dimensional to three-dimensional growth mode at t_{SK}.
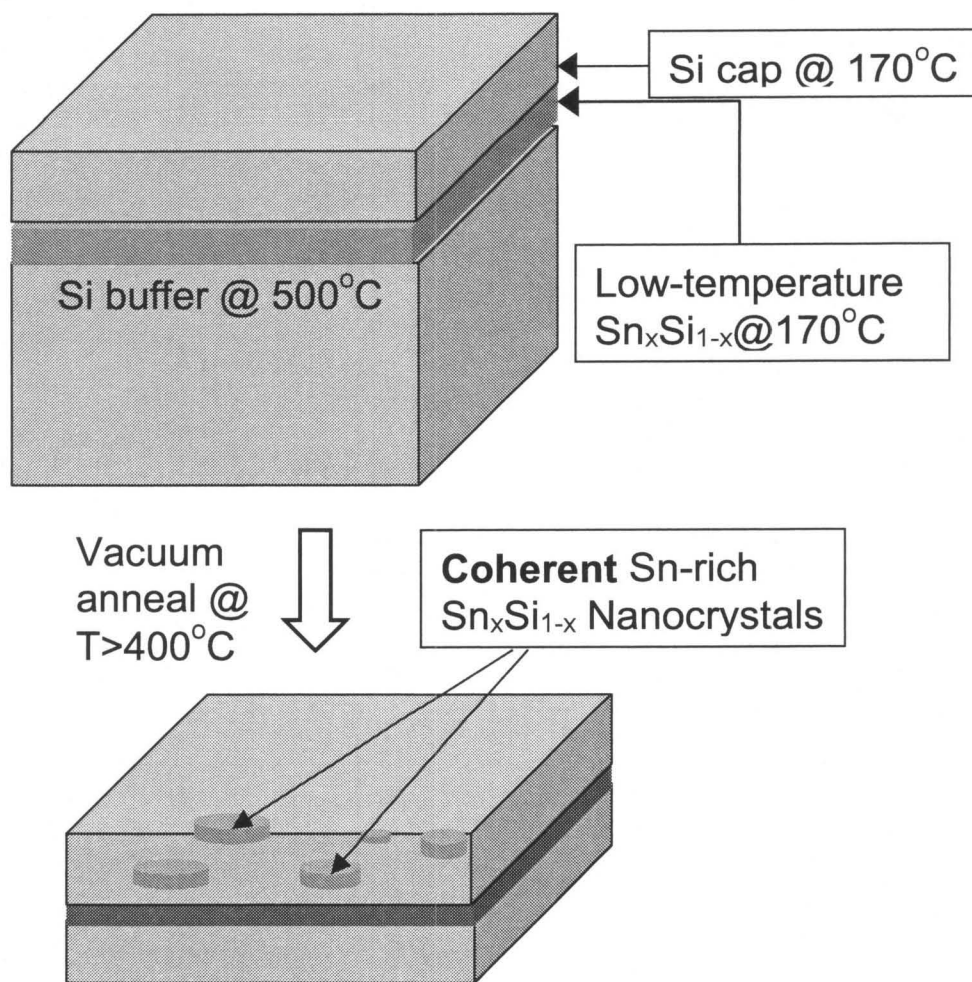
Figure 6.2. A schematic illustration of the 2-step synthesis process for Sn-rich Sn_xSi_{1-x} quantum dots in Si: the dots form via phase separation at high temperatures (T>400°C) from an embedded ultrathin Sn_xSi_{1-x} alloy layer grown by low-temperature (T=170°C) molecular beam epitaxy.

6.2 Background: Kinetic Pathways in Clustering by Diffusive Phase Transformation

The process of clustering by diffusive phase separation can be divided into early and late stages. The early stage involves the break-up of the initially homogeneous phase to form an initial distribution of stable clusters. This initial stage can be categorized as either nucleation or spinodal decomposition [26]. After this initial stage the clusters grow by atom transfer from the matrix phase into the clusters, and the size distribution evolves by cluster-cluster processes such as ripening or coalescence. Figure 6.3 shows a sketch of the different stages of clustering via the two mechanisms, i.e., by spinodal decomposition and nucleation and growth.

The initial stage can proceed by the two very different kinetic pathways depending on whether the process involves an energy barrier to achieving the two-phase regime [26]. The nucleation process involves an energy barrier to achieving the two-phase regime, whereas the spinodal decomposition process does not involve such a barrier. The spatial evolution of concentration is dramatically different in the two cases. The evolution of spatial concentration profile can be understood qualitatively, in the case of a binary solution, in terms of the magnitude of the interaction energy between the constituent atoms. In the first extreme case where there is very little preference for the like species to aggregate, the clusters simply appear and disappear, and by large the solution remains compositionally random and

homogeneous. If, in the opposite extreme, the preference for the like species is so large that the direction of atom movement is towards the direction of increasing concentration gradient, the system phase separates by spinodal decomposition. This is illustrated in Fig. 6.4(b) where a chance fluctuation leads to a buildup of the concentration gradient. The atoms always move in the direction of increasing concentration gradient, leaving behind a depleted region. The result is a rapid dissociation of the solution into regions rich and deficient in solute that are approximately periodically arranged in space. Finally, if the preference for like species is in between the two extremes, there is enough attractive driving force between the species to aggregate but not enough for the species to move up the concentration gradient. This regime describes nucleation and growth, where only clusters exceeding some critical size attract and hold the like atoms from the matrix. This is illustrated in Fig. 6.4(a). In nucleation and growth the matrix around a particle will be depleted of the solute atoms and the particles grow by ordinary diffusion down the concentration gradient.

The most fundamental distinction between spinodal decomposition and nucleation and growth is the existence of the thermodynamic barrier and the resulting direction of atom movement [24]. For a homogeneous system the diffusional flux of A atoms J_A in binary solution A_xB_{1-x} a can be written as:

$$J_A = -M(\mu_A - \mu_B) = -M \frac{\partial^2 f}{\partial c_A^2} \nabla c_A \qquad (6.1)$$

where M is the diffusion mobility, μ's are the chemical potentials, f is the free energy, and c is the concentration. From Eq. (6.1) it can be seen that the direction of atom

flux reverses whenever the curvature of the free energy $\partial^2 f / \partial c_A^2$ reverses its sign. Equation (6.1) therefore predicts where in the equilibrium phase diagram spinodal decomposition can be expected. This is schematically illustrated for a simple binary phase diagram and the free energy curve in Fig. 6.5(a) and Fig. 6.5(b), respectively. The two-phase regime is bounded by the solid line in Fig 6.5(a), between the points 'a' and 'b' at the schematic temperature T_1. Within the two phase regime, phase separation by nucleation and growth is expected in the region between the solid line and the dotted line, between the points 'a' and 'c' and between the points 'd' and 'b' at T_1. The curvature of the free energy is positive in these regions, as shown in Fig. 6.5(b). Phase separation by spinodal decomposition is expected in the region bounded by the dotted line in Fig. 6.5(a), between the points 'c' and 'd' at T_1, where the curvature of the free energy curve is negative.

After the initial phase separation by nucleation or spinodal decomposition, the microstructure evolves by diffusive growth, as illustrated in Fig. 6.3. The late stage growth starts when the solute concentration of an average-sized cluster is in microscopic balance with that of the matrix, such that the net atom movement between the average-sized cluster and the matrix is zero. Clusters bigger and smaller than the average-size, on the other hand, are out of balance and the net atom movement is not zero. The concentration of solute atoms in equilibrium with the matrix is least for the largest clusters and largest for the smallest clusters. This imbalance produces a solute gradient from smaller clusters to larger clusters and diffusion will then cause a net atom movement from smaller clusters to larger clusters. As a result, the smallest clusters shrink and eventually disappear.

Therefore, the average cluster size increases and the density of clusters decreases as coarsening proceeds. The fundamental instability or driving force for coarsening is described by the Gibbs-Thompson effect [26] which gives the solute concentration $c(r)$ in equilibrium with a cluster of radius r of a solute-rich spherical precipitate for a dilute solid solution as

$$c(r) = c_\infty \exp\left[\frac{2\sigma v_m}{rkT}\right]$$

(6.2)

where c_∞ is the solute concentration in equilibrium with an infinitely large cluster, σ is the interface energy, and v_m is the molar volume of the cluster. The first analytical treatment for the growth driven by Gibbs-Thompson effect was first developed by Lifshitz and Slyzov [27] and extended by Wagner [28]. Provided that the interfacial energy is the only driving force for the instability, the general time dependence of the linear dimension, d, of a cluster is given by the expression

$$d^n(t) = d_o^n + \alpha G t$$

(6.3)

where d_o is the value of d at $t=0$, G is the parameter for the appropriate mass transport process, and α is a factor that depends on the dimensionality of the cluster [29]. For example, for volume diffusion-limited and interface-limited particle coarsening of spherical particles, $n=3$ and $n=2$, respectively [28,30]. Therefore, the particle linear dimension exhibits a $t^{1/3}$ and $t^{1/2}$ dependence on annealing time for volume diffusion-limited and interface-limited particle coarsening, respectively.
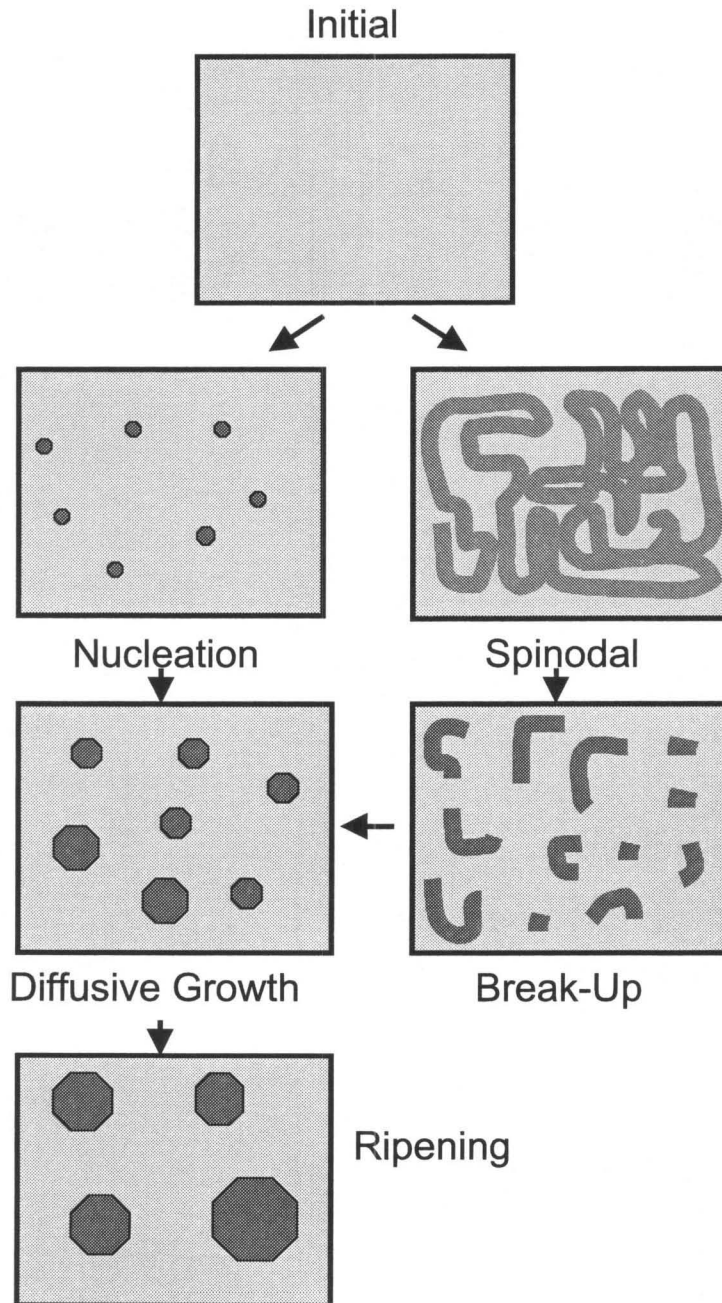
Figure 6.3. A sketch of different stages of phase separation for the two different initial kinetic routes. Various stages in phase separation via random nucleation and spinodal decomposition are illustrated.
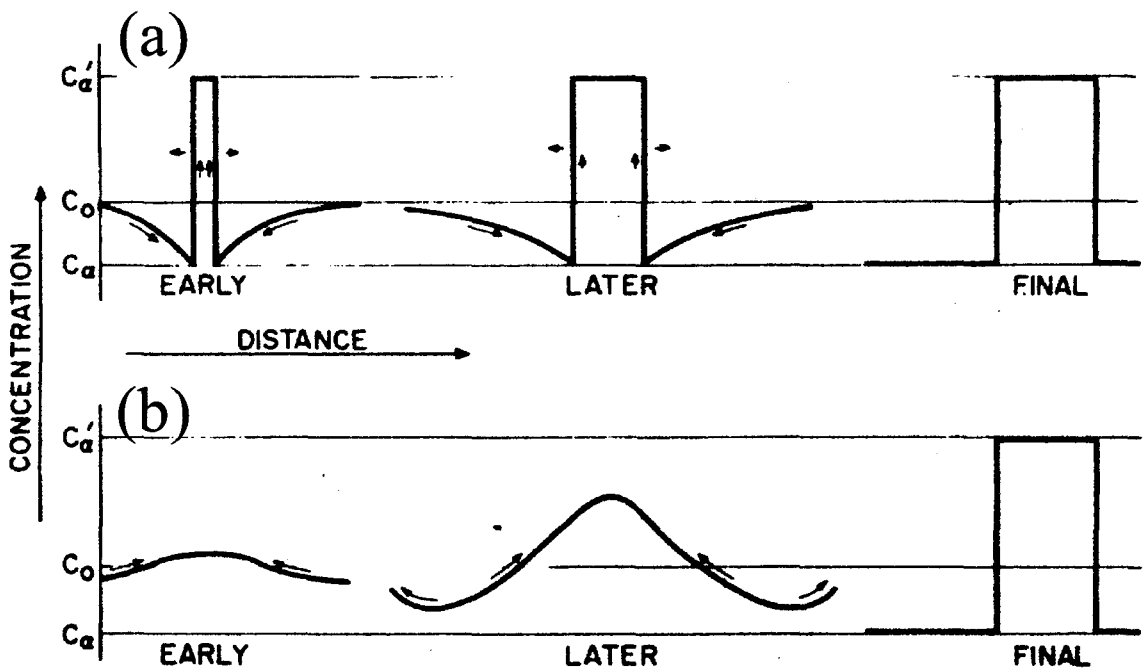
Figure 6.4. Two possible sequences for the formation of a two-phase structure by diffusion (from Ref. 24): (a) nucleation and growth where only clusters exceeding some critical size attract and hold the like atoms. The matrix around a particle will be depleted of the solute atoms and the particles grow by ordinary diffusion down the concentration gradient; (b) spinodal decomposition where a chance fluctuation leads to a buildup of the concentration gradient. The atoms always move in the direction of increasing concentration gradient, leaving behind a depleted region.
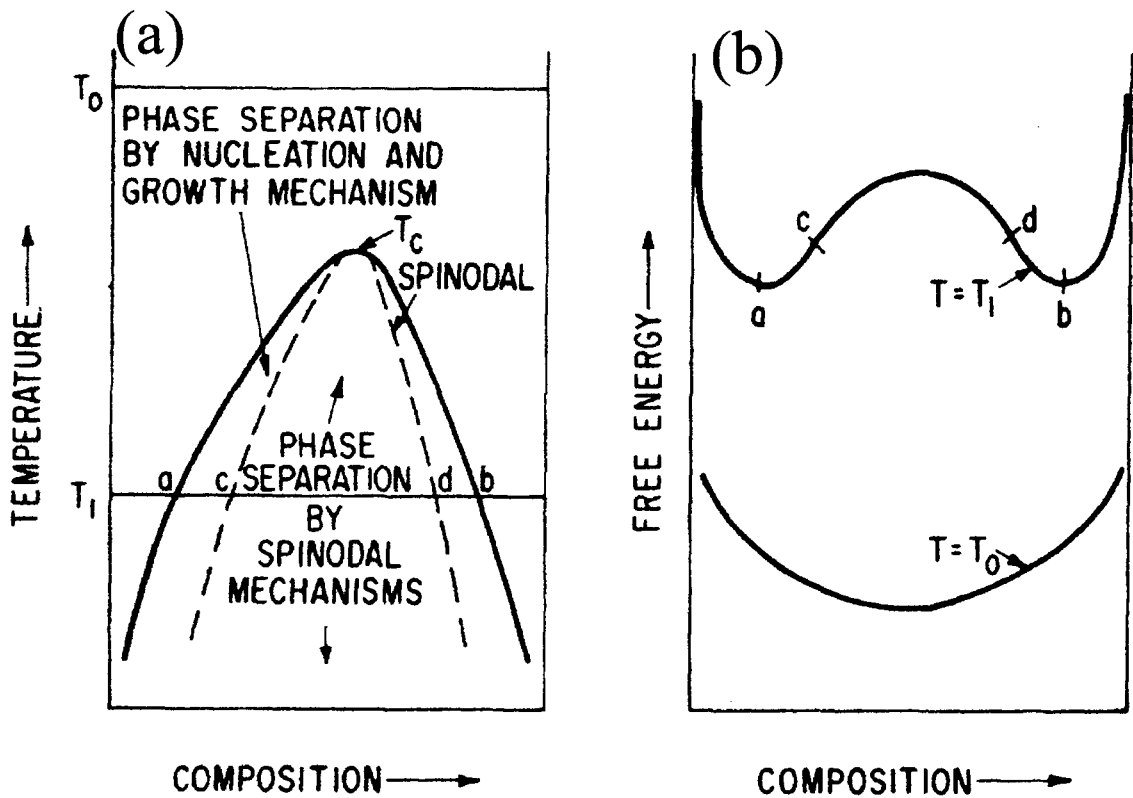
Figure 6.5. A schematic illustration of the two phase separation mechanisms in (a) a simple binary phase diagram and (b) the free energy curve (from Ref. 24). At the schematic temperature T_1, the two-phase regime is bounded by the points 'a' and 'b' and the spinodal is expected in the region bounded by 'c' and 'd.' Spinodal decomposition is expected within the region bounded by a negative curvature of the free energy curve.

6.3 Experimental: Synthesis of Sn-Rich Sn_xSi_{1-x} Quantum Dots in Si by Phase Separation from Ultrathin Sn_xSi_{1-x}/Si Grown by Low Temperature Molecular Beam Epitaxy

Relative to growth of chemically stable heterostructures like Ge_xSi_{1-x}/Si, growth of heterostructures based on Sn_xSi_{1-x}/Si is generally much more difficult. The difficulty arises from a large lattice mismatch between α-Sn and Si (19.5%), extremely low solid solubility of Sn in crystalline Si ($\sim 5 \times 10^{19}$ cm^{-3}) [21], and severe Sn segregation to the surface during growth at ordinary Si epitaxy temperatures (T>~ 400°C). As discussed in Section 6.1, the growth of quantum dots via the strain-driven Stranski-Krastonow growth mode [23], which is the growth mode of Ge and Ge_xSi_{1-x} quantum dots on Si, requires high substrate temperatures, or more correctly, a low ratio of the atomic flux to the surface diffusivity. This requirement represents the main obstacle for Stranski-Ktrastonow growth of Sn_xSi_{1-x} on Si. Co-evaporation of Sn and Si on Si at ordinary Si epitaxy temperatures (T>~400°C) results in severe Sn segregation to the surface to form incoherent β-Sn droplets.

In order to overcome these difficulties, therefore, a novel two-step process has been developed for synthesis of quantum dots in a chemically metastable system. The technique involves Sn-rich Sn_xSi_{1-x} quantum dot formation in Si via phase separation at high temperatures (>500°C) from an ultrathin Sn_xSi_{1-x} epitaxial alloy

layer grown and capped at a low temperature (170°C) to prevent Sn surface segregation. The synthesis process is schematically illustrated in Fig. 6.2. In effect, the Sn atoms are epitaxially 'frozen' in the lattice of Si at low temperatures to prevent their segregation. Subsequently, upon annealing, the atoms are given enough thermal energy to diffuse and transform into their thermodynamically favored end states, which consist of almost pure Sn dots in Si. And because the dots precipitate within the Si matrix, the Sn-rich Sn_xSi_{1-x} quantum dots retain the parent matrix crystal structure and remain diamond cubic. Although the technique is demonstrated for the synthesis of Sn-rich Sn_xSi_{1-x} quantum dots in Si, the approach should be generally applicable to quantum dot synthesis in any other chemically metastable system such as Sn_xGe_{1-x}.

The ultrathin Sn_xSi_{1-x} epitaxial alloy layers from which the quantum dots are precipitated are grown by low-temperature molecular beam epitaxy. An electron beam evaporation source and an effusion cell was used for Si and Sn deposition, respectively. Just prior to growth of the Si buffer layer, the Si (001) substrates were heated to 550°C to obtain a clean (2×1) surface reconstructed surface. Si and Sn were deposited by electron beam evaporation and thermal effusion, respectively. Si deposition rates were controlled using a quartz crystal monitor and Sn deposition rate was controlled via effusion cell temperature. The Sn effusion cell temperature was varied between 675-755°C to yield deposition rates between 0.003-0.02 ML/sec (1 ML = 6.79×10^{14}/cm^2). For all samples, Si buffer layers were grown at 550°C at 0.05 nm/sec to obtain a smooth Si surface prior to deposition of the Sn_xSi_{1-x} layers. After the buffer layer deposition, the growth was interrupted to cool the substrate to 170°C

prior to Sn_xSi_{1-x} alloy layer deposition. The deposited Sn_xSi_{1-x} alloy layers were 1-4 nm in thickness and 5%–20% Sn in composition and the deposition rate was 4–5 ML/min. Subsequently, in order to cap the alloy layer with minimal Sn segregation to the surface, 14 nm of Si overlayer was grown at 170°C at a growth rate of 0.03 nm/sec.

The samples were subsequently annealed in high vacuum (base pressure of 5×10^{-7} torr), where upon the alloy layer underwent phase separation into Sn dots in Si matrix as observed by transmission electron microscopy. The analyzed films either received isothermal or isochronal anneals at temperatures ranging from 500°C–800°C and times ranging from 5 min. to 72 hours.

6.4 Phase Separation of Sn-Rich Sn_xSi_{1-x} Quantum Dots from Ultrathin Sn_xSi_{1-x}/Si

The early stage phase separation of the epitaxially stabilized ultrathin Sn_xSi_{1-x}/Si and late stage growth of rich-Sn Sn_xSi_{1-x} quantum dots was studied using transmission electron microscopy (TEM) using 300 keV electrons and Rutherford backscattering spectrometry using a 2 MeV He^{++} beam.

6.4.1 Nanostructural Evolution of Sn_xSi_{1-x}/Si into Sn-Rich Sn_xSi_{1-x} Quantum Dots in Si

The nanostructural evolution of the early and late phase separation process has been investigated using cross-sectional and planar-view transmission electron microscopy. Figure 6.6(a) shows a [110] axis cross-sectional bright field image of an embedded 2 nm $Sn_{0.10}Si_{0.90}$ film as grown at 170°C. The continuous horizontal dark band indicates the buried $Sn_{0.10}Si_{0.90}$ alloy layer. Figure 6.6(b) shows the film in Fig. 6.6(a) annealed in vacuum at 400°C for 30 min. The alloy layer is apparently homogeneous and no obvious phase separation into Sn dots can be observed in the cross-sectional view. As will be shown later in planar-view analyses, however, the alloy film has already undergone early stage phase separation. Figure 6.6(c) shows

the film in Fig. 6.6(a) after annealing in vacuum at 800°C for 30 min. The precipitation of Sn-rich quantum dots is clearly observed. It should be noted that in the cross-sectional view, the obtained transmission electron micrographs present views of projected columns of material. The image therefore is an "average" image over the electron transparent sample of about 100 nm in thickness. The apparent density of particles, therefore, is higher than the actual density and some particles appear to have coalesced. As will be shown later in planar-view images, however, the particles are well separated. Figure 6.7 show a high-resolution transmission electron micrograph of one Sn-rich Sn_xSi_{1-x} precipitate from the same sample as in Fig. 6.6(c) under <110> projection. No interface-related defects are observed and the particle is coherent with the matrix.

More insight into the nanostructural evolution can be obtained from planar-view electron microscopy studies. Figures 6.8(a)-6.8(c) are planar-view transmission electron micrographs of the as deposited $Sn_{0.10}Si_{0.90}$ alloy at 170°C, the film annealed at 500°C for 3 hours, and the film annealed at 800°C for 30 min., respectively. It should be noted that all images are bright field images taken away from strongly diffracting conditions. This was done to reduce strain contrast in order to minimize error in the subsequent size analysis. Therefore, the resulting contrast results mainly from compositional differences. One clearly sees that the as-grown alloy layer shown in Fig. 6.8(a) has already started to phase separate into Sn-rich (dark) and Sn-deficient (light) regions. The inset shows an intensity line scan through the section A-A. The intensity varies gradually in a continuous fashion as the diffuse boundary between the Sn-rich and Sn-deficient regions is crossed. The nature of spatial

intensity variation suggests that the alloy film has begun to phase separate by spinodal decomposition. A gradual variation in composition across the phase boundary is a key feature of spinodal decomposition [24]. Figure 6.8(b) shows that after the film is annealed at 500°C for 3 hours, the gradual variation in concentration has been significantly reduced. At the same time, nucleation of well-defined, ~1 nm clusters is observed. As a result, the line scan of the intensity across B-B shows that there is a sharp drop in intensity as the cluster/matrix boundary is crossed, in addition to a gradually varying background contrast. The sharp change in composition across the cluster/matrix boundary is a key feature of nucleation. This suggests that at 500°C the nanostructure exhibits nucleation occurring within the Sn-rich regions from the initial break-up of the alloy layer. When the film is annealed at 800°C for 30 min., the gradual variation in contrast disappears, as evident in Fig. 6.8(c). As can be seen by the line scan C-C, there are only sharp contrast variations across the nanocrystal/matrix boundaries. The gradual variation in contrast has disappeared altogether. One also clearly sees that the average size of the nanocrystals have clearly increased. Another notable feature in Fig. 6.8(c) is that all nanocrystals appear to be faceted along the <100> crystallographic direction, which is the elastically soft direction in Si.
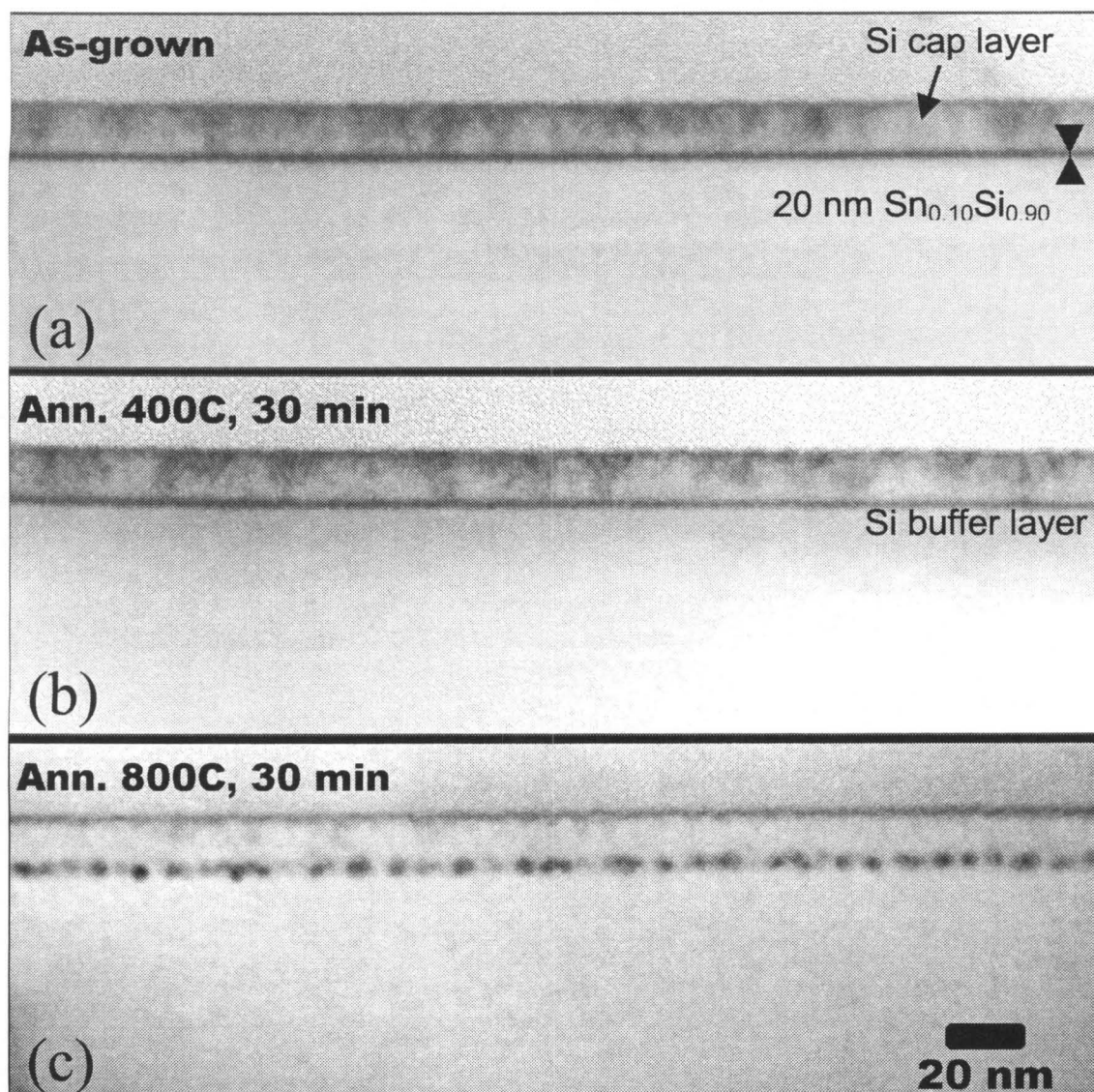
Figure 6.6. [110] axis cross-sectional transmission electron micrographs of 2 nm $Sn_{0.10}Si_{0.90}$ capped with 14 nm Si. Bright-field images are those of the (a) as-grown film at 170°C and (b) after annealing in vacuum at 400°C for 30 min. and (c) after annealing in vacuum at 800°C for 30 min.
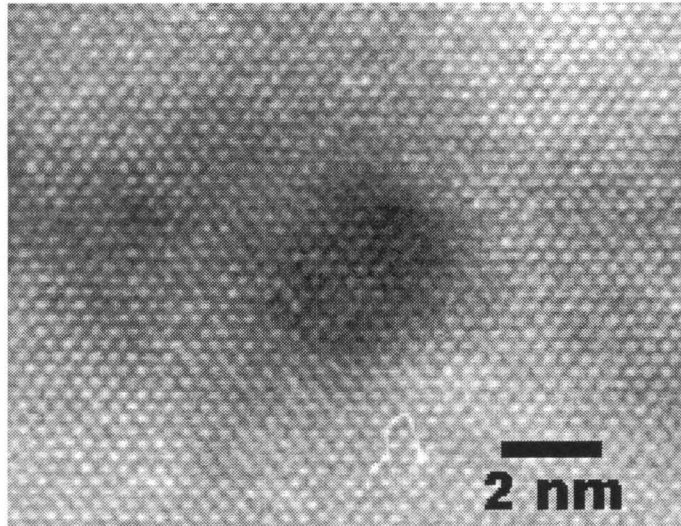
Figure 6.7. High-resolution cross-sectional transmission electron micrograph in the [110] projection of a Sn-rich Sn_xSi_{1-x} quantum dot formed by annealing 2 nm $Sn_{0.10}Si_{0.90}$ capped with 14 nm Si at 800°C for 30 min.

20 nm
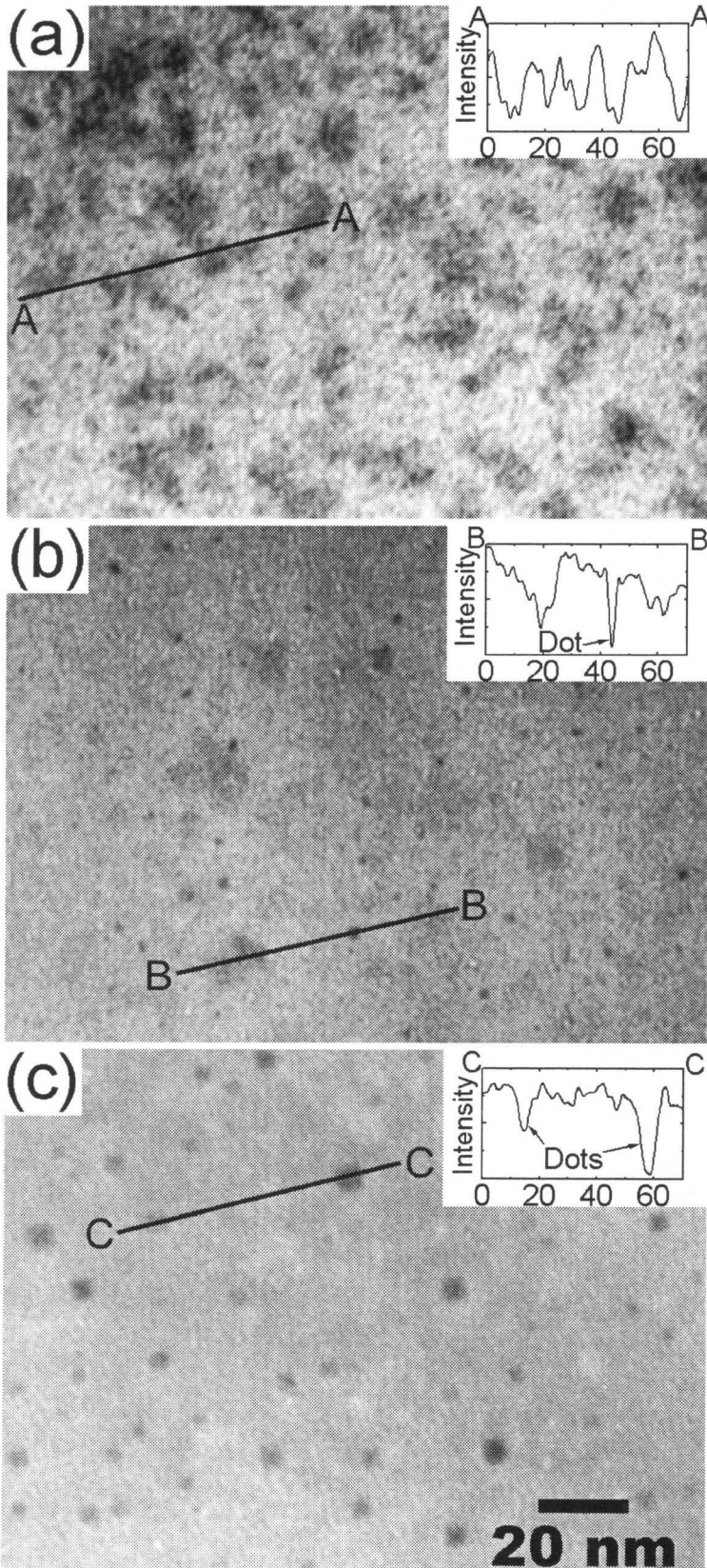
Figure 6.8. Nanostructural evolution of 2 nm $Sn_{0.10}Si_{0.90}$ capped with 14 nm Si as observed in planar-view transmission electron microscopy. Bright-field transmission electron micrographs of (a) the as-grown film at 170°C, (b) the film annealed at 500°C for 3 hours, and (c) the film annealed at 800°C for 30 min. The insets show intensity line-scans across A-A, B-B, and C-C, respectively. The images were taken away from strongly diffracting conditions to minimize error in particle size analysis. The contrast, therefore, comes mainly from compositional differences between different regions.

6.4.2 Early Stage Phase Separation of Sn_xSi_{1-x}/Si by Spinodal Decomposition

Nanostructural evidence of spinodal decomposition observed in Fig. 6.8 leads one to ask whether the Si-Sn system is expected to exhibit spinodal decomposition. A simplistic prediction can be made using Cahn's analysis [24], starting with the regular solution approximation [31] for the Si-Sn system. In the regular solution approximation, the free energy change upon the formation of the solid solution Sn_xSi_{1-x} is given as

$$\Delta g_{mix} = \Delta h_{mix} - T\Delta s_{mix}$$
$$= \Omega x(1-x) - RT\left[x\ln x + (1-x)\ln(1-x)\right] \tag{6.4}$$

where Ω is the regular solution interaction parameter. The interaction parameter Ω can be extracted by fitting the free energy expression for the regular solution to the solidus in the published experimental Si-Sn phase diagram [32] (Fig. 5.3). The condition for coherent spinodal in cubic crystals for {100} plane compositional waves is given as [33]:

$$\frac{\partial^2 f}{\partial x^2} + 2\eta^2 Y(100) = 0 \tag{6.5}$$

where $Y(100)$ is the elastic energy and η is the strain along the <100> direction. For a biaxially strained epitaxial film $\eta(x) = \varepsilon_\parallel^2(x)$ and

$$Y(100) = \varepsilon_\parallel^2(x)\left[C_{11}^2(x) + C_{12}^2(x) - \frac{2C_{12}^2(x)}{C_{11}(x)}\right]. \tag{6.6}$$

Substitution of Eq. (6.6) and Eq. (6.4) into Eq. (6.5) yields the composition-dependent

temperature $T_s(x)$ of metastability for an epitaxial cubic alloy layer that is biaxially

strained along <100> directions in the regular solution approximation as

$$T_S(x) = \frac{2x(1-x)}{k_B}\left\{\Omega - \varepsilon_{\parallel}^2(x)\left[C_{11}(x) + C_{12}(x) - \frac{2C_{12}^2(x)}{C_{11}(x)}\right]\right\} \quad (6.7)$$

where k_B is the boltzman constant, $\varepsilon_{\parallel}$ is the in-plane biaxial strain, C's are the elastic

constants, and Ω is the regular solution interaction parameter which is composition-

independent to the zeroth order [31]. Figure 6.9 shows the predicted chemical and

coherent spinodal of the Si-Sn system based on the regular solution approximation.

The spinodal curve obtained without the strain term (second term in curly brackets) in

Eq. (6.7) gives the chemical spinodal. As shown in Fig. 6.9, the presence of the large

strain suppresses the spinodal by as much as 3000°C.

Two aspects about the epitaxially stabilized Si-Sn system make it a strong

candidate for a system that undergoes spinodal decomposition. First, the preference

for like species is very large, as is evidenced by the extremely low solid solubility. In

other words, in a concentration gradient the flux of the atoms is in the direction in

which they are attracted, i.e., up the concentration gradient. Second, the epitaxial

stabilization preserves the crystal structure; i.e., the composition across the phase

boundary varies continuously across a coherent interface and therefore no nucleation

barrier due to the positive interface energy is involved. Since the new phase forms by

a continuous process in spinodal decomposition, the parent and the child phases must

share the same crystal structure. Although bulk diamond cubic α-Sn is only stable up

to 13.2°C [34], the embedded ultrathin Sn_xSi_{1-x} alloy layer is epitaxially stabilized to retain the diamond cubic structure, thus favoring spinodal decomposition. This is evident in the high-resolution transmission electron micrograph of Fig. 6.7.

According to Fig. 6.9, for the deposition and annealing temperatures used in this work, (170°C ≤ T ≤ 800°C), coherent spinodal decomposition is expected only for Sn concentration exceeding x≈0.30. This is significantly higher than the Sn concentration of the film analyzed thus far with x=0.10. This discrepancy could be arising from several factors. A small amount of strain relaxation that occurs via stacking faults can reduce the strain term in Eq. (6.7), thus leading to smaller suppression of the spinodal. It could also be due to the deviation of the current system from the regular solution approximation and to the fact that in the current system the atomic mobility is described more accurately by a two-dimensional diffusional system, whereas the theory is intended for three-dimensional systems.
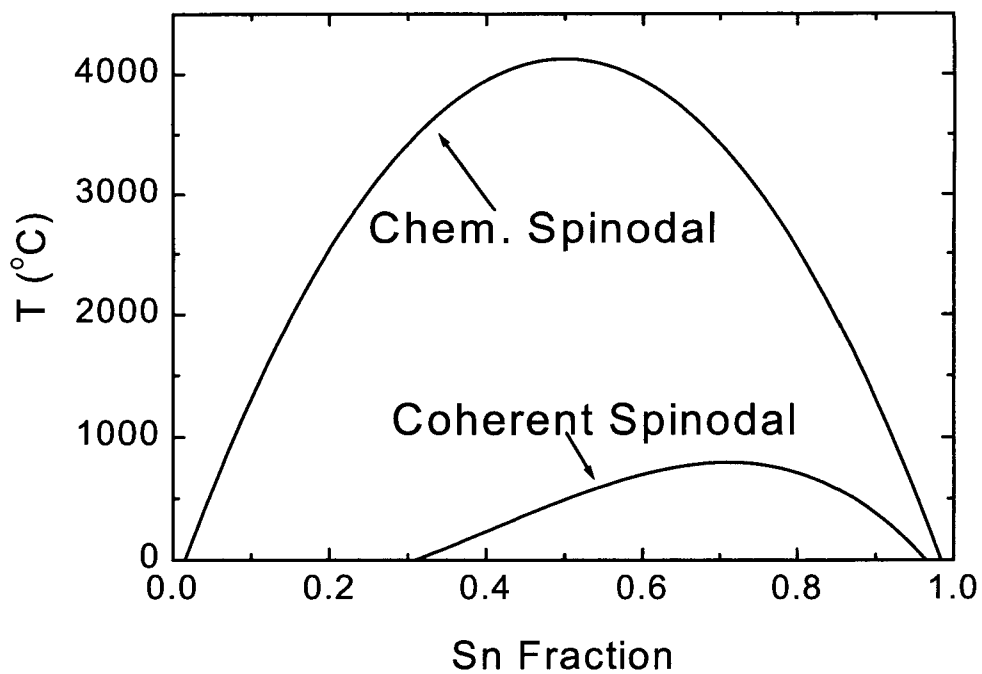
Figure 6.9.   Chemical and coherent spinodal curves calculated in the regular solution

approximation, using Eq. (6.7).

6.4.3   Late Stage Growth of Sn-Rich Sn_xSi_{1-x} Quantum Dots by Coarsening

After the early stage break-up of the ultrathin Sn_xSi_{1-x} alloy layer via spinodal decomposition and subsequent nucleation, the late stage growth of regularly shaped nanocrystals takes place via coarsening upon annealing the film at elevated temperatures. The evolution of the nanostructure at different temperatures has been summarized in the transmission electron micrographs of Fig. 6.8 in Section 6.4.1. Figure 6.10 shows the dependence of particle size on the annealing temperature. The average particle size is plotted in terms of the particle size parameter r. The particle size parameter r is the square root of the area of the nanocrystal measured from planar view transmission electron micrographs and is therefore proportional to the linear dimension of the particle. For isochronal annealing for 2 hours in vacuum, the measured values of the average linear dimension <r> were 1.3±0.4 nm, 2.3±0.8 nm, and 3.0±1.2 nm for the films annealed at 500°C, 650°C, and 800°C, respectively. The error bars indicate the standard deviation. For mass-conserved systems, coarsening is most readily recognized when the temporal evolution of growth kinetics is characterized by an increase in the average particle size and a decrease in the particle density [26]. Figures 6.11(a)–6.11(c) show the histograms of size distribution of the precipitated Sn-rich Sn_xSi_{1-x} dots for the isothermal annealing at 650°C for 5 min., 2 hrs., and 72 hrs., respectively. It can clearly be seen that the average particle size increases with increasing annealing time. The trend can be seen

more clearly in Figure 6.12 which illustrates the time evolution of the particle volume for the same isothermal series as in Fig. 6.11, expressed in terms of the average nanocrystal volume parameter $<r>^3$. The parameter $<r>$ is the average value of the linear dimension parameter r. Therefore, $<r>^3$ is a parameter proportional to the average volume of the nanocrystals. One sees in Fig. 6.12 that there is a transient period where the average size increases rapidly in a short amount time. This transient period can be attributed to the initial alloy break-up/nucleation regime between the initial spinodal decomposition regime and the late-stage coarsening regime. Subsequently, the volume increases roughly linearly with time. The solid line is a linear fit. Figure 6.12 illustrates that the linear dimension of the clusters follows a sublinear power law in time. The left axis of Fig. 6.13 shows the temporal evolution of the average area per nanocrystal $<l^2>$. The circles represent the average area per nanocrystal and the solid line is a linear fit. As in Fig. 6.12 for the average volume parameter $<r>^3$, the average area per nanocrystal $<l^2>$ increases roughly linearly in time after a transient period. For a system undergoing diffusion-limited coarsening, the critical size and the area per particle are expected to obey the same time dependence [26]. The right axis of Fig. 6.13 shows the change in particle density as a function of time. The solid line serves as a guide to the eye. Again, after a transient period where the density drops off rapidly, the density decreases monotonically.

Late stage growth can be described by coarsening (Ostwald ripening) models when clusters larger than the average size grow at the expense of smaller ones [26]. The driving force is the imbalance of the concentration of solute atoms in equilibrium with the matrix between clusters smaller and larger than the average. This imbalance

produces a solute gradient from smaller clusters to larger clusters and diffusion then causes a net atom movement from smaller clusters to larger clusters. Therefore, the average cluster size increases and the density of clusters decreases as coarsening proceeds. The cube of the critical radius increasing linearly with time, as it appears to occur in Fig. 6.12, is expected to occur, provided that strain does not play a significant role in mass transfer, for diffusion-limited growth of three-dimensional islands and for interface transfer-limited growth of two-dimensional islands [28,30]. A more relevant model, however, should take into account of the effect of strain. Nevertheless, the two late-stage trends, namely increasing average nanocrystal size and decreasing nanocrystal density with time, indicate that the particles are clearly undergoing coarsening.

The presence of facets along the elastically soft <100> directions, as seen in Fig. 6.8 (c), is not unexpected, in light of the presence of a large misfit strain, since the interfacial stress can be most efficiently relieved along such directions. In planar view, the nanocrystals look almost square-shaped. In the corresponding cross-sectional image along the [110] projection in Fig. 6.6, however, the nanocrystals almost look spherical, and the presence of facets is not obvious. This is not inconsistent with what one would observe, however, if the shape of the nanocrystals is similar to that of the equilibrium shape of Si, which has been demonstrated to be tetrakaidecahedron from equilibrium shape of voids in Si [36]. The equilibrium shape of Si is composed mainly of {111} and {100} facets. Along <110> axis cross section, the nanocrystal then would resemble an octagon, and along <100> planar view the nanocrystal would resemble a square. If some facets are slightly rounded, as

observed in Ref. 36, the observed shape of Sn_xSi_{1-x} nanocrystals would be consistent with the equilibrium shape of Si.

As discussed in the introduction, in order for the band gap of Sn_xSi_{1-x} quantum dots to be direct, the composition of the dots must be in the Sn-rich end. However, it is difficult to be quantitative about the composition of the dots due to a lack of precise information about the shape and the atomic density of the nanocrystals. Nevertheless, one can make a rough estimate of the composition of the Sn_xSi_{1-x} quantum dots and the matrix with reasonable assumptions. First of all, in order to make an estimate of the composition, the absolute amount of Sn in the alloy film needs to be determined. Therefore, Rutherford backscattering spectrometry has been performed on the embedded 2 nm-thick $Sn_{0.10}Si_{0.90}$ films on which all the particle size analyses have been performed. Figure 6.14 shows the Rutherford backscattering spectra showing the Sn peak of the 2 nm-thick $Sn_{0.10}Si_{0.90}$ film before and after annealing at 800°C for 30 min. Upon annealing, the absolute amount of Sn decreases by about 18%. The decrease can be either attributed to out-diffusion of Sn from the alloy layer to the surface, or evaporation of a small amount of segregated Sn on the surface upon vacuum annealing. With the absolute amount of Sn determined, the composition of Sn_xSi_{1-x} quantum dots has been estimated from the known average volume from Fig. 6.12 and the density of nanocrystals from Fig. 6.13. The number of atoms making up the total volume of the nanocrystals has been determined to always remain less than the total number of Sn atoms measured from the Rutherford backscattering spectra. The total amount of the embedded Sn atoms is 1×10^{15} atoms/cm^2 after annealing at 800°C for 30 min. After annealing for 30 min. and 72 hours at 650°C, the volume

occupied by the nanocrystals corresponds to 3×10^{14} atoms/cm^2 and 5×10^{14} atoms/cm^2, respectively. Therefore, provided that strain does not limit the concentration, the composition of the dots should be close to being pure Sn with the matrix retaining rest of the Sn atoms. Accordingly, the Sn concentration of the matrices of the films annealed for 30 min. and 72 hours at 650°C remain at about 7% and 5%, respectively.
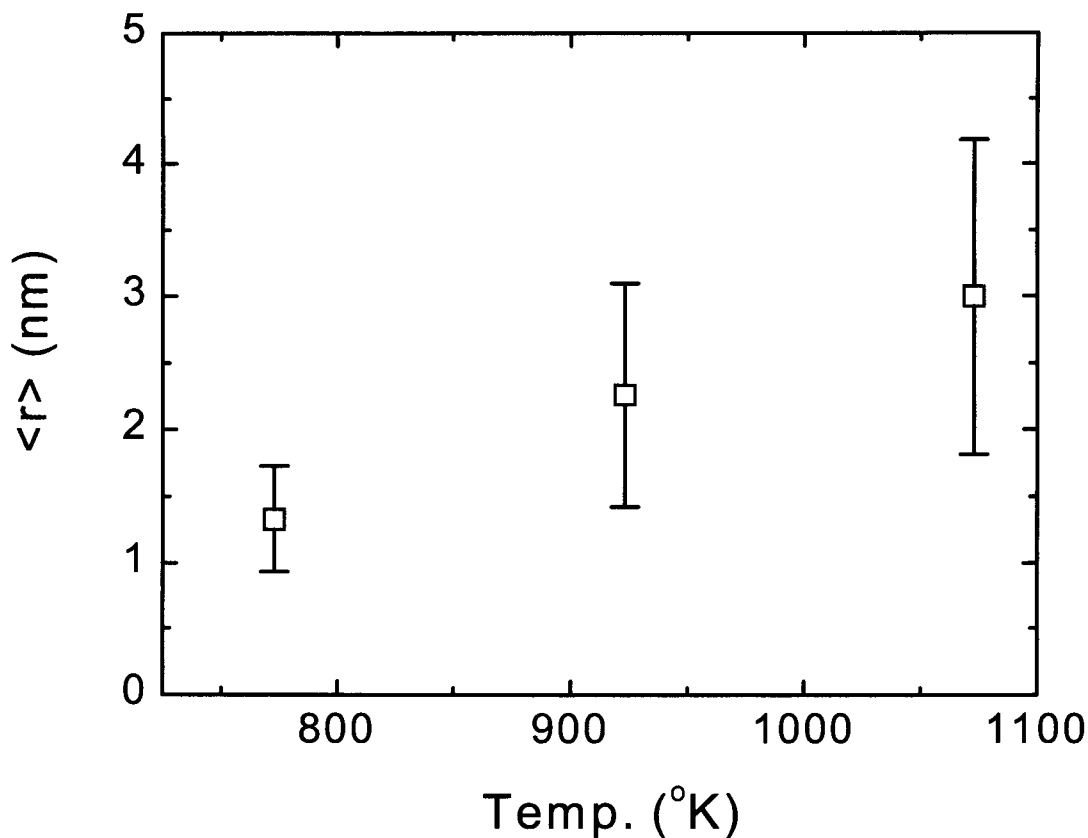
Figure 6.10. The dependence of the average nanocrystal size <r> on the annealing

temperature. The particle size parameter r is the square root of the area of the

nanocrystal measured from planar view transmission electron micrographs and is

therefore proportional to the linear dimension of the particle. The films were

annealed for 30 min. in vacuum at 500°C, 650°C, and 800°C. The error bars indicate
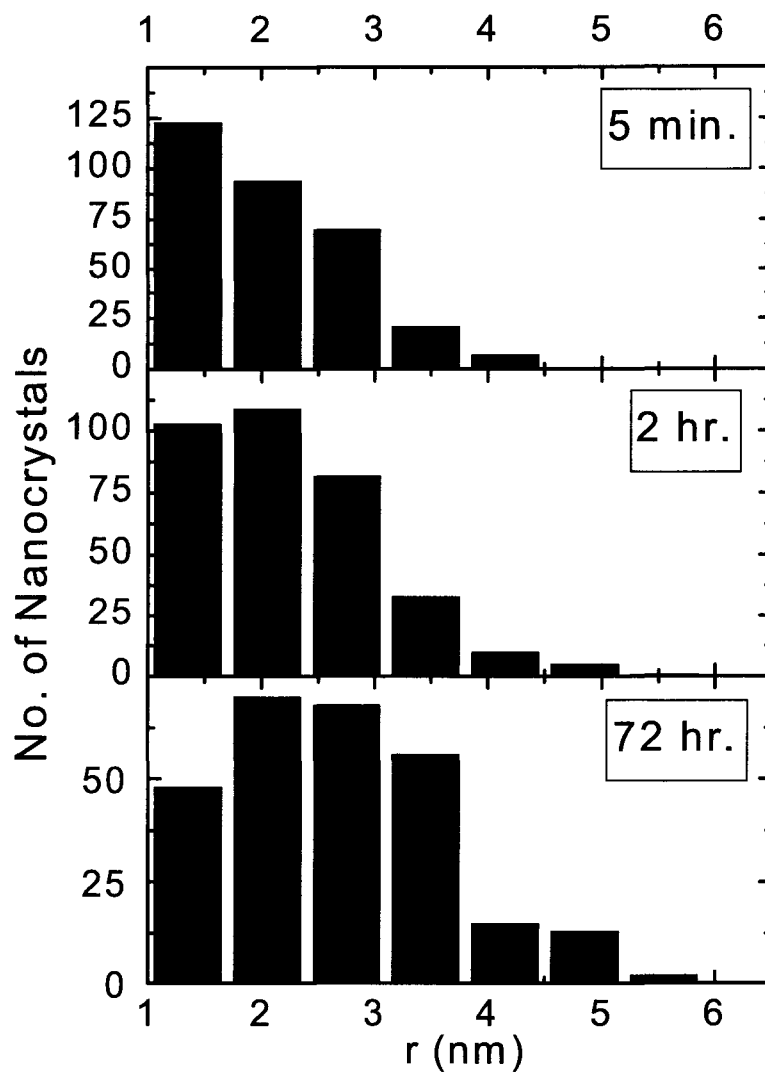
the standard deviation.

Figure 6.11. Histogram of the distribution of Sn-rich Sn_xSi_{1-x} nanocrystal size for isothermal annealing at 650°C for (a) 5 min. (b) 2 hr. (c) 72 hr.

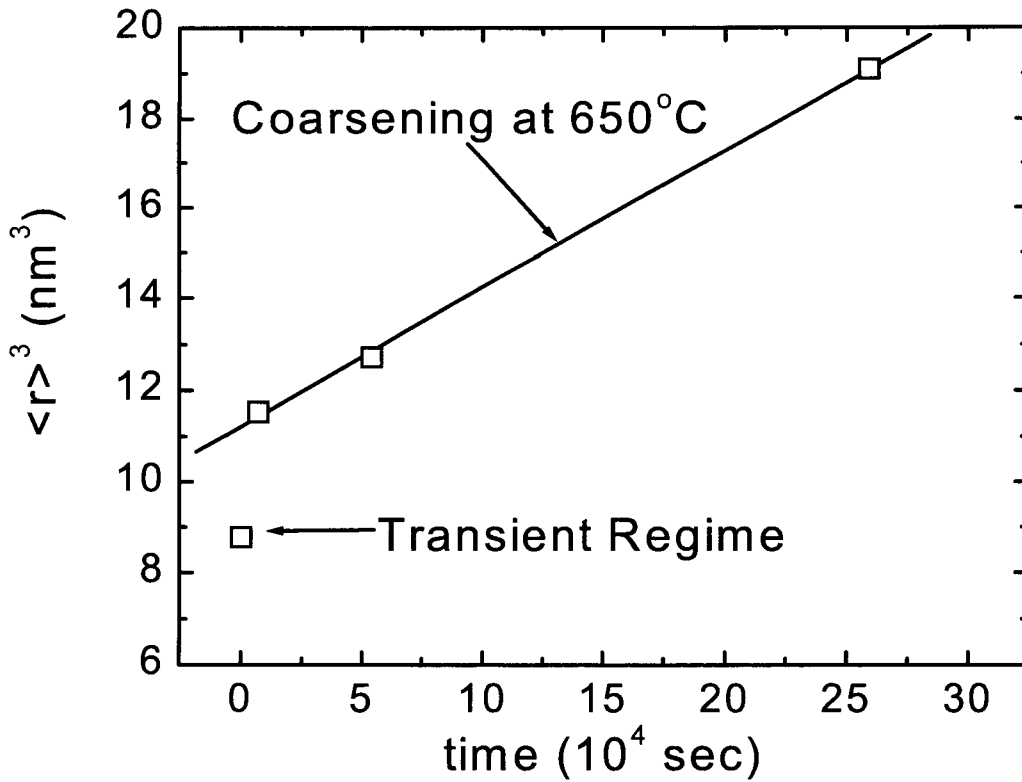Figure 6.12. Coarsening kinetics for isochronal annealing at 650°C: the average volume parameter $<r>^3$ as a function of annealing time. The squares are experimental values obtained from planar-view transmission electron micrographs and the solid line is a linear fit.

Figure 6.13. Coarsening kinetics for isochronal annealing at 650°C: average area per nanocrystal (left y axis) and the particle density (right y axis) as a function of annealing time. The circles and the squares are experimental values obtained from pla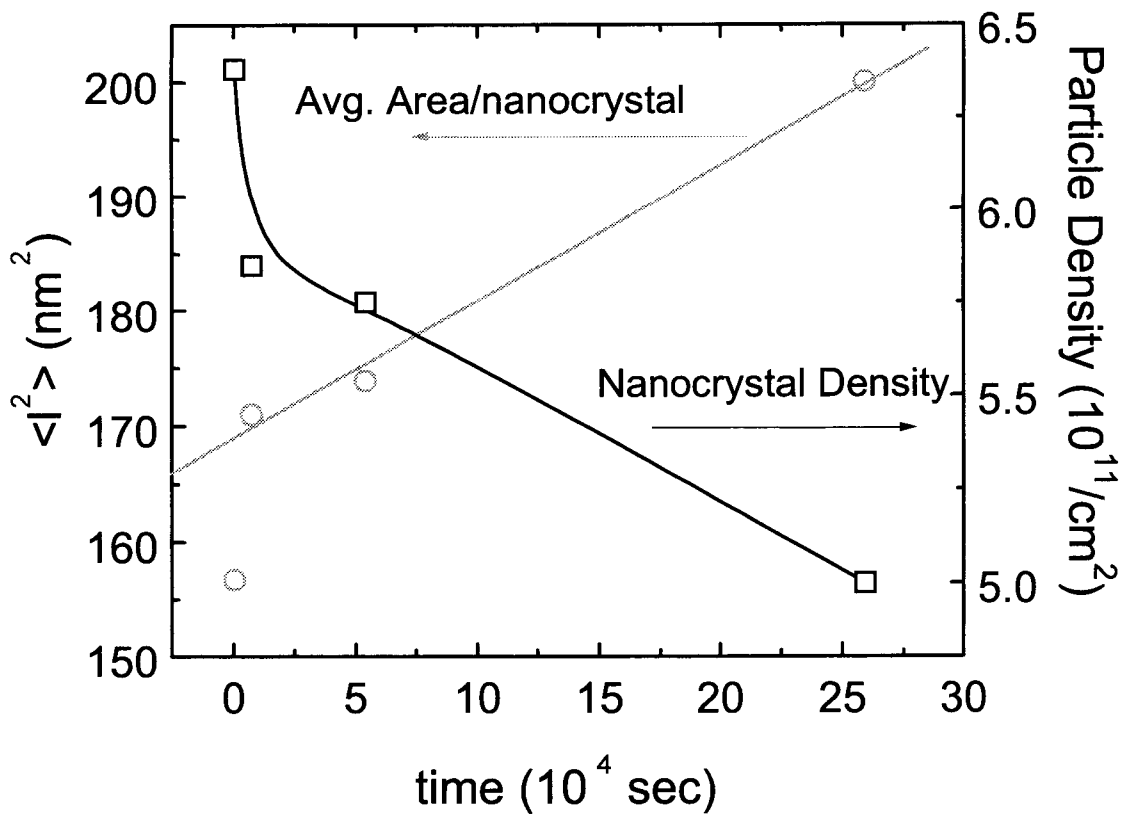nar-view transmission electron micrographs. The solid line for the average area per nanocrystal is a linear fit and the solid line for the nanocrystal density is a guide to the eye.
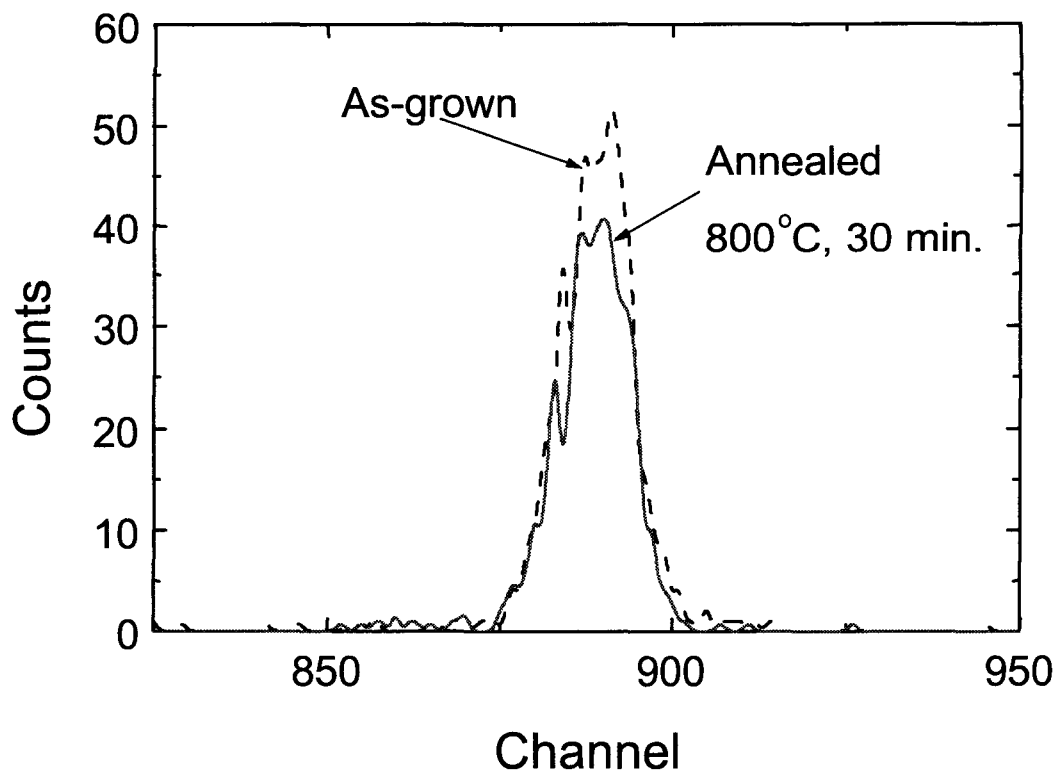
Figure 6.14. Rutherford backscattering spectra showing the Sn peak of the 2 nm $Sn_{0.10}Si_{0.90}$ film before and after post-growth annealing at 800°C for 30 min. The incorporated Sn decreases by about 18%.

6.5 Infrared Absorption of Sn-Rich Sn_xSi_{1-x} Quantum Dots in Si

As discussed in Section 5.2.1 (Fig. 5.2), results of the Slater-Koster parameter model predict the energy gap of Sn_xSi_{1-x} to be direct and semiconducting for the composition window $0.82 \leq x \leq 0.95$, corresponding to an energy gap window of $0 \leq E_g$ (eV) ≤ 0.40. In order for the Sn_xSi_{1-x} alloy system to have a direct gap, therefore, the alloy must be Sn-rich in composition. In Section 6.4 the composition of Sn-rich Sn_xSi_{1-x} quantum dots formed via phase separation from 2 nm $Sn_{0.10}Si_{0.90}$/Si films were estimated to be close to that of pure Sn, and therefore the dots can be expected to possess a direct energy gap. To gain insight into the optical properties, the Sn-rich Sn_xSi_{1-x} quantum dots synthesized from 2 nm $Sn_{0.10}Si_{0.90}$/Si films were analyzed using infrared absorption spectroscopy in the attenuated total reflection mode [37].

In the attenuated total reflection geometry, the angle of incidence of an infrared radiation entering a transmitting crystal of high refractive index like Si exceeds the critical angle θ_c and the radiation is reflected internally. Multiple passes can be made with a single crystal and the number of passes N scales directly with the length of the crystal l, given by $N = l/t \cot\theta$, where t is the crystal thickness and θ is the angle of incidence. The attenuated total reflection geometry is therefore an ideal geometry for absorption and vibrational spectroscopy of ultrathin materials on an infrared transmitting substrate.

The schematic geometry of the total internal reflection mode is shown in Fig. 6.15(a). The absorption measurements were made using a Fourier Transform Infrared Spectrometer equipped with a liquid nitrogen-cooled InSb detector. All samples were polished into trapezoids, with the bevel angle of 45 degrees. The thickness of the samples was 450 μm–500 μm. The tip-to-tip length l of the crystals was 25 mm. And the corresponding number of passes were 50-55 for normal entrance on the face of the beveled edge. A float zone Si (100) substrate polished into a trapezoid was used as the reference sample for background correction. The phase-separated Sn-rich Sn_xSi_{1-x} quantum dots were near the surface of the shorter face of the trapezoid, as indicated in Fig. 6.15(a). The as-grown 2 nm $Sn_{0.10}Si_{0.90}$/Si films were polished into trapezoids and spectra were taken before and after annealing in vacuum at 800°C for 30 min. No significant surface roughness of the order of the wavelength of the incident radiation was observed, so that the absorption features are not a result of scattering.

Figure 6.15(b) shows the absorption spectra before and after annealing at 800°C for 30 min. The absorbance is plotted in relative absorbance because the thickness of the reference Si crystal is not exactly the same as the thickness of the crystal containing the quantum dots. The thickness difference was approximately 20 μm. The relative absorbance spectra of the annealed film and the as-grown film can, however, be directly compared with each other since both were corrected using the background spectrum collected from the same reference Si crystal. The spectra have been translated so that the minimum value of absorbance around 2200 cm^{-1} has been taken as the baseline value of zero. The spectra have an absorption feature starting at about 0.27 eV (2250 cm^{-1}) that increases in intensity by a factor of two upon

annealing. The energy of 0.27 eV does not correspond to any intraband transitions with high joint density of states in bulk α-Sn [14], suggsting that the absorption edge is that of quantum-confined carrier absorption in Sn-rich Sn_xSi_{1-x} quantum dots. For the case of bulk Sn_xSi_{1-x} according to the prediction in Fig. 5.2, the energy of 0.27 eV corresponds to Sn composition of at least 85%. Since the carriers are quantum-confined, the corresponding the composition of the quantum dots would be higher in Sn content.

Taking the thickness of the encapsulated alloy layer containing quantum dots to be that of the original thickness of 2 nm, and taking the number of bounces determined from the geometry, a rough estimate of the absorption coefficient can be made. The absorption coefficient as a function of energy is shown in Fig. 6.16. Since the original absorption spectra were translated such that the points of minimum absorption were taken as the zero baseline, the absorption spectra shown in Fig. 6.16 represent a lower bound spectra. It is noteworthy that the relatively high values ($>5\times10^3 cm^{-2}$) of absorption coefficient is consistent with the absorption due to a direct gap interband transition.
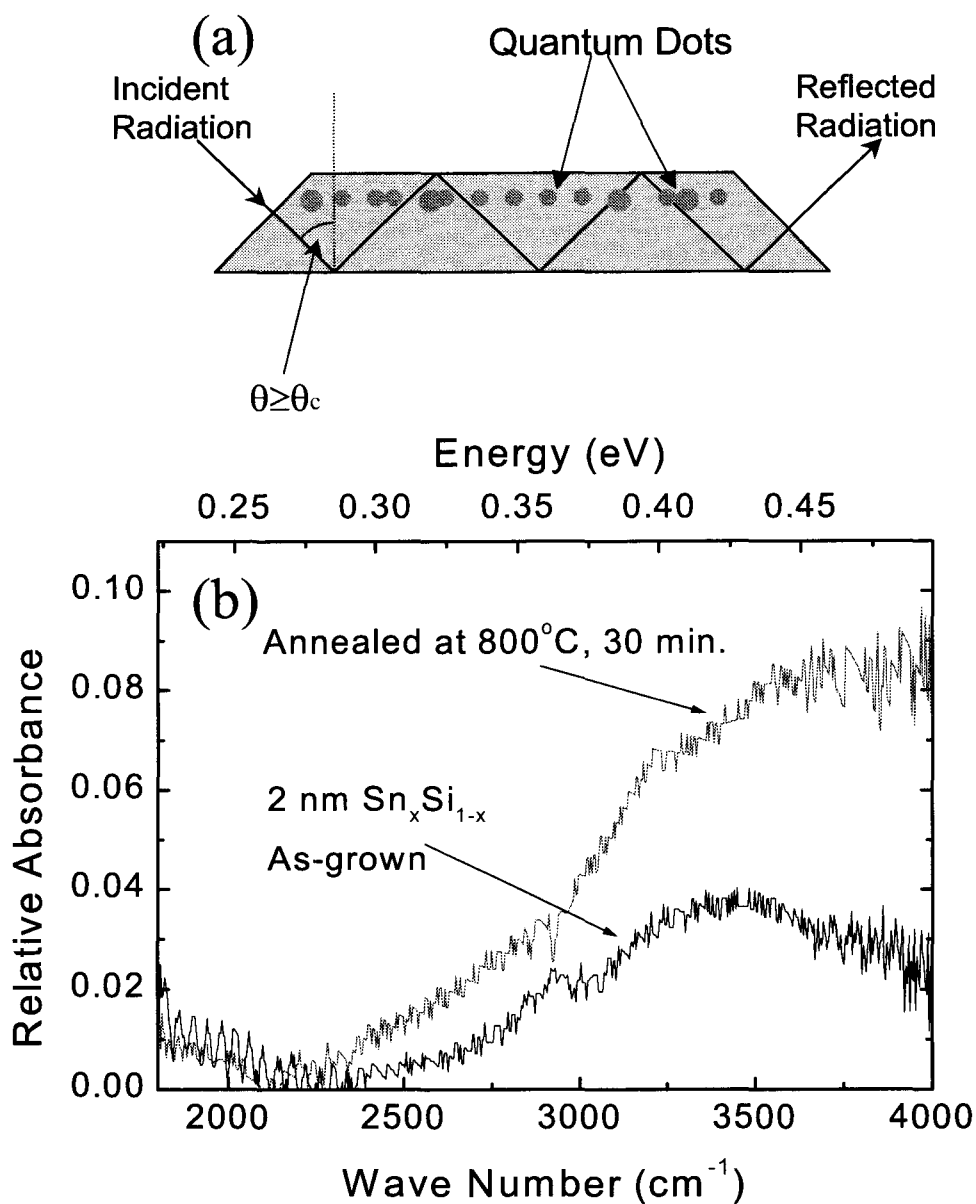
Figure 6.15. (a) A schematic illustration of the geometry of the attenuated total

reflectance infrared absorption spectroscopy. (b) Infrared absorption spectra of 2 nm

$Sn_{0.10}Si_{0.90}$/Si film before and after annealing at 800°C for 30 min., taken in the total

internal reflection mode.

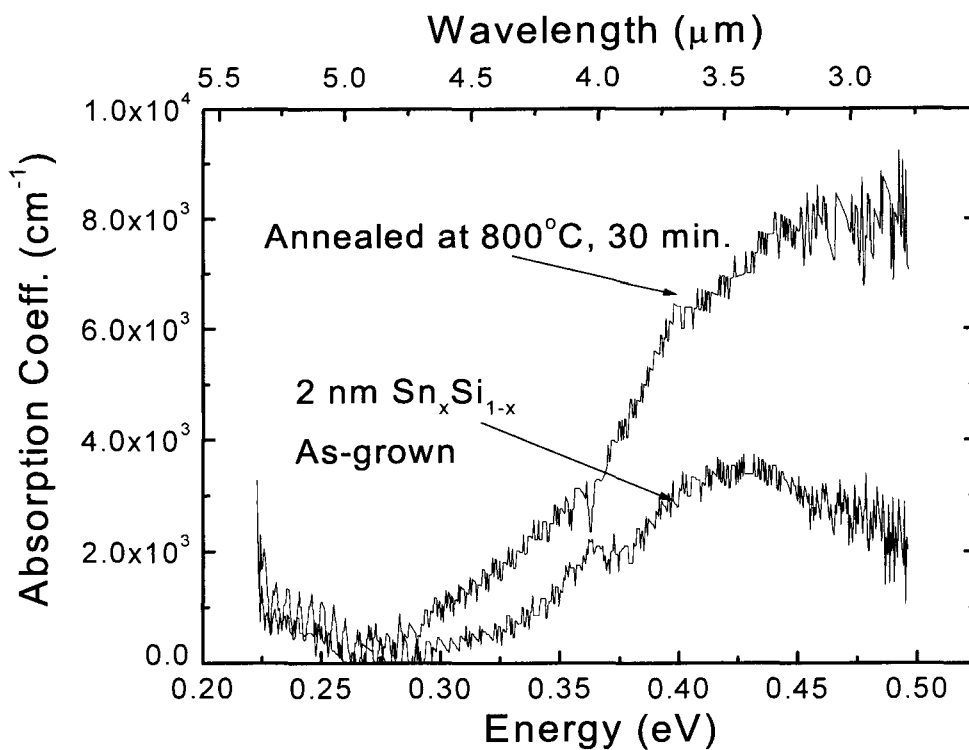Figure 6.16. Absorption coefficient as a function of energy (eV) and wavelength (μm) of 2 nm $Sn_{0.10}Si_{0.90}$/Si film before and after annealing at 800°C for 30 min., obtained from the infrared absorption spectra in Fig. 6.15 taken in the total internal reflection mode.

6.6 Conclusions

In sum, the formation of coherently strained Sn-rich Sn_xSi_{1-x} quantum dots inside Si matrix has been demonstrated to occur by two-dimensional phase separation from an epitaxally stabilized Sn_xSi_{1-x} metastable solid solution. Transmission electron microscopy studies reveal that the phase separation initially proceeds by spinodal decomposition and subsequent thermal annealing results in the nucleation of regularly shaped Sn-rich Sn_xSi_{1-x} quantum dots. The nucleated dots grow by a coarsening mechanism. Cross-sectional high-resolution transmission electron microscopy reveals that the dots are completely coherent with the Si matrix and that the shape of the nanocrystals resembles that of the equilibrium shape of Si, namely tetrakaidecahedron dominated by {100} and {111} facets. Infrared absorption spectra taken in the total internal reflection geometry show an absorption feature starting at about 0.27 eV (2250 cm^{-1}) that increases in intensity by a factor of two upon annealing. The absorption coefficient spectra obtained from the absorption spectra are consistent with interband transitions of quantum confined carriers across the direct gap of Sn-rich Sn_xSi_{1-x} quantum dots with Sn composition exceeding 85%.

Bibliography

[1]   G. Medeiros-Ribeiro, A.M. Bratkovski, T.I. Kamins, D.A.A. Ohlberg, and R.S.Williams, Science **279**, 353 (1998).

[2]   D.J. Eaglesham and M. Cerullo, Phys. Rev. Lett. **64**, 1943 (1990).

[3]   Y.-W. Mo, D.E. Savage, B.S. Swartzentruber, and M.G. Lagally, Phys. Rev. Lett. **65**, 1020 (1990).

[4]   M. Krishnamurty, J.S. Drucker, and J.A. Venables, J. Appl. Phys. **69**, 6461 (1991).

[5]   J.A. Floro, E. Chason, M.B. Sinclair, L.B Freund, and G.A. Lucadamo, Appl. Phys. Lett. **73**, 951 (1998).

[6]   S. Guha, A. Madhukar, and K.C. Rajkumar, Appl. Phys. Lett. **57**, 2110 (1990).

[7]   D.E. Jesson, K.M. Chen, S.J. Pennycook, T. Thundat, and R.J. Warmack, Science **268**, 1161 (1995).

[8]   J. Tersoff and F.K. LeGoues, Phys. Rev. Lett. **72**, 3570 (1994).

[9]   M. Hammar, F.K. LeGoues, J. Tersoff, M.C. Reuter, and R.M. Tromp, Surf. Sci **349**, 129 (1996).

[10] H. Sunamura, N. Usami, Y. Shiraki, and S. Fukatsu, Appl. Phys. Lett. **66**, 3024 (1995).

[11] R. Apetz, L. Vescan, A. Hartmann, C. Dieker, and H. Luth, Appl. Phys. Lett. **66**, 445 (1995).

[12] P. Schittenhelm, M. Gail, J. Brunner, J.F. Nützel, and G. Abstreiter, Appl. Phys. Lett. **67**, 1292 (1995).

[13] K. A. Johnson and N.W. Ashcroft, Phys. Rev. **B 20**, 14480 (1996).

[14] Y. Li and P.J. Lin-Chung, Phys. Rev. **B 27**, 3465 (1983).

[15] R.A. Soref and C. H. Perry, J. Appl. Phys. **69**, 539 (1991).

[16] H. A. Atwater, G. He, and K. Saipetch, Mat. Res. Symp. Proc. **355**, 123 (1995).

[17] S. Groves and W. Paul, Phys. Rev. Lett. **11**, 194 (1963).

[18] G. He and H. A. Atwater, Phys. Rev. Lett. **79**, 1937 (1997).

[19] B. I. Craig, Superlattices and Microstructures **12**, 1 (1992).

[20] See, for example, A.D. Yoffe, Adv. Phys. **42**, 173 (1993), and the references therein.

[21] T.B. Massalski *et al.*, *Binary Alloy Phase Diagrams*, 2nd edition., Am. Soc. Metals, Materials Park, 1990.

[22] P.M. Petroff and G. Medeiros-Ribeiro, Mat. Res. Soc. Bull. **21**, 50 (1996).

[23] E. Bauer, Z. Kristallogr. **110**, 372 (1958).

[24] J.W. Cahn, Trans. Metall. Soc. AIME **242**, 166 (1968).

[25] See, for example, K.B. Rundman and J.E. Hilliard, Acta. Metall. **15**, 1025 (1967).

[26] M. Zinke-Allmang, L.C. Feldman, and M.H. Grabow, Surf. Sci. Rep. **16**, 377 (1992).

[27] I.M. Lifshitz and V.V. Slyzov, J. Phys. Chem. Solids **19**, 35 (1961).

[28] C. Wagner, Z. Elektrochem.**65**, 581 (1961).

[29] C. Herring, J. Appl. Phys. **21**, 301 (1950).

[30] R.D. Doherty, Met. Sci. J **16**, 1 (1982).

[31] R. Swalin, *Thermodynamics of Solids, 2nd ed.*, John Wiley and Sons, New York, 1972, pp. 141-148.

[32] N.J. Choly, Senior Thesis, California Institute of Technology, 1998, pp. 4-8.

[33] J.W. Cahn, Acta Metall. **10**, 179 (1962).

[34] W. Klemm and H. Stöhr, A. Anorg. Chem. **241**, 305 (1939).

[35] H. Nakayama, M. Sekine and H. Fujita, Vacuum **42**, 547 (1991).

[36] D.J. Eaglesham, A.E. White, L.C. Feldman, N. Moriya, and D.C. Jacobson, Phys. Rev. Lett. **70**, 1643 (1993).

[37] N.J. Harrick, Appl. Spectrosc. **41**, 1 (1987).